

AN ABSTRACT OF THE THESIS OF

Richard Turton for the degree of Doctor of Philosophy

in Chemical Engineering presented on July 31, 1986

Title: HEAT TRANSFER STUDIES IN FINE PARTICLE FLUIDIZED BEDS

Abstract approved: _____

Redacted for Privacy

Two new experimental techniques are presented which enable the direct measurement of heat transfer coefficients in fine particle gas fluidized beds.

The first technique uses fine electrically heated Alumel wires to probe fluidized beds of fine particles. The wires varied in diameter from 50.8 to 813 μ m while the bed material consisted of uniformly sized sand, glass, aluminum and polyethylene particles from 105 to 754 μ m. The wires are loose and hence are free to move around and sample the cross-section of the bed. By measuring the voltage and current flow in the wire the temperature and hence heat transfer coefficient can be determined. The heat transfer coefficients obtained varied from 262 to 2100 W/m²·K and these were successfully correlated by a new equation. The heat transfer coefficients obtained for fine wires in fine particle fluidized beds are greater than for fine wires in air alone. The significance of this enhancement in heat transfer is discussed.

The second technique uses the change in magnetic properties of a low Curie-point ferrite to track the changing temperature of a cold sample of particles injected into a hot fluidized bed. The hot

fluidized bed is surrounded by a detector coil which is connected to an electronic sensor. This coil-sensor arrangement is capable of detecting small changes in the magnetic properties of the material in the fluidized bed. A model was developed to take into account the effects of particle size distribution, mixing, equipment lag, and changing magnetic permeability on the output response of the ferrite sensor. By comparing the data and model the heat transfer coefficient could be evaluated. The size of particles studied varied from 125 μm to 355 μm while the heat transfer coefficients obtained varied from 70 to 230 $\text{W/m}^2\cdot\text{K}$.

The heat transfer coefficients evaluated using this technique are greater than the previously reported values but lie below those predicted for a single particle in air alone. A qualitative discussion is presented that supports the argument that the true fluid-particle heat transfer coefficients for fine particle fluidized systems lie above the correlation for single spheres in air.

© Copyright by Richard Turton
July 31, 1986

All Rights Reserved

HEAT TRANSFER STUDIES IN FINE PARTICLE FLUIDIZED BEDS

by

Richard Turton

A THESIS

submitted to

Oregon State University

in partial fulfillment of
the requirements for the
degree of

Doctor of Philosophy

Completed July 31, 1986

Commencement June 1987

APPROVED:

Redacted for Privacy

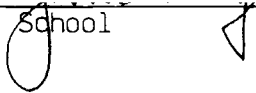
Professor of Chemical Engineering in Charge of Major

Redacted for Privacy

Head of Department of Chemical Engineering

Redacted for Privacy

Dean of Graduate School



Date Thesis is Presented: July 31, 1986

Typed By: Meredith J. Bacon-Turton

ACKNOWLEDGEMENT

First and foremost, I would like to thank my advisor, mentor and friend, Dr. Octave Levenspiel. I feel very honored to have worked under such a gifted educator and researcher and hope that one day I may be able to inspire my graduate students as he has inspired me.

My thanks also go to the other faculty members in the Chemical Engineering Department, especially Professors Wicks, Knudsen and Mrazek, whose help I have often sought and have never been denied.

I would also like to thank the graduate students of the department from whom I have learnt a great deal. In particular I would like to recognize Ty Daniel and Con Kambitsis whose friendship I have greatly enjoyed and I hope that one day we three can take that trip around the world.

My thanks to Nick Wannenmacher without whose technical help I would surely have been lost and who has taught me that "doing it right the first time" does make sense.

Special thanks go to the Bacon family and in particular Marion, Meric, Frank and Murphy. The former two for supporting my golfing habit and 19th hole activities, and the latter two for just being themselves.

Penultimately I would like to thank my parents, Don and Joyce for their love and support and also for setting me on the road to higher education. I have never been able to put my finger on what

made me pursue this wonderful career but I'm sure that they had a lot to do with it.

Finally, I would like to thank Meredith, my wife and best friend, not only for the outstanding typing job under adverse conditions but also for her love and support under difficult circumstances which allowed me to reach my goal.

TABLE OF CONTENTS

	<u>Page</u>
I. INTRODUCTION	1
II. PREVIOUS WORK	5
II-1. Experimental Techniques	5
II-1-1. Steady State Batch Experiment	5
II-1-2. Unsteady State Batch Experiment	7
II-1-3. Steady State Continuous Experiment	8
II-1-4. Dynamic Response Methods	8
II-1-5. Experiments Using Immersed Surfaces	10
II-2. Theories Explaining Experimental Heat Transfer Data	11
III. HEAT TRANSFER BETWEEN A FREELY MOVING FINE WIRE AND A FLUIDIZED BED OF FINE PARTICLES	15
III-1. Introduction and Description of Experiment	15
III-2. Apparatus and Experimental Procedure	16
III-2-1. Apparatus	16
III-2-2. Experimental Procedure	21
III-3. Experimental Results	22
III-3-1. Calculation of Heat Transfer Coefficients	22
III-3-2. Calibration of Horizontal Wires in Flowing Air	24
III-3-3. Heat Transfer Coefficients for Loose Wires in Fluidized Beds	27
III-4. Comparison of Results with Previous Work	31
III-5. Discussion of Results	38
III-6. Conclusions	40

	<u>Page</u>
IV. TRANSIENT HEATING OF A SAMPLE OF COLD MAGNETIC PARTICLES INJECTED INTO A HOT FLUIDIZED BED	41
IV-1. Introduction and Description of Experiment	41
IV-2. Apparatus and Experimental Procedure	48
IV-2-1. Apparatus	48
IV-2-2. Experimental Procedure	57
IV-3. Experimental Results	60
IV-3-1. Cold Fluidized Bed Mixing Studies	60
IV-3-2. Hot Fluidized Bed Mixing Studies	64
IV-3-3. Analysis of Data	69
IV-3-3-1. Theory and Formulation of Model	69
IV-3-3-2. Parametric Studies	80
IV-3-3-3. Comparison of Model with Experimental Data	86
IV-4. Comparison of Results with Previous Work	91
IV-5. Discussion of Results	91
IV-6. Conclusions	98
IV-7. Recommendations for Future Work	98
BIBLIOGRAPHY	100
APPENDICES	
A. Determination of Some Physical Constants of Alumel	104
B. Determination of the Temperature Profile and Average Temperature in an Electrically Heated Wire or Cylinder	113
C. Experimental Results for Straight Alumel Wires in a Flowing Air Stream	116

	<u>Page</u>
D. Evaluation of the Properties of the Particles Used in the Heated Wire Experiments	122
E. Results for Heat Transfer from Loose Alumel Wires to Fluidized Beds	136
F. Error Analysis for the Wire Experiment	153
G. Evaluation of the Physical Properties of Ferrite TC-71	168
H. Ferrite Sensor-Electronic Circuitry	184
I. Determination of Size Distribution and u_{mf} of Ferrite TC-71 and Zirconia	201
J. Computer Programs	207
K. Preliminary Studies on the Ferrite Sensor	215
L. Experimental Results for Hot and Cold Mixing Studies Discussed in Chapter IV	226

LIST OF FIGURES

<u>Figure</u>		<u>Page</u>
I-1	Previously Reported Fluid-Particle Heat Transfer Data in Fluidized Beds	2
III-1	Schematic Diagram of Equipment Used in the Heated Wire Experiment	19
III-2	Nusselt Number vs. Reynolds Number for Straight Horizontal Wires in Air.	25
III-3	Nusselt Number vs. Reynolds Number for Wires in Fluidized Beds of Glass Particles.	30
III-4	Comparison of Correlation Eq. III-9 with Experimental Data	32
III-5	Comparison of Jacob and Osberg's (31) Results with Eq. III-9	34
III-6	Comparison of Data from this study with Vreedenberg's (51), (52) Correlation for Heat Transfer from Horizontal Tubes to Fluidized Beds	35
III-7	Comparison of Present Experimental Results for Fine Freely Moving Wires in Fluidized Beds with Fine Wires in Flowing Air	37
IV-1	Relative Change of Magnetic Permeability with Temperature for Ferrite TC-71.	44
IV-2	Schematic Diagram of Fluidized Bed System Used in the Transient Heating Experiments	50
IV-3	Fluidized Bed Unit Used in Transient Heating Experiments.	52
IV-4	Detector Coil for Sensing Changes in Magnetic Permeability.	54
IV-5	Injection Device Used in Transient Heating Experiments.	56
IV-6	Details of Computer Data Acquisition System	58
IV-7	Processes Occuring During a Cold Mixing Experiment	62

<u>Figure</u>		<u>Page</u>
IV-8	Typical Response Curves for Cold Mixing Experiments, System A	63
IV-9	Typical Response Curves for Hot Mixing Studies, System A	70
IV-10	Output Response for a Hot Mixing Experiment for an Ideal Process	72
IV-11	Hot Mixing Data for System A, Run No. 1. The Effects of Adjusting the Data to Take Account of Mixing	74
IV-12	The Three Effects Tending to Cause a Smearing of the Response Signal	77
IV-13	Comparison of Rigorous and Simplified Models	81
IV-14	The Effect of Changes in h on the Profiles Generated by the Rigorous Model	82
IV-15	The Effect of a ± 10 Percent Change in the Specific Heat Value on the Profiles Generated by the Rigorous Model	84
IV-16	The Effect of a $\pm 2.5^{\circ}\text{C}$ Change in Hot Bed Temperature on the Profiles Generated by the Rigorous Model	85
IV-17	Comparison of Experimental Data and Least Squares Error Profile Generated from Rigorous Model -- System A, Run No. 1	88
IV-18	Comparison of Experimental Data and Least Squares Error Profile Generated from Rigorous Model -- System A, Run No. 2	89
IV-19	Comparison of Experimental Data and Least Squares Error Profile Generated from Rigorous Model -- System A, Run No. 3	90
IV-20	Comparison of the Results of the Present Work with Previously Reported Data	92
A-1	Experimental Set Up for the Determination of the Temperature Coefficient of Resistance " α " of Alumel Wire	105

<u>Figure</u>		<u>Page</u>
A-2	Temperature vs. Resistance Data for Various Diameter Alumel Wires	107
A-3	Experimental Set Up Used in Determining the Resistivity of Alumel Wires	110
D-1	Pressure Drop Versus Superficial Air Velocity for 230 μ m Diameter Glass Beads	128
G-1	Experimental Equipment Used in the Evaluation of the Specific Heat Capacity of Ferrite TC-71	169
G-2	Heating Curve for the Experimental Determination of the Specific Heat Capacity of Aluminum	174
G-3	Experimental Equipment used to Determine the Thermal Conductivity of Ferrite TC-71	176
G-4	Temperature vs. Thermal Conductivity Curve for Teflon	178
G-5	Sample Container Used in the Magnetic Permeability vs. Temperature Experiments	180
G-6	Ferrite Sensor Output Voltage vs. Temperature of a 1.25 g Ferrite TC-71 Sample	182
H-1	Block Diagram of Circuit	193
H-2	Schematic Diagram of Main Circuit	194
H-3	Schematic Diagram of Auxillary, Phase Tracking, Card	195
H-4	Front Panel Layout	196
H-5	Layout of Main Circuit Amplifier Card	197
H-6	Layout of Auxillary Card	198
H-7	Key Waveforms on Main Circuit Card	199
H-8	Key Waveforms on Auxillary Card, and Test Points	200
I-1	Pressure drop vs. Superficial Velocity for 50 $^{\circ}$ -60 $^{\circ}$ Zirconia	203

<u>Figure</u>		<u>Page</u>
I-2	Comparison of Data for Zirconia and Ferrite TC-71 with the Correlation Due to Wen and Yu (64)	206
K-1	Sensitivity Map of the Detector Coil	216
K-2	Results of Linearity Test on Ferrite Sensor	219
K-3	Output Voltage vs. Length/Diameter Ratio of Ferrite Sample	223
L-1	Results for the Cold Mixing Studies on System B	227
L-2	Results for the Cold Mixing Studies on System C	228
L-3	Results for the Cold Mixing Studies on System D	229
L-4	Results for the Cold Mixing Studies on System E	230
L-5	Results for the Cold Mixing Studies on System F	231
L-6	Results for the Hot Mixing Studies on System B, Run No. 1	232
L-7	Results for the Hot Mixing Studies on System B, Run No. 2	233
L-8	Results for the Hot Mixing Studies on System B, Run No. 3	234
L-9	Results for the Hot Mixing Studies on System C, Run No. 1	235
L-10	Results for the Hot Mixing Studies on System C, Run No. 2	236
L-11	Results for the Hot Mixing Studies on System C, Run No. 3	237
L-12	Results for the Hot Mixing Studies on System D, Run No. 1	238
L-13	Results for the Hot Mixing Studies on System D, Run No. 2	239
L-14	Results for the Hot Mixing Studies on System D, Run No. 3	240

<u>Figure</u>		<u>Page</u>
L-15	Results for the Hot Mixing Studies on System E, Run No. 1	241
L-16	Results for the Hot Mixing Studies on System E, Run No. 2	242
L-17	Results for the Hot Mixing Studies on System E, Run No. 3	243
L-18	Results for the Hot Mixing Studies on System F, Run No. 1	244
L-19	Results for the Hot Mixing Studies on System F, Run No. 2	245
L-20	Results for the Hot Mixing Studies on System F, Run No. 3	246

LIST OF TABLES

<u>Table</u>		<u>Page</u>
III-1	Physical Properties of Alumel	17
III-2	Particle and Wire Size Combinations Used in Study	18
III-3	Summary of the Physical Properties of Fluidized Particles	28
IV-1	Some Physical Properties of TC-71 Ferrite	43
IV-2	Some Physical Properties of Zirconia	46
IV-3	Minimum Fluidization Velocities for Zirconia and Ferrite TC-71 Particles	47
IV-4	Combinations of Ferrite TC-71 and Zirconia Used in Experimental Runs	49
IV-5	Fitted Constants for Eq. IV-1 and Fluidization Levels Used in Cold Mixing Experiments	65
IV-6	Fluidized Bed Temperatures at the Beginning and End of the Hot Mixing Experiments	67
IV-7	Output Voltage from the Ferrite Sensor Predicted by Theory	78
IV-8	Heat Transfer Coefficients for a Cold Sample of Particles Injected into a Hot Fluidized Bed	87
IV-9	Characteristic Times for Heating and Mixing of Different Sized Particles	95
A-1	Summary of α Values for Alumel Wires	108
A-2	Summary of Resistivity Data for Alumel Wires	111
C-1	Experimental Data for Alumel Wires in Flowing Air	117
D-1	Size Distribution and Average Particle Size Calculation for 106 μ m Glass Beads	123
D-2	Size Distribution of Particles	124

<u>Table</u>		<u>Page</u>
D-3	Pressure Drop Versus Superficial Air Velocity Data for All the Particle Systems	129
D-4	Bulk Density, Void Fraction and Sphericity of Particles in Fluidized and Packed Beds	133
E-1	Resistance Measurements for Loose Alumel Wire (127 μm diameter) in a Fluidized Bed of Glass Beads (106 μm diameter) at Different Levels of Fluidization	138
E-2	Experiment Results of Jacob and Osberg (31)	141
E-3	Results for Heat Transfer from Loose Wires in Fluidized Beds -- Material: Glass	142
E-4	Results for Heat Transfer from Loose Wires in Fluidized Beds -- Material: Sand	145
E-5	Results for Heat Transfer from Loose Wires in Fluidized Beds -- Material: Polyethylene	148
E-6	Results for Heat Transfer from Loose Wires in Fluidized Beds -- Material: Aluminum	152
F-1	Results for 100 Repetition Experiments to Determine the Resistance of a Wire	156
F-2	Errors in the Experimentally Determined Nusselt Numbers for Straight Wires in Air	158
F-3	Errors for the Experimentally Determined Nusselt Numbers for Wires in Fluidized Beds	159
F-4	Relative Error in the Predicted Nusselt Number	167
G-1	Results of Specific Heat Capacity Measurements	171
G-2	The Temperature History of the Deionized Water Sample During the Experimental Determination of the Specific Heat of Aluminum	173
G-3	The Change in Magnetic Properties of Ferrite TC-71 with Temperature	181
H-1	Integrated Circuits Used in Ferrite Sensor	191
H-2	Connections to 8 pin Auxillary Card	192

<u>Table</u>		<u>Page</u>
I-1	Particle Size Distribution of Ferrite TC-71	202
I-2	u_{mf} for Ferrite TC-71 and Zirconia	204
K-1	Linearity Experiments on Ferrite Sensor	218
K-2	Results of Experiments on the Effect of the Sample Shape on the Output Voltage of the Ferrite Sensor	222

NOMENCLATURE

Symbol

a	surface area per unit volume of bed (m^2/m^3)
A	cross-sectional area of bed (m^2)
A_1	a constant defined in Eq. III-5 (m^{-2})
A_1	a constant defined in Eq. IV-1 (mV)
B_1	a constant defined in Eq. III-5 (K/m^2)
B_1	a constant defined in Eq. IV-1 (mV)
Bi	Biot number
C_1	a constant defined in Eq. IV-1 (s^{-1})
C_p	specific heat capacity ($\text{J}/\text{kg}\cdot\text{K}$)
d	diameter (m)
$E()$	first order exponential time lag function
$ Fo$	Fourier number
G_o	superficial mass velocity ($\text{kg}/\text{m}^2\cdot\text{s}$)
Gr	Grashof number
h	heat transfer coefficient ($\text{W}/\text{m}^2\cdot\text{K}$)
I	electric current (amperes)
k	thermal conductivity ($\text{W}/\text{m}\cdot\text{K}$)
L	half length of wire (m)
N	number of replications in an experiment
Nu	Nusselt number
P	pressure (Pa)
Pr	Prandtl number
$P_x()$	mass fraction probability density function

Symbol

q	quantity of heat (J)
Q	sum of squares error
r	radial distance (m)
R	electrical resistance (ohms)
Re	Reynolds number
t	time (s)
T	temperature (K)
ΔT	temperature change (K)
u	gas velocity (m/s)
V	voltage (volts)
ΔV	voltages change (volts)
W	weight of bed (kg)
x	mass fraction
Z	distance or height of bed (m)

Greek Symbols

α	temperature coefficient of resistance (K^{-1})
Γ	resistivity (ohm-m)
ϵ	voidage
$\theta = (T/67)$	dimensionless temperature
λ	a constant defined in Eq. IV-1 (m^{-1})
μ	viscosity (kg/m \cdot s)
ρ	density (kg/m 3)
τ	characteristic time (s)
ϕ	sphericity

<u>Symbol</u>	<u>Subscripts</u>
a	air and/or fluidized bed
AL	aluminum
bed	bed
bot	bottom
bulk	bulk
curie	curie
coil	coil
corr	corrected
f	film or final
g	gas
h	heating
i	initial or replication
in	inlet
m	mixing
mf	minimum fluidization
o	reference or superficial
p	particle
pk	packed bed
r	radial
ref	reference
s	solid
screen	Tyler screen
top	top

Symbol

w	wire
wt	water

Superscripts

\wedge	model
$-$	average
\cdot	rate
exp	experimental
K	from Kothari's (58) equation
RM	from Ranz and Marshall's (1) equation

HEAT TRANSFER STUDIES IN FINE PARTICLE FLUIDIZED BEDS

I. INTRODUCTION

Over the past forty years numerous studies have been conducted into the heat transfer processes occurring in fluidized beds.

Broadly speaking these studies can be divided into two categories.

The first category consists of processes in which heat is transferred from a fluidized bed to a surface immersed in the bed. The surfaces studied have varied both in geometry and size with considerable emphasis on horizontal and vertical cylinders. The information gained in this type of experiment is essential for the successful design of commercial fluidized bed reactors where often heat must be removed or added to the bed.

The second category of studies concerns the heat transfer process occurring between the solids in the bed and the fluid used to fluidize them. This information is needed to verify or explain the fundamental mechanisms of heat transfer occurring within the bed and is essential if we are to understand the roles played by both the solids and the fluid in the heat transfer process.

The purpose of this work is to review the heat transfer data in the second category of studies and to investigate an anomaly between theory and experiment which has come about over the years.

The experimental results of previous workers are shown in Figure I-1 as a plot of the dimensionless Nusselt number (Nu_p) versus the dimensionless particle Reynolds number (Re_p). Also shown in Figure I-1 is the Ranz-Marshall (1) correlation (Eq. I-1) which

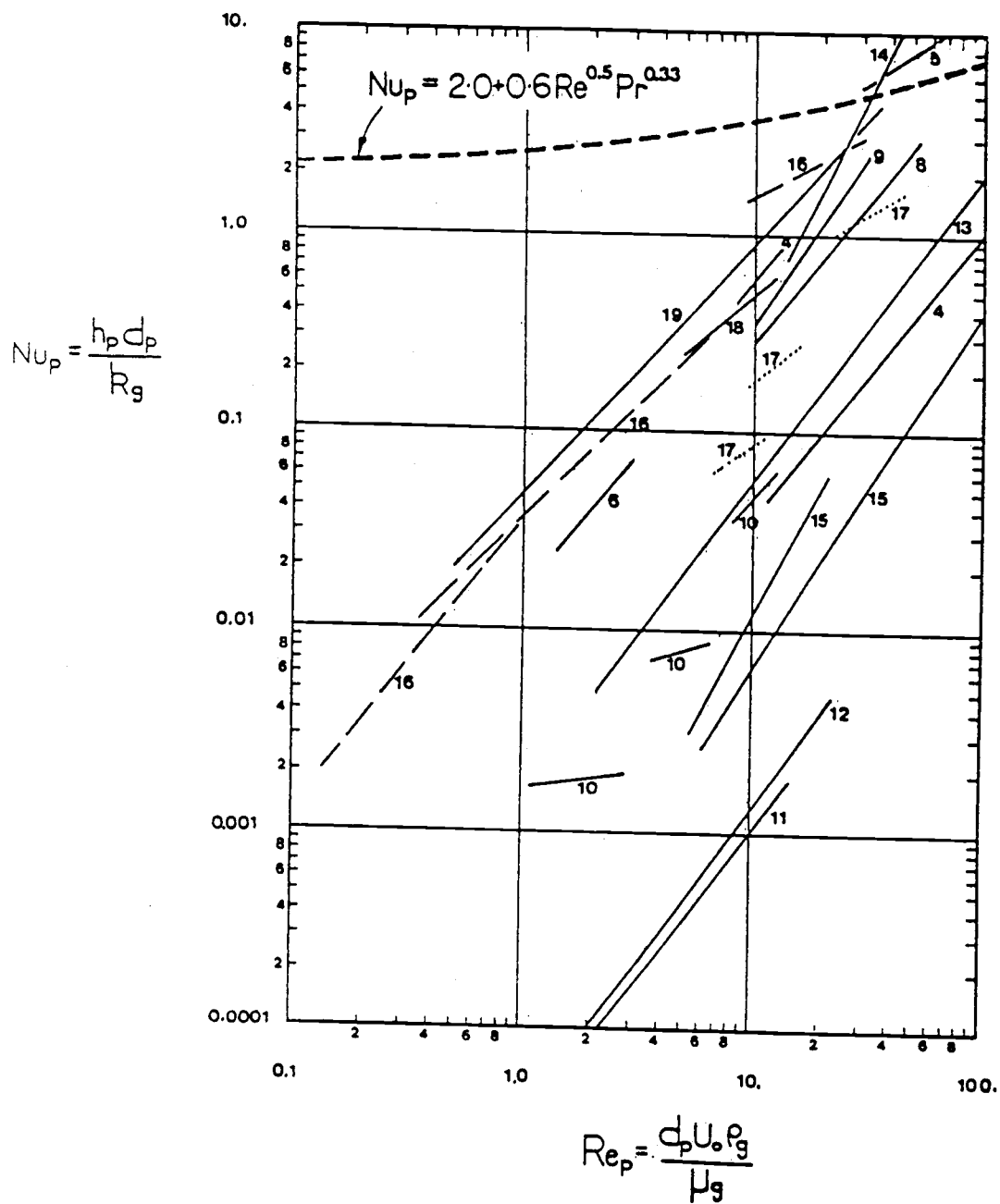


Figure I-1. Previously Reported Fluid-Particle Heat Transfer Data in Fluidized Beds (numbers refer to references given in Bibliography)

describes the heat transfer from a single sphere to a fluid stream flowing past it:

$$Nu_p = \frac{h_p d_p}{k_g} = 2.0 + 0.6 Re_p^{1/2} Pr^{1/3} \quad (I-1)$$

Eq. I-1 is semi-empirical and shows that disregarding natural convection effects there exists a limiting Nusselt number of 2.0 for the zero flow condition, i.e., as $Re_p \rightarrow 0$. This limiting value of 2.0 for the Nusselt number of spheres in a stagnant medium is theoretically derivable and the available data in this region agree well with this limit.

The physical picture of a single sphere transferring heat to a flowing fluid is very different from that of a spherical particle transferring heat to a fluidized bed. However, qualitative reasoning suggests that since the fluidized bed is by nature turbulent, with solids and gas bubbles moving about and creating considerable mixing, that the mechanisms for transferring heat from a sphere or particle would be enhanced in a fluidized bed. Thus we might expect the data for fluidized bed heat transfer to lie somewhere above the correlation for a single sphere in a fluid.

This is the case for high Reynolds numbers ($Re_p > 100$). However, as particle size and hence Reynolds number decrease, we find that the experimental data fall below the correlation for a single sphere. Moreover, the Nusselt number drops more rapidly than the Reynolds number and appears to have no limiting value as

$Re_p \rightarrow 0$. This result seems contrary to our intuition and has been the subject of much controversy over the years.

This whole question could be resolved if a direct measurement of h_p in fine particle beds could be made. However, no one has been able to measure h_p directly in these systems, and by direct measure we mean measure q and ΔT as a fine particle cools or heats up in the bed. All the reported h_p data in Figure I-1 come from indirect measurements, which require assuming some flow pattern for gas and for solids, measuring the changing bed temperature and back calculating h_p .

The object of this work is, therefore, to attempt to clear up the apparent anomaly between theory and experiment by conducting a series of novel experiments in which the heat transfer coefficient for small fluidized particles will be measured directly. Two basic types of experiment were undertaken and are described in this work.

In Part I, an analogy is used between the heat transfer from a very fine wire in a fine particle fluidized bed and a sphere in a fine particle bed.

In Part II, a truly direct method is used to determine the heat transfer coefficient at low Reynolds number by taking advantage of the change in magnetic properties of a material with temperature.

Before the above experimental work is described a review of previous work and the various arguments given in favor and against a limiting Nusselt number will be given.

II. PREVIOUS WORK

Much work has been done in the past on fluid-particle heat transfer in fluidized beds. Both the experimental technique and the analysis of the data have varied widely between researchers. The purpose of this section is to summarize the various techniques used and the underlying assumptions used to interpret the data. Following this is a brief discussion of the various theories used to explain the data.

II-1. Experimental Techniques

Excellent reviews of the experimental techniques used for fluid-particle heat transfer in fluidized beds are given by Kunii and Levenspiel (2) and Botterill (3). These techniques can be broadly categorized into the following five groups.

II-1-1. Steady State Batch Experiment

This procedure was adopted by Chen (4), Delvosalle and Vandershuren (5), Frantz (6), Heertjes and McKibbins (7), Kettenring et al. (8) and Walton et al. (9). The idea is to fluidize a batch of particles by a fluid (gas) whose temperature is different from that of the solids. Heat must be either added or removed from the bed in order to achieve steady state. Once this has been reached the temperature of both gas and solids just above the distributor plate is measured. To obtain the fluid-particle heat transfer coefficient from the above measurements the experimenters assumed that the solids were stationary and that the gas moved

through the bed in plug flow. Using these assumptions, an integrated heat balance for the bed yields the following expression:

$$\log_e \left(\frac{T_g - T_s}{T_{g,in} - T_s} \right) = - \frac{h_p a Z}{G_o C_{p,g}} \quad (\text{II-1})$$

A plot of the left-hand side of Eq. II-1 versus the height Z gives a straight-line whose slope is proportional to h_p .

The procedure used by Chen (4) and Delvosalle and Vandershuren (5) is somewhat different from that described above since these researchers used moisture-containing particles during their constant rate drying period. By using a simultaneous heat and mass transfer analysis they were able to back calculate heat transfer coefficients from their data.

One of the major sources of error in this experimental technique is the determination of the gas temperature. Some researchers used a suction thermocouple to measure the gas temperature while others relied on bare thermocouples. Kunii and Levenspiel (2) discuss this point at some length and conclude that the bare thermocouple readings lie somewhat below those of the suction thermocouple. An additional source of error in this type of experiment is the need to evaluate the surface area of solid per unit volume a . Some researchers back calculated a from pressure drop measurements in packed beds while others measured a directly for a random sample of particles.

II-1-2. Unsteady State Batch Experiment

The following researchers adopted this procedure: Wamsley and Johanson (10), Fritz (11), Ferron (12), Shakhova (13), Sunkoori and Kaparathi (14), Yoshida (15), and Donnadieu (16). This technique essentially consists of making a step change in the temperature of the fluidizing gas (or liquid in the case of Sunkoori and Kaparathi (14)) and noting the temperature history of the gas leaving the bed. The heat transfer coefficient can then be back calculated from this data by assuming a flow pattern for both the gas and solids.

All the investigators assumed that the solids were well-mixed and all but Donnadieu (16) noting that the gas temperature was nearly constant throughout the bed, assumed the gas to also be well-mixed. Kunii and Levenspiel (2) point out that the observed gas temperature profile could be easily explained in terms of the flat tail of an exponential curve corresponding to the plug flow of gas through the bed. Using this assumption they derived the following integrated expression for the heat balance over the bed:

$$\log_e \left(\frac{\Delta T_g}{\Delta T_{g,in}} \right) = \frac{C_{p,g} G_o A}{W C_{p,s}} \left(\exp \left(- \frac{h_p a Z_f}{C_{p,g} G_o} \right) - 1 \right) t \quad (\text{II-2})$$

Using Eq. II-2, they recalculated the heat transfer coefficients and found that the scatter of the results was significantly reduced from the results based on mixed flow of gas. They, therefore, concluded that their initial assumption of plug flow for the gas was the correct one.

This method does not require the determination of the solids temperature and only the inlet and outlet gas temperatures are required thus any ambiguities in thermocouple readings are eliminated. However, the surface area per volume of particles is still required.

II-1-3. Steady State Continuous Experiment

Chen (4), Sato et al. (17), Anton (18) and Richardson and Ayers (19) used this technique. In essence the idea is to continuously feed and remove a stream of solids from a gas fluidized bed. At steady state the temperature of the gas and solids are determined and assuming plug flow of gas the total rate of heat transfer is given by:

$$q = h_p a \int_0^z \Delta T dz \quad (II-3)$$

The value of q in Eq. II-3 was determined by an overall heat balance on the gas while the integral on the right-hand side was determined graphically.

Again, determination of a and the use of bare thermocouples to measure the gas temperature are possible sources of error.

II-1-4. Dynamic Response Methods

More recently several researchers have used experimental methods in which a gas fluidized bed is excited by a varying temperature signal and the fluid-particle heat transfer coefficient is back calculated using various types of flow models. Littman and

Stone (20), Littman and Barile (21) and Lindauer (22) all imposed a sinusoidally varying temperature signal on the inlet fluidizing gas. They then observed the phase displacement of the outlet gas temperature and related that back to a heat transfer coefficient. In order to extract this coefficient from the data it was necessary to use a flow model to describe the heat transfer processes occurring in the bed. The assumptions used in the model were: plug flow of gas, infinite solids mixing, constant voidage, no radial temperature gradients and constant physical properties. Littman (20), (21) concluded that since the solids were well-mixed only minimum heat transfer coefficients could be inferred from the data, while Lindauer (22) compares his data for packed and fluidized beds and shows very similar values.

Gunn and Narayanan (23), on the otherhand, use a dispersion model to calculate the heat transfer coefficient from a series of heat impulse experiments. Their work is based on a technique originally proposed by Gunn (24) and Gunn and deSouza (25) for packed bed heat transfer. Their results indicate that the dispersion of heat in the axial direction is an important factor and must be considered if true fluid-particle heat transfer coefficients are to be obtained. It is interesting to note that their results give values of Nusselt number above the Ranz-Marshall equation down to Reynolds numbers of 2.0.

II-1-5. Experiments Using Immersed Surfaces

Chang and Wen (26) and Wen and Chang (27) determined heat transfer coefficients between a gas fluidized bed and a tagged particle immersed in the bed. They used a miniature thermocouple embedded into a fluidized particle approximately 5mm in diameter to determine the center point temperature. The cold tagged particle was secured in a bed of like particles and its temperature was recorded with time as the inlet gas temperature was changed. Knowing the gas temperature and solids mid-point temperature it was possible to back calculate the heat transfer coefficient. By varying the size of the tagged particle with respect to other particles in the bed it was possible to determine the individual roles played by particle-particle and gas-particle interactions. They concluded that between 10 and 35 percent of the total heat transfer is accounted for by a particle to particle transfer mode.

Ziegler et al. (28), Ziegler and Brazelton (29) and Shirai (30) conducted similar experiments as those described above with the exception that the tagged particles used by these investigators were between 80 and 200 times the size of the particles in the fluidized bed. They found that between 80 and 95 percent of the heat transferred was by way of particle to particle conduction. It should be noted that the large size differences between tagged and fluidized particles greatly affects the mechanism by which heat is transferred. These latter experiments more closely represent the situation of heat transfer between a bed and a large immersed surface (i.e., a tube) and therefore will not be considered further.

Jacob and Osberg (31) used a straight piece of heated tungsten wire, 125 μ m diameter and 4cm long, to probe a bed of glass particles. They measured heat transfer coefficients for different particle sizes and fluidizing gases they found maximum values of h_w for air in the range 1200-2900 W/m²·K.

Lastly, Barker (32) proposed an ingenious technique whereby a heat source, thermistor, current source and transmitter were all encapsulated into a 1cm diameter particle and this tagged particle was inserted into a fluidized bed. Although the device was built there were, unfortunately, no experimental results published.

II-2. Theories Explaining Experimental Heat Transfer Data

There has been widespread disagreement concerning the reasons for the very low values of Nusselt number obtained for fluidized bed systems at low Reynolds number. Similar results have been found for mass transfer in fluidized beds and for heat and mass transfer in packed beds. The following discussion includes arguments for and against the existence of a limiting Nusselt number in both packed and fluidized beds.

In Section I of this work it was noted that for a single sphere in a infinite stagnant medium there exists a limiting value of the Nusselt number equal to 2.0 and this value is theoretically derivable as well as being verified by experiment. One of the assumptions on which the theoretical analysis is based is that there is zero heat flux at a distance far away from the sphere, i.e.,

$$\lim_{r \rightarrow \infty} \frac{\partial T}{\partial r} \rightarrow 0$$

This assumption is equivalent to having a heat source or sink at infinity.

Cornish (33) was the first to point out that low Nusselt numbers ($Nu_p < 2.0$) could be achieved in multiparticulate beds due to the absence of a heat source or sink. This idea was extended by Nelson and Galloway (34) who used an analysis combining potential flow theory and a penetration model with a no flux condition at a finite distance from the particle. Their results indicate that for zero flow ($Re_p = 0$) the Nusselt number is zero. Rowe (35) extended their work, which was strictly derived for packed beds, to liquid fluidized beds.

Kato and Wen (36) suggest that the low observed Nusselt numbers can be attributed to the fact that the thermal boundary layers set up are much larger than the diameter of the particles. Thus the boundary layers overlap each other and hence greatly reduce the effective heat transfer surface area.

Zabrodsky (37) was the first to consider the effects of gas bypassing in his "Microbreak" theory. He assumes that all the gas in excess of that required for fluidization is capable of bypassing several horizontal rows of particles before it recombines with the rest of the gas stream. This splitting and recombination of streams continues up the bed and he shows that for $u_o/u_{mf} = 2$ and $d_p = 100\mu\text{m}$ the "Microbreak" theory predicts effective Nusselt numbers ≈ 0.04 .

Kunii and Levenspiel (2) also showed that gas bypassing could explain the low values of Nu_p . They used their "bubbling bed" model to calculate effective Nusselt numbers from the data of Heertjes and McKibbins (7) and Kettenring et al. (8). Their values of effective Nusselt number compared very favorably with those reported by those researchers. Delvosalle and Vanderschuren (5) developed a model along similar lines for large particle beds and the model predictions agreed well with their experimental findings.

Kunii and Suzuki (38) presented a flow model for packed beds in which low heat transfer coefficients obtained experimentally are explained in terms of the bypassing of gas around clusters of particles and stagnant gas. These clusters tend to act like large particles with the result that the measured effective Nusselt number is significantly below 2.0. Hughmark (39) presented a similar type of cluster model for fluidized beds and was able to correlate well the data of Richardson and Ayers (19) and Heertjes and McKibbins (7).

Glicksman and Joos (40) made a systematic study of packed and fluidized bed heat transfer and they concluded that, at least for packed beds, the effects of channeling and axial dispersion of heat were considerable and led to the anomalously low values of Nu_p . Martin (41) used a channeling model in which a fraction of the packed bed had a higher voidage than the rest. He showed that for quite modest differences in voidage for a small fraction of the bed, very low effective Nusselt numbers could be achieved. Shen et al. (42) also conclude that the effects of axial dispersion are the main cause of the apparently low values of Nu_p in packed beds. Gunn and

Narayanan (23) and Littman and Barile (21) conclude the same for fluidized beds.

To summarize this discussion we can say that Cornish (33), Nelson and Galloway (34), Rowe (35) and Kato and Wen (36) all present theories which say that the true Nusselt number for low or zero flow in a packed or fluidized bed should be zero. These researchers believe that the experimental findings represent true or local Nusselt numbers. All the other investigators give theories which show that the experimental results merely represent an apparent Nusselt number. Local or true Nusselt numbers may well have limiting values above 2.0 but due to the experimental techniques used only some integrated or overall effect can be measured which leads to very low apparent Nusselt numbers.

As pointed out previously no one has been able to devise an experiment which gives a direct measure of h_p for particles smaller than 500 μ m. The purpose, therefore, of this work is to present two methods by which local or true heat transfer coefficients for low Reynolds number can be determined directly.

III. HEAT TRANSFER BETWEEN A FREELY MOVING FINE WIRE AND A FLUIDIZED BED OF FINE PARTICLES

III-1. Introduction and Description of Experiment

The object of this experiment is to determine heat transfer coefficients h_w and Nusselt numbers Nu_w for a heated wire in a fluidized bed of particles with the same diameter as the wire. A comparison between these results and those obtained for a thin wire in air will indicate whether heat transfer is enhanced or degraded when carried out in a fluidized bed. By analogy this will indicate whether fluid-particle heat transfer in a fluidized bed should lie above or below the correlation for a single sphere (Eq. I-1) and hence whether a limiting Nusselt number exists.

The only similar experiments that have been done were those carried out by Jacob and Osberg (31), however these experimenters used a straight wire to probe the bed. In this study the wire is loose and thus can move fairly freely in the fluidized bed hence sampling the whole cross-section of the bed. The wire, in some ways, represents a string of fluidized particles moving within the bed and hence the heat transfer processes for the wire will be in many ways similar to a single or string of fluidized particles.

The information needed to calculate h_w includes the temperature of the fluidized bed, the power dissipated by the wire and the temperature of the wire. The first two quantities can be found directly by measurement, the wire temperature, however must be inferred by the change in its electrical resistance.

In order to obtain an accurate measurement of the change in resistance of the wire the wire material should possess both a high temperature coefficient of resistance α , for temperature sensitivity, and also a high resistivity ρ to ensure accuracy in the current I and voltage V measurements. The material chosen for all the wires was Alumel which gave the best combination of these desired properties. The temperature coefficient of resistance and the resistivity of Alumel were determined experimentally and were found to be in good agreement with the published data. The physical properties for Alumel used throughout this study are given in Table III-1 and the experimental determination of α and ρ is described in Appendix A.

The particles comprising the fluidized bed were of varying sizes and materials. In all, various combinations of 6 sizes of wires were tested in 12 sizes of 4 different types of solids. The different particle and wire size combinations used in this study are given in Table III-2.

It can be seen from Table III-2 that for each particle size and material an experimental run was carried out using at least one wire diameter smaller and one wire diameter larger than the fluidized particle. This allowed an estimate of the situation when wire and particle diameters are the same.

III-2. Apparatus and Experimental Procedure

III-2-1. Apparatus

The apparatus used in all the experimental runs in this study is shown schematically in Figure III-1. Fluidizing air supplied by

Table III-1. Physical Properties of Alumel

Physical Property	Experimentally Determined Value	Literature Value	Reference Source
Temperature Coefficient of Resistance α , (K^{-1})	0.00243	0.00239*	American Institute of Physics Handbook (43)
Thermal Conductivity k_w , ($W/m \cdot K$)	---	29.3 @ $90^{\circ}C$ * 29.7 @ $116^{\circ}C$ * 30.1 @ $132^{\circ}C$ *	Touloukian et al. (44)
Resistivity Γ , ($ohms \cdot m^2/m$)	28.7×10^{-8}	29.4×10^{-8} *	Omega Engineering (45)

* Represent values used in calculations in this study.

Table III-2. Particle and Wire Size Combinations Used in Study

Fluidized Material	Particle Size d_p (μm)	Wire Diameter d_w (μm)
Glass	106	50.8
	106,230	127.0
	106,230,465,613	254.0
	106,230,465,613	381.0
	465,613	508.0
	230,465,613	813.0
Polyethylene	246,494,754	127.0
	246,494,754	254.0
	246,494,754	381.0
	246,494,754	508.0
	246,494,754	813.0
Sand	105	50.8
	105,223	127.0
	105,223,670	254.0
	105,223,670	381.0
	105,223,670	508.0
	105,223,670	813.0
Aluminum	314,423	254.0
	314,423	381.0
	314,423	508.0
	423	813.0

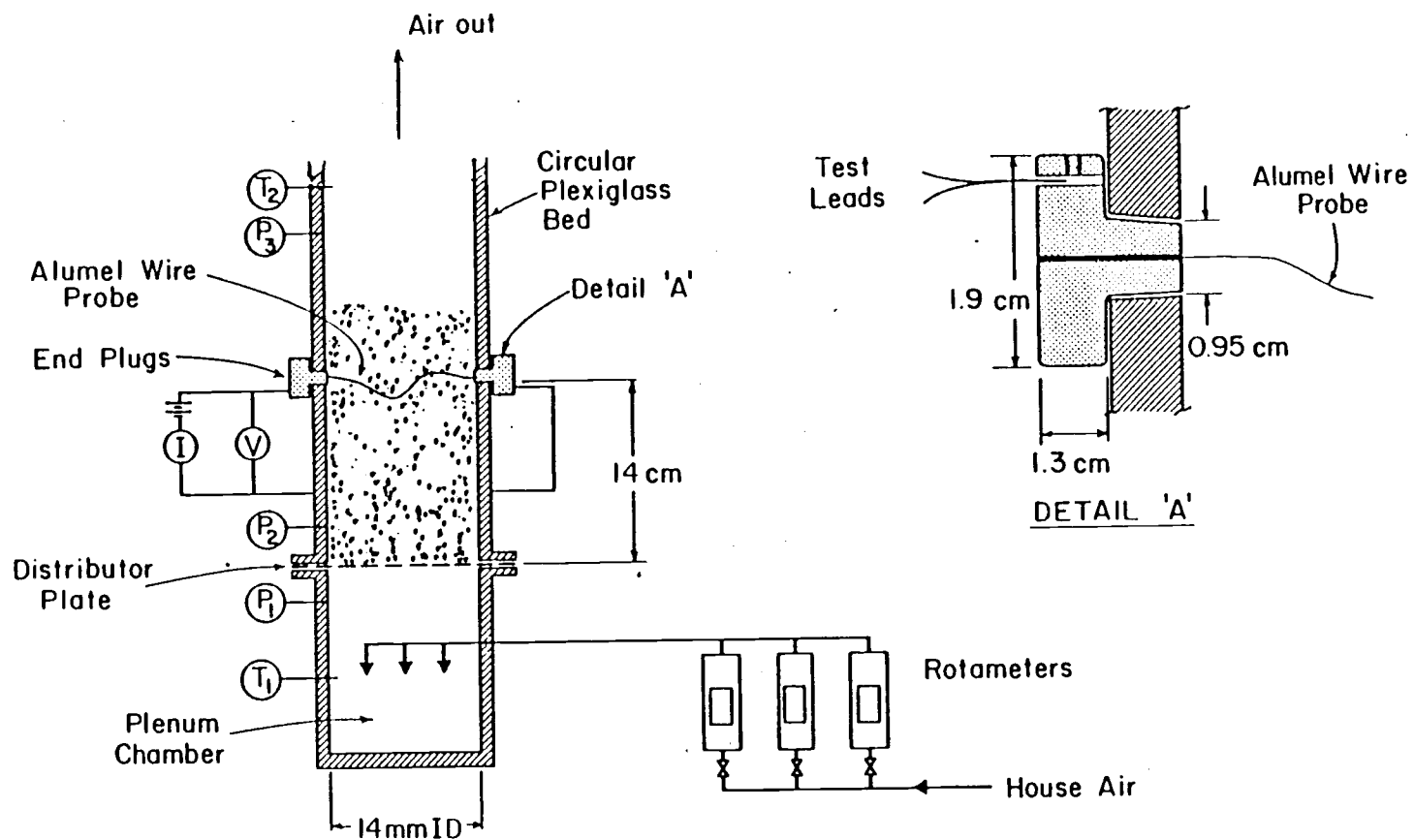


Figure III-1. Schematic Diagram of Equipment Used in the Heated Wire Experiment.

a Sutorbilt 3HV-B blower is first passed through a water cooled 1-2 shell and tube heat exchanger then is fed via one of three calibrated rotameters to the plenum chamber located below the distributor plate of the fluidized bed. The air is introduced to the chamber via a square gas distributor pointing downwards. The air then passes upward through the distributor plate which consists of a layer of fine nylon (270 mesh) sandwiched between two coarser layers of wire (40 mesh). After passing through the bed the air is vented to the atmosphere via an overhead extraction system.

The fluidized bed was constructed from 14cm I.D., 15cm O.D. Plexiglass tubing. A solids feed port is located 32cm above the distributor plate. Solids removal is achieved via a 1.2cm diameter hole drilled into the side of the bed just above the distributor plate and provision is made to fit a vacuum removal system which speeds the emptying of the bed. The position of pressure taps and thermocouple locations are shown in Figure III-1.

Located 14cm above the distributor plate are two holes, 180° apart, which hold the force fit plugs into which the Alumel wire probe and test leads are secured. A detail of one of the plugs is given in Figure III-1. The test leads connecting the plugs to the power supply and voltmeter are 16 AWG copper and are held in place by a set screw in addition to being soldered. The Alumel wires used to probe the fluidized bed can be adjusted to any length greater than or equal to the inside diameter of the bed (14cm) and are secured in place by soldering. The plugs are made from solid brass and when fitted into the bed are flush with the inside wall.

III-2-2. Experimental Procedure

Two types of experiment were performed with the equipment described above. First, heat transfer coefficients between fixed horizontal wires and flowing air were measured. Second, heat transfer coefficients between freely moving wires and fluidized beds were determined.

The purpose of the first type of experiment was to confirm the results of previous investigators for cylinders in air, thus verifying the accuracy of the proposed experimental technique.

There were only two differences in procedure for the two types of experiment. In the first experiment the wires were soldered tight, i.e., the wire length was equal to the inside diameter of the bed, and also there were no fluidized solids present in the bed, although a 5cm layer of 1.5mm copper shot was used as an additional gas distributor.

Taking note of the two differences described above the experimental technique used was as follows. The resistance of the wire was determined by passing a slow stream of air at known temperature through the bed and at the same time passing a very small but known current through the wire and noting the voltage drop across the wire. The power dissipated in the wire was always less than 1.0 mW and hence the heating in the wire was assumed negligible. The average of several readings was used to determine the resistance of the wire at the temperature of the flowing air thus:

$$R_o = \frac{1}{N} \sum_{i=1}^N \frac{V_i}{I_i} \quad (\text{III-1})$$

The next step was to increase the air flow rate to some predetermined level and then pass sufficient electric current through the wire to heat it above the temperature of the fluidized bed and/or air. The temperature of the wire was not fixed but allowed to vary between 20°C to 130°C above that of the incoming air. By measuring the current flow, voltage drop across the wire and air/fluidized bed temperature it was possible to determine the average temperature of the wire and its heat transfer coefficient.

III-3. Experimental Results

III-3-1. Calculation of Heat Transfer Coefficients

The procedure for calculating the heat transfer coefficient for a wire from the measured data is outlined below.

If the wire can be considered to be infinitely long then the conduction of heat along the wire is negligible and the equations describing the heat transfer process are given by Eqs. III-2 and III-3 below.

$$\dot{q} = IV = 2\pi d_w L (T_w - T_a) h_w \quad (\text{III-2})$$

$$R = \frac{V}{I} = R_o (1 + \alpha(T_w - T_o)) \quad (\text{III-3})$$

where:

- L = half the length of wire
- T_a = temperature of air/fluidized bed
- T_o = reference temperature
- R_o = resistance of wire at T_o

Eliminating T_w from III-2 and III-3 we get:

$$h_w = \frac{IV\alpha R_o}{2\pi d_w L((T_o - T_a)\alpha R_o + V/I - R_o)} \quad (\text{III-4})$$

All the terms on the right-hand side of Eq. III-4 are known hence h_w can be found. In the case when conduction along the wire cannot be neglected the governing equations are not so straightforward. The result is an implicit equation in h_w which must be solved for by trial and error. This equation is given below and its derivation is given by Carslaw and Jaeger (46) and is repeated in Appendix B.

$$\frac{V}{I} = R_a + \frac{R_a \alpha B_1}{\lambda^2} \left(1 - \frac{\tanh(\lambda L)}{\lambda L}\right) \quad (\text{III-5})$$

where:

$$\lambda^2 = A_1 - \alpha B_1$$

$$A_1 = \frac{4h_w}{k_w d_w}$$

$$B_1 = \frac{2I_a^2 R_a}{k_w \pi L d_w^2}$$

Eq. III-5 above was used to back calculate the heat transfer coefficient h_w from all the experimental runs. Although for the majority (greater than 90 percent) of the runs the approximate analysis, Eq. III-4, gave results which differed by less than 5 percent from those given by the more rigorous analysis, Eq. III-5.

III-3-2 Calibration of Horizontal Wires in Flowing Air

The results for straight horizontal heated wires in a stream of flowing air are plotted in Figure III-2 and the raw data points and details of calculations are given in Appendix C.

Figure III-2 shows the Nusselt number for the wires plotted against the Reynolds number based on the diameter of the wire. The properties of air used in these dimensionless groups are taken at the arithmetic mean temperature of the wire and the air, i.e., $(T_w + T_a)/2$.

A comprehensive survey of published data on the heat transfer between horizontal cylinders and flowing fluid was carried out by Churchill and Bernstein (47). They recommend the following correlation equations:

$$Nu_{w,f} = \frac{h_w d_w}{k_{g,f}} = 0.3 + \frac{0.62 Re_f^{1/2} Pr_f^{1/3}}{(1 + (\frac{0.4}{Pr_f})^{2/3})^{1/4}} \left(1 + (\frac{Re_f}{282,000})^{5/8}\right)^{4/5}$$

(III-6a)

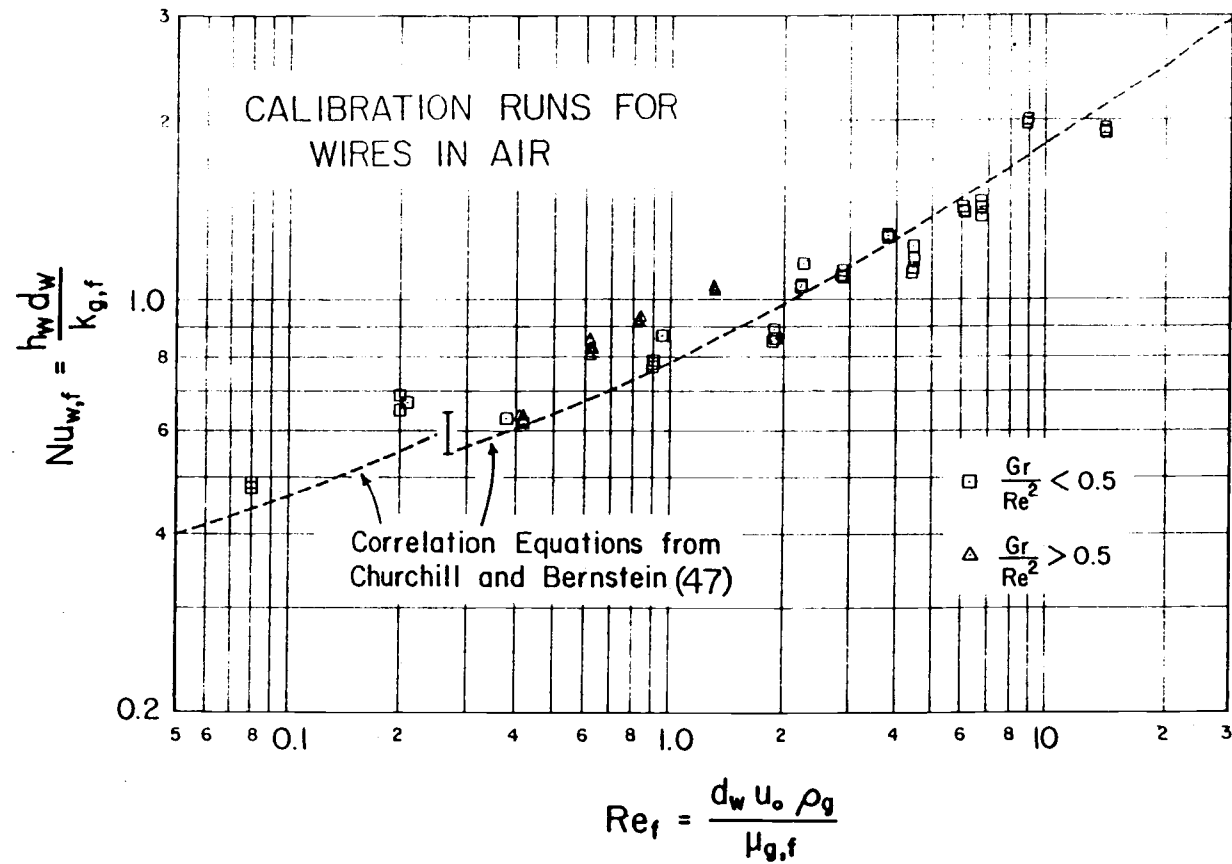


Figure III-2. Nusselt Number vs. Reynolds Number for Straight Horizontal Wires in Air.

for $Re_f Pr_f > 0.2$, and

$$Nu_{w,f} = \frac{h_w d_w}{k_{g,f}} = \frac{1}{(0.8237 - \log_e(Re_f Pr_f)^{1/2})} \quad (III-6b)$$

for $Re_f Pr_f \leq 0.2$.

Eqs. III-6a and III-6b are plotted as dotted lines in Figure III-2. The experimental data compare favorably with the above correlation.

It is interesting to note that in the low Reynolds number regime the effects of natural convection may be important and the data should be checked to see if buoyancy effects do, in fact, intrude.

A criterion for when natural convection becomes important can be obtained by an order of magnitude analysis of the Navier-Stokes equations. This is given in several heat transfer texts, e.g., Eckert and Drake (48) and Chapman (49) and will not be repeated here. The result of this analysis shows that natural convection effects become important when

$$\frac{Gr}{Re^2} \geq 1 \quad (III-7)$$

In Figure III-2, the data points for which $Gr/Re^2 > 0.5$ are shown and it is assumed that for these points some buoyancy forces have come into play. All these points lie above the correlation curve which is consistent with an increase in heat transfer coefficient due to natural convection effects. These data points should be

adjusted downwards to represent a true forced convection situation. This was not done but it is believed that this would move the data closer to the correlation line hence improving the fit.

In conclusion, this technique gives accurate predictions of heat transfer coefficients for straight wires in air and is thus suitable for use in the proposed fluidized bed experiments.

III-3-3. Heat Transfer Coefficients for Loose Wires in Fluidized Beds

The main object of this part of the study was to determine the heat transfer coefficients between beds of variously sized fluidized particles and loose, current carrying Alumel wires. The term loose, as used here, describes the ability of the wires to move around in the fluidized bed. The length of each wire exposed to the fluidized solids was approximately 20cm, 6cm longer than the inside diameter of the bed. Thus the wires were relatively free to move around and sample the cross-section of the bed. The heat transfer coefficients thus obtained represent some average value over the bed cross-section.

The properties of the particles used in these experiments are presented in Table III-3. The particle diameter is a surface average value determined according to Eq. III-8 below:

$$\bar{d}_p = \frac{1}{\sum_{d_{p,i,screen}} \frac{x_i}{d_{p,i,screen}}} \quad (\text{III-8})$$

Table III-3. Summary of the Physical Properties of Fluidized Particles

Material	\bar{d}_p (μm)	ρ_s (kg/m^3)	ρ_{bulk} (kg/m^3)	u_{mf} (m/s)	k_s ($\text{W}/\text{m}\cdot\text{K}$)	$C_{p,s}$ ($\text{kJ}/\text{kg}\cdot\text{K}$)	ϵ_{mf}	Geldart Classification
Glass	106	2500	1480	0.0095	0.74	670	0.47	A/B
	230		1550	0.0400			0.44	B
	465		1570	0.1500			0.42	B
	613		1530	0.2800			0.43	B
Polyethylene	246	920	460	0.0270	0.43	2100	0.59	A/B
	494		410	0.0900			0.62	B
	754		400	0.1900			0.64	B
Sand	105	2550	1450	0.0220	0.33	800	0.52	A/B
	223		1530	0.0720			0.45	B
	670		1540	0.3000			0.50	B
Aluminum	314	2700	1220	0.1580	204.2	900	0.62	B
	423		1110	0.2550			0.67	B

Details of the determination of the other properties shown in Table III-3 are given in Appendix D.

The level of fluidization was chosen to be $u_o/u_{mf} \cong 1.8$ which for the majority of the solids gave a well-fluidized bubbling bed. It is interesting to note that the smallest particle sizes for glass, polyethylene and sand all lie very close to the border between Type A and Type B particles on the classification map due to Geldart (50). All the other particles used were situated in the middle of the Type B region. These three small particle systems all exhibited considerable bed expansion after reaching minimum fluidizing conditions which is consistent with Geldart's findings. It was decided, therefore, to adjust the level of fluidization for these three small particle systems to $u_o/u_{mf} \cong 2.7$, which visually gave a similar level of fluidization as the other larger (Type B) particle systems. Other levels of fluidization were tried up to $u_o/u_{mf} = 5.4$, however little or no change, in the heat transfer coefficient obtained at the initial fluidization level, was observed.

In all, 405 data points were collected; Figure III-3 shows the results for the glass particles as a plot of Nusselt number versus Reynolds number. Both quantities are based on the diameter of the wire and the velocity used in the Reynolds number is u_{mf}/ϵ_{mf} which is the interstitial velocity in the emulsion phase. Details of the calculations for the data are given in Appendix E. From Figure III-3, it can be seen that the ratio of the particle diameter to the wire diameter (d_p/d_w) strongly affects the heat transfer coefficient

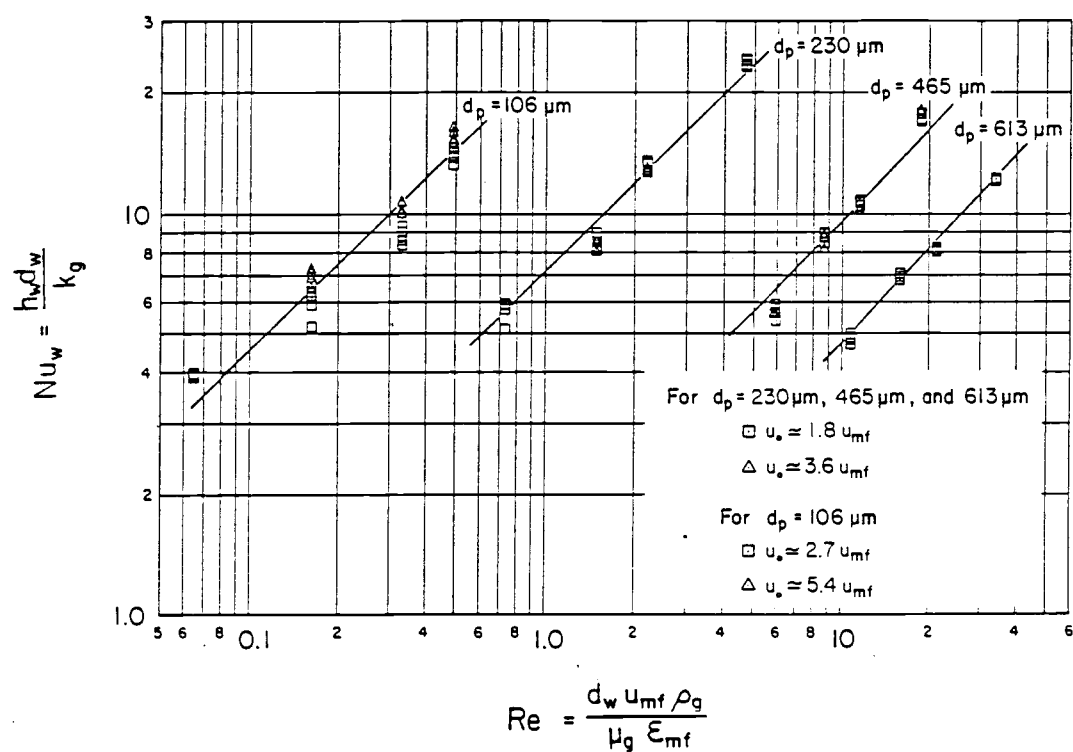


Figure III-3. Nusselt Number vs. Reynolds Number for Wires in Fluidized Beds of Glass Particles.

between wire and bed, while the level of fluidization (u_o/u_{mf}) has but a slight effect. The data for the other materials show similar trends and since very little published data is available for this type of system it was decided to formulate a new correlation to fit the results of these experiments.

The resulting correlation is given below:

$$Nu_w = \frac{h_w d_w}{k_g} = 0.46 \left(\frac{d_w u_{mf} \rho_g}{\mu_g \epsilon_{mf}} \right)^{0.09} \left(\frac{d_w}{d_p} \right)^{0.51} \left(\frac{1 - \epsilon_{mf}}{\epsilon_{mf}} \frac{\rho_s C_{p,s}}{\rho_g C_{p,g}} \right)^{0.36} \quad (III-9)$$

The four arbitrary constants in Eq. III-9 were calculated to minimize the sum of squares error Q defined below:

$$Q = (\log_{10} Nu_w - \log_{10} \hat{Nu}_w)^2 \quad (III-10)$$

Equation III-9 is plotted against the experimental data in Figure III-4 and it can be seen that over 95 percent of the data lie within ± 20 percent of Eq. III-9. Also shown in Figure III-4 are error bars indicating the variability of data points due to accountable experimental error. The calculations of these errors are given in Appendix F.

III-4. Comparison of Results with Previous Work

As was pointed out earlier there has been very little work done in fluidized bed heat transfer in which the heat transfer surface has two of its characteristic dimensions the same order of magnitude

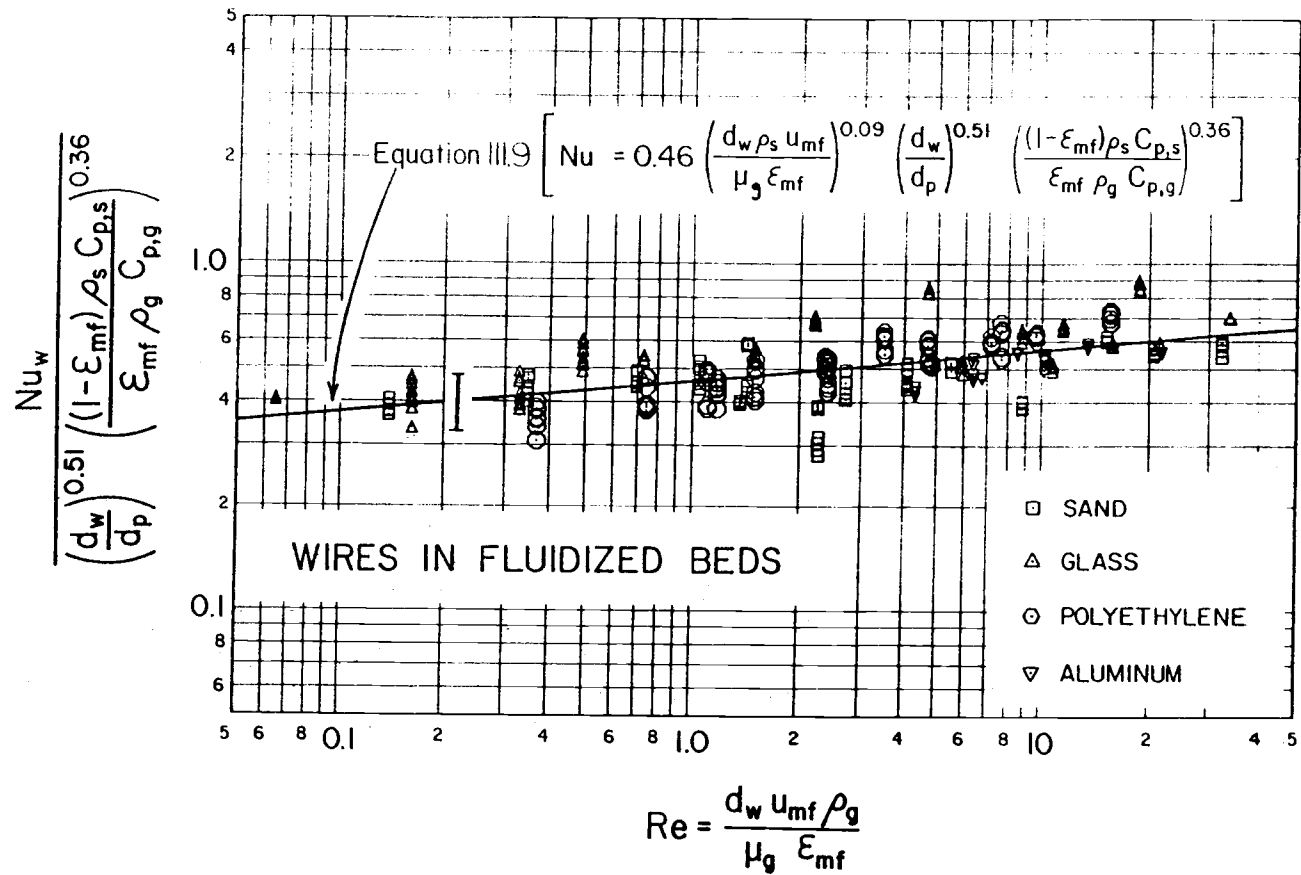


Figure III-4. Comparison of Correlation Eq. III-9 with Experimental Data.

as the fluidized particles. In fact, only Jacob and Osberg (31) have used a system similar to the one described here. However, they only used one size of wire and this was held tightly in their probe so that the wire was not free to move around when it was immersed in the fluidized bed. They varied the position of the wire probe to give the maximum heat transfer coefficient for a given fluidized system. Their results are plotted against Eq. III-9 in Figure III-5 and details of the calculations are given in Appendix E. It is evident from Figure III-5 that their data is well-correlated by Eq. III-9 and although all the data lie above the correlation it is within the limits of the data taken in this study.

A second comparison can be made between the present work and the results for horizontal tubes in fluidized beds. Vreedenberg (51), (52) carried out a considerable amount of work in this area and recommends the following correlation for fine particle beds:

$$Nu_w = \frac{h_w d_w}{k_g} = 0.66 \left(\frac{C_{p,g} \mu_g}{k_g} \right)^{0.3} \left(\frac{\rho_g u_o d_w}{\mu_g} \frac{\rho_s}{\rho_g} \frac{(1 - \epsilon)}{\epsilon} \right)^{0.44} \quad (\text{III-11})$$

for

$$\frac{\rho_g u_o d_w}{\mu_g} \leq 2000$$

In Figure III-6, Eq. III-11 is plotted against the experimental data from this study. It is obvious that Eq. III-11 does not correlate this data at all well with a systematic overprediction of Nusselt number by factors of up to 10. This, however, is not surprising

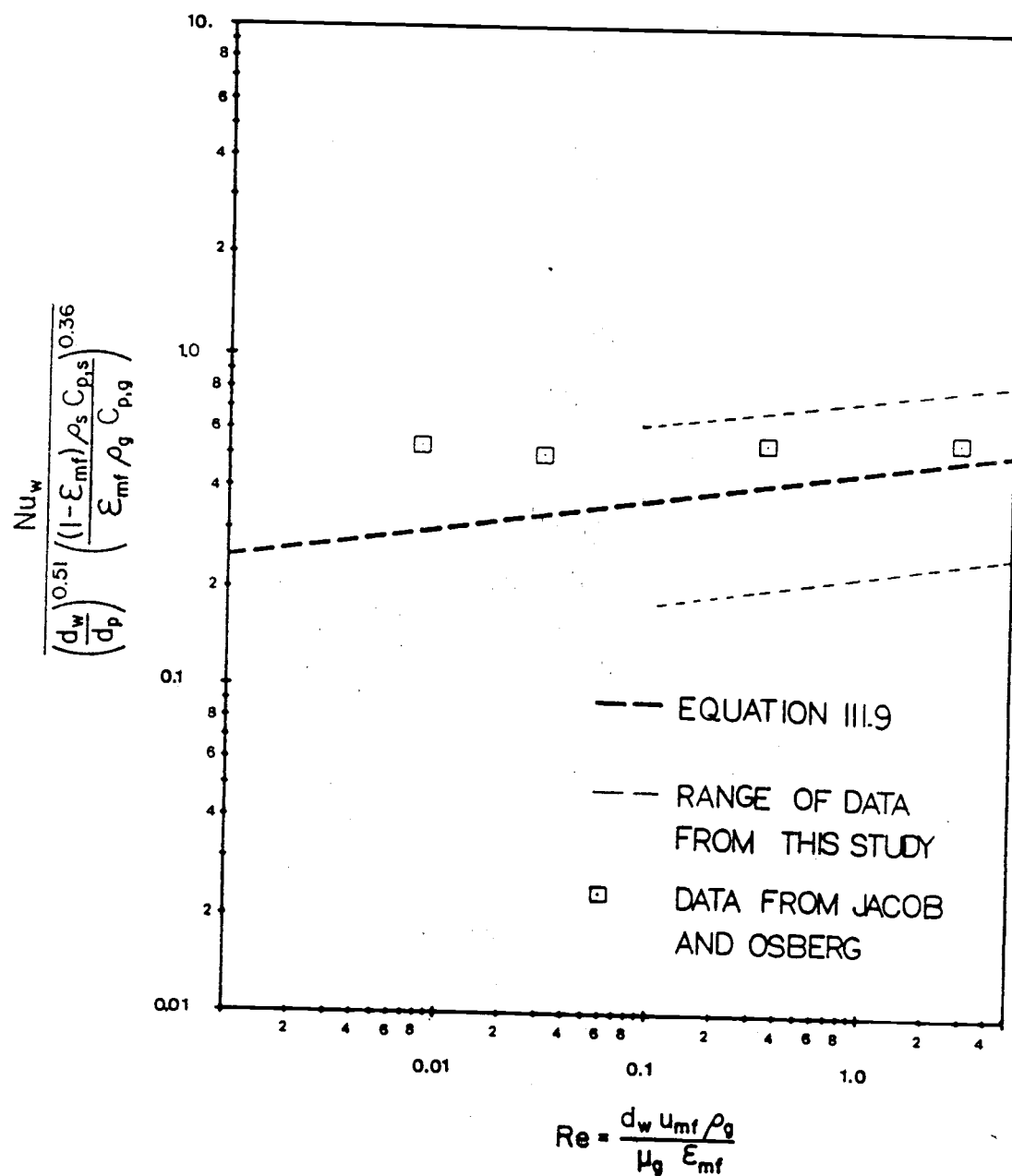


Figure III-5. Comparison of Jacob and Osberg's (31) Results with Eq. III-9.

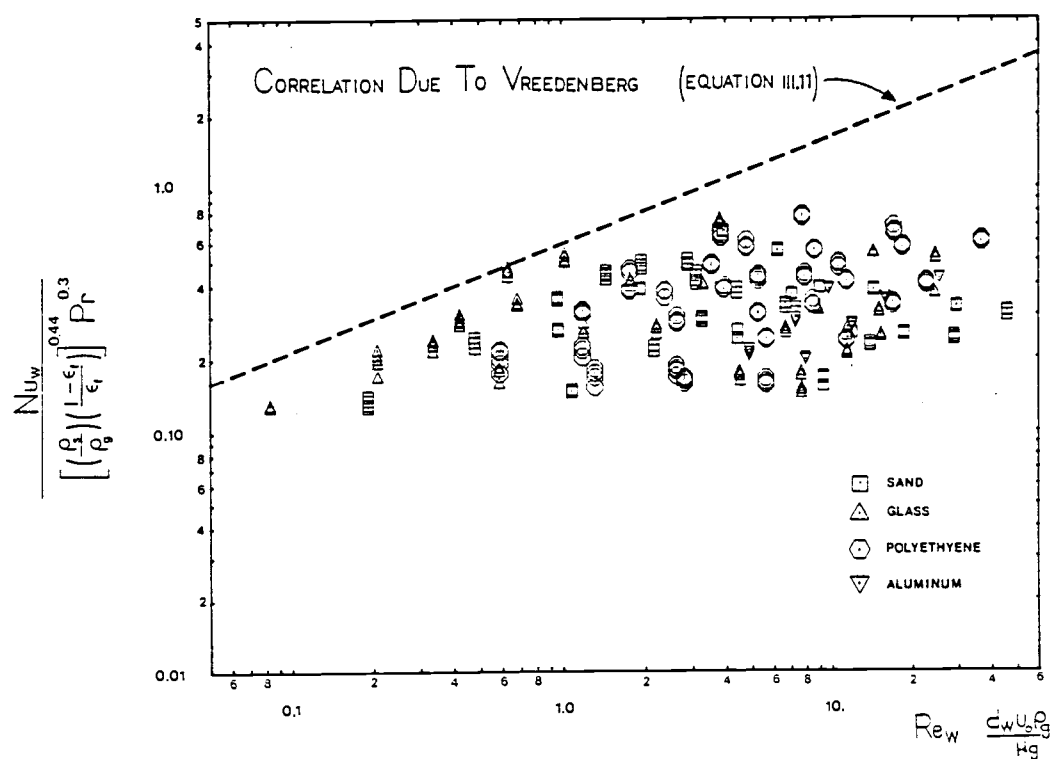


Figure III-6. Comparison of Data from this study with Vreedenberg's (51), (52) Correlation for Heat Transfer from Horizontal Tubes to Fluidized Beds.

since Eq. III-11 was proposed for heat transfer surfaces whose dimensions were at least one order of magnitude greater than the fluidized particles' diameter. Thus, it would be expected that the mechanisms for heat transfer for these two situations would be different.

At this point it would be very useful to compare the present data with the results for heat transfer to small surfaces immersed in fluidized beds. The available data, Wen and Chang (27), Chang and Wen (26), Ziegler et al. (28), Ziegler and Brazelton (29) and Shirai et al. (30), is unfortunately for much higher Reynolds numbers (> 200) than those used here and hence a comparison would be meaningless.

Finally a comparison can be made between the present work and previous work on fine wire heat transfer in flowing air. For this purpose, Eq. III-9 with d_w set equal to d_p , was used to represent the situation of a fine freely moving wire in a fluidized bed of particles the same diameter as the wire. Eqs. III-6a and III-6b were used to represent the results for a bare wire in a stream of air. These two correlations are plotted in Figure III-7 where the two curves marked "polyethylene" and "sand" represent the upper and lower limits of the present experimental data. From Figure III-7 it is obvious that the effect of immersing the wire in a fluidized bed of particles with the same diameter as the wire is to increase the heat transfer coefficient significantly. This increase being as great as one order of magnitude at $Re_w = 0.1$.

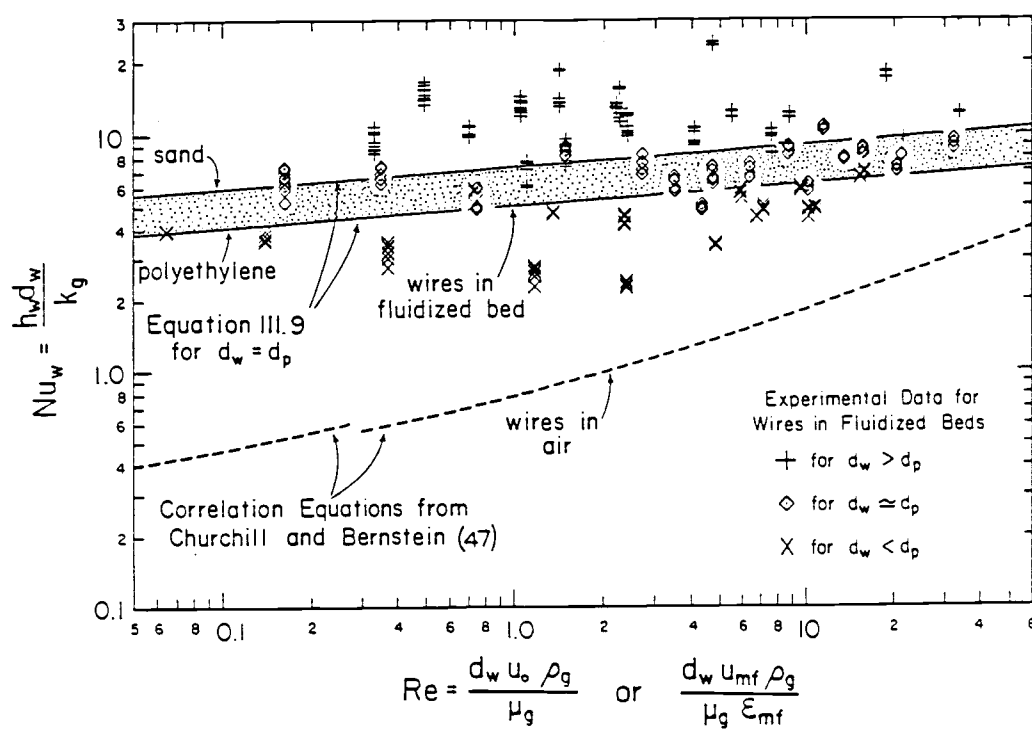


Figure III-7. Comparison of Present Experimental Results for Fine Freely Moving Wires in Fluidized Beds with Fine Wires in Flowing Air.

III-5. Discussion of Results

It is apparent that the heat transfer process occurring between loose wires and fluidized beds cannot readily be compared with previous studies on heat transfer between large immersed surfaced and fluidized beds. Mechanistic models such as Mickley and Fairbank's (53) "packet theory" which have been used successfully to account for heat transfer to large surfaces lose physical meaning when the heat transfer surface has two dimensions the same order of magnitude as the fluidized particles. For this type of system it is more reasonable to consider the interaction of individual particles and the wire.

Although a mechanistic model is not presented here to explain the heat transfer processes occurring the correlation given by Eq. III-9 does give some insight into the processes which are taking place. From Eq. III-9, it is evident that the Reynolds number based on the interstitial gas velocity through the emulsion (u_{mf}/ϵ_{mf}) does not play an important role, since a change in Reynolds number from 0.1 to 10 changes the Nusselt number by a factor of only 2. This coupled with the strong influence of the ratio of d_w to d_p suggests that the main heat transfer mechanism is strongly influenced by particle-wire contacts. If this is true then the average time that a particle stays in contact with the wire will be an important factor in the heat transfer process. Since the wire is free (or fairly free) to move around the bed and does so with the slowly moving solids of the emulsion phase it is difficult to estimate what

this contact time might be. The last term in Eq. III-9, however, shows that the thermal capacity of the solids plays an important role. The fact that this group influences h_w suggests that the contact time between wire and particles is not too short since researchers Denloye and Botterill (54), Botterill and Denloye (55), and Schlunder (56), have shown both experimentally and theoretically that for very short contact times (in the order of 20 ms) the heat transfer coefficient reaches a limiting value which is independent of the thermal properties of the solid.

From the above discussion it would seem that heat transfer processes occurring are aptly described by the interaction of a long cylindrical particle and a bed of fluidized particles. Bearing this in mind and referring back to Figure III-7 which shows an increase in the Nusselt number for wires in fluidized beds compared with wires in air, one is tempted to extrapolate these results to the situation of a small particle transferring heat to a fluidized bed of like particles. Previous experimental results and theoretical analysis are at odds as to whether the Nusselt number should lie above the curve for a single sphere in air or whether the Nusselt number should continually decrease with decreasing Reynolds number. It is felt that this work lends strong support to the argument that a limiting Nusselt number does exist for small particle heat transfer in fluidized beds and that this limiting value should lie above 2.0, the limiting value for conduction into a stagnant gaseous medium.

III-6. Conclusions

Heat transfer coefficients between fine Alumel wires ($50.8\mu\text{m} \leq d_w \leq 813\mu\text{m}$) and flowing air streams were determined and found to be in excellent agreement with previously published results.

Using a similar technique as used above, heat transfer coefficients were determined for fine particle ($105\mu\text{m} \leq \bar{d}_p \leq 754\mu\text{m}$) fluidized beds of various materials. All experimental data could be correlated well by Eq. III-9:

$$Nu_w = \frac{h_w d_w}{k_g} = 0.46 \left(\frac{d_w u_{mf} \rho_g}{\mu_g \epsilon_{mf}} \right)^{0.09} \left(\frac{d_w}{d_p} \right)^{0.51} \left(\frac{(1 - \epsilon_{mf})}{\epsilon_{mf}} \frac{\rho_s C_{p,s}}{\rho_g C_{p,g}} \right)^{0.36} \quad (\text{III-9})$$

with an average error of 14 percent.

The results for loose wires in fluidized beds show that the heat transfer coefficient for a wire in a fluidized bed is greater than for a wire in a stream of air at the same Reynolds number. This lends considerable support to the argument that a limiting Nusselt number exists for fluid-particle heat transfer in a fluidized bed as Reynolds number tends to zero.

IV. TRANSIENT HEATING OF A SAMPLE OF COLD MAGNETIC PARTICLES INJECTED INTO A HOT FLUIDIZED BED

IV-1. Introduction and Description of Experiment

The object of this experiment is to determine the heat transfer coefficient " h_p " between a sample of cold particles which is injected into a fluidized bed of hot particles. The change in temperature of the cold particles is inferred from the change in magnetic permeability of the material making up the sample. Knowing the change in temperature of the magnetic particles as a function of time allows the heat transfer coefficient between the cold particles and hot fluidized bed to be determined. The idea of using a change in magnetic permeability to measure a change in temperature is a novel one and hitherto untried in fluidized bed research. Moreover, since this technique is suitable for any size of particle it makes possible the determination of heat transfer coefficients in fluidized beds of fine particles by direct measurement of temperature change, something which was not previously possible.

In order for this technique to be successful several criteria must be met. First, the size of the injected sample must be small compared with the size of the hot fluidized bed. This ensures that the temperature of the hot bed will not change greatly over the period when the cold particles are being heated. Second, the magnetic permeability of the injected material must change appreciably over the temperature range of interest. Third, a very sensitive detection device must be used in order to pick up the

changes in magnetic permeability. Finally a fast data acquisition system must be used to accurately record the transient heating of the cold particles.

The first three constraints discussed above can be met by the suitable choice of magnetic material and detection device. While the fourth criterion can be easily fulfilled by using one of the many high-speed computer data acquisition systems available today.

After a lengthy search the material chosen for the sample was a low-Curie point ferrite TC-71 supplied by TDK Corporation (Japan). This material possesses a high magnetic permeability at ambient temperature which allows a reasonable signal level to be obtained for very small sample sizes. In addition, the magnetic properties of the ferrite change appreciably over the temperature range used in these experiments, 20°C to 100°C. Some of the physical properties of the ferrite are given in Table IV-1 and Figure IV-1 and full details of their experimental determination are given in Appendix G.

The device used to detect the magnetic permeability of the particles is, in essence, a modified airport metal detector. The principles of how this instrument operates are given in detail in Appendix H. It will be noted here that this ferrite detector or sensor is very sensitive and is capable of delivering a 200 mV signal when only approximately 0.5 grams of ferrite is present. This fine sensitivity is at the same time an advantage and a disadvantage. The advantage of such a device is that a very small sample of cold ferrite may be detected when placed within the detector coil. The disadvantage is that the hot bed material cannot

Table IV-1. Some Physical Properties of TC-71 Ferrite

Density	4780	kg/m ³
Thermal Conductivity (@ 120°C)	1.78	W/m.K
Specific Heat Capacity	648	J/kg.K

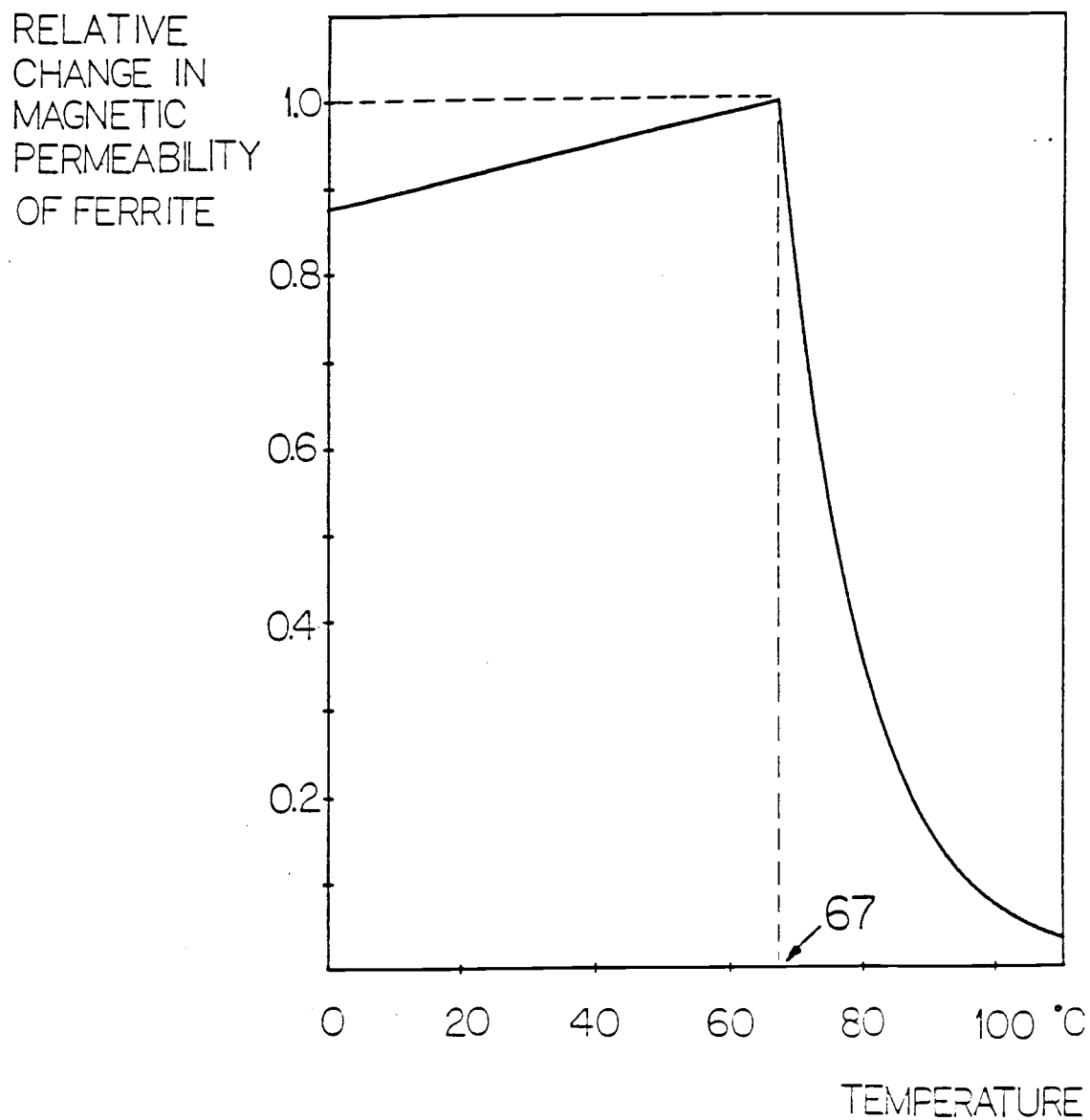


Figure IV-1. Relative Change of Magnetic Permeability with Temperature for Ferrite TC-71.

be the same ferrite as the cold injected sample. The reason for this is that even though the bed material is hot (approximately 90°C) and would consequently have a relatively low magnetic permeability the fact that there would be so much material in the bed (approximately 60 grams) would cause a high level of background noise. This noise would tend to completely mask the signal due to the cold ferrite sample heating up.

This disadvantage can be overcome by using a non-magnetic material in the hot fluidized bed. This material should, ideally, have very similar properties to the ferrite TC-71. In practice some compromise will have to be made in choosing the hot bed material. After searching at some length, it was decided to use zirconia as the hot bed material. The physical properties of zirconia are given in Table IV-2.

Comparing Tables IV-1 and IV-2, it can be seen that the ferrite is less dense than zirconia. Thus, if a sample of ferrite were injected into a fluidized bed of zirconia, all particles being the same size, then the ferrite would tend to sit on top of the bed. Mixing of ferrite and zirconia would occur but would be slower than if the ferrite were injected into a bed of similar sized ferrite particles. This reluctance to mix can be overcome by adjusting the size of the zirconia particles so that both the ferrite and zirconia have the same minimum fluidizing velocity. The minimum fluidization velocities were determined for each size cut of ferrite and zirconia used in these experiments. These results are given in Table IV-3 and details are given in Appendix I.

Table IV-2. Some Physical Properties of Zirconia

			Reference
Density	5900	kg/m ³	(57)
Thermal Conductivity	0.16	W/m.K	(57)
Specific Heat Capacity	456	J/kg.K	(57)

Table IV-3. Minimum Fluidization Velocities for Zirconia and Ferrite TC-71 Particles

Size Cut (Tyler Screen No.)	Average Particle Size (μm)	Minimum Fluidization Velocity (m/s)	
		<u>Zirconia</u>	<u>Ferrite</u>
45 ⁻ - 50 ⁺	327.5		0.141
50 ⁻ - 60 ⁺	275.0	0.166	0.110
60 ⁻ - 70 ⁺	231.0	0.103	0.103
70 ⁻ - 80 ⁺	196.0	0.082	0.068
80 ⁻ - 100 ⁺	165.0	0.065	0.047
100 ⁻ - 120 ⁺	137.5	0.050	0.030
120 ⁻ - 140 ⁺	115.5	0.030	0.022

The combinations of ferrite and zirconia used for the sample and bed respectively are given in Table IV-4 and are based on matching the minimum fluidization velocities of ferrite and zirconia as closely as possible. It can be seen that the largest discrepancy in matching u_{mf} is for System A and this is only a 15 percent difference.

IV-2. Apparatus and Experimental Procedure

IV-2-1. Apparatus

A schematic diagram of the fluidized bed system used in this experiment is shown in Figure IV-2. House air is fed via a 30 psi regulator and a 50 SCFH rotameter to a Swagelock 12.7mm tee. From the tee the air can flow to either one of two fluidized beds. The piping to both beds is identical and consists of a gate valve followed by a 90° elbow and 380mm of 3.6mm O.D. aluminum tube. On the upper 200mm of each aluminum tube are wound approximately 100 turns of 24 AWG insulated copper wire. The inside of the tubes are filled with 3.2mm copper shot and the outside of the tube and coil are wound with asbestos tape and fiberglass insulation. The copper coils are wired in series and connected across a D.C. power supply capable of delivering up to 10 amperes of current to the coils. In this way the air to the fluidized beds can be heated to the desired temperature (approximately 110°C).

The heated air flows up through the aluminum pipe and into the fluidized bed unit and finally out to the atmosphere. The fluidized bed unit is connected to the aluminum pipe by a Swagelock

Table IV-4. Combinations of Ferrite TC-71 and Zirconia Used in Experimental Runs

System	Zirconia (size cut)	Ferrite (size cut)	$\frac{(u_{mf})_{\text{ferrite}}}{(u_{mf})_{\text{zirconia}}}$
A	$50^- - 60^+$	$45^- - 50^+$	0.85
B	$60^- - 70^+$	$50^- - 60^+$	1.07
C	$60^- - 70^+$	$60^- - 70^+$	1.00
D	$80^- - 100^+$	$70^- - 80^+$	1.05
E	$100^- - 120^+$	$80^- - 100^+$	0.94
F	$120^- - 140^+$	$100^- - 120^+$	1.00

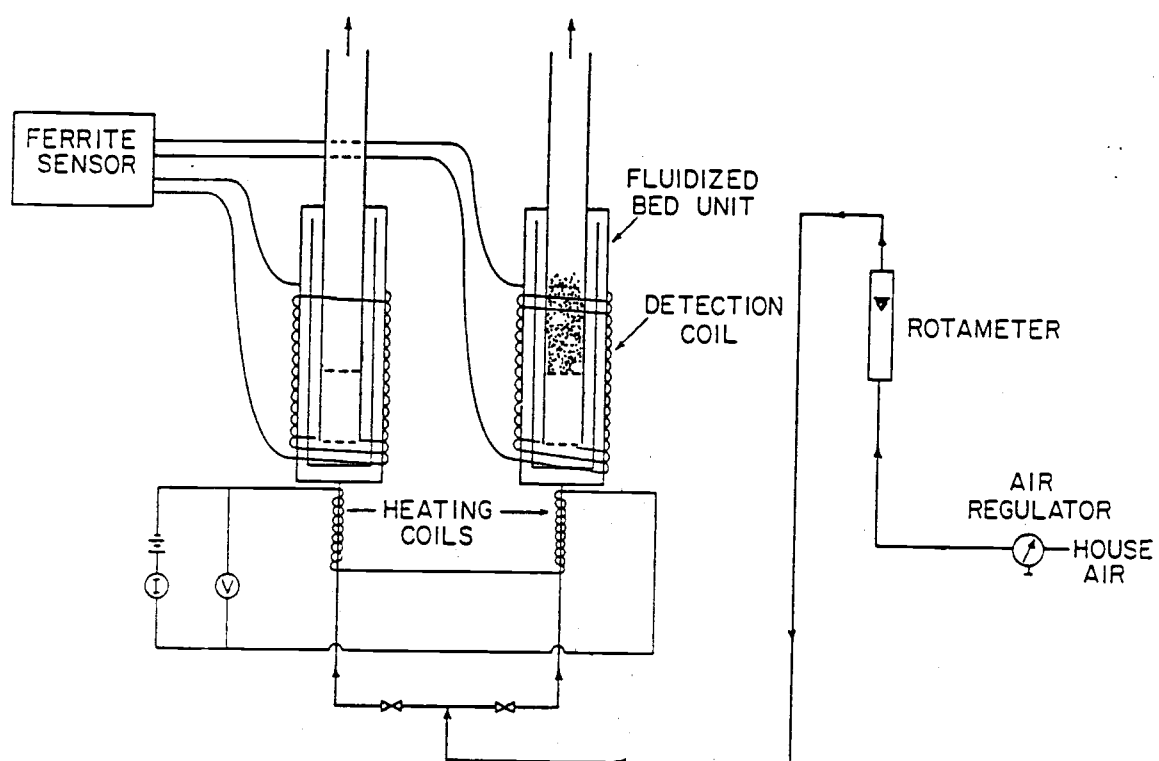


Figure IV-2. Schematic Diagram of Fluidized Bed System Used in the Transient Heating Experiments

compression fitting. Around the fluidized bed is the detector coil which is connected to the ferrite sensor. The bed and detector coil are held in a vertical position using spacers and a rigid vertical 76mm I.D. plastic tube which surrounds the whole experimental bed/coil unit.

A diagram of one of the fluidized beds is shown in Figure IV-3. The bed is constructed from transparent butyrate plastic tube, this plastic is suitable for use at the air temperatures employed in these experiments. Since it is important in this experiment to maintain the temperature of the fluidized solids as uniformly as possible the fluidized bed is constructed with a double pass heating section around the inner tube. This arrangement, in effect, acts as an adiabatic wall around the fluidized bed section and considerably reduces the heat loss from the walls of the bed. From Figure IV-3 it can be seen that the incoming hot air first passes upward through the annular channel between the outer and middle tube. The air then flows through a set of circular holes in the top of the middle tube and, reversing its direction, flows downward in the annular gap between the middle and inner tube. Finally the air once again changes direction and flows upward through a perforated distributor plate, a 200 mesh nylon screen, a fixed bed of 1.5mm glass beads, another 200 mesh nylon screen and through the fluidized bed of hot particles and into the atmosphere. The flow path of air is illustrated in Figure IV-3 along with the location of the 127 μ m type K thermocouples.

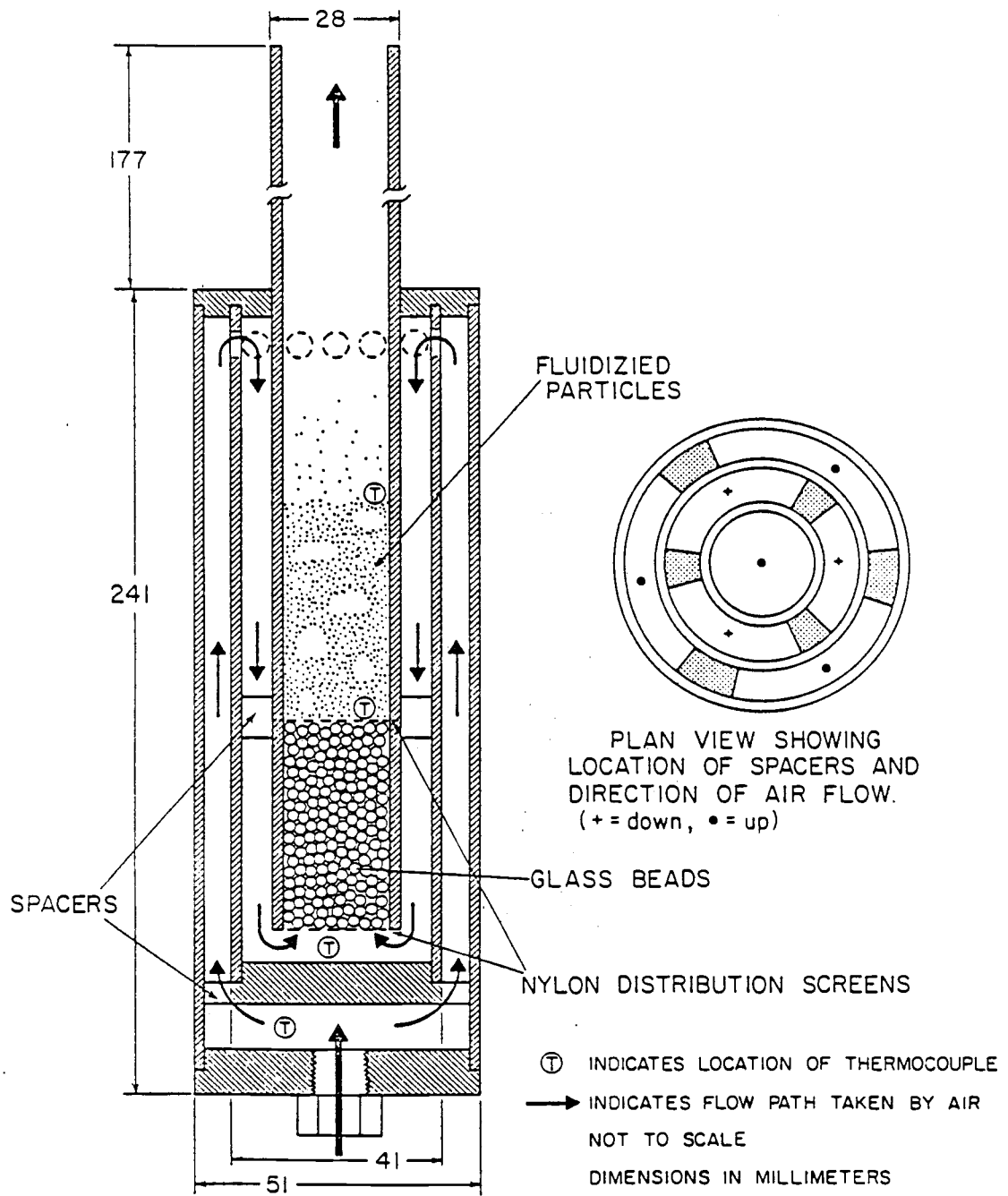


Figure IV-3. Fluidized Bed Unit Used in Transient Heating Experiments.

In order for the change in magnetic properties of the ferrite to be measured it is necessary for a detector coil to be placed around the fluidized bed. The location and dimensions of this coil are illustrated in Figure IV-4. The coil consists of 2300 turns of 34 AWG insulated copper wire, arranged in four layers. The coil is approximately 100mm long and is mounted on a 44mm I.D. butyrate tube, which fits snugly over the fluidized bed unit. Around the detector coil is wound a helix of copper tape which acts as a grounded shield and on top of this is a layer of mylar which acts as a protective shield for the coil, ground and connections.

The electronic detection instrumentation, as mentioned previously, is a modified metal detector similar to those used in airports. The electronic circuitry is described in detail in Appendix H. The principle by which this device operates will be described briefly. The detector coils act as two legs of an inductive bridge circuit. A low distortion sine wave (950Hz and 20V peak to peak) is delivered to the bridge and with no ferro-magnetic material in either coil the bridge is adjusted to give the same voltage in each leg. Now when a magnetic material is placed in one of the coils the impedance of that coil changes (increases) and different amplitude sine wave voltages will appear in each leg of the bridge. The difference between these two signals is amplified and conditioned to give a constant voltage at the output of the ferrite sensor. This output voltage is directly proportional to the amount of magnetic material in the coil or in other words its magnetic permeability. Therefore, by injecting magnetic material

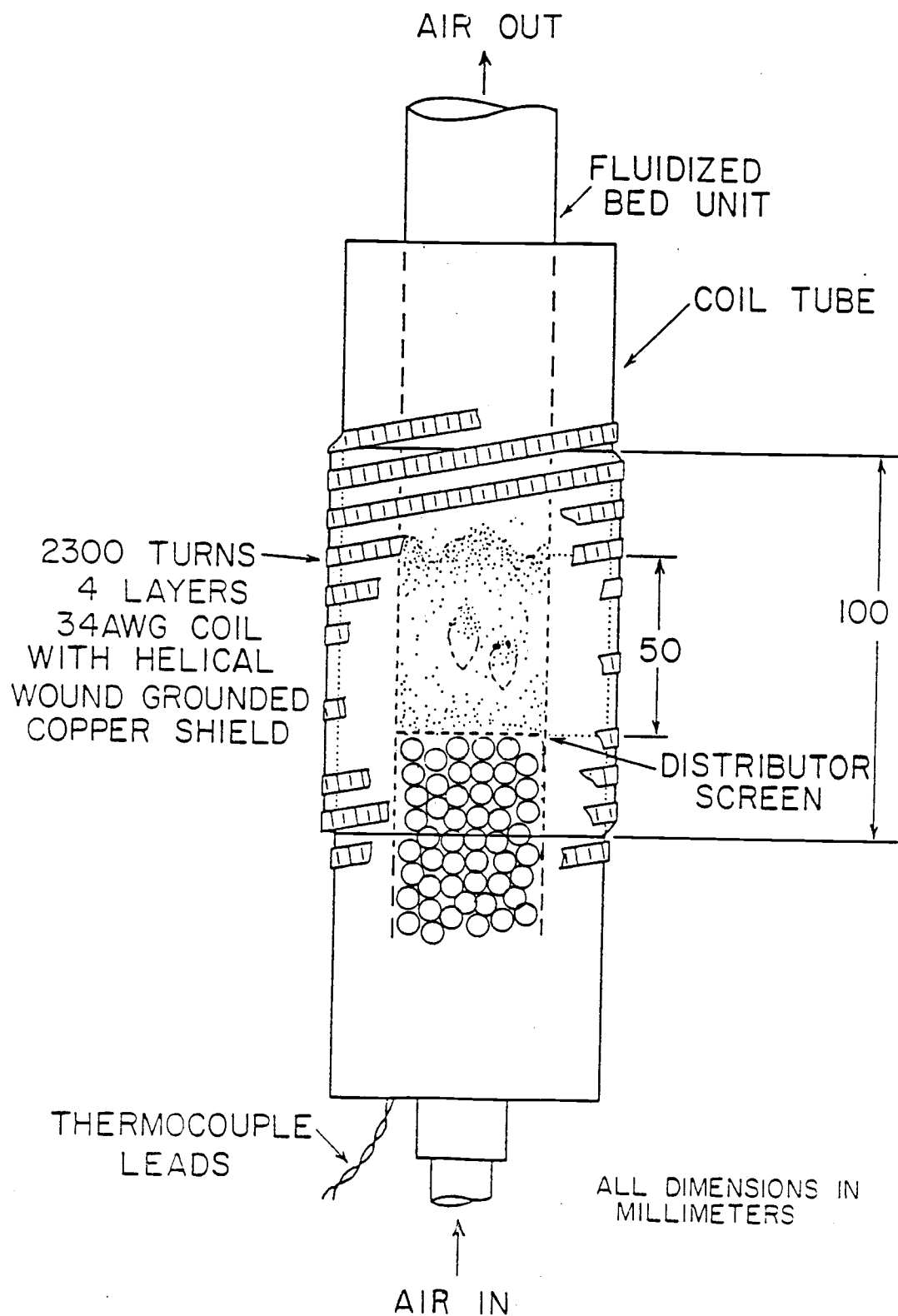


Figure IV-4. Detector Coil for Sensing Changes in Magnetic Permeability.

into one of the fluidized beds while keeping the other one empty the magnetic permeability of the injected sample will be indicated by the output voltage of the ferrite sensor.

The injection device used in these experiments is illustrated in Figure IV-5 and discussed next. The injection device consists of a PVC plunger inside a clear plastic (Plexiglass) tube. Attached to the lower end of the plunger is a thin cylindrical tube into which the ferrite sample is placed. A rubber stopper is force fit on the end of the outer tube and holds the particles in place. This rubber plug is attached to the outer tube by a piece of nylon thread. This ensures that the stopper is removed when the injection device is removed from the bed after the particles have been released. The top of the plunger has a 33mm disk secured to it and when this is depressed it will meet with a similar disk secured to the top of the outer tube. A small roller type switch is countersunk in the lower disk such that when the plunger is depressed and the two disks meet this switch will be closed. The closing of this switch is thus synchronized with the rubber stopper opening and the particles leaving the lower end of the tube. This switch is connected to the computer data acquisition system and triggers the software program to start taking data. Thus the data is taken only when the injection device has been inserted into the bed and the particles have been released.

Data acquisition is made possible with an IBM-PC computer and an IMI-Adalab system. This system is capable of taking data at a rate of up to 20kHz from 8 analog input channels and 8 digital input

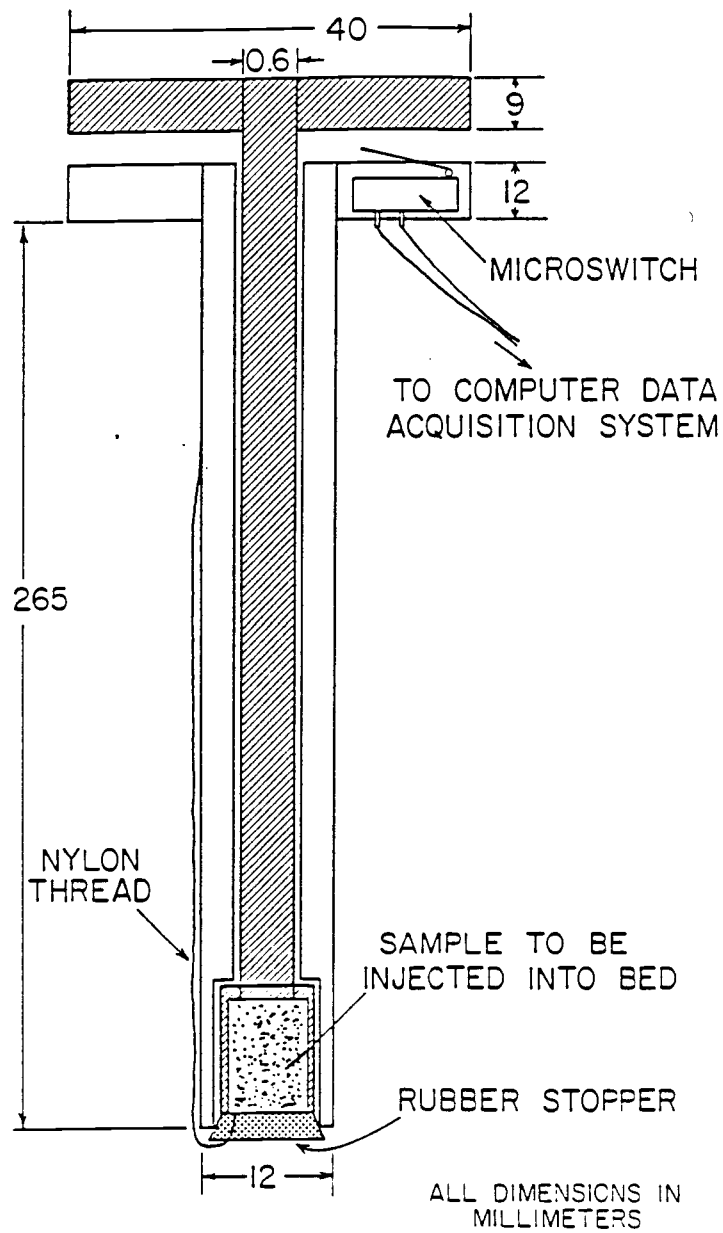


Figure IV-5. Injection Device Used in Transient Heating Experiments.

channels. This capability is far in excess of the speed required to record data in this experiment. As mentioned above the data acquisition program is triggered by the opening of the injector device and this represents the most convenient method of program initiation. The connections to the computer and logic flow diagram for the data acquisition program are given in Figure IV-6 and details of the program are given in Appendix J. It should be noted that all runs using the computer were carried out for a total of 10 seconds with a sampling frequency of 250Hz from the ferrite sensor. This combination gave 2500 data points and was more than enough to trace the transient change of temperature (magnetic permeability) for all the systems studied.

IV-2-2. Experimental Procedure

The experimental procedure followed for each system of ferrite and zirconia was the same. Basically two types of experiments were performed. The first involved injecting a sample of cold ferrite particles into a cold fluidized bed of zirconia particles. The second involved injecting a sample of cold ferrite particles into a hot fluidized bed of zirconia particles.

From some preliminary studies discussed in Appendix K it was decided to use a cold sample of particles of which 50 percent by weight was ferrite and the remainder was zirconia. The total mass of the sample was set equal to 1 gram and the mass of zirconia in the fluidized bed was set at 60 grams. Under these conditions with an initial temperature difference of 65°C between sample and bed the

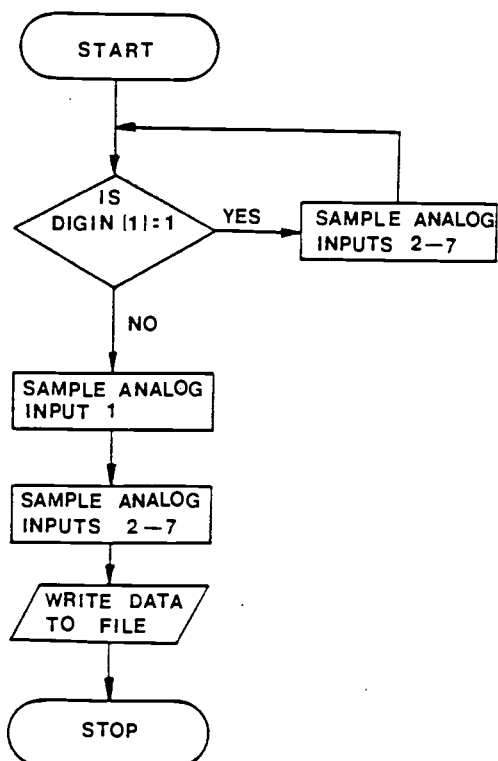
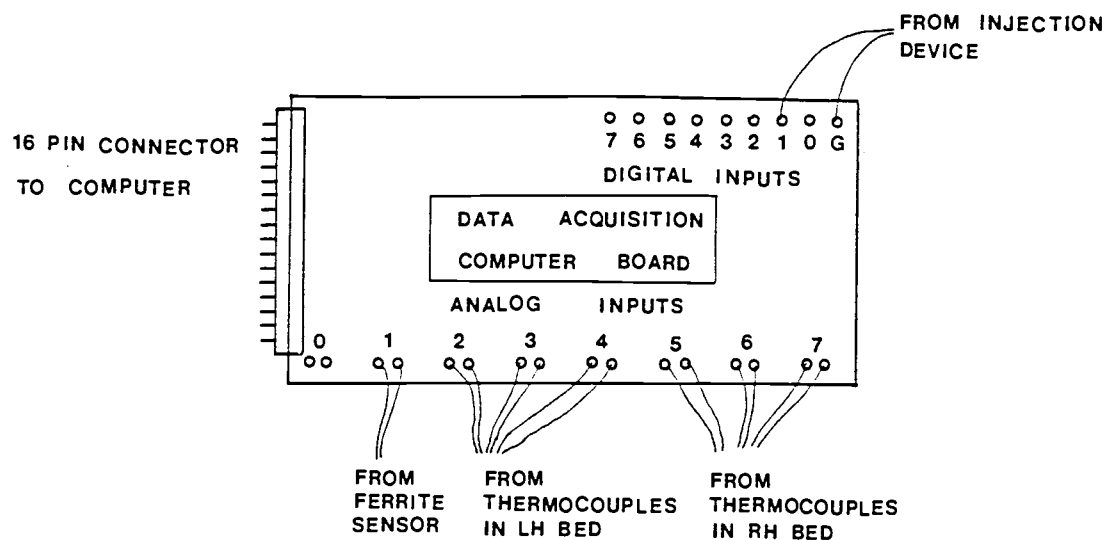


Figure IV-6. Details of Computer Data Acquisition System.

overall temperature of the bed would drop by approximately 1.2°C . Thus the average bed temperature over the course of an experiment would deviate only $\pm 0.6^{\circ}\text{C}$ which is well within the accuracy of this technique.

The zirconia was weighed and then added to the left-hand fluidized bed. When a hot run was being performed the bed was allowed to come to thermal equilibrium, this was checked using a temperature scanning program which monitored the various thermocouples and averaged their values over 1 second intervals. Steady state was assumed when the last twenty readings from each thermocouple varied by no more than 0.2°C .

Three 1 gram samples of 50/50 by weight zirconia and ferrite particles were made up. Each sample was shaken thoroughly to ensure as homogeneous a mixture as possible. The use of a mixed sample effectively smoothes the response signal and is discussed in the next section and Appendix K.

When the fluidized bed had come to equilibrium the temperature scanning program was stopped and the data acquisition program started. The next step was to inject the sample of cold particles into the fluidized bed. The technique used to inject the solids into the bed was carried out manually. The injector device was inserted into the left-hand fluidized bed with the bottom disk resting on the top of the inner tube of the fluidized bed. At this point the bottom of the injector is immersed about 6mm into the top of the fluidized solids. The top disk is rapidly depressed causing the rubber stopper to spring out, thus releasing the sample

particles into the bed. At the same time the data acquisition program is initiated.

The injection device (including rubber stopper) is then removed from the fluidized bed as quickly as possible. This whole procedure takes less than a second to complete and for this reason the heating of the particles before they are injected into the bed can be ignored. As mentioned previously this procedure is carried out manually and care was taken to repeat each injection in the manner described above. However, exact replication is very difficult to achieve and hence there is some scatter in the data, this is discussed later on.

Once the data has been taken the ferrite is removed from the fluidized bed. This is achieved by inserting a cold magnet into the bed which attracts the ferrite to it. The ferrite recovered in this manner is weighed to check that all of the 0.5 grams inserted is removed. The bed is allowed to come back to thermal equilibrium (for the hot bed runs) and then the procedure is repeated with the next sample. Since no zirconia is removed during the set of three runs the bed weight of zirconia changes from 60 grams to 61 grams during the course of an experiment. This increase in bed weight is not significant and is not considered in any of the calculations.

IV-3. Experimental Results

IV-3-1. Cold Fluidized Bed Mixing Studies

Preliminary studies were carried out on the effect of sample shape on the response of the ferrite sensor and these are described

in Appendix K. The steady state response is that achieved when all the ferrite in the sample is completely mixed in the fluidized bed. The magnitude of the steady state response depends only on how much ferrite is introduced into the bed. The initial response, however, is a function of the shape of the sample being injected. A long thin sample will give a greater response than a short fat one. The initial response is also affected by the packing of ferrite in the sample. The less diluted the sample is, the greater the response. This is due to the fact that the closer the ferrite particles are to each other the more numerous and concentrated are the lines of flux. This results in an increase in the output signal.

All these factors contribute to the overall response signal when a cold sample of particles is injected into a cold fluidized bed. This response will be some type of exponential decay. Initially the signal will have a high value when the slug of cold particles entering the bed is not well-mixed. As the slug breaks up the signal will decrease until the steady state response is reached corresponding to the ferrite being completely mixed in the zirconia bed. The processes occurring during the injection and mixing are illustrated in Figure IV-7 along with a typical response.

For the six ferrite-zirconia systems studied (A-F) three repetitions of the cold mixing experiment were carried out. A typical response, for system A, is given in Figure IV-8 and the responses for the other systems are given in Appendix L. From

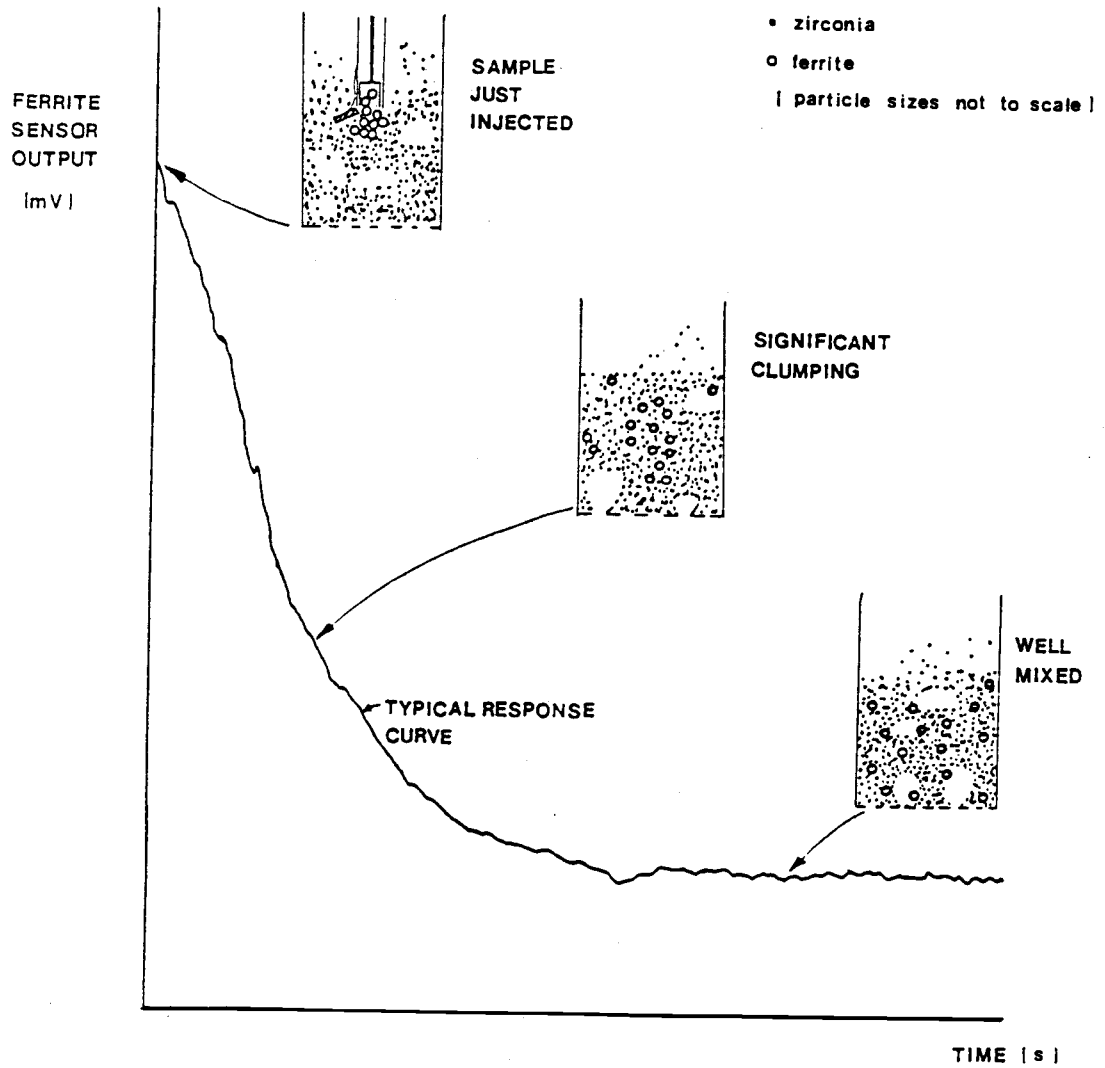


Figure IV-7. Processes Occuring During a Cold Mixing Experiment.

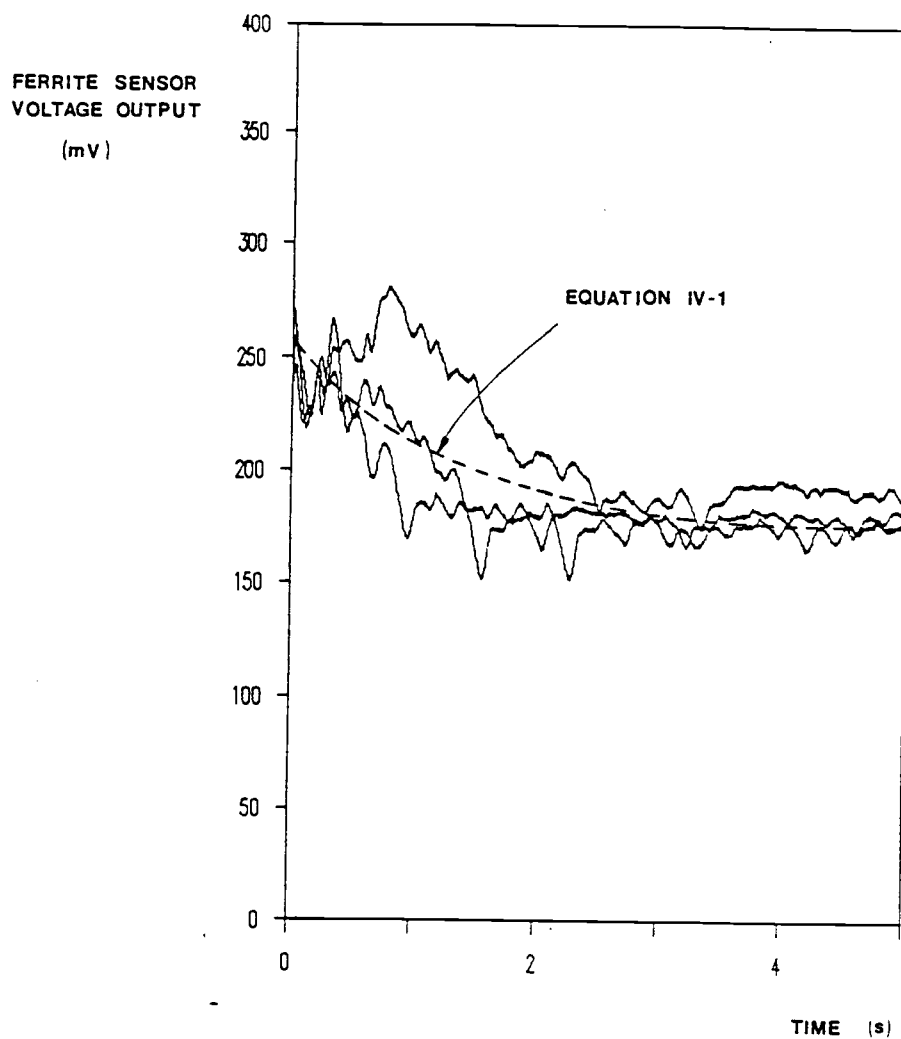


Figure IV-8. Typical Response Curves for Cold Mixing Experiments, System A.

Figure IV-8 it can be seen that there is a definite decay in the signal and although there is a considerable amount of scatter between replications the trend for each run is similar. This decay in the response signal must be accounted for when the hot mixing studies are analyzed. The reason for this is that it is necessary to correctly differentiate between this mixing effect and the signal decay due to the ferrite heating up. For this reason it was decided to approximate the decay in signal due to mixing by the following exponential equation:

$$V = A_1 + B_1 \exp(-C_1 t) \quad (\text{IV-1})$$

The parameters A_1 , B_1 , and C_1 were fitted using a least squares error criterion to the combined data of the three cold mixing replications for each system. The constants for each system are given in Table IV-5 along with the levels of fluidization used in each set of runs. The equation for system A is shown in Figure IV-8 as a dotted line.

IV-3-2. Hot Fluidized Bed Mixing Studies

The hot mixing studies were carried out following the same procedure described in the previous section. The only difference between the hot and cold mixing studies was that in the former the zirconia solids in the fluidized bed were preheated to approximately 90°C by the incoming air. The temperature of the fluidized solids was monitored by two type K thermocouples located at the bottom and top of the fluidized bed. Ideally these two temperatures should be

Table IV-5. Fitted Constants for Eq. IV-1 and Fluidization Levels Used in Cold Mixing Experiments.

System	Constants for Eq. IV-1			u_o/u_{mf}
	A'_1 (mv)	B'_1 (mv)	C'_1 (s ⁻¹)	
A	178.5	80.3	0.88	2.0
B	183.9	79.4	0.73	2.0
C	185.5	61.7	1.03	2.0
D	180.0	90.5	0.59	2.0
E	176.4	96.7	0.61	3.0
F	174.6	103.7	0.77	3.0

equal indicating that the bed solids are well-mixed. This, however, was not the case and a small temperature difference was measured across the bed. The maximum measured temperature difference was 4.5°C for the first run for system A. The average temperature difference for all runs was 2.3°C . This non-uniformity of bed temperature should be considered in the analysis of the data. However, a sensitivity analysis of the model used to calculate the heat transfer coefficient from the data indicates that this non-uniformity is not very important and does not greatly affect the value of the heat transfer coefficient calculated from the experimental runs.

The temperatures at the top and bottom of the fluidized bed before and after the cold sample was injected are given in Table IV-6. Also shown in Table IV-6 is the average bed temperature used in the calculations and this is based on Eq. IV-2:

$$\bar{T}_{\text{bed}} = \frac{(T_{\text{bot}} + T_{\text{top}})_{\text{initial}}}{2} - 0.6^{\circ}\text{C} \quad (\text{IV-2})$$

Eq. IV-2 is the arithmetic average temperature of the bed just before the cold particles are injected minus 0.6°C . This correction of 0.6°C is to take into account the heating of the cold particles which will effectively lower the temperature of the hot fluidized bed during a run.

There are a few anomalously low temperatures in Table IV-6 and these are discussed in the footnotes to the table.

Table IV-6. Fluidized Bed Temperatures at the Beginning and End of the Hot Mixing Experiments

System	Run No.	Initial Fluidized Bed Temperature (°C)		Final Fluidized Bed Temperature (°C)		Average Temperature in Bed During Run (°C)
		Top	Bottom	Top	Bottom	
A	1	86.7	91.2	55.3*	88.3	88.35
	2	88.1	91.6	87.0	91.5	89.25
	3	88.3	90.4	86.7	90.9	88.75
B	1	87.4	90.3	86.1	90.2	88.25
	2	88.6	91.9	87.4	92.2	89.65
	3	89.4	92.7	88.3	93.1	90.45
C	1	90.0	92.1	88.5	93.0	90.45
	2	90.5	92.9	89.2	93.2	91.10
	3	90.7	92.6	89.7	93.3	91.05
D	1	88.7	90.4	87.4	90.9	88.95
	2	90.0	91.8	88.4	91.8	90.30
	3	90.2	91.5	88.9	91.7	90.25

Table IV-6. Continued

System	Run No.	Initial Fluidized Bed Temperature (°C)		Final Fluidized Bed Temperature (°C)		Average Temperature in Bed During Run (°C)
		Top	Bottom	Top	Bottom	
E	1	88.3	90.2	87.7	90.7	88.65
	2	84.1**	90.0	87.1	90.9	88.40
	3	86.6	89.3	84.7	90.1	87.35
F	1	88.0	88.3	86.6	88.8	87.55
	2	88.0	88.1	86.5	89.0	87.45
	3	87.5	88.4	87.0	88.9	87.35

Notes:

* Thermocouple was pulled out of the bed when the injection device was removed.

** Injection device touched thermocouple. 2°C temperature difference between top and bottom of bed was assumed.

The response curves for system A are shown in Figure IV-9 and the complete set of response curves for the hot mixing studies is given in Appendix L.

IV-3-3. Analysis of Data

IV-3-3-1. Theory and Formulation of Model

In order to calculate the heat transfer coefficient between the cold sample particles and the hot fluidized bed it is necessary to identify and correctly account for all the effects influencing the heating of the particles.

Before all these effects are taken into account it may be instructive to consider a simplified or ideal situation. For this purpose the following assumptions will be made:

1. the particles are isothermal;
2. the magnetic permeability of the ferrite is a step function with respect to temperature, therefore

$$\begin{aligned} V_{\text{coil}} &= V_1 \text{ at } T \leq T_{\text{curie}} \\ V_{\text{coil}} &= V_2 \text{ at } T > T_{\text{curie}} \end{aligned} \tag{IV-3}$$

and

3. the particles are well-mixed in the bed at the instant they are introduced into the bed.

With these assumptions we can make the following analysis. For isothermal particles the temperature history of a cold particle

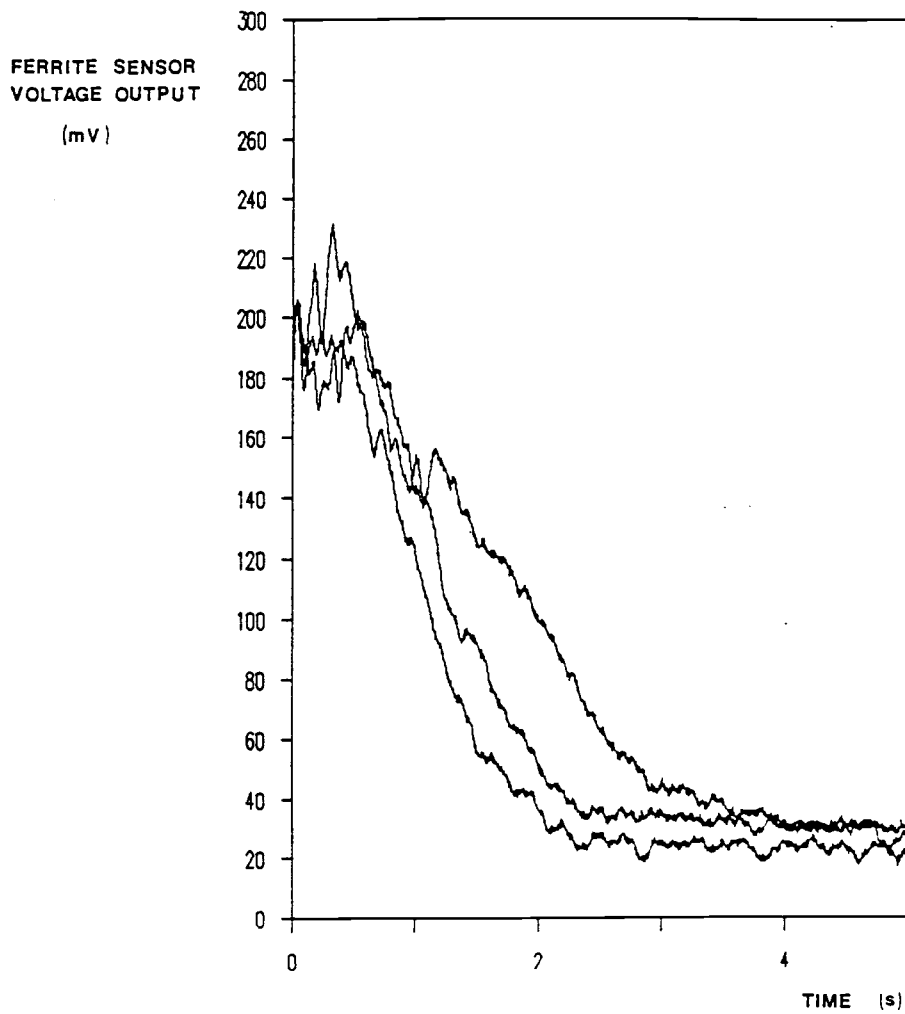


Figure IV-9. Typical Response Curves for Hot Mixing Studies, System A.

initially at some temperature T_i and immersed into a hot bed at a temperature T_f is given by:

$$\frac{T_f - T}{T_f - T_i} = \exp(-Fo \cdot Bi) = \exp\left(-\frac{6h_p t}{d_p \rho_s C_{p,s}}\right) \quad (IV-4)$$

and the output voltage from the ferrite sensor is given by:

$$\begin{aligned} V_{\text{coil}} &= V_1 \text{ for } t \leq \frac{d_p \rho_s C_{p,s}}{6h_p} \log_e \left(\frac{T_f - T_i}{T_f - T_{\text{curie}}} \right) \\ V_{\text{coil}} &= V_2 \text{ for } t > \frac{d_p \rho_s C_{p,s}}{6h_p} \log_e \left(\frac{T_f - T_i}{T_f - T_{\text{curie}}} \right) \end{aligned} \quad (IV-5)$$

This idealized process is described by Eqs. IV-3, 4, and 5 and is shown diagrammatically in Figure IV-10. From the time at which the sharp drop in output voltage occurs the heat transfer coefficient h can be determined.

In the real world situation the voltage response from the ferrite sensor will not be a sharp front because there are several effects which will tend to smear this signal. These effects are given below:

1. mixing of the sample of solids in the fluidized bed;
2. non-ideal magnetic permeability vs. temperature characteristic of ferrite TC-71;
3. different size particles in the sample;
4. electronic equipment has a finite time lag; and
5. particles are non-isothermal.

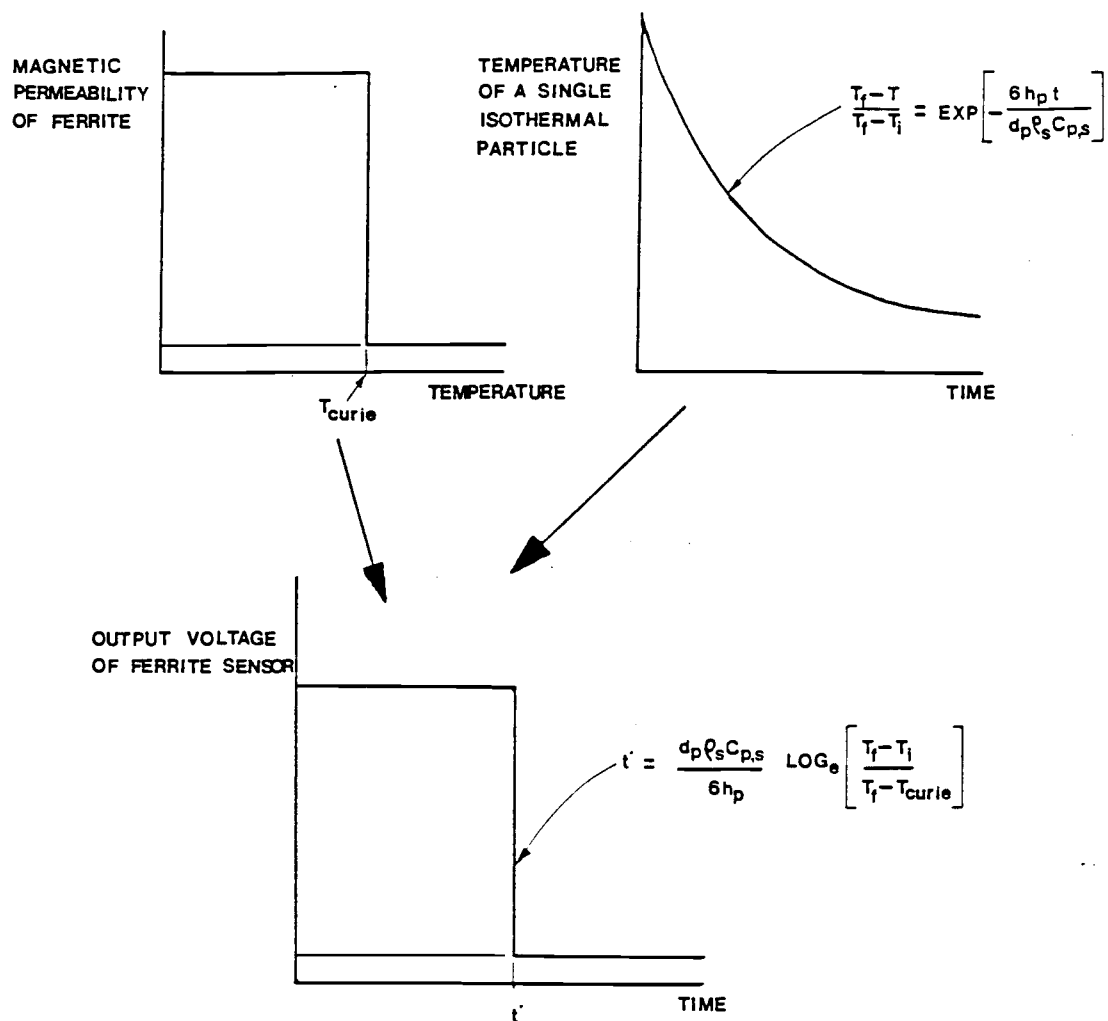


Figure IV-10. Output Response for a Hot Mixing Experiment for an Ideal Process.

An attempt is made here to take account of the first four processes. The possibility of the particles being non-isothermal can be safely ignored since for all the systems studied here the particle Biot numbers all lie well below 0.01.

The first effect due to mixing is the most difficult to account for successfully. It is likely that the heat transfer coefficient for a clump of particles will change as that clump breaks up and disperses among the hot particles. This effect is discussed at some length later in this report. However, for now the heat transfer coefficient is assumed to be constant throughout the length of the experiment. The decay in the response signal due to the mixing of the sample and discussed in Section IV-3-1 can, however, be accounted for. If the hot mixing data is divided by Eq. IV-1 with the appropriate constants for the system of interest then a new response signal is obtained. This new signal represents the part of the original signal which corresponds to the transient heating of the sample particles. This procedure is carried out on all the hot mixing data and the results for system A, Run No. 1 are shown in Figure IV-11. The overall effect is to spread the signal out with respect to time. All comparisons of the model developed in this section will be made with this adjusted experimental data.

The magnetic permeability-temperature characteristics of ferrite TC-71 were measured and are reported in Appendix G. The output voltage from the ferrite sensor can be expressed by the following equation:

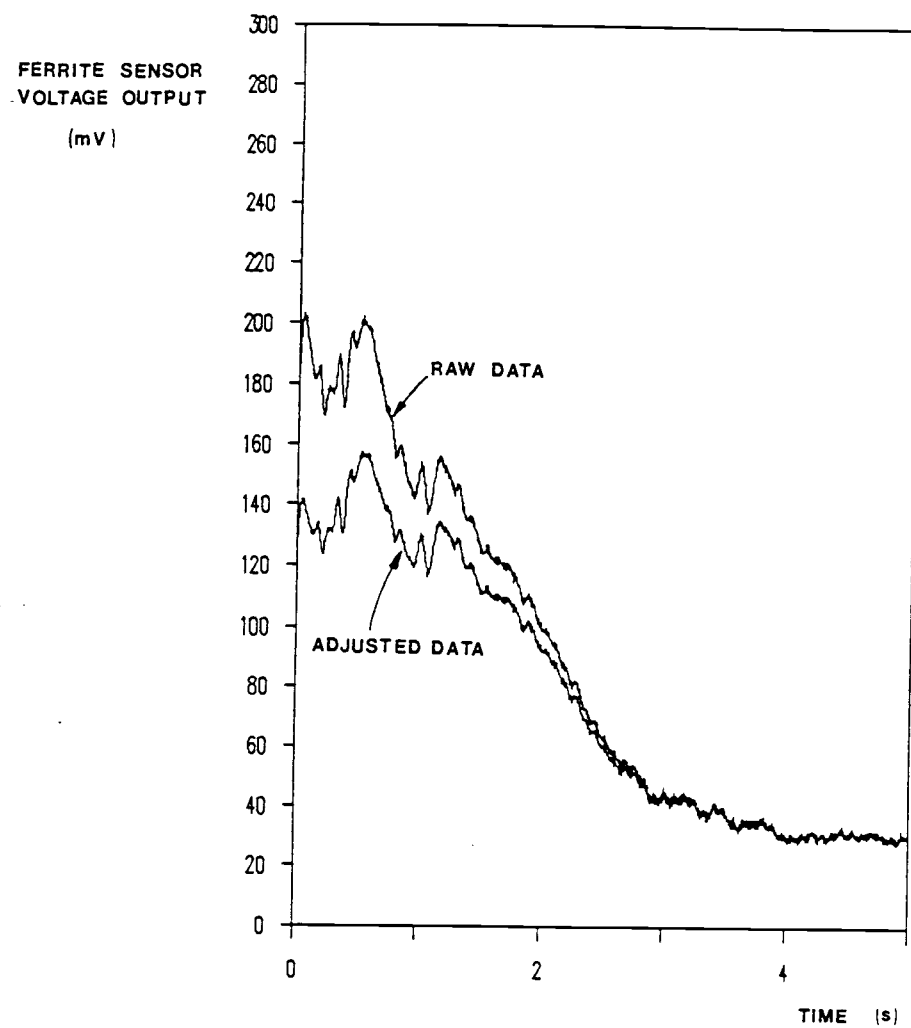


Figure IV-11. Hot Mixing Data for System A, Run No. 1. The Effects of Adjusting the Data to Take Account of Mixing.

$$V_{\text{coil}} = 0.296 + 0.042\theta \quad \theta \leq 1 \quad (\text{IV-6})$$

$$V_{\text{coil}} = 70.4 \exp(-5.34\theta) \quad \theta > 1$$

where:

V_{coil} is the ferrite sensor output voltage for 1 gram of dispersed ferrite in the fluidized bed; and
 θ is the temperature of ferrite in $^{\circ}\text{C}$ divided by 67.0.

Eq. IV-6 is based on the fact that a standard reference sample has an output voltage of 0.245 volts. The equation must be adjusted for any shift in amplifier gain that may occur.

The size distribution of particles in the 1 kg sample of TC-71 ferrite provided by TDK Corporation (Japan) is given in Appendix I. The 1 kg sample was sieved and separated into the six size cuts given in Table IV-4 and referred to as systems A through F. Within each of these size cuts it is assumed that the mass distribution of particles is uniform with respect to diameter:

$$P_x(d_p) = \frac{1}{d_2 - d_1} \quad d_1 \leq d_p \leq d_2 \quad (\text{IV-7})$$

$$= 0 \quad \text{otherwise}$$

where:

$P_x(d_p)$ is the mass fraction probability density function.

Finally the electronic equipment has a time lag associated with it. This lag can be adequately represented by a first order system with time constant τ_1 . The input and output voltages from the ferrite sensor may therefore be related by the following convolution integral:

$$V_{out}(t) = \frac{1}{\tau_1} \int_0^t V_{in}(\tau) \exp\left(-\frac{(t-\tau)}{\tau_1}\right) d\tau \quad (IV-8)$$

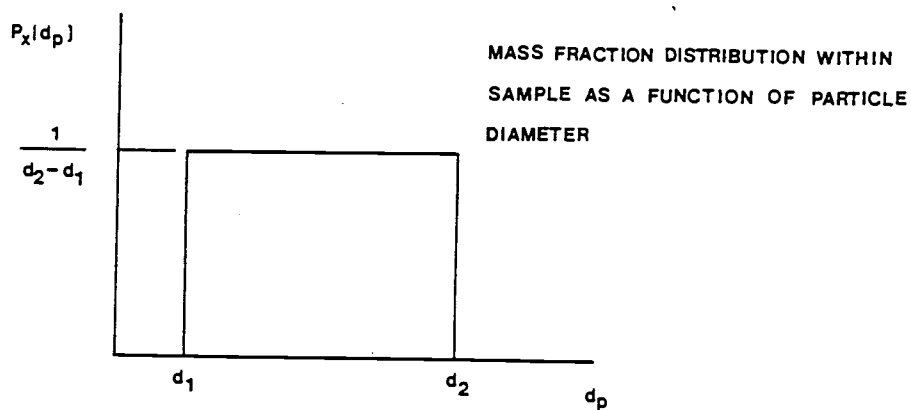
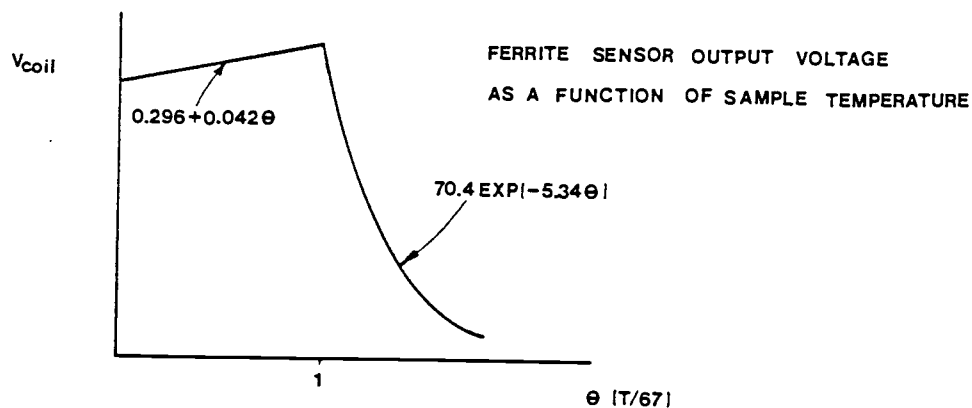
The three smearing effects described by Eqs. IV-6, 7 and 8 are illustrated in Figure IV-12.

By combining Eqs. IV-4, 6, 7 and 8 we can obtain the output voltage from the ferrite sensor as a function of time for the case when cold ferrite particles are injected into a hot fluidized bed. The output voltage obtained is of the following form:

$$V_{out}(t) = \int_0^t \int_0^\infty E(t-\tau) V_{coil}(d_p, \tau) P_x(d_p) d(d_p) d\tau \quad (IV-9)$$

where E is a first order exponential time lag function. The complete integral obtained by substituting the functional relationships from Eqs. IV-4, 6, 7 and 8 is given in Table IV-7. From Table IV-7 it can be seen that the only unknown in the integral is h_p the heat transfer coefficient. Thus if a value of h_p is chosen the output voltage from the ferrite sensor, according to this model, can be generated.

The evaluation of the integral must be carried out numerically. Since this generated voltage-time profile will be compared with the



TIME LAG IN ELECTRONIC EQUIPMENT

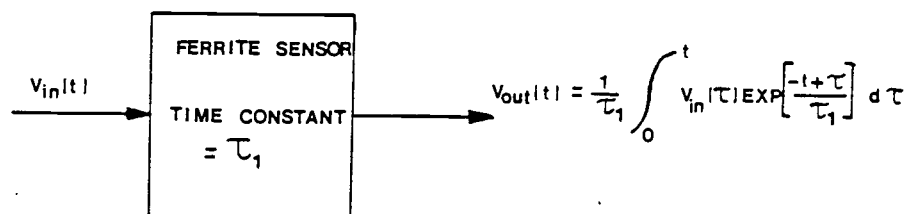


Figure IV-12. The Three Effects Tending to Cause a Smearing of the Response Signal.

Table IV-7. Output Voltage from the Ferrite Sensor Predicted by Theory

$$i. \quad v_{out}(t) = \frac{1}{\tau_1} \frac{1}{d_2 - d_1} \int_0^t \int_{d_1}^{d_2} (0.296 + 0.042(\theta_f - (\theta_f - \theta_i) \exp(-\frac{6h\tau}{d_p \rho_s C_{p,s}}))) \exp(-\frac{(t-\tau)}{\tau_1}) d(d_p) d\tau$$

$$\text{for } t \leq \frac{d_1 \rho_s C_{p,s}}{6h} \log_e \left(\frac{\theta_f - \theta_i}{\theta_f - 1} \right)$$

$$ii. \quad v_{out}(t) = \frac{1}{\tau_1} \frac{1}{d_2 - d_1} \left(\int_0^t \int_{d_0}^{d_2} (0.296 + 0.042(\theta_f - (\theta_f - \theta_i) \exp(-\frac{6h\tau}{d_p \rho_s C_{p,s}}))) \exp(-\frac{(t-\tau)}{\tau_1}) d(d_p) d\tau + \right.$$

$$\left. \int_0^t \int_{d_1}^{d_0} 70.4 \exp(-5.34(\theta_f - (\theta_f - \theta_i) \exp(-\frac{6h\tau}{d_p \rho_s C_{p,s}}))) \exp(-\frac{(t-\tau)}{\tau_1}) d(d_p) d\tau \right)$$

$$\text{for } \frac{d_1 \rho_s C_{p,s}}{6h} \log_e \left(\frac{\theta_f - \theta_i}{\theta_f - 1} \right) \leq t \leq \frac{d_2 \rho_s C_{p,s}}{6h} \log_e \left(\frac{\theta_f - \theta_i}{\theta_f - 1} \right) \quad \text{where:} \quad d_0 = \frac{6ht}{\rho_s C_{p,s} \log_e \left(\frac{\theta_f - \theta_i}{\theta_f - 1} \right)}$$

$$iii. \quad v_{out}(t) = \frac{1}{\tau_1} \frac{1}{d_2 - d_1} \int_0^t \int_{d_1}^{d_2} 70.4 \exp(-5.34(\theta_f - (\theta_f - \theta_i) \exp(-\frac{6h\tau}{d_p \rho_s C_{p,s}}))) \exp(-\frac{(t-\tau)}{\tau_1}) d(d_p) d\tau$$

$$\text{for } t \geq \frac{d_2 \rho_s C_{p,s}}{6h} \log_e \left(\frac{\theta_f - \theta_i}{\theta_f - 1} \right)$$

experimentally measured output which consists of 2500 equally spaced data points, it is most convenient to solve the integral in Table IV-7 using a grid of equally spaced points in time. Thus it is most convenient to generate a vector of points from the model on the same time intervals as in the experimental data.

Both the inner and outer integrals in Table IV-7 are evaluated using a Simpson's rule algorithm. It is most convenient to completely evaluate the inner integral and then go back and evaluate the outer convolution integral. The inner integral uses 20 intervals in the region $d_2 - d_1$ to evaluate the function at time increments of 2 milliseconds. The convolution integral is evaluated using the previous 96 evaluations to predict the next value. Since the time constant of the equipment is 12 milliseconds this is equivalent to looking at information 16 time constants ago. The accuracy of both integrals was checked by halving the increments for diameter and time and negligible differences were found.

A final check was made between the rigorous model described in Table IV-7 and a simpler model which ignores equipment time lags and uses the arithmetic mean particle diameter. For this model the output voltage is given by Eq. IV-10:

$$\begin{aligned}
 V_{\text{out}}(t) &= 0.296 + 0.042(\theta_f - (\theta_f - \theta_i)\exp(-\frac{6h_p t}{\bar{d}_p \rho_s C_{p,s}})) \\
 \text{for } t &\leq \frac{\bar{d}_p \rho_s C_{p,s}}{6h_p} \log_e\left(\frac{\theta_f - \theta_i}{\theta_f - 1}\right) \\
 &\hspace{25em} \text{(IV-10)} \\
 V_{\text{out}}(t) &= 70.4 \exp(-5.34(\theta_f - (\theta_f - \theta_i)\exp(-\frac{6h_p t}{\bar{d}_p \rho_s C_{p,s}}))) \\
 \text{for } t &> \frac{\bar{d}_p \rho_s C_{p,s}}{6h_p} \log_e\left(\frac{\theta_f - \theta_i}{\theta_f - 1}\right)
 \end{aligned}$$

Profiles were generated, using typical parameter values, for both the rigorous and simplified models. These profiles are compared in Figure IV-13. It can be seen from this figure that there are only small differences between the two models suggesting that the spread of the signal due to equipment time lag and particle size distribution is not large. For comparison with the experimental data the rigorous model is used throughout.

IV-3-3-2. Parametric Studies

At this point it may be instructive to look at how the profiles generated by the rigorous model, described above, are affected by changes in parameter values.

The most important parameter is h_p the heat transfer coefficient. Profiles were generated for a typical experimental run using different values of h_p and are shown in Figure IV-14. The effect of a decreasing h_p is to flatten and spread the output

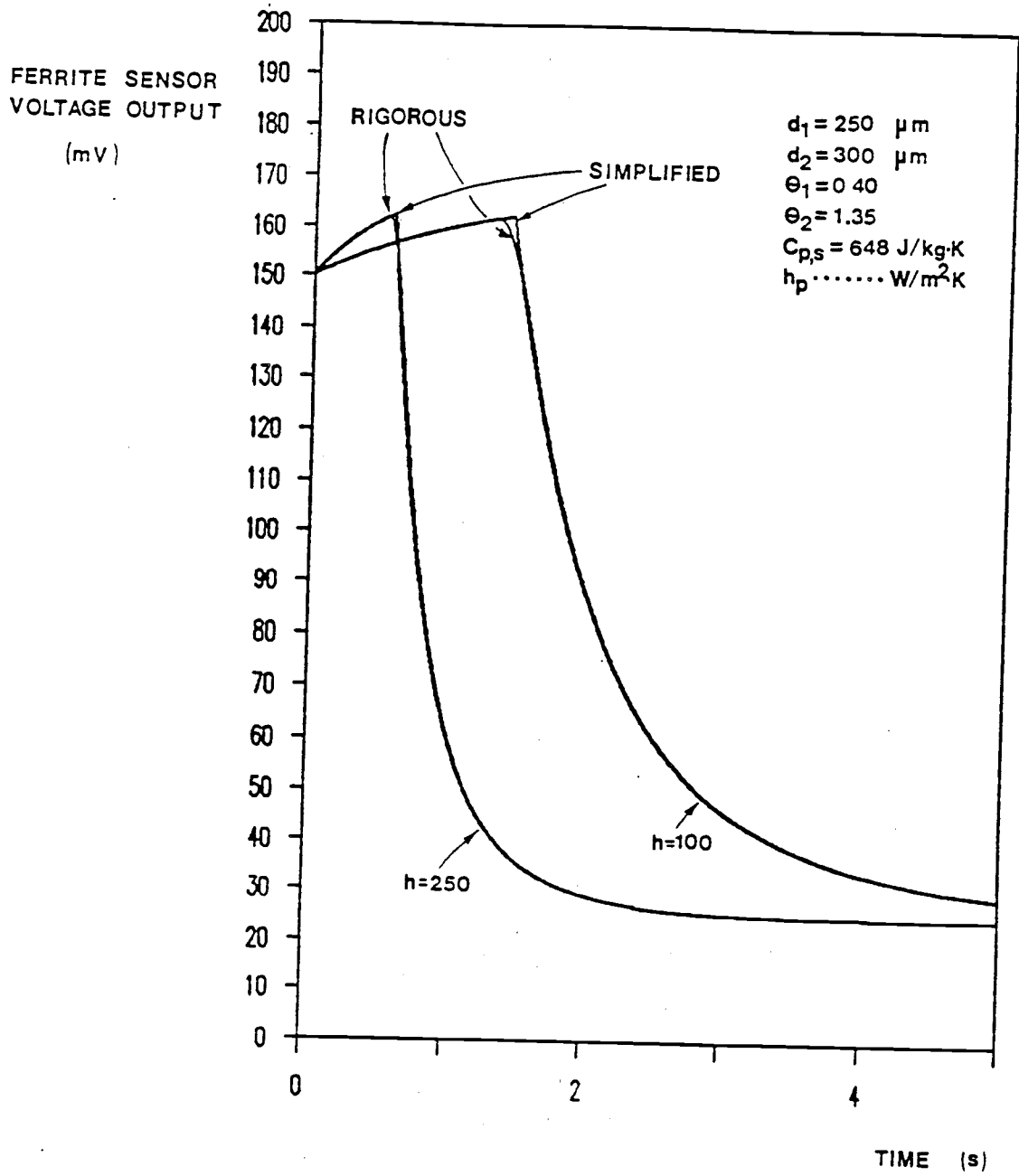


Figure IV-13. Comparison of Rigorous and Simplified Models.

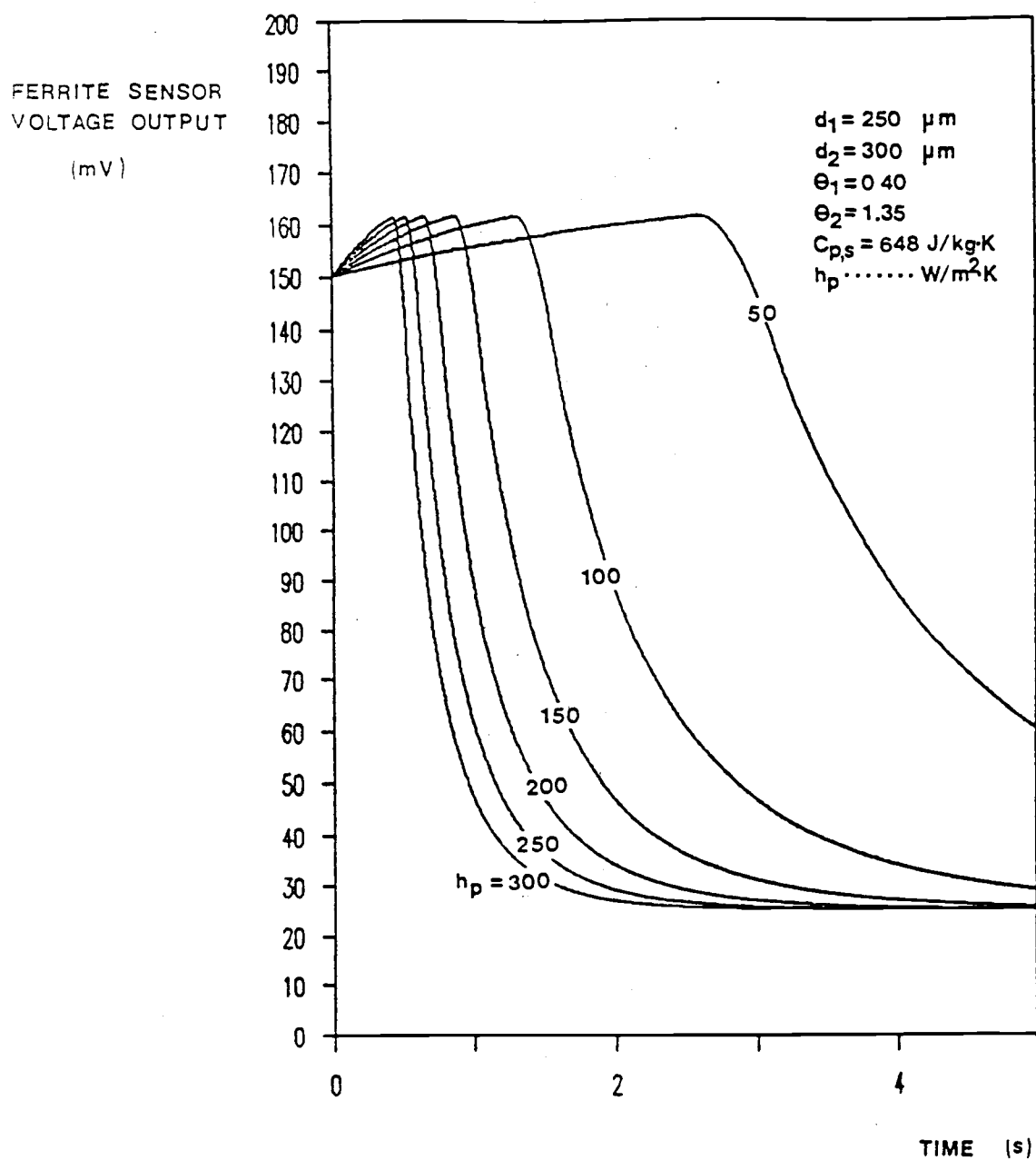


Figure IV-14. The Effect of Changes in h on the Profiles Generated by the Rigorous Model.

response. This is in accord with our intuition which suggests that the lower the heat transfer coefficient the longer it will take for the particles, injected into the bed, to heat up.

Another important parameter is the specific heat capacity of the ferrite. This was determined in an experiment described in Appendix G. The effect of a ± 10 percent change in specific heat due to experimental error was considered. The profiles for two typical sets of parameters are shown in Figure IV-15. The effect of a 10 percent increase in specific heat is exactly equivalent to a 10 percent decrease in heat transfer coefficient and vice-versa. Therefore, if the specific heat capacity of the ferrite were actually greater than the experimentally found value the generated profiles would be sharper than they should be while the reverse is true if the specific heats are actually lower than used here.

The third parameter to be considered is the dimensionless hot bed temperature θ_f . It was stated earlier that in some test runs there was as much as 4.5°C temperature difference across the bed. Therefore it was decided to look at the effect that a $\pm 2.5^{\circ}\text{C}$ temperature change in bed temperature would make on the generated profiles.

The profiles for two typical sets of parameters are shown in Figure IV-16. The effect of increasing the bed temperature is to speed the response while the reverse is true for a decrease in bed temperature. Therefore, if the actual bed temperature is greater than that assumed the generated profile will be later and slower than it should be and vice-versa. However, looking at Figure IV-16

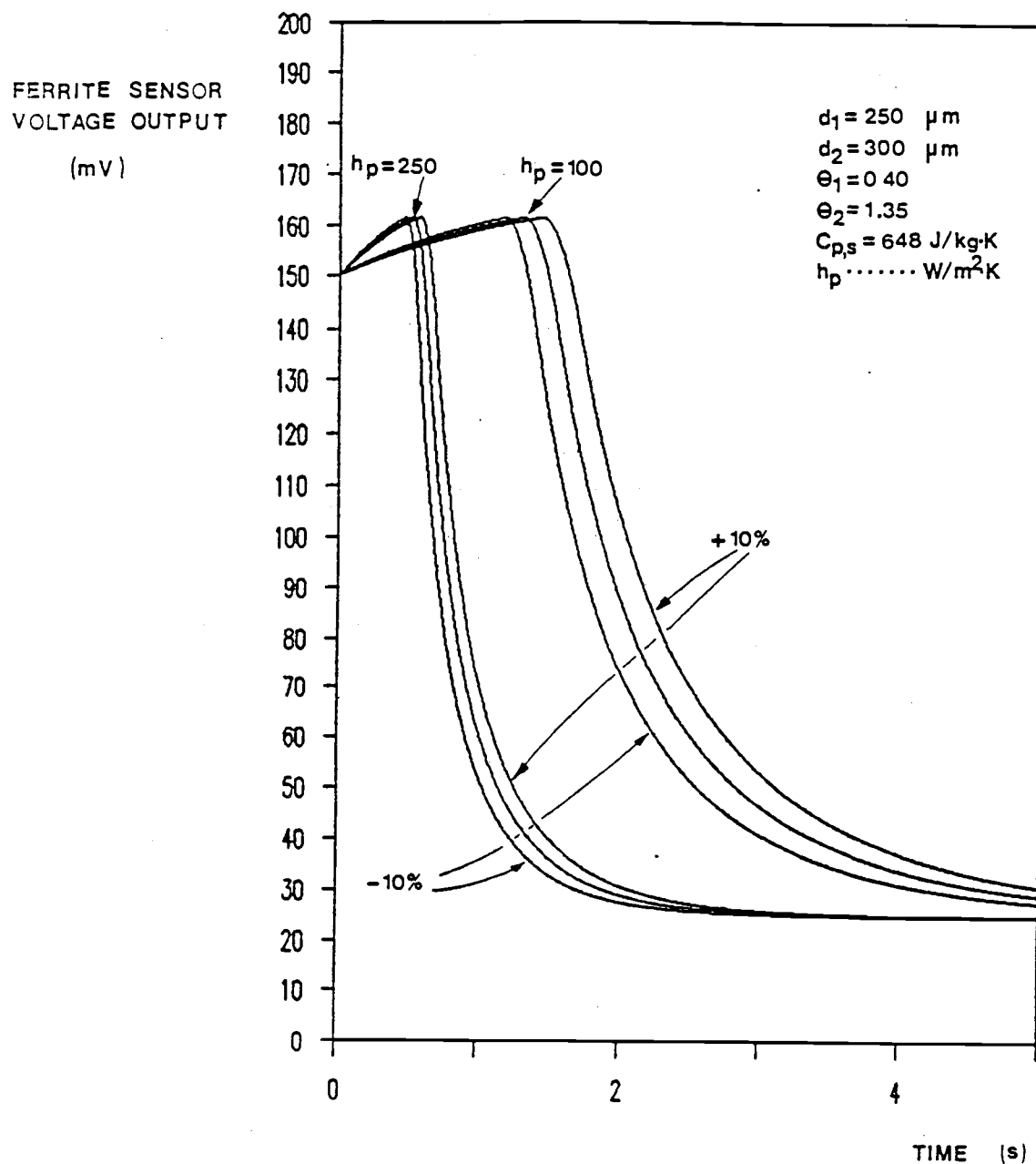


Figure IV-15. The Effect of a ± 10 Percent Change in the Specific Heat Value on the Profiles Generated by the Rigorous Model.

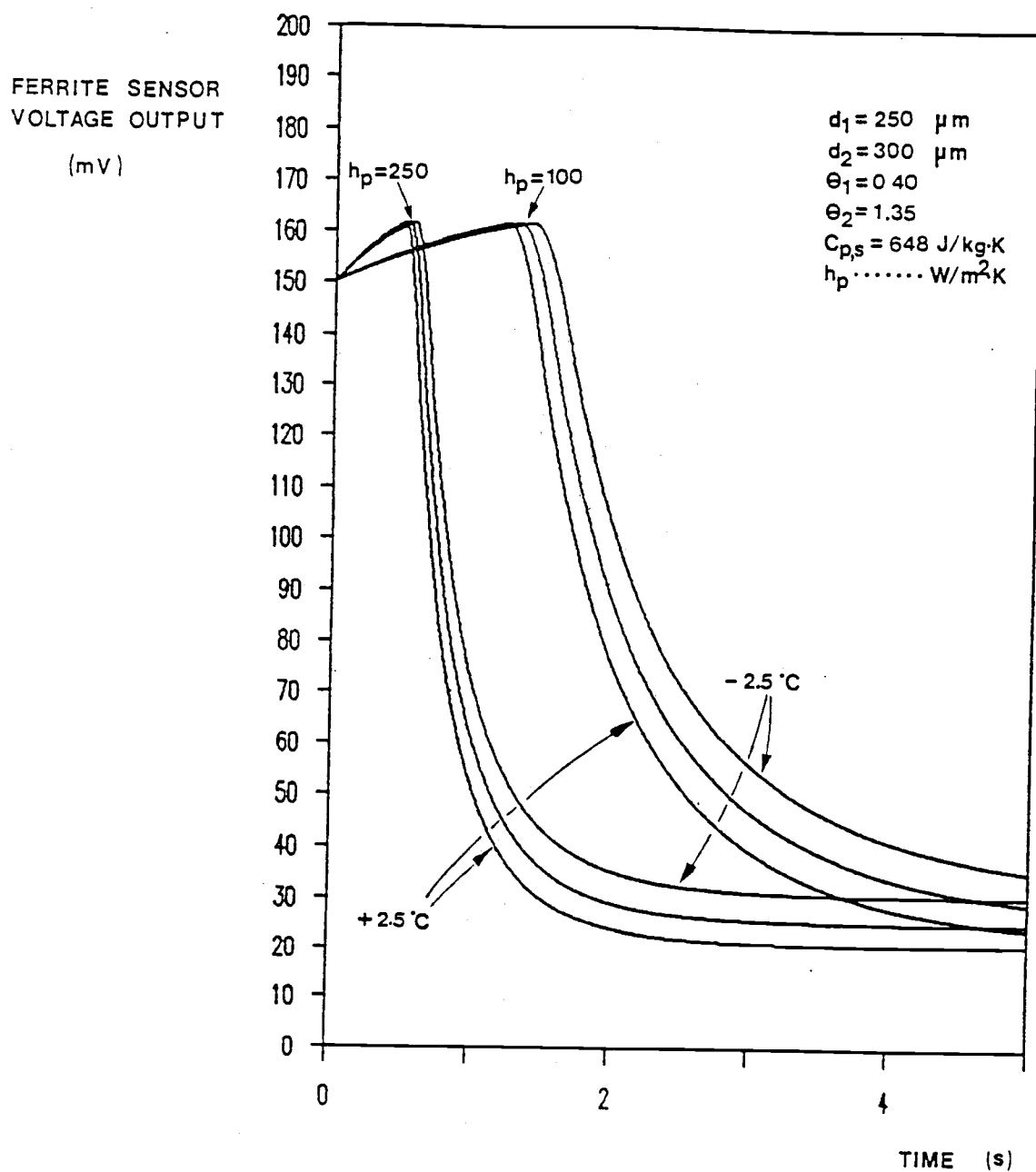


Figure IV-16. The Effect of a $\pm 2.5^\circ\text{C}$ Change in Hot Bed Temperature on the Profiles Generated by the Rigorous Model.

it is clear that a $\pm 2.5^{\circ}\text{C}$ change in bed temperature does not greatly affect the generated profile.

IV-3-3-3. Comparison of Model with Experimental Data

In order to determine the heat transfer coefficients for a cold sample of particles injected into a hot fluidized bed the voltage-time profiles for the model and experimental data must be compared. The heat transfer coefficient which minimized the sum of squares error between the data and the model was chosen to represent the best estimate of the true heat transfer coefficient.

The algorithm used to minimize the sum of squares error was a simple one. A high value of heat transfer coefficient was initially guessed, the model profile was generated using this value and then the sum of squares error between the model and data was calculated. The heat transfer coefficient was reduced and the procedure repeated. If the latest sum of squares error is smaller than the previous value then the program guesses a new value of h and continues. If the new sum of squares error is greater than the previous value then the previous heat transfer coefficient is the one which minimizes the sum of squares error. The tolerance used for the heat transfer coefficients was $\pm 5\text{W/m}^2\cdot\text{K}$.

The heat transfer coefficients found by the above method are given in Table IV-8 for each of the three replications of the six systems of particles studied. The experimental and model generated profiles for system A are given in Figures 17, 18, and 19. The profiles for the other five systems are given in Appendix L.

Table IV-8. Heat Transfer Coefficients for a Cold Sample of Particles Injected into a Hot Fluidized Bed.

System	Run No.	Heat Transfer Coefficient h_p (W/m ² ·K)	Nusselt Number $Nu_p = \frac{h_p d_p}{k_g}$	Reynolds Number $Re_p = \frac{u_o \bar{d}_p \rho_g}{\mu_g}$	Biot Number $Bi = \frac{h_p \bar{d}_p}{6k_s}$
A	1	120	1.51	7.24	.0037
	2	225	2.83	7.24	.0069
	3	180	0.27	7.24	.0055
B	1	120	1.27	3.77	.0031
	2	170	1.80	3.77	.0044
	3	230	2.43	3.77	.0059
C	1	130	1.16	3.17	.0028
	2	145	1.29	3.17	.0031
	3	120	1.07	3.17	.0026
D	1	80	0.60	1.70	.0015
	2	100	0.75	1.70	.0018
	3	110	0.83	1.70	.0020
E	1	105	0.67	1.65	.0016
	2	130	0.82	1.65	.0020
	3	90	0.57	1.65	.0013
F	1	70	0.37	0.82	.0009
	2	80	0.42	0.82	.0010
	3	100	0.53	0.82	.0013

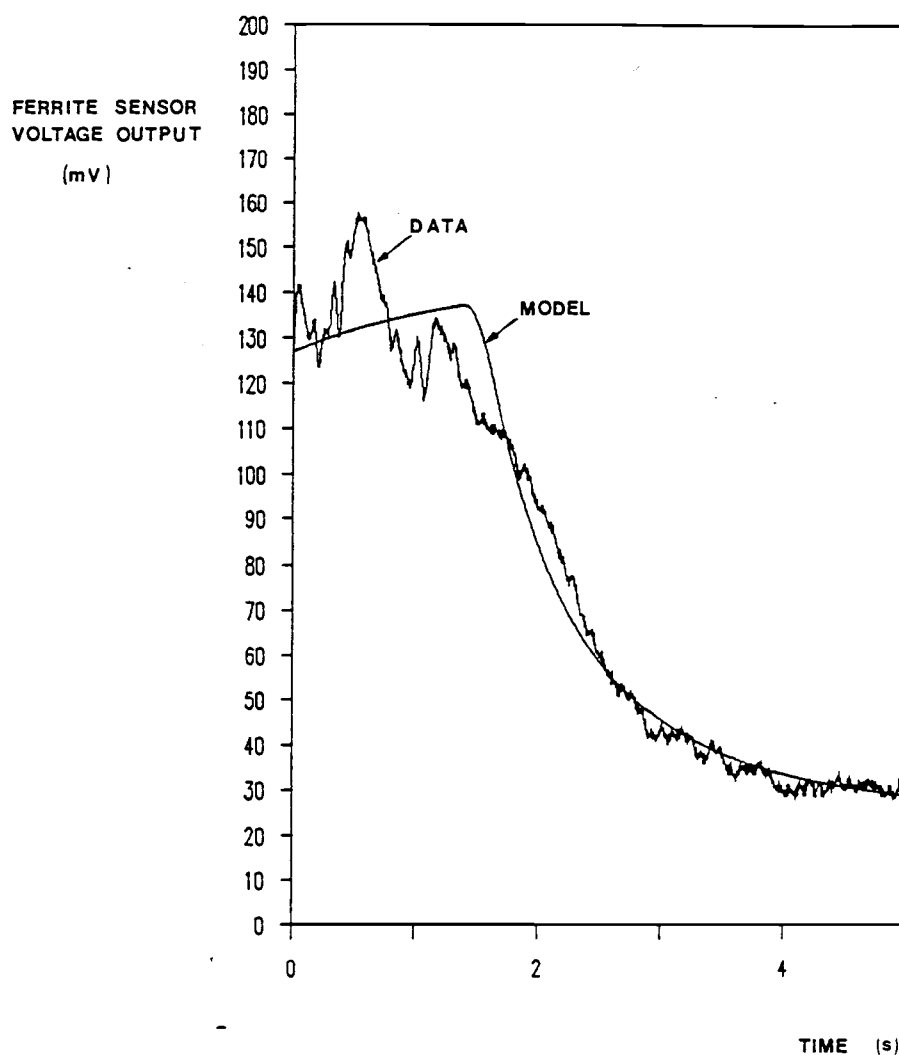


Figure IV-17. Comparison of Experimental Data and Least Squares Error Profile Generated from Rigorous Model -- System A, Run No. 1.

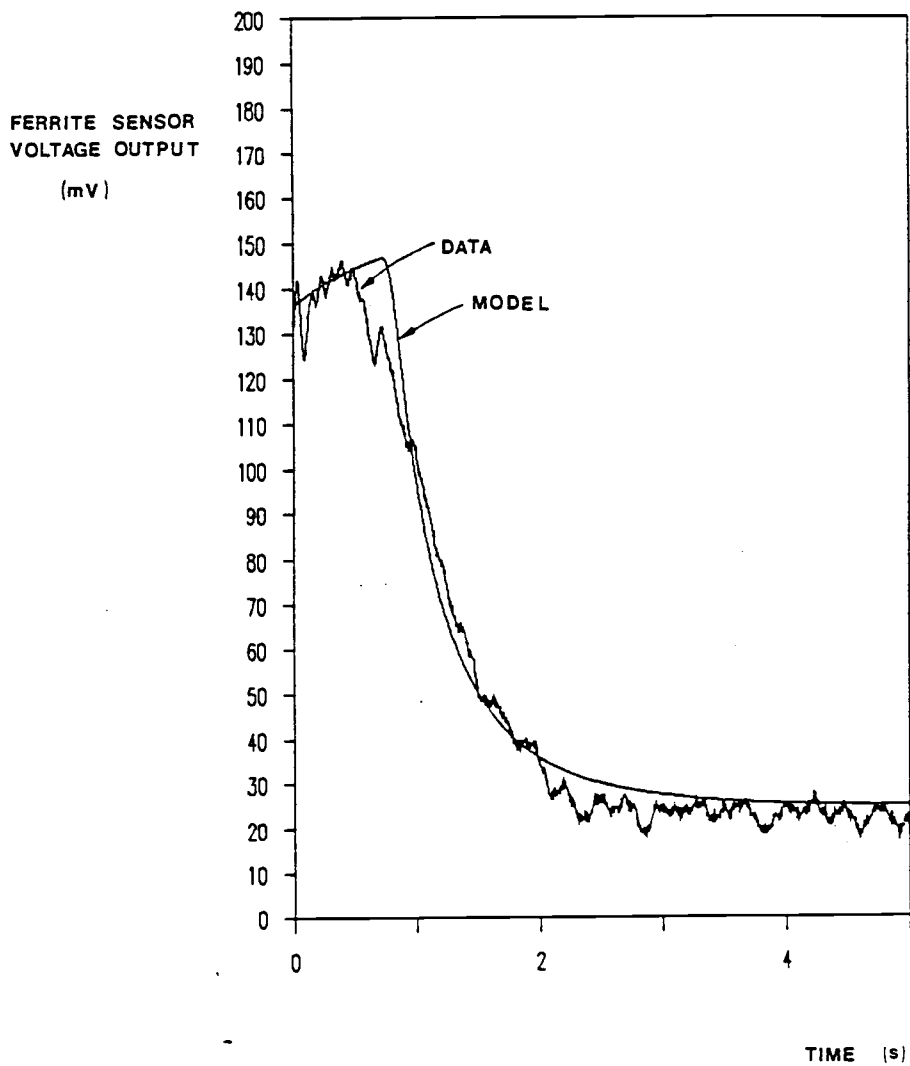


Figure IV-18. Comparison of Experimental Data and Least Squares Error Profile Generated from Rigorous Model -- System A, Run No. 2.

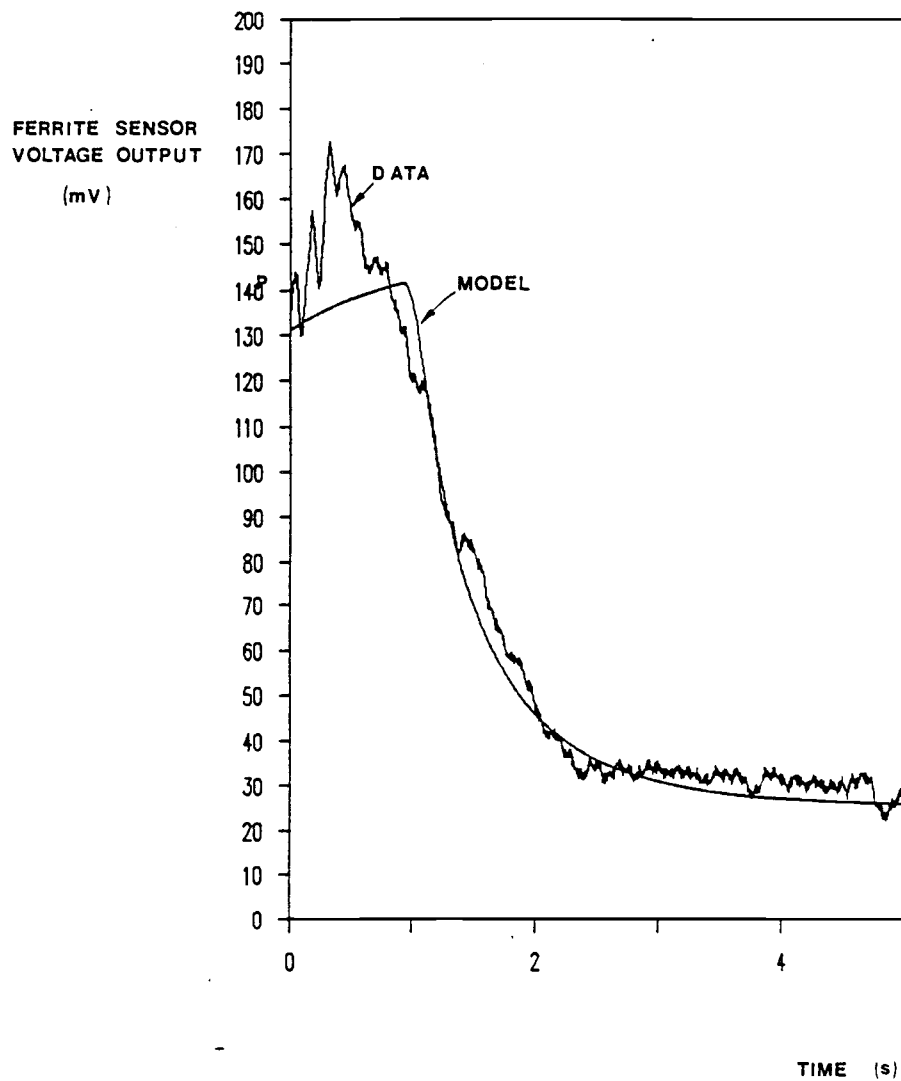


Figure IV-19. Comparison of Experimental Data and Least Squares Error Profile Generated from Rigorous Model -- System A, Run No. 3.

IV-4. Comparison of Results with Previous Work

The results presented in Table IV-7 are compared with previously reported data on gas-solid fluidized bed heat transfer in Figure IV-20.

It can be seen from Figure IV-20 that the data from this work lie between the previously reported data and the Ranz and Marshall (1) equation shown as a dotted line. These results do not provide conclusive proof that heat transfer coefficients in fluidized beds should be greater than for a single sphere in air. On the one hand all the data lie above that of previous workers with coefficients up to ten times larger than previously found. On the other hand the data lie below the curve for a single sphere in air.

The author believes that the true Nusselt numbers for small particles in fluidized beds lie above the correlation for single spheres in air. It is believed that the reason the present results lie below this correlation is that the heat transfer processes is masked by the effects of mixing. This is discussed in the next section.

IV-5. Discussion of Results

As pointed out previously there are several different processes occurring when a cold sample of ferrite particles is injected into a hot fluidized bed. These different effects were modeled and the heat transfer coefficients determined by comparing the model and data.

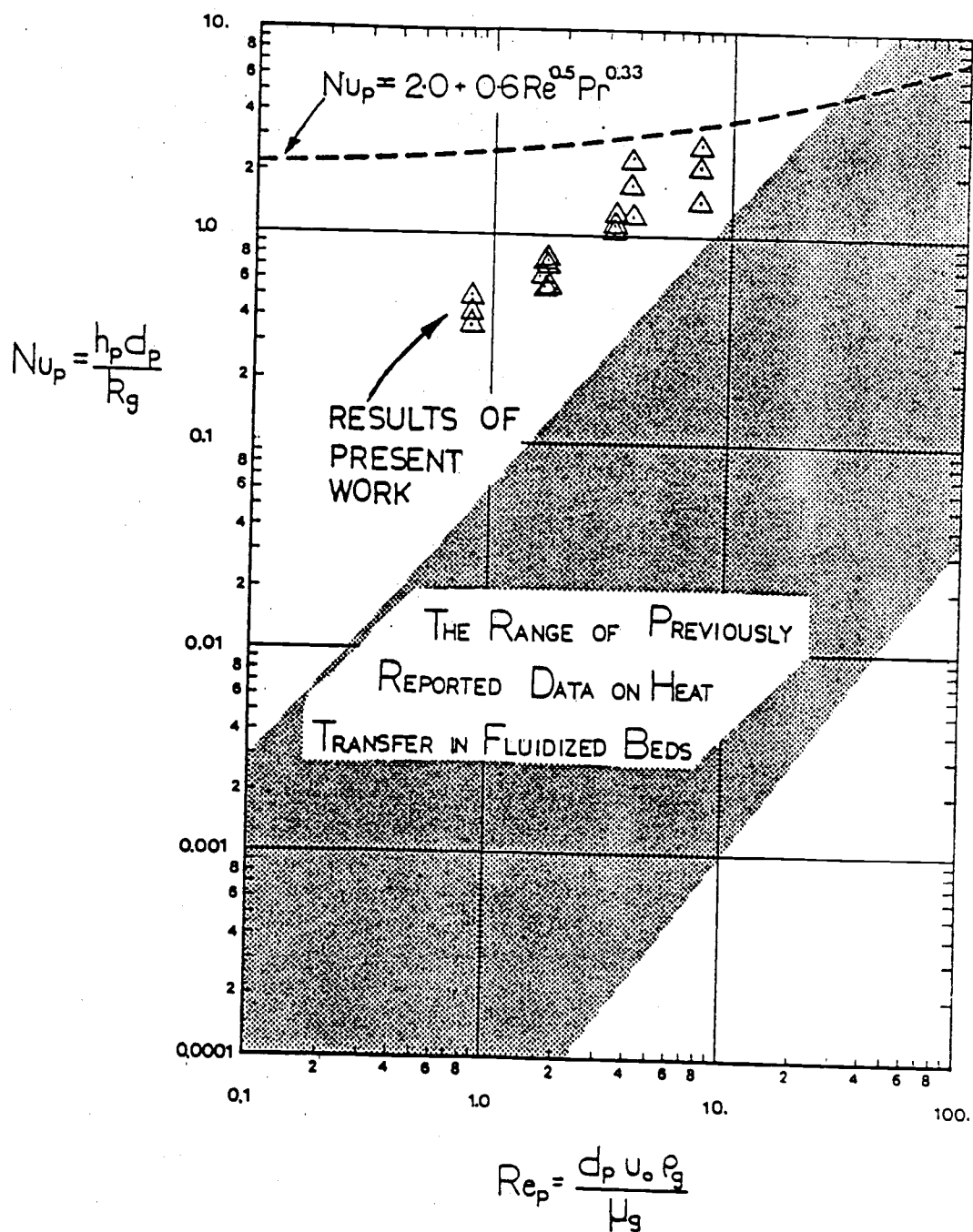


Figure IV-20. Comparison of the Results of the Present Work with Previously Reported Data.

The effects of changing some of the experimentally determined parameters needed in the model were investigated. The effects of changes in the specific heat capacity of ferrite and the temperature of the hot bed on the profile generated by the model were small. Hence the values of the heat transfer coefficients obtained by comparing the model and data are not greatly influenced by experimental errors in these parameters.

As mentioned previously the most difficult effect to take account of is the mixing of the cold particles in the hot fluidized bed. One of the major assumptions of the model was that each particle was isothermal and independent of the other sample particles. This is equivalent to assuming that the sample particles are instantaneously mixed into the hot bed. If, on the other hand, the injected particles do not disperse at all (i.e., they remain in a clump during the heating period), then the model will give some average heat transfer coefficient for the clump of particles based on a single particle diameter.

In practice the data will almost certainly lie somewhere between these two extremes. Since the mixing and heating processes are both effectively exponential functions we can talk about the characteristic time for heating and mixing. These characteristic times are given below:

For heating:

$$\tau_H = \frac{d_p \rho_s C_{p,s}}{6h_p} \quad (\text{IV-11})$$

and for mixing:

$$\tau_m = 1/C_1' \quad (IV-12)$$

where C_1' is the constant in Eq. IV-1 and Table IV-5.

In practice we can say that mixing effects will not be important if:

$$\tau_m \ll \tau_H \quad (IV-13)$$

and that the clumping of particles will be very important if

$$\tau_H \ll \tau_m \quad (IV-14)$$

In order to evaluate τ_H it is necessary to know the true h_p for a single particle. The value of h_p found in these experiments may or may not be the true value depending on which criterion, Eq. IV-13 or IV-14, is met. However, the experimentally determined value of τ_H will always be greater or equal to the true τ_H since the effects of clumping will always slow the heat transfer process down. The experimentally determined values of τ_H and τ_m from this work are given in Table IV-9. Also shown are the values of τ_H based on heat transfer coefficients calculated from the Ranz and Marshall (1) equation and correlation due to Kothari (58) which represents the upper line of the previously reported data in Figure IV-20 and is given by:

$$Nu_p = 0.03 Re_p^{1.3} \quad (IV-15)$$

Table IV-9. Characteristic Times for Heating and Mixing of Different Sized Particles

System	d_p (μm)	τ_H^{exp} (s)	τ_m^{exp} (s)	τ_H^{RM} (s)	τ_H^{K} (s)
A	327.5	1.0	1.1	0.62	5.4
B	275.0	0.8	1.4	0.49	8.9
C	231.0	0.9	1.0	0.36	7.9
D	196.0	1.0	1.7	0.28	12.8
E	165.0	0.8	1.6	0.20	9.4
F	137.5	0.9	1.3	0.15	16.2

Two questions are now addressed. First, is the experimental data consistent with either the Ranz and Marshall (1) correlation or that due to Kothari (59)? Second, what conclusions, if any, can be drawn from these results?

Let us assume that the true heat transfer coefficient is given by Kothari's (59) correlation. From Table IV-9 it can be seen that the characteristic heating times τ_H^K are between 5 and 12 times longer than the experimentally determined mixing times τ_m^{exp} . This satisfies the criterion of Eq. IV-13 and hence the mixing effect can be ignored. Thus, the experimentally determined characteristic times τ_H^{exp} should be close to τ_H^K . They are not and are all smaller by factors of 5 to 10. This is inconsistent and hence we must reject the hypothesis that the true heat transfer coefficient for a single particle in a fluidized bed could be given by Kothari's (59) correlation.

Now let us assume that the true heat transfer coefficients are given by the Ranz and Marshall (1) equation. The characteristic heating times τ_H^{RM} are given in Table IV-9. These are all smaller than the corresponding τ_H^{exp} which is consistent with the hypothesis that the true heat transfer coefficients for a single particle in a fluidized bed could be given by the Ranz and Marshall (1) equation.

Another interesting point about the data in Table IV-9 is that the value of τ_H^{exp} is nearly constant for all the systems studied and shows no trend to increase or decrease with particle size. There are two possible explanations for this. Firstly, the heat

transfer coefficient could be directly proportional to the particle diameter. This supports the argument that $h_p \rightarrow 0$ as d_p or $Re_p \rightarrow 0$. However, there is a second argument which supports the view of a limiting Nusselt number for small particle heat transfer.

From the values of τ_m^{exp} it can be seen that the mixing processes for each system appear to be similar. This is not surprising since the mechanism of mixing should be the same for the narrow range of particle systems studied here. If we consider the dispersion of the sample in terms of the clump of particles splitting to form smaller clumps and these in turn splitting, etc., then at a given time after injection the number and size of clumps of particles in the bed will be the same for any system. The effective density, effective specific heat capacity and size of these clumps will be similar for all systems. Therefore, the effective heat transfer between the hot bed and the individual clumps will be similar for all systems. With this picture of the mechanism of mixing and heat transfer in the bed it can be seen that the heating of the sample in each system will occur at the same rate, i.e., the characteristic heating time will be independent of the system studied. This argument agrees with the experimental findings that τ_H^{exp} is approximately the same for all systems. Moreover, if this is true the characteristic times for heating the clumps must be much less than the values of τ_m^{exp} which means that the individual particle heat transfer coefficients could lie well above the Ranz and Marshall (1) correlation.

IV-6. Conclusions

Heat transfer coefficients for cold samples of particles injected into hot fluidized beds were determined. The particle sizes varied from 137.5 μm to 327.5 μm and the heat transfer coefficients were found to vary between 70 and 230 $\text{W/m}^2\text{K}$.

The present data was found to lie approximately half way between the highest data previously obtained and the Ranz and Marshall (1) equation for single spheres in air. The present results do not provide conclusive proof that heat transfer coefficients for individual particles in fluidized beds lie above those for single spheres in air.

An explanation was presented to demonstrate that these results do not contradict the possibility of an "h" value in fluidized beds above the Ranz-Marshall value for particles in air.

The author believes that the results presented in Section III along with the data from this section lend strong support to the argument of a limiting Nusselt number for small particle fluidized beds. He also believes that this limit is greater than 2.0, the value for single spheres in air.

IV-7. Recommendations for Future Work

It is apparent from the previous discussions that the primary problem to be overcome is the speed at which the sample can be mixed within the bed. This mixing time needs to be reduced by an order of magnitude in order for true heat transfer coefficients to be

obtained from this experiment. The injection device should be rebuilt to provide an improved, faster injection technique. The use of compressed air or a spring loaded mechanism might be effective. The use of a computer controlled activation mechanism might also provide improved reproducibility.

BIBLIOGRAPHY

1. Ranz, W.E., and Marshall, W.R., Chem. Eng. Prog., 1952, 48(4) 173.
2. Kunii, D. and Levenspiel, O., Fluidization Engineering, Krieger, New York, 1977.
3. Botterill, J.S.M., Fluidized Bed Heat Transfer, Academic Press, New York, 1975.
4. Chen, C.C., Proc. Nat. Sci., Council Taiwan, 1975, 8(3) 357.
5. Delvosalle, C., and Vanderschuren, J., Chem. Eng. Sci., 1985, 40 769.
6. Frantz, J.F., Chem. Engr. Prog , 1961, 57(7) 35.
7. Heertjes, P.M., and McKibbins, S.W., Chem. Eng. Sci., 1956, 5 161.
8. Kettenring, K.N., Manderfield, E.L., and Smith, J.M., Chem. Eng. Prog., 1950, 46(3) 139.
9. Walton, J.S., Olson, R.L., and Levenspiel, O., Ind. Engng. Chem., Proc. Devl., 1952, 44(6) 1474.
10. Wamsley, W.W., and Johanson, L.N., Chem. Engng. Progr., 1954, 50(7) 347.
- 11.* Fritz, J.R., Ph.D. Thesis, Univ. of Wisconsin, 1956.
- 12.* Ferron, J.R., Ph.D. Thesis, Univ. of Wisconsin, 1958.
- 13.* Shadkhova, Ph.D. Thesis, Moscow Inst. of Chem. Machinery, USSR, 1955.
14. Sunkoori, N.R., and Kaparathi, R., Chem. Engng. Sci., 1960, 12 166.
- 15.* Yoshida K., B.S. Thesis, Univ. of Tokyo, Japan, 1961.
- 16.* Donnadieu, G., Rev. Inst. Franc. du Petrole, 1961, 16 1330.
- 17.* Sato, K., Shirai, T., and Aizawa, M., Paper presented at the annual meeting of Soc. Chem. Engrs., Japan, 1950.
- 18.* Anton, J.R., Ph.D. Thesis, State Univ. of Iowa, 1953.

19. Richardson, J.F., and Ayers, P., Trans. Inst. Chem. Engrs., 1959, 37 314.
20. Littman, H., and Stone, A.P., Chem. Engng. Progr. Symp. Ser., 1966, 62(62) 47.
21. Littman, H., and Barile, R.G., Chem. Engng. Progr. Symp. Ser., 1966, 62(67) 10.
22. Lindauer, G.C., AIChE Jnl., 1967, 13(6) 1181.
23. Gunn, D.J., and Narayanan, P.V., Chem. Engng. Sci., 1981, 36(12) 1985.
24. Gunn, D.J., Chem. Engng. Sci., 1970, 25(1) 53.
25. Gunn, D.J., and deSouza, J.F.C., Chem. Engng. Sci., 1974, 29(6) 1363.
26. Chang, T.M., and Wen, C.Y., Chem. Engng. Progr. Symp. Ser., 1966, 62(67) 111.
27. Wen, C.Y., and Chang, T.M., Int. Symp. on Fluidization
Drinkingburg, Netherlands University Press, Amsterdam, 1967, 491.
28. Ziegler, E.N., Koppel, L.B., and Brazelton, W.T., Ind. Engng. Chem. Fundls., 1964, 3(4) 324.
29. Ziegler, E.N., and Brazelton, W.T., Ind. Engng. Chem. Fundls., 1964, 3(2) 94.
30. Shirai, T., Yoshitome, H., Shati, Y., Tanaka S., Hojo, E., and Yoshida, S., Chem. Engr., Japan, 1966, 4(1) 162.
31. Jacob, A., and Osberg, G.L., Can. Jnl. Chem. Engng., 1957, 35 5.
32. Barker, J.J., Ind. Engng. Chem. Fundls., 1967, 6(1) 139.
33. Cornish, A.R.H., Trans. Inst. Chem. Engrs., 1965, 43 T332.
34. Nelson, P.A., and Galloway, T.R., Chem. Engng. Sci., 1975, 30 1.
35. Rowe, P.N., Chem. Engng. Sci., 1975, 30 7.
36. Kato, K., and Wen, C.Y., Chem. Engng. Progr. Symp. Ser., 1970, 66(105) 100.
37. Zabrodsky, S.S., Intl. Jnl. Heat Mass Transfer, 1963, 6 23.

38. Kunii, D., and Suzuki, M., Intl. Jnl. Heat Mass Transfer, 1967, 10 845.
39. Hughmark, G.A., AIChE Jnl., 1973, 19(3) 658.
40. Glicksman, L.R., and Joos, F.M., Trans. ASME, 1980, 102 736.
41. Martin, H., Chem. Engng. Sci., 1978, 33 913.
42. Shen, J., Kaguei, S., and Wakao, N., Chem. Engng. Sci., 1981, 33 913.
43. American Institute of Physics Handbook, McGraw-Hill, New York, 1972.
44. Thermophysical Properties of Matter, Vol. 1, Touloukian, Y.S., Powell, R.W., Ho, C.Y., and Komens, P.G., Plenum, New York, 1972.
45. Temperature Measurement Handbook, Omega Engineering, Inc., 1985.
46. Conduction of Heat in Solids, Carslaw, H.S., and Jaeger, J.C., Oxford Univ. Press, 1959.
47. Churchill, S.W., and Bernstein, M., Jnl. Heat Trans., 1977, 99 300.
48. Analysis of Heat and Mass Transfer, Eckert, E.R.G., and Drake, R.M., McGraw-Hill, New York, 1972.
49. Heat Transfer, Chapman, A.J., MacMillan, New York, 1984.
50. Geldart, D., Powd. Technol., 1973, 7 285.
51. Vreendenberg, H.A., Jnl. Appl. Chem., 1952, 2(1) 526.
52. Vreendenberg, H.A., Chem. Engng. Sci., 1958, 9 52.
53. Mickley, H.S., and Fairbanks, D.F., AIChE Jnl., 1955, 1 374.
54. Denloye, A.O.O., and Botterill, J.S.M., Chem. Engng. Sci., 1977, 32 461.
55. Botterill, J.S.M., and Denloye, A.O.O., Chem. Engng. Sci., 1978, 33 509.
56. Schlunder, E.U., Intl. Chem. Engng., 1980, 20(4) 550.
57. Colakyan, M., and Levenspiel, O., AIChE Symp. Ser., 1984, 80(241) 156.

58. Kothari, A.K., M.S. Thesis, Illinois Inst. of Technol., 1967.
59. Unit Operations, Brown, G.G., and Associates, Wiley, New York, 1950.
60. Ergun, S., Chem. Engng. Progr., 1952, 48(2) 89.
61. MacDonald, I.F., El-Sayed, M.S., Mow, K., and Dullien, F.A.L., Ind. Engng. Chem. Fundls., 1979, 18(3) 199.
62. The Fluke Catalog, Fluke Corp., 1986.
63. Settlege, P.H., and Siegle, J.C., Phys. Chem. Aerody. Space Flight Proc. Conf., Philadelphia, Pergammon, 1961.
64. Wen, C.Y., and Yu, Y.H., AIChE Jnl., 1966, 12 610.

* cited from reference (2)

APPENDICES

APPENDIX A

DETERMINATION OF SOME PHYSICAL CONSTANTS OF ALUMEL

A-1. Determination of the Temperature Coefficient
of Resistance " α " of Alumel WireA-1-1. Equipment and Experimental Procedure

The apparatus used for this experiment is shown schematically in Figure A-1. It consists of a constant temperature bath filled with deionized water. A Plexiglass former onto which several loops of Alumel wire are wound. A Fluke 8050A digital multimeter to measure the resistance of the wire, and a -10°C - 110°C mercury thermometer to measure the water bath temperature.

The experimental procedure followed was very straightforward. First the water bath was allowed to come to thermal equilibrium with the surroundings then the plastic former with the Alumel wire wound on it was placed in the bath, making sure that all the wire was immersed in the water. The resistance of the wire was measured both in and out of the water and no difference was observed implying that electrical conduction through the water was, as expected, negligible. The temperature of the water bath was then altered and when the bath came to equilibrium the resistance was again measured. This procedure was repeated for various temperatures between ambient and 100°C .

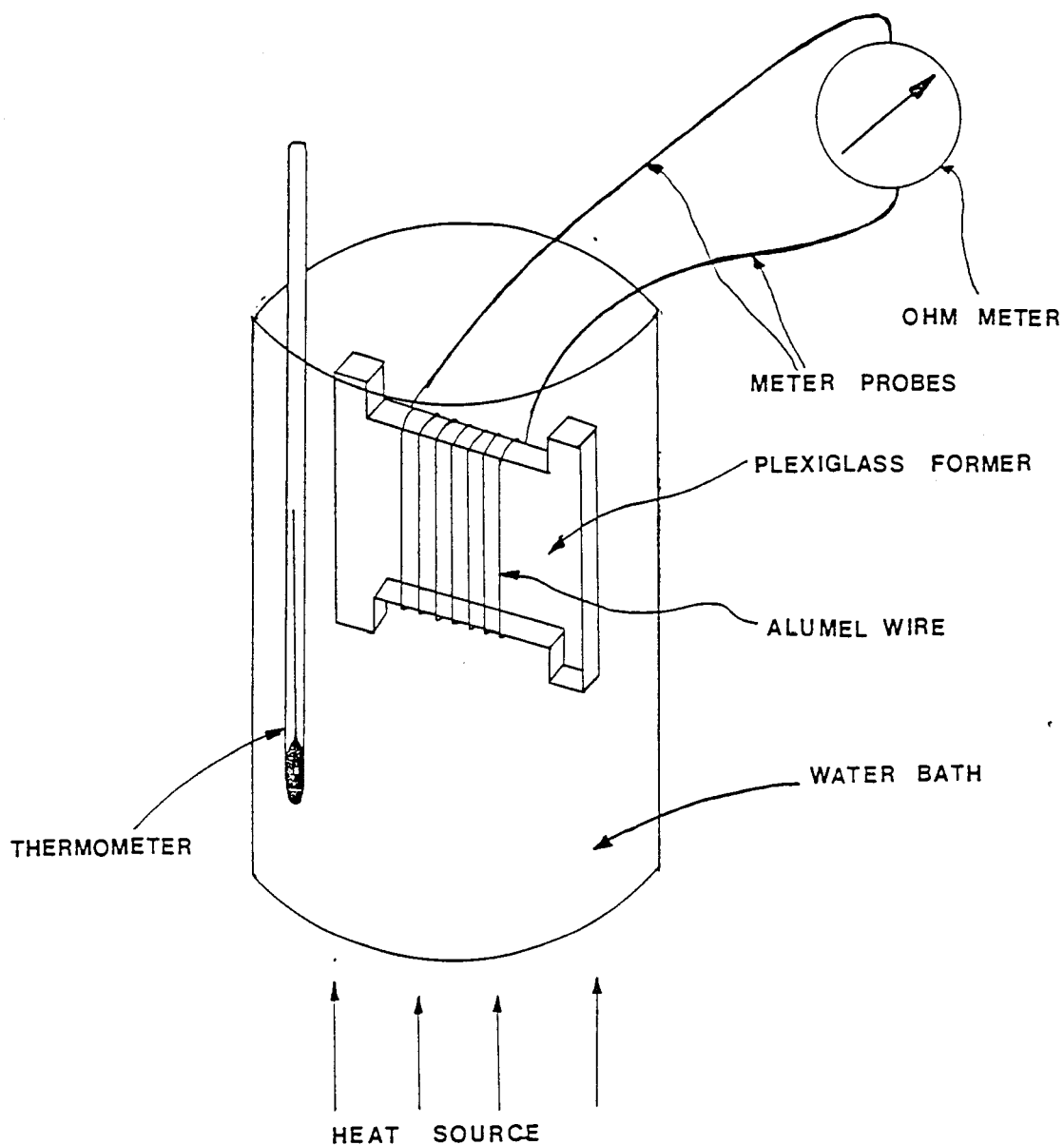


Figure A-1. Experimental Set Up for the Determination of the Temperature Coefficient of Resistance " α " of Alumel Wire

A-1-2. Results

The results for 50.8 μ m and 127 μ m diameter Alumel wires are given in Figure A-2 as a plot of resistance versus temperature. The following example calculation shows how the α value is determined and a summary of the results for the two wire sizes is given in Table A-1.

Example Calculation

The best fit straight line through the data for the 127 μ m diameter Alumel wire is given by Eq. A-1:

$$R = 7.92 + 0.0187T \quad (A-1)$$

where:

R is the resistance in ohms

T is the temperature in $^{\circ}\text{C}$

The temperature coefficient of resistance α is defined by Eq. A-2:

$$\alpha = \frac{R - R_0}{R_0 \Delta T} \quad (A-2)$$

For the data above,

$$\alpha = \frac{7.92 + 0.0187(T - 0) - 7.92}{7.92(T - 0)}$$

$$\alpha = \frac{0.0187}{7.92} = 0.00236^{\circ}\text{C}^{-1}$$

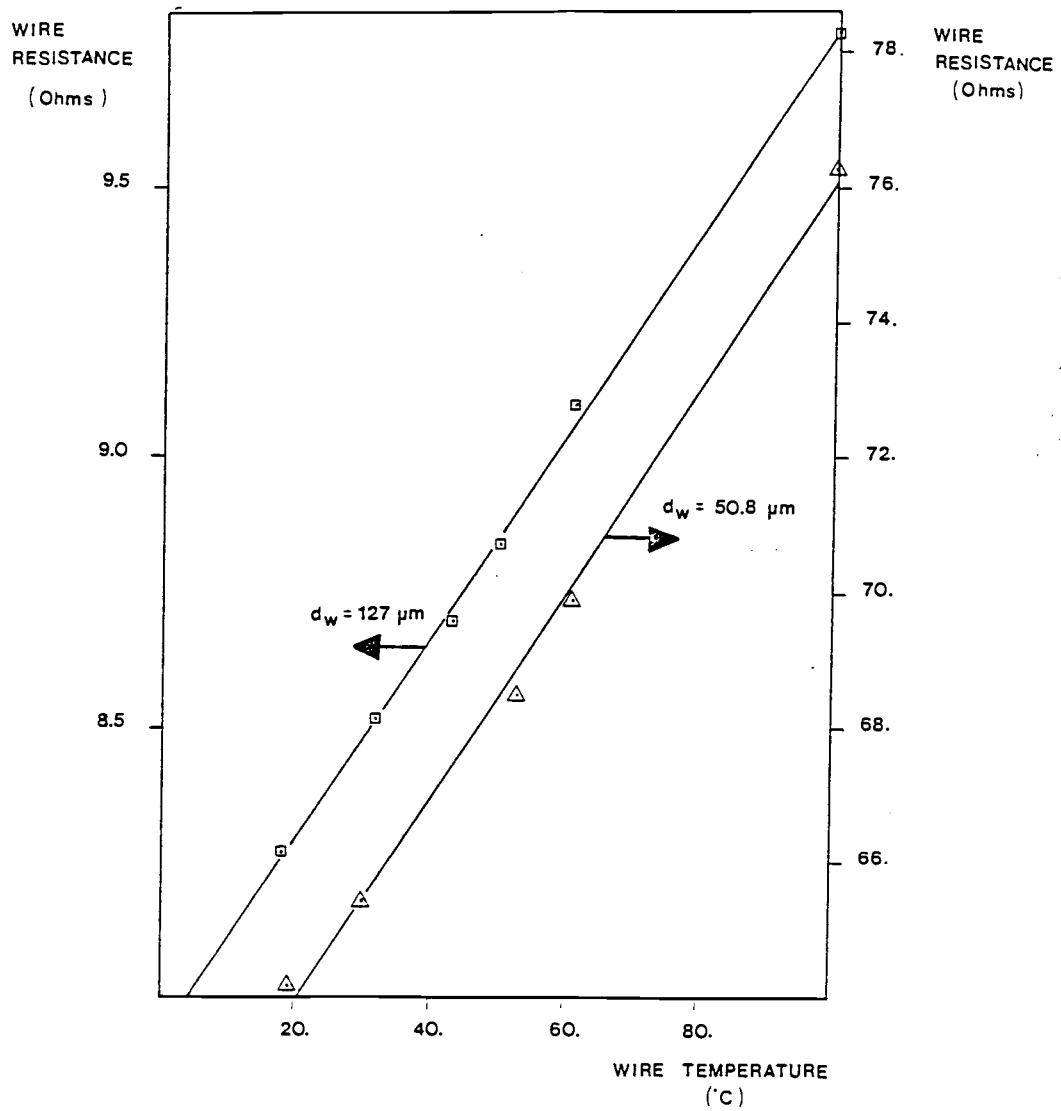


Figure A-2. Temperature vs. Resistance Data for Various Diameter Alamel Wires

Table A-1. Summary of α Values for Alumel Wires

Wire Diameter (μm)	Best Fit Straight Line	α ($^{\circ}\text{C}^{-1}$)
50.8	$R = 60.88 + 0.1517T$	0.00249
127.0	$R = 7.92 + 0.0187T$	<u>0.00236</u>
		$\bar{\alpha} = $ <u>0.00243</u>

The average value of α was equal to $0.00243^{\circ}\text{C}^{-1}$ and this compares very well with the literature value of $0.00239^{\circ}\text{C}^{-1}$.

A-2. Determination of the Resistivity " ρ " of Alumel

A-2-1. Equipment and Experimental Procedure

The experimental set up used for this determination is shown schematically in Figure A-3. The procedure used here was simply to take a known length of wire and solder either end into the brass plugs previously mentioned and illustrated in Figure III-1. The resistance of the wire was then determined by trickling a known current through the wire and measuring the voltage drop across the wire. This method was found to be more accurate than measuring the resistance directly since the internal resistance of the meters can be effectively eliminated in this procedure.

Five measurements of resistance were made for each wire size and the average of these readings was taken to be the resistance of the wires at ambient temperature. The heating effect on the wires was assumed to be negligible due to the very low power dissipation.

A-2-2. Experimental Results

The experimental data are summarized in Table A-2 and a sample calculation is given below.

Example Calculation

The resistivity ρ of a material is defined by Eq. A-3:

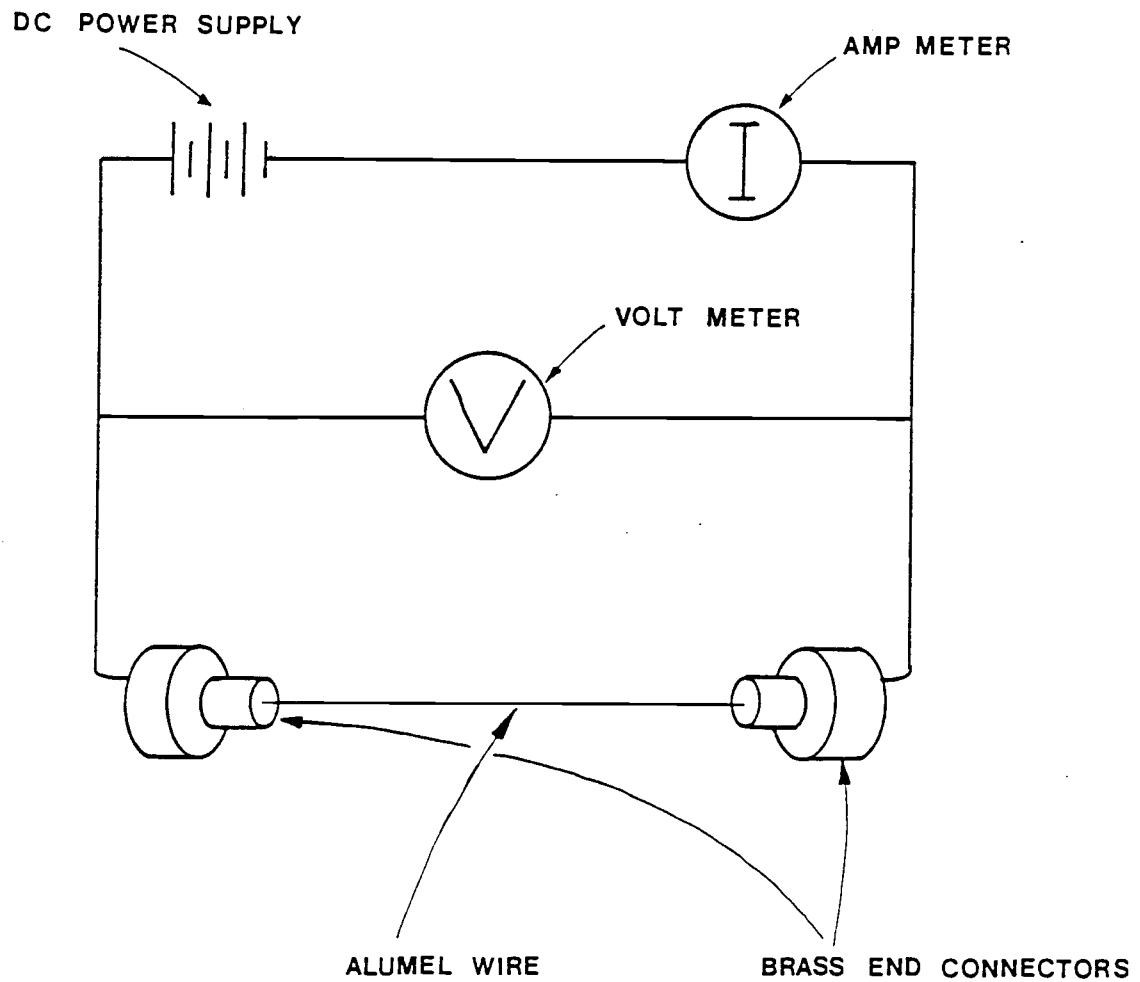


Figure A-3. Experimental Set Up Used in Determining the Resistivity of Alumel Wires

Table A-2. Summary of Resistivity Data for Alumel Wires

Nominal Wire Diameter (μm)	Wire Length (m)	Resistance at $T = 23.3^\circ\text{C}$ (Ω)	Resistivity, $\bar{\rho}$ (Ωm)
50.8	0.4255	63.9500	3.04×10^{-8}
127.0	0.3962	8.8200	2.82×10^{-8}
254.0	0.4125	2.3200	2.85×10^{-8}
381.0	0.3734	0.8370	2.80×10^{-8}
508.0	0.3632	0.5160	2.87×10^{-8}
813.0	0.4166	0.2269	2.83×10^{-8}
			$\bar{\rho} = 2.87 \times 10^{-8}$

$$\Gamma = \frac{R \cdot A_w}{2L} \quad (A-3)$$

where:

R is the resistance of the wire at ambient temperature;

A_w is the cross-sectional area of wire; and

L is one-half the length of the wire.

For the 127 μm diameter wire the following results were obtained:

$$R = 8.82\Omega$$

$$A_w = 1.2668 \times 10^{-8} \text{ m}^2$$

$$2L = 0.3962 \text{ m}$$

and from Eq. A-3:

$$\begin{aligned} \Gamma &= \frac{(8.82)(1.2668 \times 10^{-8})}{(0.3962)} \\ &= 2.82 \times 10^{-8} \Omega\text{m} \end{aligned}$$

From Table A-2, it is apparent that the average resistivity of Alumel Wire at 23.3°C is $2.87 \times 10^{-8} \Omega\text{m}$ which is in close agreement with the literature value of $2.9 \times 10^{-8} \Omega\text{m}$.

APPENDIX B

DETERMINATION OF THE TEMPERATURE PROFILE AND
AVERAGE TEMPERATURE IN AN ELECTRICALLY HEATED WIRE OR CYLINDER

Assumptions used in Analysis

1. No radial temperature variation within wire.
2. Constant thermal conductivity of wire material.
3. Constant heat transfer coefficient between wire and surrounding fluid.
4. Ends of wire are maintained at the bulk temperature of the fluid.

Steady-State Heat Balance on Wire

A steady-state heat balance on the current carrying wire yields the following ordinary differential equation:

$$-\frac{\pi d_w^2}{4} k_w \frac{d^2 T_w}{dz^2} + \pi d_w h_w (T_w - T_a) - \frac{I^2 R}{2L} = 0 \quad (B-1)$$

now resistance of wire, $R = R_a(1 + \alpha(T_w - T_a))$, substituting into Eq. B-1 and simplifying, we get:

$$\frac{k_w d_w}{4} \frac{d^2 T_w}{dz^2} = h_w (T_w - T_a) - \frac{I^2 R_a}{2L \pi d_w} (1 + \alpha(T_w - T_a)) \quad (B-2)$$

Defining

$$A_1 = \frac{4h_w}{k_w d_w}, B_1 = \frac{2I_a^2 R_a}{k_w L \pi d_w^2}, \text{ and } T = T_w - T_a$$

and substituting into Eq. B-2, we get:

$$\frac{d^2 T}{dz^2} = (A_1 - \alpha B_1)T - B_1 \quad (\text{B-3})$$

with the following boundary conditions:

$$\begin{aligned} T &= 0 \quad \text{at } z = 0 \text{ and } z = 2L \\ \frac{dT}{dz} &= 0 \quad \text{at } z = L \end{aligned} \quad (\text{B-4})$$

Integrating Eq. B-3 with the boundary conditions, we get:

$$T = \frac{B_1}{\lambda^2} \left(1 - \frac{\cosh \lambda(L - z)}{\cosh \lambda L} \right) \quad (\text{B-5})$$

where:

$$\lambda^2 = A_1 - \alpha B_1$$

Defining the mean or average temperature over the length of the wire, we have:

$$\bar{T} = \frac{1}{2L} \int_0^{2L} T \, dz \quad (\text{B-6})$$

Using Eq. B-5, and carrying out the integration in Eq. B-6, we get:

$$\bar{T} = \frac{B_1}{\lambda^2} \left(1 - \frac{\tanh(\lambda L)}{\lambda L} \right) \quad (\text{B-7})$$

But from experiments, we know that:

$$\bar{T} = \frac{V/I - R_a}{\alpha R_a} \quad (\text{B-8})$$

Equating Eqs. B-7 and B-8, we get:

$$\frac{V/I - R_a}{\alpha R_a} = \frac{B_1}{\lambda^2} \left(1 - \frac{\tanh(\lambda L)}{\lambda L} \right) \quad (\text{B-9})$$

APPENDIX C
EXPERIMENTAL RESULTS FOR STRAIGHT ALUMEL WIRES IN A
FLOWING AIR STREAM

C-1. Experimental Data

The experimental results for straight Alumel wires are given in Table C-1.

C-2. Example Calculation

The raw data for Run No. 1 is given below:

Diameter of Wire	$d_w = 813 \times 10^{-6} \text{ m}$
Length of Wire	$2L = 0.140 \text{ m}$
Resistance of Wire at 20°C	$R_o = 0.0753 \text{ m}$
Temperature of Air Stream	$T_a = 20.5^\circ\text{C}$
Superficial Air Velocity	$u_o = 0.0259 \text{ m/s}$
Pressure of Air	$P = 1.013 \times 10^5 \text{ Pa}$
Current Flow through the Wire	$I = 3.00 \text{ A}$
Voltage Drop across the Wire	$V = 0.2522 \text{ V}$
Resistance of Wire at $T_a = 20.5^\circ\text{C}$	$R_a = R_o(1 + \alpha(T_a - T_o))$ $= 0.0753(1 + .00236(0.5))$ $= 0.075389 \text{ } \Omega$

Table C-1. Experimental Data for Alumel Wires in Flowing Air.

Run No.	Wire Diameter d_w (μm)	Superficial Gas Velocity u_o (m/s)	Heat Transfer Coefficient h_w ($\text{W}/\text{m}^2\cdot\text{K}$)	Film Reynolds Number $\text{Re}_{w,f}$	Film Nusselt Number $\text{Nu}_{w,f}$	Gr $\frac{\text{Gr}}{\text{Re}_{w,\infty}^2}$
1	813.0	.0259	35.8	1.32	1.05	1.9686
1	813.0	.0259	36.1	1.31	1.06	2.0998
1	813.0	.0259	35.3	1.32	1.04	1.9351
1	813.0	.0259	35.9	1.32	1.05	2.0353
2	813.0	.1185	47.0	6.11	1.40	.0772
2	813.0	.1185	47.4	6.09	1.41	.0816
2	813.0	.1185	48.4	6.06	1.43	.0914
2	813.0	.1185	48.5	6.04	1.43	.0974
3	813.0	.2770	64.0	14.31	1.90	.0150
3	813.0	.2770	65.8	14.24	1.94	.0165
3	813.0	.2770	65.4	14.18	1.92	.0177
3	813.0	.2770	65.2	14.14	1.91	.0188
4	508.0	.0259	50.7	.84	.94	1.0136
4	508.0	.0259	49.8	.83	.92	1.2211
4	508.0	.0259	50.7	.83	.93	1.2792
4	508.0	.0259	50.1	.83	.93	1.2113
5	508.0	.1185	68.5	3.83	1.28	.0509
5	508.0	.1185	68.9	3.81	1.27	.0570
5	508.0	.1185	70.2	3.79	1.29	.0627
5	508.0	.1185	69.0	3.81	1.28	.0569
6	508.0	.2770	108.2	8.98	2.01	.0098
6	508.0	.2770	106.7	8.92	1.97	.0110
6	508.0	.2770	107.9	8.88	1.98	.0119
6	508.0	.2770	108.3	8.93	2.00	.0108
7	381.0	.0259	58.7	.62	.81	.8871
7	381.0	.0259	62.3	.62	.86	.9969
7	381.0	.0259	59.6	.63	.83	.7207
7	381.0	.0259	59.8	.62	.83	.7910
8	381.0	.1185	79.4	2.89	1.12	.0293
8	381.0	.1185	77.5	2.88	1.09	.0318
8	381.0	.1185	80.1	2.86	1.12	.0366
8	381.0	.1185	79.4	2.84	1.10	.0428
9	381.0	.2770	98.8	6.73	1.38	.0073
9	381.0	.2770	105.5	6.71	1.46	.0079
9	381.0	.2770	103.1	6.72	1.43	.0075
9	381.0	.2770	102.1	6.74	1.42	.0071
10	254.0	.0259	69.9	.41	.64	.6700
10	254.0	.0259	68.2	.42	.63	.5650
10	254.0	.0259	66.1	.42	.62	.4898
10	254.0	.0259	69.4	.42	.64	.5545

Table C-1. Continued.

Run No.	Wire Diameter d_w (μm)	Superficial Gas Velocity u_o (m/s)	Heat Transfer Coefficient h_w ($\text{W}/\text{m}^2\cdot\text{K}$)	Film Reynolds Number $\text{Re}_{w,f}$	Film Nusselt Number $\text{Nu}_{w,f}$	Gr $\frac{\text{Gr}}{\text{Re}_{w,\infty}^2}$
11	254.0	.1185	92.1	1.91	.86	.0231
11	254.0	.1185	92.8	1.90	.86	.0267
11	254.0	.1185	96.9	1.89	.89	.0294
11	254.0	.1185	94.0	1.87	.85	.0349
12	254.0	.2770	132.8	4.45	1.23	.0051
12	254.0	.2770	121.6	4.40	1.11	.0062
12	254.0	.2770	126.4	4.47	1.17	.0046
12	254.0	.2770	122.2	4.45	1.13	.0052
13	127.0	.0259	154.2	.20	.69	.4147
13	127.0	.0259	144.1	.20	.65	.3754
13	127.0	.0259	145.6	.21	.67	.3275
14	127.0	.1185	186.9	.96	.87	.0120
14	127.0	.1185	188.7	.95	.87	.0158
14	127.0	.1185	188.4	.96	.87	.0134
15	127.0	.2770	246.8	2.26	1.15	.0022
15	127.0	.2770	229.5	2.22	1.05	.0030
15	127.0	.2770	229.3	2.23	1.06	.0027
16	50.8	.0259	265.3	.08	.49	.1376
16	50.8	.0259	265.1	.08	.48	.1512
16	50.8	.0259	264.1	.08	.49	.1257
16	50.8	.0259	263.8	.08	.48	.1385
17	50.8	.1185	339.8	.38	.63	.0050
17	50.8	.1185	338.1	.38	.63	.0055
17	50.8	.1185	339.0	.38	.63	.0060
17	50.8	.1185	339.2	.38	.63	.0055
18	50.8	.2770	423.5	.91	.79	.0009
18	50.8	.2770	423.6	.90	.79	.0009
18	50.8	.2770	415.9	.90	.77	.0010
18	50.8	.2770	419.3	.90	.78	.0009

Average Wire Temperature
above Temperature of Air

$$\begin{aligned}\bar{T} &= \frac{\frac{V}{I} - R_a}{R_a \alpha} \\ &= \frac{\frac{.2522}{3} - .075389}{(.075389)(.00236)} \\ &= 48.77^{\circ}\text{C}\end{aligned}$$

Average Temperature of the Wire $T_w = \bar{T} + T_B = 69.27^{\circ}\text{C}$

Thermal Conductivity of Alumel at T_w , $k_w = 29.0 \text{ W/m}\cdot\text{K}$

To calculate the average heat transfer coefficient h_w , we must solve Eq. (B-9):

$$\bar{T} = \frac{B_1}{\lambda^2} \left(1 - \frac{\tanh(\lambda L)}{\lambda L} \right) \quad (\text{B-9})$$

with,

$$\bar{T} = 48.77^{\circ}\text{C}$$

$$L = 0.07 \text{ m}$$

$$B_1 = \frac{2I^2 R_a}{k_w \pi L d_w^2} = \frac{(2)(3.00)^2 (0.075389)}{(29.0)(\pi)(0.07)(813 \times 10^{-6})^2} = 3.2192 \times 10^5$$

Solving Eq. B-9 for the only unknown λ by trial and error, we get:

$$\lambda^2 = 5306$$

and,

$$A_1 = \frac{4h_w}{k_w d_w} = \lambda^2 + \alpha B_1 = 5306 + (.00236)(3.2195 \times 10^5)$$

therefore,

$$\frac{4h_w}{k_w d_w} = 6065.8$$

and,

$$h_w = \frac{(6065.8)(29.0)(813 \times 10^{-6})}{4} = 35.80 \text{ W/m}^2\text{K}$$

$$\begin{aligned} \text{The Film Nusselt Number, } Nu_{w,f} &= \frac{h_w d_w}{k_{g,f}} \\ &= \frac{(35.80)(813 \times 10^{-6})}{(27.45)} \\ &= 1.05 \end{aligned}$$

$$\begin{aligned} \text{The Film Reynolds Number, } Re_{w,f} &= \frac{u_o d_w \rho_g}{\mu_{g,f}} \\ &= \frac{(.02594)(813 \times 10^{-6})(1.204)}{19.30 \times 10^{-6}} \\ &= 1.32 \end{aligned}$$

$$\begin{aligned}
 \text{The Grashoff Number, Gr} &= \frac{g d_w^3 \rho_g^2 (T_w - T_a)}{\mu_g^2 T_a} \\
 &= \frac{(9.81)(813 \times 10^{-6})(1.204)^2(48.77)}{(18.17 \times 10^{-6})^2(293.5)} \\
 &= 3.86
 \end{aligned}$$

$$\begin{aligned}
 \text{The Reynolds Number} &= \frac{u_o d_w \rho_g}{\mu_g} \\
 \text{at Bulk Conditions, } Re_{w,\infty} &= \frac{(.02594)(813 \times 10^{-6})(1.204)}{18.17 \times 10^{-6}} \\
 &= 1.40
 \end{aligned}$$

therefore,

$$\frac{Gr}{Re_{w,\infty}^2} = \frac{3.86}{(1.40)^2} = 1.97$$

APPENDIX D
EVALUATION OF THE PROPERTIES OF THE PARTICLES USED IN THE
HEATED WIRE EXPERIMENTS

D-1. Mean Particle Diameter

The surface average particle diameter defined by Eq. III-8 and repeated below was calculated for all particles used in this study.

$$\bar{d}_p = \frac{1}{\sum \frac{x_i}{d_{p,i,screen}}} \quad (\text{III-8})$$

In Table D-1, the size distribution and calculation procedure for the surface average diameter is presented for 106 μm glass beads. In Table D-2 the size distributions for the remaining particles used in the study are presented.

D-2. Minimum Fluidizing Velocity

The minimum fluidizing velocity of each type of particle used was found experimentally. The procedure used was to measure the pressure drop across the bed for various known gas flowrates and then to plot the data as pressure drop versus superficial gas velocity. Figure D-1 shows the data for 230 μm glass beads and for this case the minimum fluidization velocity was estimated to be 0.04 m/s.

Pressure drop and superficial gas velocity data are given for all the particle systems used here in Table D-3.

Table D-1. Size Distribution and Average Particle Size Calculation for 106 μ m Glass Beads.

Tyler Mesh	Average Particle Size, $d_{p,i,screen}$ (μ m)	Weight Collected (g)	Mass Fraction, x_i	$\frac{x_i}{d_{p,i,screen}}$
100 ⁻ -120 ⁺	137.5	3.97	0.0103	74.91
120 ⁻ -140 ⁺	115.5	267.31	0.6970	6034.63
140 ⁻ -170 ⁺	98.0	67.22	0.1753	1788.78
170 ⁻ -200 ⁺	82.5	38.62	0.1007	1220.61
200 ⁻ -230 ⁺	69.0	3.37	0.0088	127.53
230 ⁻ -270 ⁺	58.0	2.10	0.0055	94.83
Pan	26.5	<u>0.91</u>	<u>0.0024</u>	<u>90.57</u>
		383.50	1.0000	9431.86
$\bar{d}_p = \frac{1}{\sum \frac{x_i}{d_{p,i,screen}}} = \frac{1}{9431.86} = 106 \mu\text{m}$				

Table D-2. Size Distribution of Particles

<u>Material -- Glass</u>					
$\bar{d}_p = 230 \text{ } \mu\text{m}$		$\bar{d}_p = 465 \text{ } \mu\text{m}$		$\bar{d}_p = 613 \text{ } \mu\text{m}$	
Tyler Mesh	Mass Fraction, x_i	Tyler Mesh	Mass Fraction, x_i	Tyler Mesh	Mass Fraction, x_i
45 ⁻ -60 ⁺	.0057	25 ⁻ -28 ⁺	.0084	16 ⁻ -20 ⁺	.0011
60 ⁻ -70 ⁺	.4966	28 ⁻ -35 ⁺	.3829	20 ⁻ -25 ⁺	.1504
70 ⁻ -80 ⁺	.3882	35 ⁻ -40 ⁺	.4291	25 ⁻ -28 ⁺	.4692
80 ⁻ -100 ⁺	.0842	40 ⁻ -45 ⁺	.1414	28 ⁻ -35 ⁺	.3331
100 ⁻ -120 ⁺	.0192	45 ⁻ -60 ⁺	.0332	35 ⁻ -40 ⁺	.0381
120 ⁻ -140 ⁺	.0037	60 ⁻ -70 ⁺	.0017	40 ⁻ -45 ⁺	.0069
140 ⁻ -170 ⁺	<u>.0024</u>	70 ⁻ -80 ⁺	<u>.0032</u>	45 ⁻ -60 ⁺	<u>.0012</u>
	<u>1.0000</u>		<u>1.0000</u>		<u>1.0000</u>

Table D-2. Continued.

Material -- Polyethylene					
$\bar{d}_p = 246 \text{ } \mu\text{m}$		$\bar{d}_p = 494 \text{ } \mu\text{m}$		$\bar{d}_p = 754 \text{ } \mu\text{m}$	
Tyler Mesh	Mass Fraction, x_i	Tyler Mesh	Mass Fraction, x_i	Tyler Mesh	Mass Fraction, x_i
40 ⁻ -45 ⁺	.1301	20 ⁻ -25 ⁺	.0024	10 ⁻ -16 ⁺	.0017
45 ⁻ -50 ⁺	.2794	25 ⁻ -30 ⁺	.0340	16 ⁻ -20 ⁺	.3074
50 ⁻ -60 ⁺	.3143	30 ⁻ -35 ⁺	.5277	20 ⁻ -25 ⁺	.2712
60 ⁻ -70 ⁺	.1071	35 ⁻ -40 ⁺	.3249	25 ⁻ -30 ⁺	.3491
70 ⁻ -100 ⁺	.1149	40 ⁻ -45 ⁺	.0932	30 ⁻ -35 ⁺	.0643
100 ⁻ -140 ⁺	.0352	45 ⁻ -50 ⁺	.0144	35 ⁻ -Pan	<u>.0063</u>
140 ⁻ -Pan	<u>.0190</u>	50 ⁻ -Pan	<u>.0034</u>		
	<u>1.0000</u>		<u>1.0000</u>		<u>1.0000</u>

Table D-2. Continued

Material -- Sand					
$\bar{d}_p = 105 \mu\text{m}$		$\bar{d}_p = 223 \mu\text{m}$		$\bar{d}_p = 670 \mu\text{m}$	
Tyler Mesh	Mass Fraction, x_i	Tyler Mesh	Mass Fraction, x_i	Tyler Mesh	Mass Fraction, x_i
60 ⁻ -80 ⁺	.0851	30 ⁺	.0073	16 ⁺	.0122
80 ⁻ -100 ⁺	.1060	30 ⁻ -40 ⁺	.1359	16 ⁻ -20 ⁺	.2558
100 ⁻ -120 ⁺	.1652	40 ⁻ -50 ⁺	.3064	20 ⁻ -25 ⁺	.2355
120 ⁻ -170 ⁺	.3589	50 ⁻ -60 ⁺	.1404	25 ⁻ -30 ⁺	.2374
170 ⁻ -200 ⁺	.1362	60 ⁻ -70 ⁺	.0933	30 ⁻ -40 ⁺	.1951
200 ⁻ -230 ⁺	.0696	70 ⁻ -80 ⁺	.0867	40 ⁻ -50 ⁺	.0571
230 ⁻ -Pan	<u>.0790</u>	80 ⁻ -100 ⁺	.0910	50 ⁻ -Pan	<u>.0069</u>
	<u>1.0000</u>	100 ⁻ -120 ⁺	.0532		<u>1.0000</u>
		120 ⁻ -Pan	<u>.0858</u>		
			<u>1.0000</u>		

Table D-2. Continued.

<u>Material -- Aluminum</u>			
$\bar{d}_p = 314 \text{ } \mu\text{m}$		$\bar{d}_p = 423 \text{ } \mu\text{m}$	
Tyler Mesh	Mass Fraction, x_i	Tyler Mesh	Mass Fraction, x_i
45 ⁻ -50 ⁺	.8282	25 ⁻ -30 ⁺	.0719
50 ⁻ -60 ⁺	.1662	30 ⁻ -35 ⁺	.1465
60 ⁻ -70 ⁺	.0032	35 ⁻ -40 ⁺	.2247
70 ⁻ -80 ⁺	.0003	40 ⁻ -45 ⁺	.4431
80 ⁻ -100 ⁺	-	45 ⁻ -50 ⁺	.1084
100 ⁻ -140 ⁺	-	50 ⁻ -60 ⁺	.0021
140 ⁻ -Pan	<u>.0021</u>	60 ⁻ -Pan	<u>.0033</u>
	<u>1.0000</u>		<u>1.0000</u>

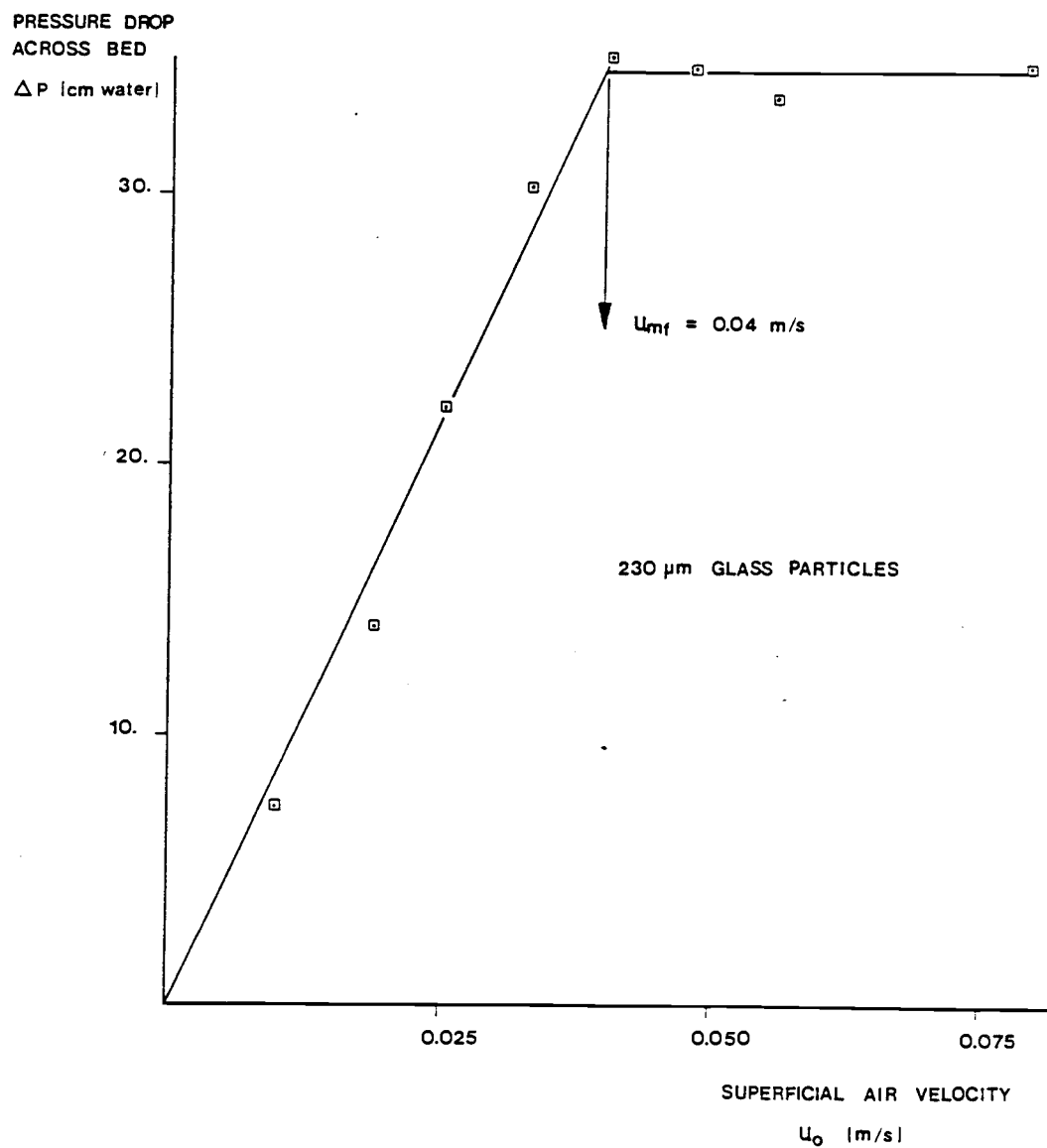


Figure D-1. Pressure Drop Versus Superficial Air Velocity for 230μm Diameter Glass Beads.

Table D-3. Pressure Drop Versus Superficial Air Velocity Data for All the Particle Systems.

<u>Material -- Glass</u>							
$\bar{d}_p = 106 \mu\text{m}$		$\bar{d}_p = 230 \mu\text{m}$		$\bar{d}_p = 465 \mu\text{m}$		$\bar{d}_p = 613 \mu\text{m}$	
u_o	ΔP	u_o	ΔP	u_o	ΔP	u_o	ΔP
(m/s)	(cmH ₂ O)	(m/s)	(cmH ₂ O)	(m/s)	(cmH ₂ O)	(m/s)	(cmH ₂ O)
.0046	8.1	.0099	7.4	.0372	10.9	.0913	7.5
.0075	26.1	.0176	15.0	.0522	13.9	.1337	11.3
.0088	28.6	.0251	22.2	.0816	19.6	.1631	14.8
.0101	31.6	.0329	30.3	.1142	24.2	.1912	19.0
.0179	31.6	.0408	35.0	.1370	30.5	.2186	23.1
		.0483	34.6	.1468	34.8	.2479	27.4
		.0558	33.5	.1631	35.9	.2760	30.6
		.0789	34.6	.1938	36.4	.3047	29.5
				.2218	36.8	.3432	29.5
				.1533	36.2		
u_{mf}	0.0095 m/s	0.04 m/s		0.15 m/s		0.28 m/s	

Table D-3. Continued

Material -- Polyethylene

$\bar{d}_p = 246 \text{ } \mu\text{m}$		$\bar{d}_p = 494 \text{ } \mu\text{m}$		$\bar{d}_p = 754 \text{ } \mu\text{m}$	
u_o	ΔP	u_o	ΔP	u_o	ΔP
(m/s)	(cmH ₂ O)	(m/s)	(cmH ₂ O)	(m/s)	(cmH ₂ O)
.0101	3.5	.0101	1.2	.0254	1.0
.0179	6.5	.0254	2.0	.0564	2.0
.0254	10.3	.0408	3.6	.0871	3.4
.0333	9.8	.0564	5.1	.1178	5.0
.0408	9.8	.0718	6.7	.1484	6.5
		.0871	8.3	.1615	7.1
		.1024	8.6	.1908	7.9
		.1178	8.7	.2186	7.9
		.1331	8.5	.2479	8.0
u_{mf}	0.027 m/s	0.09 m/s		0.19 m/s	

Table D-3. Continued

Material -- Aluminum

$\bar{d}_p = 314 \text{ } \mu\text{m}$		$\bar{d}_p = 423 \text{ } \mu\text{m}$	
u_o	ΔP	u_o	ΔP
(m/s)	(cmH ₂ O)	(m/s)	(cmH ₂ O)
.052	8.2	.042	3.1
.091	12.2	.091	5.8
.134	19.5	.134	8.6
.163	22.8	.163	11.5
.191	23.1	.191	14.3
.219	23.2	.219	17.4
.148	23.0	.248	18.9
.114	17.0	.276	19.1
		.305	19.1
u_{mf}	.158 m/s	.255 m/s	

D-3. Bulk Density, Void Fraction and Sphericity

In order to estimate the void fraction of a bed of particles at minimum fluidized conditions the following experimental procedure was adopted. A small test bed made from 5cm I.D. polyethylene tubing was filled with a known mass of the particles of interest. The tube was tapped and shaken until the height of the particles in the bed would not decrease further. The height of this closely packed bed was recorded and the bulk density of the bed was calculated. For a given particle system this procedure was repeated three times and the arithmetic average was taken to represent the bulk density of a closely packed bed of particles.

The closely packed bed was then fluidized at an air velocity equal to that required for minimum fluidization. The volume (height) increase of the bed was recorded and from this the void fraction at minimum fluidization was calculated.

An estimate of sphericity was made from the data presented by Brown et al. (59) for loose packing. The voidage of loose packing was taken here as the voidage at minimum fluidization.

An example calculation follows while the results for all the particle systems are given in Table D-4.

Example Calculation

For 314 μm aluminum particles the following bulk density measurements on closely packed beds were made:

Table D-4. Bulk Density, Void Fraction and Sphericity of Particles in Fluidized and Packed Beds

Material	Particle Diameter d_p (μm)	Bulk Density ρ_{bulk} (kg/m^3)	Packed Bed Voidage ϵ_{Pk}	$\frac{\text{Packed Bed Height}}{\text{Fluidized Bed Height}}$ Z_{Pk}/Z_f	Fluidized Bed Voidage ϵ_{mf}	Sphericity ϕ
Glass	106	1476	0.41	0.902	0.47	1.0
Glass	230	1548	0.38	0.906	0.44	1.0
Glass	465	1574	0.37	0.925	0.42	1.0
Glass	613	1533	0.39	0.929	0.43	1.0
Polyethylene	246	459	0.50	0.821	0.59	0.58
Polyethylene	494	411	0.55	0.843	0.62	0.53
Polyethylene	754	399	0.56	0.832	0.64	0.50
Sand	105	1450	0.43	0.836	0.52	0.71
Sand	223	1530	0.40	0.910	0.45	0.90
Sand	670	1540	0.40	0.838	0.50	0.76
Aluminum	314	1220	0.55	0.850	0.62	0.52
Aluminum	423	1110	0.59	0.815	0.67	0.49

Run No.	Mass of Bed (kg)	Volume of Bed (m ³)	Bulk Density (kg/m ³)
1	.4646	380×10^{-6}	1223
2	.5004	410×10^{-6}	1220
3	.5625	470×10^{-6}	<u>1197</u>
		$\bar{\rho}_{\text{bulk}}$	<u>1220</u>

The density of aluminum is $\rho_s = 2700 \text{ kg/m}^3$, and,

$$(1 - \epsilon_{pk})\rho_s = \rho_{\text{bulk}}$$

therefore,

$$\epsilon_{pk} = \text{voidage of closely packed bed} = 1 - \frac{\rho_{\text{bulk}}}{\rho_s} = 1 - \frac{1200}{2700}$$

$$\epsilon_{pk} = 0.55$$

For the same particle system the bed expansion occurring from a closely packed bed to a fluidized state was found to be:

Run No.	Height of Close Packed Bed (Z_{pk}, cm)	Height of Fluidized Bed (Z_f, cm)	Z_{pk}/Z_f
1	18.5	21.8	0.8486
2	17.3	20.3	<u>0.8522</u>
			$(Z_{pk}/Z_f)_{\text{ave}} = \underline{0.8504}$

now,

$$Z_f(1 - \epsilon_{mf}) = Z_{pk}(1 - \epsilon_{pk})$$

therefore,

$$\epsilon_{mf} = 1 - \frac{Z_{Pk}}{Z_f} (1 - \epsilon_{Pk}) = 1 - 0.8504 (1 - 0.55)$$

$$\epsilon_{mf} = 0.62$$

From Brown et al. (59) the sphericity of the particles can be estimated using $\epsilon_{mf} = 0.62$ to give sphericity, $\phi = 0.52$.

APPENDIX E
RESULTS FOR HEAT TRANSFER FROM LOOSE
ALUMEL WIRES TO FLUIDIZED BEDS

E-1. Results of Preliminary Studies for Fluidized Systems

Some preliminary studies were carried out in order to determine whether certain criticisms voiced about the experimental technique were valid. These preliminary studies are outlined below.

E-1-1. Stresses on Wire and Signal to Noise Ratio

A high signal to noise ratio is desirable but it had been pointed out that the changing stresses exerted on a wire in a fluidized bed would cause changes in its resistance during the fluidizing process. This would tend to yield a high noise to signal ratio and also physically change the wire's characteristics during the experiment. Obviously both these factors would greatly affect the accuracy of the measurements and the calculated heat transfer coefficients.

It was decided to carry out some experiments to check the validity of these criticisms. The equipment used for these studies was identical to that used in the other experiments on fluidized bed heat transfer and previously described in Part III of this thesis. In addition, however, an oscilloscope could be hooked up to measure the time varying voltage across the Alumel wire.

The procedure used consisted of trickling a very small known current through the wire and measuring the voltage drop across it.

The very low power dissipation in the wire would not affect its temperature which was assumed to be the same as the air and fluidized bed. This procedure was used for a loose 127 μm Alumel wire immersed in a fluidized bed of 106 μm glass beads. The resistance of the wire was checked at three different air velocities $0.2 u_{mf}$, $1.8 u_{mf}$ and $3.6 u_{mf}$, and again at the end of the experiment at $0.2 u_{mf}$. The results are presented in Table E-1 -- it is evident that the resistance of the wire does not change during fluidization nor is it permanently affected after fluidization. The data given in Table E-1 was taken with a Fluke multimeter (current) and a Fluke multimeter (voltage). The readings for current and voltage were both very steady for all levels of fluidization and varied only by one unit of the last digit, i.e., 0.01 mA and 0.01 mV. This very low noise level was confirmed when the oscilloscope was hooked up across the wire and the transient voltage drop was monitored.

It should be pointed out that during the actual experiments, when the wire is heated above the temperature of the bed, some noise is observed in the current and voltage measurements. However, this noise is probably due to the slight changes in heat transfer coefficient occurring between the wire and fluidized bed and not to stress induced changes of resistance in the wire. This explanation was verified by random checks done on wires after the fluidization tests which confirm that the resistance of the wire did not change during the experiment (at least not permanently).

Table E-1. Resistance Measurements for Loose Alumel Wire (127 μm diameter) in a Fluidized Bed of Glass Beads (106 μm diameter) at Different Levels of Fluidization.

Temperature = 23⁰C for all runs.

Fluidization Level -- $u_o = 0.2 u_{mf}$ (Packed Bed)

V(mV)	31.65	35.70	28.14	37.18	
I(mA)	6.89	7.77	6.12	8.09	
$R_o(\Omega)$	4.593	4.594	4.598	4.596	$\bar{R}_o = 4.595\Omega$

Fluidization Level -- $u_o = 1.8 u_{mf}$ (Fluidized Bed)

V(mV)	33.41	31.05	34.92	37.10	
I(mA)	7.28	6.76	7.60	8.08	
$R_o(\Omega)$	4.589	4.593	4.595	4.592	$\bar{R}_o = 4.592\Omega$

Fluidization Level -- $u_o = 3.6 u_{mf}$ (Fluidized Bed)

V(mV)	34.66	26.23	34.98	38.49	
I(mA)	7.54	5.71	7.61	8.38	
$R_o(\Omega)$	4.597	4.594	4.597	4.593	$\bar{R}_o = 4.595\Omega$

Fluidization Level -- $u_o = 0.2 u_{mf}$ (Packed Bed)

V(mV)	31.73	34.85	24.20	36.58	
I(mA)	6.90	7.59	5.26	7.97	
$R_o(\Omega)$	4.599	4.592	4.600	4.590	$\bar{R}_o = 4.595\Omega$

E-1-2. Structural Homogeneity of Alumel Wires

Another criticism of the experiment is the possibility of a wire having structural irregularities causing non-uniform resistance and hence giving rise to hot spots on the wire. This is a difficult question to resolve without the aid of some quite sophisticated testing techniques. However, an attempt was made to check the homogeneity of the wire. These tests were carried out at random after the experimental runs. After emptying the bed of solids and passing a stream of air through the empty bed, the lights in the laboratory were dimmed and a high electric current was passed through the wire until it glowed red. In all the wires checked the color of the wire was uniform along its length (except, of course, at both ends) which suggests, if not confirms, the fact that the wire's structure was homogeneous.

E-2. Experimental Results of Jacob and Osberg (31)

In Section III of this thesis, the results of Jacob and Osberg (31) were plotted against the correlation based on the data of this work. In order to do this it was necessary to estimate the minimum fluidizing velocity of the glass beads used in Jacob and Osberg's (31) work. The usual way that the minimum fluidizing velocity is calculated is to equate the pressure drop through a packed bed to the weight of the bed, the superficial gas velocity at which this occurs is the minimum fluidizing velocity. The pressure drop through a packed bed can be estimated by the Ergun (60) equation or the modification of this equation due to McDonald et al. (61). The

modified form due to McDonald et al. (61) is used here and the resulting equation for small particle beds is given below.

$$u_{mf} = \frac{(d_p \phi)^2 (\rho_s - \rho_g) g \epsilon^{3.6}}{180 \mu_g (1 - \epsilon)} \quad (E-1)$$

The experimental results of Jacob and Osberg (31) are presented in Table E-2 and the u_{mf} values were calculated from Eq. E-1.

E-3. Experimental Results for Loose Wires in Fluidized Beds

The experimental results for all the fluidized systems studied are presented in Tables E-3, E-4, E-5, and E-6. The calculations required to obtain the heat transfer coefficients are similar to those presented in Appendix C for wires in a flowing air stream and will not be repeated here.

Table E-2. Experiment Results of Jacob and Osberg (31).

Particle Diameter d_p	Wire Diameter d_w	Maximum Heat Transfer Coefficient $h_{w,max}$	Maximum Nusselt Number Nu_{max}	Voidage ϵ_{mf}	Specific Heat Capacity $C_{p,s}$	Minimum Fluidizing Velocity u_{mf}	Reynolds Number $\frac{u_{mf} \rho_g d_p}{\mu_g \epsilon_{mf}}$
(μm)	(μm)	($W/m^2 \cdot K$)			(J/kgK)	(m/s)	
31	132	2913	13.49	.585	670	.0023	0.0081
61	132	2242	10.38	.487	670	.0037	0.0307
153	132	1646	7.62	.441	670	.0150	0.3449
292	132	1192	5.52	.463	670	.0676	2.8253

Table E-3. Results for Heat Transfer from Loose Wires in Fluidized Beds -- Material: Glass.

Run No.	d_w (μm)	d_p (μm)	h_w ($\text{W}/\text{m}^2\cdot\text{K}$)	u_o (cm/s)	u_{mf} (cm/s)	Nu_w $(\frac{h_w d_w}{k_g})$	Re_w $(\frac{d_w u_{mf} \rho_g}{\mu_g \epsilon_{mf}})$
1	50.8	106.0	2100.9	2.57	.95	4.00	.065
1	50.8	106.0	2080.7	2.57	.95	3.96	.065
1	50.8	106.0	2049.1	2.57	.95	3.90	.065
1	50.8	106.0	2084.0	2.57	.95	3.97	.065
1	50.8	106.0	2068.1	2.57	.95	3.93	.064
2	127.0	106.0	1091.6	2.57	.95	5.21	.163
2	127.0	106.0	1239.7	2.57	.95	5.91	.163
2	127.0	106.0	1293.2	2.57	.95	6.16	.163
2	127.0	106.0	1339.7	2.57	.95	6.38	.163
2	127.0	106.0	1403.2	2.57	.95	6.68	.163
3	127.0	106.0	1383.5	4.15	.95	6.58	.163
3	127.0	106.0	1462.6	4.15	.95	6.96	.163
3	127.0	106.0	1508.0	4.15	.95	7.18	.163
3	127.0	106.0	1544.7	4.15	.95	7.35	.163
3	127.0	106.0	1535.3	4.15	.95	7.31	.163
4	127.0	230.0	1077.4	7.25	4.00	5.13	.729
4	127.0	230.0	1249.1	7.25	4.00	5.94	.729
4	127.0	230.0	1208.9	7.25	4.00	5.75	.729
4	127.0	230.0	1209.3	7.25	4.00	5.75	.728
4	127.0	230.0	1241.6	7.25	4.00	5.91	.728
5	254.0	613.0	487.5	45.78	28.00	4.71	10.738
5	254.0	613.0	507.3	45.78	28.00	4.90	10.738
5	254.0	613.0	517.6	45.78	28.00	5.00	10.738
5	254.0	613.0	506.6	45.78	28.00	4.89	10.732
5	254.0	613.0	500.5	45.78	28.00	4.83	10.732
6	254.0	465.0	556.2	26.70	15.00	5.39	5.951
6	254.0	465.0	583.4	26.70	15.00	5.65	5.945
6	254.0	465.0	611.9	26.70	15.00	5.92	5.938
6	254.0	465.0	598.6	26.70	15.00	5.79	5.932
6	254.0	465.0	598.0	26.70	15.00	5.78	5.921
7	254.0	465.0	587.3	45.81	15.00	5.65	5.851
7	254.0	465.0	586.9	45.81	15.00	5.64	5.851
7	254.0	465.0	611.7	45.81	15.00	5.88	5.851
7	254.0	465.0	591.6	45.81	15.00	5.69	5.847
8	254.0	230.0	852.2	7.20	4.00	8.21	1.493
8	254.0	230.0	882.4	7.20	4.00	8.50	1.493
8	254.0	230.0	932.2	7.20	4.00	8.98	1.491
8	254.0	230.0	846.5	7.20	4.00	8.15	1.491
8	254.0	230.0	855.9	7.20	4.00	8.24	1.488
9	254.0	230.0	838.1	13.35	4.00	8.06	1.491
9	254.0	230.0	887.5	13.35	4.00	8.54	1.491
9	254.0	230.0	918.4	13.35	4.00	8.84	1.491
9	254.0	230.0	843.5	13.35	4.00	8.11	1.491

Table E-3. Continued

Run No.	d_w (μm)	d_p (μm)	h_w ($\text{W}/\text{m}^2\cdot\text{K}$)	u_o (cm/s)	u_{mf} (cm/s)	Nu_w $(\frac{h_w d_w}{k_g})$	Re_w $(\frac{d_w u_{mf} \rho_g}{\mu_g \epsilon_{mf}})$
10	254.0	106.0	869.8	2.55	.95	8.37	.331
10	254.0	106.0	937.2	2.55	.95	9.01	.331
10	254.0	106.0	970.2	2.55	.95	9.33	.331
10	254.0	106.0	895.5	2.55	.95	8.61	.331
10	254.0	106.0	908.9	2.55	.95	8.74	.331
11	254.0	106.0	1073.9	4.13	.95	10.31	.331
11	254.0	106.0	1051.2	4.13	.95	10.10	.331
11	254.0	106.0	1124.3	4.13	.95	10.80	.331
11	254.0	106.0	1123.4	4.13	.95	10.79	.331
11	254.0	106.0	1052.6	4.13	.95	10.11	.331
12	381.0	230.0	886.3	7.23	4.00	12.74	2.214
12	381.0	230.0	937.1	7.23	4.00	13.47	2.214
12	381.0	230.0	928.8	7.23	4.00	13.34	2.210
12	381.0	230.0	946.3	7.23	4.00	13.58	2.210
12	381.0	230.0	946.9	7.23	4.00	13.59	2.210
13	381.0	230.0	896.4	13.41	4.00	12.87	2.210
13	381.0	230.0	914.5	13.41	4.00	13.13	2.210
13	381.0	230.0	912.3	13.41	4.00	13.10	2.210
13	381.0	230.0	911.1	13.41	4.00	13.07	2.206
13	381.0	230.0	902.3	13.41	4.00	12.93	2.202
14	381.0	106.0	988.0	2.56	.95	14.21	.489
14	381.0	106.0	1011.9	2.56	.95	14.54	.489
14	381.0	106.0	962.5	2.56	.95	13.83	.489
14	381.0	106.0	971.4	2.56	.95	13.96	.489
14	381.0	106.0	923.7	2.56	.95	13.27	.489
15	381.0	106.0	1071.2	4.13	.95	15.38	.489
15	381.0	106.0	1057.7	4.13	.95	15.19	.489
15	381.0	106.0	1116.2	4.13	.95	16.02	.489
15	381.0	106.0	1150.8	4.13	.95	16.51	.489
15	381.0	106.0	1078.5	4.13	.95	15.47	.489
16	381.0	465.0	586.3	26.84	15.00	8.44	8.759
16	381.0	465.0	605.3	26.84	15.00	8.71	8.750
16	381.0	465.0	606.9	26.84	15.00	8.73	8.740
16	381.0	465.0	619.0	26.84	15.00	8.90	8.730
16	381.0	465.0	625.6	26.84	15.00	8.99	8.720

Table E-3. Continued

Run No.	d_w (μm)	d_p (μm)	h_w ($\text{W}/\text{m}^2\cdot\text{K}$)	u_o (cm/s)	u_{mf} (cm/s)	Nu_w $(\frac{h_w d_w}{k_g})$	Re_w $(\frac{d_w u_{mf} \rho_g}{\mu_g \epsilon_{mf}})$
17	381.0	465.0	570.4	45.88	15.00	8.19	8.714
17	381.0	465.0	612.5	45.88	15.00	8.80	8.711
17	381.0	465.0	619.9	45.88	15.00	8.90	8.711
17	381.0	465.0	610.7	45.88	15.00	8.77	8.705
18	381.0	613.0	491.5	45.90	28.00	7.07	15.907
18	381.0	613.0	473.3	45.90	28.00	6.81	15.898
18	381.0	613.0	474.7	45.90	28.00	6.82	15.889
18	381.0	613.0	490.3	45.90	28.00	7.05	15.881
18	381.0	613.0	482.8	45.90	28.00	6.94	15.871
19	508.0	465.0	549.2	26.98	15.00	10.50	11.557
19	508.0	465.0	549.6	26.98	15.00	10.49	11.531
19	508.0	465.0	567.6	26.98	15.00	10.83	11.505
19	508.0	465.0	567.0	26.98	15.00	10.80	11.481
19	508.0	465.0	561.3	26.98	15.00	10.68	11.455
20	508.0	465.0	561.6	46.11	15.00	10.68	11.448
20	508.0	465.0	539.2	46.11	15.00	10.26	11.448
20	508.0	465.0	546.3	46.11	15.00	10.40	11.455
20	508.0	465.0	539.1	46.11	15.00	10.26	11.455
21	508.0	613.0	422.3	45.79	28.00	8.12	21.339
21	508.0	613.0	416.4	45.79	28.00	8.01	21.339
21	508.0	613.0	419.7	45.79	28.00	8.07	21.339
21	508.0	613.0	427.3	45.79	28.00	8.21	21.339
21	508.0	613.0	417.1	45.79	28.00	8.02	21.339
22	813.0	613.0	398.2	45.84	28.00	12.25	34.110
22	813.0	613.0	393.7	45.84	28.00	12.10	34.070
22	813.0	613.0	400.1	45.84	28.00	12.29	34.033
22	813.0	613.0	398.4	45.84	28.00	12.23	33.995
22	813.0	613.0	398.2	45.84	28.00	12.22	33.955
23	813.0	465.0	577.8	45.64	15.00	17.80	18.858
23	813.0	465.0	552.6	45.64	15.00	17.01	18.837
23	813.0	465.0	560.1	45.64	15.00	17.22	18.795
23	813.0	465.0	578.2	45.64	15.00	17.76	18.754
24	813.0	465.0	588.1	26.77	15.00	18.06	18.724
24	813.0	465.0	594.7	26.77	15.00	18.26	18.716
24	813.0	465.0	586.8	26.77	15.00	18.01	18.704
24	813.0	465.0	587.6	26.77	15.00	18.03	18.695
25	813.0	230.0	782.9	7.22	4.00	23.95	4.708
25	813.0	230.0	766.2	7.22	4.00	23.44	4.708
25	813.0	230.0	790.8	7.22	4.00	24.19	4.708
25	813.0	230.0	756.7	7.22	4.00	23.15	4.708

Table E-4. Results for Heat Transfer from Loose Wires in Fluidized Beds -- Material: Sand.

Run No.	d_w (μm)	d_p (μm)	h_w ($\text{W/m}^2\cdot\text{K}$)	u_o (cm/s)	u_{mf} (cm/s)	Nu_w $\left(\frac{h_w d_w}{k_g}\right)$	Re_w $\left(\frac{d_w u_{mf} \rho_g}{\mu_g \epsilon_{mf}}\right)$
1	813.0	670.0	305.0	53.56	30.00	9.55	32.481
1	813.0	670.0	300.4	53.56	30.00	9.40	32.481
1	813.0	670.0	301.7	53.56	30.00	9.44	32.481
1	813.0	670.0	304.2	53.56	30.00	9.52	32.481
2	813.0	670.0	276.1	83.10	30.00	8.64	32.481
2	813.0	670.0	289.0	83.10	30.00	9.04	32.481
2	813.0	670.0	277.1	83.10	30.00	8.67	32.481
2	813.0	670.0	291.2	83.10	30.00	9.12	32.481
3	813.0	223.0	370.8	12.61	7.20	11.70	8.798
3	813.0	223.0	366.6	12.61	7.20	11.57	8.798
3	813.0	223.0	369.6	12.61	7.20	11.66	8.798
3	813.0	223.0	367.2	12.61	7.20	11.59	8.798
4	813.0	223.0	382.9	25.66	7.20	12.09	8.798
4	813.0	223.0	388.5	25.66	7.20	12.26	8.798
4	813.0	223.0	382.6	25.66	7.20	12.08	8.798
4	813.0	223.0	383.2	25.66	7.20	12.09	8.798
5	813.0	105.0	357.4	5.60	2.15	11.28	2.278
5	813.0	105.0	404.1	5.60	2.15	12.75	2.278
5	813.0	105.0	371.6	5.60	2.15	11.71	2.263
5	813.0	105.0	389.7	5.60	2.15	12.26	2.263
6	813.0	105.0	496.8	11.23	2.15	15.64	2.263
6	813.0	105.0	500.8	11.23	2.15	15.76	2.263
6	813.0	105.0	493.9	11.23	2.15	15.55	2.263
6	813.0	105.0	488.8	11.23	2.15	15.38	2.263
7	511.0	105.0	714.4	5.61	2.15	14.13	1.423
7	511.0	105.0	661.7	5.61	2.15	13.09	1.423
7	511.0	105.0	683.1	5.61	2.15	13.51	1.423
7	511.0	105.0	684.2	5.61	2.15	13.54	1.423
8	511.0	105.0	948.7	11.24	2.15	18.77	1.423
8	511.0	105.0	932.1	11.24	2.15	18.42	1.423
8	511.0	105.0	939.6	11.24	2.15	18.55	1.413
8	511.0	105.0	940.9	11.24	2.15	18.56	1.413
9	511.0	223.0	624.7	12.63	7.20	12.36	5.500
9	511.0	223.0	592.6	12.63	7.20	11.72	5.500
9	511.0	223.0	590.7	12.63	7.20	11.69	5.500
9	511.0	223.0	593.3	12.63	7.20	11.74	5.500
10	511.0	223.0	624.7	25.71	7.20	12.36	5.505
10	511.0	223.0	623.4	25.71	7.20	12.32	5.494
10	511.0	223.0	631.6	25.71	7.20	12.47	5.484
10	511.0	223.0	630.8	25.71	7.20	12.44	5.474

Table E-4. Continued

Run No.	d_w (μm)	d_p (μm)	h_w ($\text{W}/\text{m}^2\cdot\text{K}$)	u_o (cm/s)	u_{mf} (cm/s)	Nu_w $\left(\frac{h_w d_w}{k_g}\right)$	Re_w $\left(\frac{d_w u_{mf} \rho_g}{\mu_g \epsilon_{mf}}\right)$
11	511.0	670.0	367.2	53.43	30.00	7.24	20.539
11	511.0	670.0	370.3	53.43	30.00	7.31	20.539
11	511.0	670.0	367.0	53.43	30.00	7.24	20.539
11	511.0	670.0	375.2	53.43	30.00	7.40	20.539
12	511.0	670.0	354.0	82.90	30.00	6.98	20.539
12	511.0	670.0	357.2	82.90	30.00	7.05	20.539
12	511.0	670.0	349.3	82.90	30.00	6.89	20.539
12	511.0	670.0	364.8	82.90	30.00	7.20	20.539
13	381.0	670.0	440.4	53.36	30.00	6.50	15.414
13	381.0	670.0	446.8	53.36	30.00	6.58	15.388
13	381.0	670.0	444.5	53.36	30.00	6.54	15.353
13	381.0	670.0	458.6	53.36	30.00	6.75	15.326
14	381.0	223.0	620.9	12.65	7.20	9.13	4.078
14	381.0	223.0	608.8	12.65	7.20	8.95	4.078
14	381.0	223.0	637.8	12.65	7.20	9.38	4.078
14	381.0	223.0	629.5	12.65	7.20	9.26	4.078
15	381.0	223.0	717.9	25.74	7.20	10.56	4.081
15	381.0	223.0	694.1	25.74	7.20	10.21	4.081
15	381.0	223.0	720.1	25.74	7.20	10.59	4.081
15	381.0	223.0	727.8	25.74	7.20	10.70	4.081
16	381.0	105.0	807.3	5.62	2.15	11.88	1.054
16	381.0	105.0	854.5	5.62	2.15	12.57	1.054
16	381.0	105.0	836.1	5.62	2.15	12.30	1.054
16	381.0	105.0	874.5	5.62	2.15	12.86	1.054
17	381.0	105.0	922.8	11.27	2.15	13.57	1.054
17	381.0	105.0	917.7	11.27	2.15	13.50	1.054
17	381.0	105.0	976.7	11.27	2.15	14.34	1.047
17	381.0	105.0	940.5	11.27	2.15	13.79	1.047
18	254.0	105.0	997.9	5.63	2.15	9.76	.698
18	254.0	105.0	1029.0	5.63	2.15	10.06	.698
18	254.0	105.0	1005.9	5.63	2.15	9.84	.698
18	254.0	105.0	1023.4	5.63	2.15	10.01	.698
19	254.0	105.0	1116.8	11.28	2.15	10.92	.698
19	254.0	105.0	1101.4	11.28	2.15	10.77	.698
19	254.0	105.0	1100.8	11.28	2.15	10.76	.698
19	254.0	105.0	1110.3	11.28	2.15	10.86	.698
20	254.0	223.0	728.3	12.64	7.20	7.12	2.708
20	254.0	223.0	694.8	12.64	7.20	6.79	2.708
20	254.0	223.0	698.7	12.64	7.20	6.83	2.708
20	254.0	223.0	694.2	12.64	7.20	6.79	2.708

Table E-4. Continued

Run No.	d_w (μm)	d_p (μm)	h_w ($\text{W}/\text{m}^2\cdot\text{K}$)	u_o (cm/s)	u_{mf} (cm/s)	Nu_w $(\frac{h_w d_w}{k_g})$	Re_w $(\frac{d_w u_{mf} \rho_g}{\mu_g \epsilon_{mf}})$
21	254.0	223.0	780.5	25.73	7.20	7.63	2.711
21	254.0	223.0	780.8	25.73	7.20	7.64	2.711
21	254.0	223.0	777.3	25.73	7.20	7.60	2.711
21	254.0	223.0	845.3	25.73	7.20	8.27	2.711
22	254.0	670.0	494.1	53.43	30.00	4.85	10.212
22	254.0	670.0	501.1	53.43	30.00	4.91	10.212
22	254.0	670.0	487.2	53.43	30.00	4.78	10.212
22	254.0	670.0	455.2	53.43	30.00	4.46	10.212
23	127.0	105.0	1351.4	5.63	2.15	6.59	.347
23	127.0	105.0	1403.5	5.63	2.15	6.85	.349
23	127.0	105.0	1334.8	5.63	2.15	6.52	.349
23	127.0	105.0	1274.4	5.63	2.15	6.23	.349
24	127.0	105.0	1486.3	11.26	2.15	7.27	.349
24	127.0	105.0	1512.2	11.26	2.15	7.39	.349
24	127.0	105.0	1519.9	11.26	2.15	7.43	.349
24	127.0	105.0	1517.4	11.26	2.15	7.42	.349
25	127.0	223.0	952.6	12.66	7.20	4.66	1.353
25	127.0	223.0	967.9	12.66	7.20	4.73	1.353
25	127.0	223.0	946.0	12.66	7.20	4.63	1.353
25	127.0	223.0	970.4	12.66	7.20	4.74	1.353
26	50.8	105.0	1867.8	5.63	2.15	3.65	.140
26	50.8	105.0	2024.7	5.63	2.15	3.96	.140
26	50.8	105.0	1944.8	5.63	2.15	3.80	.140
26	50.8	105.0	1821.9	5.63	2.15	3.56	.140

Table E-5. Results for Heat Transfer from Loose Wires in Fluidized Beds -- Material: Polyethylene

Run No.	d_w (μm)	d_p (μm)	h_w ($\text{W}/\text{m}^2\cdot\text{K}$)	u_o (cm/s)	u_{mf} (cm/s)	Nu_w $\left(\frac{h_w d_w}{k_g}\right)$	Re_w $\left(\frac{d_w u_{mf} \rho_g}{\mu_g \epsilon_{mf}}\right)$
1	811.0	754.0	267.8	34.55	19.00	8.34	15.752
1	811.0	754.0	261.6	34.55	19.00	8.14	15.726
1	811.0	754.0	263.5	34.55	19.00	8.19	15.699
1	811.0	754.0	262.8	34.55	19.00	8.16	15.672
1	811.0	754.0	270.1	34.55	19.00	8.39	15.663
2	811.0	754.0	277.7	69.16	19.00	8.62	15.663
2	811.0	754.0	285.4	69.16	19.00	8.86	15.663
2	811.0	754.0	279.9	69.16	19.00	8.69	15.663
2	811.0	754.0	278.2	69.16	19.00	8.64	15.663
2	811.0	754.0	276.3	69.16	19.00	8.58	15.663
3	811.0	494.0	270.1	16.13	9.00	8.39	7.663
3	811.0	494.0	268.2	16.13	9.00	8.33	7.663
3	811.0	494.0	269.4	16.13	9.00	8.36	7.663
3	811.0	494.0	264.2	16.13	9.00	8.20	7.663
3	811.0	494.0	269.2	16.13	9.00	8.36	7.663
4	811.0	494.0	322.4	32.28	9.00	10.01	7.663
4	811.0	494.0	320.0	32.28	9.00	9.93	7.652
4	811.0	494.0	318.8	32.28	9.00	9.88	7.642
4	811.0	494.0	313.0	32.28	9.00	9.70	7.631
4	811.0	494.0	336.9	32.28	9.00	10.43	7.621
5	811.0	246.0	333.4	7.25	2.70	10.35	2.414
5	811.0	246.0	347.2	7.25	2.70	10.78	2.414
5	811.0	246.0	326.0	7.25	2.70	10.12	2.414
5	811.0	246.0	316.4	7.25	2.70	9.82	2.414
5	811.0	246.0	318.5	7.25	2.70	9.89	2.414
6	811.0	246.0	389.0	14.52	2.70	12.08	2.414
6	811.0	246.0	392.7	14.52	2.70	12.19	2.414
6	811.0	246.0	383.4	14.52	2.70	11.90	2.414
6	811.0	246.0	396.1	14.52	2.70	12.30	2.414
6	811.0	246.0	391.5	14.52	2.70	12.16	2.414
7	508.0	246.0	438.1	.07	2.70	8.47	1.495
7	508.0	246.0	388.6	.07	2.70	7.51	1.495
7	508.0	246.0	399.4	.07	2.70	7.72	1.495
7	508.0	246.0	386.2	.07	2.70	7.47	1.495
7	508.0	246.0	378.1	.07	2.70	7.31	1.495
8	508.0	246.0	460.7	14.57	2.70	8.91	1.495
8	508.0	246.0	463.4	14.57	2.70	8.96	1.495
8	508.0	246.0	463.9	14.57	2.70	8.97	1.495
8	508.0	246.0	495.8	14.57	2.70	9.59	1.495
8	508.0	246.0	471.7	14.57	2.70	9.12	1.495

Table E-5. Continued

Run No.	d_w (μm)	d_p (μm)	h_w ($\text{W}/\text{m}^2\cdot\text{K}$)	u_o (cm/s)	u_{mf} (cm/s)	Nu_w $\left(\frac{h_w d_w}{k_g}\right)$	Re_w $\left(\frac{d_w u_{mf} \rho_g}{\mu_g \epsilon_{mf}}\right)$
9	508.0	494.0	341.4	16.21	9.00	6.58	4.719
9	508.0	494.0	336.8	16.21	9.00	6.50	4.719
9	508.0	494.0	329.5	16.21	9.00	6.36	4.719
9	508.0	494.0	321.1	16.21	9.00	6.19	4.719
9	508.0	494.0	332.0	16.21	9.00	6.39	4.692
10	508.0	494.0	368.0	32.48	9.00	7.08	4.692
10	508.0	494.0	378.4	32.48	9.00	7.28	4.692
10	508.0	494.0	364.4	32.48	9.00	7.01	4.692
10	508.0	494.0	368.4	32.48	9.00	7.09	4.692
10	508.0	494.0	384.8	32.48	9.00	7.40	4.692
11	508.0	754.0	312.5	34.81	19.00	6.01	9.593
11	508.0	754.0	307.3	34.81	19.00	5.91	9.593
11	508.0	754.0	306.7	34.81	19.00	5.90	9.593
11	508.0	754.0	313.7	34.81	19.00	6.03	9.593
11	508.0	754.0	309.0	34.81	19.00	5.94	9.593
12	508.0	754.0	298.3	69.61	19.00	5.74	9.594
12	508.0	754.0	306.0	69.61	19.00	5.89	9.594
12	508.0	754.0	311.0	69.61	19.00	5.98	9.594
12	508.0	754.0	303.6	69.61	19.00	5.84	9.594
12	508.0	754.0	305.2	69.61	19.00	5.87	9.594
13	381.0	754.0	328.2	34.87	19.00	4.72	7.155
13	381.0	754.0	330.4	34.87	19.00	4.75	7.155
13	381.0	754.0	349.7	34.87	19.00	5.03	7.155
13	381.0	754.0	333.5	34.87	19.00	4.80	7.155
13	381.0	754.0	333.1	34.87	19.00	4.79	7.155
14	381.0	754.0	338.4	69.73	19.00	4.87	7.155
14	381.0	754.0	335.2	69.73	19.00	4.82	7.155
14	381.0	754.0	337.2	69.73	19.00	4.85	7.155
14	381.0	754.0	340.3	69.73	19.00	4.90	7.155
14	381.0	754.0	328.5	69.73	19.00	4.73	7.155
15	381.0	494.0	398.0	16.26	9.00	5.73	3.499
15	381.0	494.0	398.4	16.26	9.00	5.73	3.499
15	381.0	494.0	401.8	16.26	9.00	5.78	3.499
15	381.0	494.0	397.5	16.26	9.00	5.72	3.499
15	381.0	494.0	412.6	16.26	9.00	5.94	3.499
16	381.0	494.0	464.8	32.58	9.00	6.67	3.482
16	381.0	494.0	449.6	32.58	9.00	6.45	3.482
16	381.0	494.0	452.9	32.58	9.00	6.50	3.482
16	381.0	494.0	442.5	32.58	9.00	6.35	3.482
16	381.0	494.0	450.0	32.58	9.00	6.46	3.482

Table E-5. Continued

Run No.	d_w (μm)	d_p (μm)	h_w ($\text{W}/\text{m}^2\cdot\text{K}$)	u_o (cm/s)	u_{mf} (cm/s)	Nu_w $(\frac{h_w d_w}{k_g})$	Re_w $(\frac{d_w u_{mf} \rho_g}{\mu_g \epsilon_{mf}})$
17	381.0	246.0	511.7	7.30	2.70	7.36	1.103
17	381.0	246.0	497.8	7.30	2.70	7.16	1.103
17	381.0	246.0	494.3	7.30	2.70	7.11	1.103
17	381.0	246.0	415.7	7.30	2.70	5.98	1.103
17	381.0	246.0	425.1	7.30	2.70	6.12	1.103
18	381.0	246.0	526.2	14.63	2.70	7.57	1.103
18	381.0	246.0	522.5	14.63	2.70	7.52	1.103
18	381.0	246.0	530.9	14.63	2.70	7.64	1.103
18	381.0	246.0	533.0	14.63	2.70	7.67	1.103
18	381.0	246.0	539.1	14.63	2.70	7.75	1.103
19	254.0	246.0	511.4	7.28	2.70	4.93	.744
19	254.0	246.0	498.2	7.28	2.70	4.80	.744
19	254.0	246.0	517.1	7.28	2.70	4.99	.744
19	254.0	246.0	506.5	7.28	2.70	4.88	.744
19	254.0	246.0	521.1	7.28	2.70	5.03	.744
20	254.0	246.0	615.4	14.58	2.70	5.93	.744
20	254.0	246.0	580.9	14.58	2.70	5.60	.744
20	254.0	246.0	619.7	14.58	2.70	5.98	.744
20	254.0	246.0	616.3	14.58	2.70	5.94	.744
20	254.0	246.0	623.6	14.58	2.70	6.01	.744
21	254.0	494.0	429.1	16.21	9.00	4.14	2.360
21	254.0	494.0	462.0	16.21	9.00	4.45	2.360
21	254.0	494.0	437.8	16.21	9.00	4.22	2.360
21	254.0	494.0	441.6	16.21	9.00	4.26	2.360
21	254.0	494.0	439.4	16.21	9.00	4.24	2.360
22	254.0	494.0	468.4	32.41	9.00	4.52	2.360
22	254.0	494.0	479.7	32.41	9.00	4.63	2.360
22	254.0	494.0	473.9	32.41	9.00	4.57	2.360
22	254.0	494.0	472.4	32.41	9.00	4.56	2.360
22	254.0	494.0	472.9	32.41	9.00	4.56	2.360
23	254.0	754.0	361.9	34.74	19.00	3.49	4.826
23	254.0	754.0	355.1	34.74	19.00	3.42	4.826
23	254.0	754.0	359.2	34.74	19.00	3.46	4.826
23	254.0	754.0	351.9	34.74	19.00	3.39	4.826
23	254.0	754.0	355.2	34.74	19.00	3.42	4.826
24	254.0	754.0	348.6	69.47	19.00	3.36	4.825
24	254.0	754.0	355.1	69.47	19.00	3.42	4.825
24	254.0	754.0	355.3	69.47	19.00	3.43	4.825
24	254.0	754.0	356.1	69.47	19.00	3.43	4.825
24	254.0	754.0	356.5	69.47	19.00	3.44	4.825

Table E-5. Continued

Run No.	d_w (μm)	d_p (μm)	h_w ($\text{W/m}^2\cdot\text{K}$)	u_o (cm/s)	u_{mf} (cm/s)	Nu_w $(\frac{h_w d_w}{k_g})$	Re_w $(\frac{d_w u_{mf} \rho_g}{\mu_g \epsilon_{mf}})$
25	127.0	246.0	572.3	7.29	2.70	2.75	.370
25	127.0	246.0	657.1	7.29	2.70	3.16	.370
25	127.0	246.0	713.4	7.29	2.70	3.43	.370
25	127.0	246.0	700.8	7.29	2.70	3.37	.370
25	127.0	246.0	628.7	7.29	2.70	3.02	.370
26	127.0	246.0	667.0	14.60	2.70	3.21	.370
26	127.0	246.0	712.9	14.60	2.70	3.43	.370
26	127.0	246.0	739.7	14.60	2.70	3.56	.370
26	127.0	246.0	734.5	14.60	2.70	3.53	.370
26	127.0	246.0	665.9	14.60	2.70	3.20	.370
27	127.0	494.0	474.9	16.23	9.00	2.28	1.173
27	127.0	494.0	543.2	16.23	9.00	2.61	1.173
27	127.0	494.0	567.1	16.23	9.00	2.73	1.173
27	127.0	494.0	521.5	16.23	9.00	2.51	1.173
27	127.0	494.0	540.9	16.23	9.00	2.60	1.173
28	127.0	494.0	525.4	32.47	9.00	2.53	1.173
28	127.0	494.0	550.5	32.47	9.00	2.65	1.173
28	127.0	494.0	578.3	32.47	9.00	2.78	1.173
28	127.0	494.0	581.7	32.47	9.00	2.80	1.173
28	127.0	494.0	563.1	32.47	9.00	2.71	1.173
29	127.0	754.0	472.0	34.79	19.00	2.27	2.399
29	127.0	754.0	482.8	34.79	19.00	2.32	2.399
29	127.0	754.0	491.8	34.79	19.00	2.36	2.399
29	127.0	754.0	494.8	34.79	19.00	2.38	2.399
29	127.0	754.0	502.1	34.79	19.00	2.41	2.399
30	127.0	754.0	468.5	69.58	19.00	2.25	2.399
30	127.0	754.0	465.2	69.58	19.00	2.24	2.399
30	127.0	754.0	494.6	69.58	19.00	2.38	2.399
30	127.0	754.0	479.0	69.58	19.00	2.30	2.399

Table E-6. Results for Heat Transfer from Loose Wires in Fluidized Beds -- Material: Aluminum.

Run No.	d_w (μm)	d_p (μm)	h_w ($\text{W}/\text{m}^2\cdot\text{K}$)	u_o (cm/s)	u_{mf} (cm/s)	Nu_w $(\frac{h_w d_w}{k_g})$	Re_w $(\frac{d_w u_{mf} \rho_g}{\mu_g \epsilon_{mf}})$
1	381.0	423.0	386.7	45.60	25.50	5.74	9.839
1	381.0	423.0	388.4	45.60	25.50	5.76	9.839
1	381.0	423.0	404.0	45.60	25.50	5.99	9.839
1	381.0	423.0	416.1	45.60	25.50	6.17	9.839
1	381.0	423.0	422.0	45.60	25.50	6.26	9.839
2	508.0	423.0	406.7	45.60	25.50	8.04	13.121
2	508.0	423.0	400.7	45.60	25.50	7.93	13.121
2	508.0	423.0	390.9	45.60	25.50	7.73	13.121
2	508.0	423.0	398.1	45.60	25.50	7.87	13.121
2	508.0	423.0	393.8	45.60	25.50	7.79	13.121
3	813.0	423.0	301.9	45.60	25.50	9.55	20.998
3	813.0	423.0	302.6	45.60	25.50	9.58	20.998
3	813.0	423.0	302.6	45.60	25.50	9.58	20.998
3	813.0	423.0	304.2	45.60	25.50	9.63	20.998
3	813.0	423.0	305.1	45.60	25.50	9.66	20.998
4	254.0	423.0	456.2	45.60	25.50	4.51	6.560
4	254.0	423.0	451.1	45.60	25.50	4.46	6.560
4	254.0	423.0	453.2	45.60	25.50	4.48	6.560
4	254.0	423.0	451.9	45.60	25.50	4.47	6.560
4	254.0	423.0	453.6	45.60	25.50	4.49	6.560
5	254.0	314.0	495.9	28.13	15.80	4.90	4.396
5	254.0	314.0	500.1	28.13	15.80	4.95	4.396
5	254.0	314.0	484.5	28.13	15.80	4.79	4.396
5	254.0	314.0	514.2	28.13	15.80	5.09	4.396
6	381.0	314.0	514.1	28.28	15.80	7.56	6.480
6	381.0	314.0	491.8	28.28	15.80	7.23	6.480
6	381.0	314.0	463.6	28.28	15.80	6.82	6.480
6	381.0	314.0	450.9	28.28	15.80	6.63	6.480
6	381.0	314.0	442.2	28.28	15.80	6.50	6.480
7	508.0	314.0	463.0	28.30	15.80	9.08	8.648
7	508.0	314.0	457.4	28.30	15.80	8.96	8.637
7	508.0	314.0	462.9	28.30	15.80	9.07	8.624
7	508.0	314.0	466.1	28.30	15.80	9.12	8.611
7	508.0	314.0	464.5	28.30	15.80	9.08	8.598

APPENDIX F

ERROR ANALYSIS FOR THE WIRE EXPERIMENT

In order to estimate the effect of experimental error on the computed values of heat transfer coefficient, void fraction, wire diameter, etc., it was decided to carry out an error analysis of the data.

This analysis consists of two parts -- the first deals with the effect of error on the computed value of the Nusselt number, and the second looks at the effect on the Reynolds number, wire to particle diameter ratio and the other variables which were used in Chapter III to correlate the data. In this way a "typical" range over which both experimentally determined and predicted Nusselt numbers should vary can be found. These ranges are illustrated in Figure III-4.

F-1. Error Analysis for Experimentally Determined
Nusselt Numbers

Eq. III-4 can be used to determine the heat transfer coefficient from a hot wire to a fluid. Using this equation, the Nusselt number is given by:

$$Nu_w = \frac{h_w d_w}{k_g} = \frac{\alpha I V R_o}{2\pi k_g L(((T_o - T_a)\alpha - 1)R_o + V/I)} \quad (F-1)$$

The Nusselt numbers reported in Chapter III and Appendices C and E were calculated using Eq. III-5 which is more accurate than Eq. III-4 since conduction of heat along the wire is taken into account. The results using either equation are, however, very

similar and due to its simplicity it was decided to use Eq. III-4 as the basis of the error analysis.

Defining the relative error of measured variables as:

$$\delta_i = \frac{\text{error in the measured variable}}{\text{value of measured variable } i}$$

we can rewrite Eq. F-1 as:

$$\begin{aligned} Nu_w &= \frac{h_w d_w}{k_g} \\ &= \frac{\alpha I V R_o (1 \pm \delta_I)(1 \pm \delta_V)(1 \pm \delta_R)}{2\pi k_g L (1 \pm \delta_L) (((T_o - T_a)(1 \pm 2\delta_T)\alpha - 1) R_o (1 \pm \delta_R) + \frac{V}{I} \frac{1 \pm \delta_V}{1 \pm \delta_I})} \end{aligned} \quad (F-2)$$

Dividing Eq. F-2 by Eq. F-1 and simplifying we get a measure of the range over which the Nusselt number can vary due to experimental error, thus:

$$\begin{aligned} \text{Relative Error in } Nu_w &= \\ &= \frac{(1 \pm \delta_I)^2 (1 \pm \delta_V)(1 \pm \delta_R)(V - I R_o (1 - \alpha(T_o - T_a)))}{(1 \pm \delta_L)(V(1 \pm \delta_V) - I R_o (1 \pm \delta_I)(1 \pm \delta_R)(1 - \alpha(T_o - T_a)(1 \pm 2\delta_R)))} \end{aligned} \quad (F-3)$$

The relative errors in Eq. F-3 were estimated as follows:

$$\delta_I = 0.0020$$

$$\delta_V = 0.0001$$

$$\delta_R = 0.0015$$

$$\delta_L = 0.0250$$

$$\delta_T = 0.0020$$

The relative error for the resistance measurement δ_R was found by making 100 replications of an experiment in which the resistance of a given piece of wire was determined. The temperature of the wire was kept constant thus the only variability in measurement would be due to inaccuracies in the electronic equipment. The results of these experiments are presented in Table F-1 and the relative error is given by:

$$\delta_R = \frac{\text{standard deviation}}{\text{mean}} = \frac{.0013}{.8715} = .0015$$

This represents the net error in a single voltage measurement divided by a single current measurement. The manufacturers literature (62) suggests that this value of δ_R should be an order of magnitude greater than that found by experiment. It is felt, however, that this conservatism on the part of the manufacturer is not warranted and the above value of δ_R (.0015) has been used in this analysis. The values of δ_I and δ_V have been taken as 1/10 of the manufacturers values which is again consistent with the experimental data. The value of $\delta_L = 0.025$ corresponds to an accuracy of 0.5cm in a length of wire 20 cm long, this is a reasonable value considering the difficulty of accurately adjusting the wire length before soldering it to the end plugs.

Table F-1. Results for 100 Repetition Experiments to Determine the Resistance of a Wire.

Resistance (Ω)	Resistance (Ω)	Resistance (Ω)	Resistance (Ω)	Resistance (Ω)
.8701	.8702	.8704	.8704	.8704
.8705	.8705	.8705	.8706	.8706
.8706	.8706	.8707	.8707	.8707
.8707	.8707	.8707	.8707	.8707
.8708	.8708	.8708	.8708	.8708
.8708	.8708	.8708	.8709	.8709
.8709	.8709	.8709	.8709	.8709
.8709	.8709	.8710	.8710	.8710
.8710	.8710	.8710	.8710	.8710
.8710	.8710	.8711	.8711	.8711
.8711	.8711	.8712	.8712	.8712
.8712	.8712	.8712	.8712	.8712
.8713	.8713	.8713	.8713	.8713
.8713	.8714	.8714	.8714	.8715
.8715	.8716	.8717	.8717	.8717
.8718	.8718	.8718	.8718	.8718
.8719	.8719	.8720	.8720	.8720
.8720	.8723	.8724	.8724	.8724
.8725	.8725	.8726	.8726	.8728
.8757	.8764	.8765	.8774	.8774
Mean Resistance, $\bar{R} = .8715$ Standard Deviation, STD = .0013 (Ω)				

With the values of relative error given above the overall errors in the Nusselt number were calculated from Eq. F-3. The results for straight wires in air are given in Table F-2 while for wires in fluidized beds the results are given in Table F-3.

From Tables F-2 and F-3 it can be seen that the maximum error for straight wires in air is ± 7 percent while for wires in fluidized beds the maximum error is ± 10 percent. These error ranges for the data are shown in the figures of Chapter III.

F-2. Error Analysis for Dimensionless Groups Used in Correlating the Data for the Wire Experiment

It will be recalled from Chapter III that the experimental data were correlated by Eq. III-11 given below:

$$Nu_w = 0.46 \left(\frac{d_w \rho_g u_{mf}}{\mu_g \epsilon_{mf}} \right)^{.09} \left(\frac{d_w}{d_p} \right)^{0.51} \left(\frac{(1 - \epsilon_{mf}) \rho_s C_{p,s}}{\epsilon_{mf} \rho_g C_{p,g}} \right)^{0.36} \quad (III-11)$$

The measured variables in Eq. III-11 are d_w , u_{mf} , d_p , ϵ_{mf} the other variables are known at any given temperature and are assumed to be invariant. Both d_p and u_{mf} can be measured fairly accurately and any errors in these variables will tend to be overshadowed by the errors in d_w and especially ϵ_{mf} . Random samples of wire diameter with a micrometer indicated that $\delta_d \approx 0.03$. The relative error for the voidage at minimum fluidizing conditions is difficult to estimate due to the rather crude experimental technique used. A somewhat arbitrary value of $\delta_{\epsilon} \approx 0.04$ corresponding to a range of ± 0.02 for $\epsilon_{mf} = 0.5$ was chosen.

Table F-2. Errors in the Experimentally Determined Nusselt Numbers for Straight Wires in Air.

Run No.	Repetition No. 1 % Error		Repetition No. 2 % Error		Repetition No. 3 % Error		Repetition No. 4 % Error	
	Max	Min	Max	Min	Max	Min	Max	Min
1	6.4	-6.0	6.1	-5.8	6.4	-6.0	6.2	-5.9
2	7.2	-6.6	6.9	-6.5	6.5	-6.1	6.3	-5.9
3	6.9	-6.4	6.5	-6.1	6.3	-5.9	6.1	-5.8
4	7.0	-6.5	6.3	-5.9	6.2	-5.8	6.3	-6.0
5	6.9	-6.4	6.5	-6.1	6.1	-5.8	6.5	-6.1
6	6.7	-6.2	6.3	-5.9	6.0	-5.7	6.3	-5.9
7	6.5	-6.1	6.1	-5.8	7.4	-6.8	7.0	-6.5
8	8.2	-7.4	7.8	-7.1	7.1	-6.6	6.5	-6.1
9	6.9	-6.4	6.6	-6.2	6.8	-6.3	7.0	-6.5
10	6.0	-5.7	6.5	-6.1	7.1	-6.6	6.6	-6.2
11	7.1	-6.6	6.6	-6.2	6.3	-5.9	5.8	-5.5
12	6.4	-6.0	5.9	-5.6	6.8	-6.3	6.4	-6.0
13	5.5	-5.3	5.8	-5.5	6.2	-5.8		
14	7.3	-6.8	6.2	-5.9	6.9	-6.4		
15	7.4	-6.8	6.1	-5.8	6.4	-6.0		
16	5.9	-5.6	5.6	-5.4	6.2	-5.8	5.9	-5.6
17	6.7	-6.3	6.4	-6.0	6.1	-5.8	6.4	-6.0
18	7.0	-6.5	6.7	-6.3	6.4	-6.0	6.7	-6.2

Table F-3. Errors for the Experimentally Determined Nusselt Numbers for Wires in Fluidized Beds.

Material: Glass

Run No.	Repetition No. 1 % Error		Repetition No. 2 % Error		Repetition No. 3 % Error		Repetition No. 4 % Error		Repetition No. 5 % Error	
	Max	Min	Max	Min	Max	Min	Max	Min	Max	Min
1	7.1	-6.6	6.6	-6.2	6.4	-6.0	6.2	-5.8	6.3	-5.9
2	8.2	-7.5	7.6	-6.9	6.7	-6.3	6.1	-5.8	5.7	-5.4
3	7.9	-7.2	7.1	-6.6	6.5	-6.1	5.9	-5.6	6.5	-6.1
4	6.9	-6.4	5.9	-5.6	4.9	-4.7	5.3	-5.1	5.9	-5.6
5	6.6	-6.2	5.6	-5.4	4.9	-4.8	5.2	-5.0	5.6	-5.3
6	7.5	-6.9	6.2	-5.9	5.5	-5.2	5.9	-5.6	7.0	-6.5
7	7.3	-6.8	6.2	-5.9	5.8	-5.5	6.2	-5.8		
8	9.6	-8.5	8.1	-7.4	7.1	-6.6	8.8	-7.9	8.1	-7.4
9	9.1	-8.2	8.0	-7.3	7.0	-6.5	9.0	-8.0	8.0	-7.3
10	9.5	-8.5	8.3	-7.5	7.2	-6.7	7.4	-6.9	9.6	-8.5
11	9.6	-8.5	8.6	-7.8	8.3	-7.6	7.9	-7.2	9.9	-8.7
12	7.6	-7.0	6.7	-6.3	5.9	-5.6	6.3	-6.0	7.3	-6.7
13	7.6	-6.9	6.6	-6.2	6.1	-5.8	5.8	-5.5	6.9	-6.5
14	6.5	-6.1	6.1	-5.8	6.9	-6.4	8.0	-7.3	6.6	-6.1
15	8.6	-7.8	7.4	-6.9	6.9	-6.4	6.6	-6.2	7.1	-6.5
16	6.0	-5.7	5.4	-5.1	4.8	-4.7	5.2	-5.0	5.7	-5.4
17	5.8	-5.5	5.3	-5.1	4.8	-4.7	5.0	-4.8		
18	5.4	-5.2	4.4	-4.2	4.6	-4.4	5.0	-4.8	4.6	-4.5
19	5.2	-5.0	5.0	-4.8	5.2	-5.0	5.1	-4.9	5.2	-5.0
20	5.2	-5.0	4.8	-4.7	5.0	-4.8	4.9	-4.8		
21	4.7	-4.5	4.5	-4.3	4.6	-4.5	4.8	-4.6	4.8	-4.6
22	6.1	-5.8	6.5	-6.1	7.0	-6.5	6.8	-6.3	6.2	-5.9

Table F-3. Continued

Material: Glass

Run No.	Repetition No. 1 % Error		Repetition No. 2 % Error		Repetition No. 3 % Error		Repetition No. 4 % Error		Repetition No. 5 % Error	
	<u>Max</u>	<u>Min</u>	<u>Max</u>	<u>Min</u>	<u>Max</u>	<u>Min</u>	<u>Max</u>	<u>Min</u>	<u>Max</u>	<u>Min</u>
23	8.0	-7.3	8.2	-7.4	8.7	-7.9	8.0	-7.3		
24	7.7	-7.1	9.0	-8.0	8.5	-7.7	8.0	-7.3		
25	8.9	-8.0	9.2	-8.2	9.9	-8.7	9.4	-8.4		

Table F-3. Continued

Material: Polyethylene

Run No.	Repetition No. 1 % Error		Repetition No. 2 % Error		Repetition No. 3 % Error		Repetition No. 4 % Error		Repetition No. 5 % Error	
	Max	Min	Max	Min	Max	Min	Max	Min	Max	Min
1	5.1	-4.9	5.2	-5.0	5.5	-5.2	5.3	-5.1	5.1	-4.9
2	5.2	-5.0	5.6	-5.3	5.7	-5.4	5.3	-5.1	5.4	-5.1
3	5.3	-5.0	5.8	-5.5	5.4	-5.2	5.3	-5.1	5.5	-5.3
4	5.7	-5.4	6.1	-5.8	5.8	-5.5	5.9	-5.6	5.7	-5.4
5	6.9	-6.4	6.4	-6.0	6.0	-5.7	6.3	-5.9	6.1	-5.7
6	7.6	-7.0	7.1	-6.6	7.2	-6.7	6.8	-6.4	7.2	-6.7
7	5.9	-5.6	5.3	-5.1	5.9	-5.6	5.8	-5.5	5.4	-5.2
8	6.1	-5.7	5.8	-5.5	6.5	-6.1	6.4	-6.1	6.0	-5.7
9	5.2	-5.0	5.4	-5.2	5.6	-5.3	5.9	-5.6	5.8	-5.5
10	5.8	-5.5	5.7	-5.4	6.1	-5.7	6.2	-5.9	5.9	-5.6
11	6.0	-5.7	5.7	-5.4	5.4	-5.2	5.6	-5.4	5.8	-5.5
12	5.9	-5.6	5.6	-5.4	5.5	-5.2	5.5	-5.3	5.8	-5.5
13	7.7	-7.1	6.4	-6.0	5.6	-5.4	5.9	-5.6	7.0	-6.5
14	6.0	-5.6	6.2	-5.8	5.7	-5.4	5.6	-5.3	6.3	-6.0
15	6.5	-6.1	6.0	-5.7	6.3	-5.9	6.1	-5.8	6.5	-6.1
16	6.4	-6.0	6.5	-6.1	6.7	-6.3	6.8	-6.3	6.4	-6.0
17	7.7	-7.0	6.2	-5.9	6.8	-6.3	5.3	-5.1	5.5	-5.2
18	6.4	-6.0	6.8	-6.3	7.4	-6.8	6.2	-5.8	6.5	-6.1
19	5.5	-5.2	5.6	-5.3	5.8	-5.5	5.3	-5.1	5.5	-5.3
20	5.9	-5.6	6.2	-5.9	6.2	-5.8	5.9	-5.6	5.7	-5.4

Table F-3. Continued

Material: Polyethylene

Run No.	Repetition No. 1 % Error		Repetition No. 2 % Error		Repetition No. 3 % Error		Repetition No. 4 % Error		Repetition No. 5 % Error	
	Max	Min	Max	Min	Max	Min	Max	Min	Max	Min
21	6.1	-5.7	5.8	-5.5	5.1	-4.9	6.0	-5.7	5.4	-5.1
22	6.3	-6.0	5.9	-5.6	5.3	-5.1	5.5	-5.3	6.1	-5.7
23	6.2	-5.8	5.7	-5.4	5.4	-5.2	5.5	-5.3	5.9	-5.6
24	6.0	-5.7	5.7	-5.4	5.4	-5.2	5.6	-5.3	5.9	-5.6
25	8.4	-7.6	6.6	-6.2	6.0	-5.6	6.4	-6.0	7.1	-6.6
26	8.2	-7.5	7.0	-6.5	6.1	-5.7	6.5	-6.1	7.4	-6.8
27	6.6	-6.2	5.9	-5.6	5.6	-5.4	6.3	-6.0	5.9	-5.6
28	7.0	-6.5	6.5	-6.1	5.7	-5.4	6.2	-5.8	6.6	-6.2
29	6.6	-6.1	6.1	-5.7	5.6	-5.4	5.9	-5.6	6.4	-6.0
30	6.4	-6.0	5.9	-5.6	5.6	-5.4	5.8	-5.5		

F-3. Continued.

Material: Sand

Run No.	Repetition No. 1 % Error		Repetition No. 2 % Error		Repetition No. 3 % Error		Repetition No. 4 % Error	
	<u>Max</u>	<u>Min</u>	<u>Max</u>	<u>Min</u>	<u>Max</u>	<u>Min</u>	<u>Max</u>	<u>Min</u>
1	5.6	-5.4	5.9	-5.6	5.7	-5.5	5.5	-5.3
2	5.4	-5.2	5.4	-5.1	5.6	-5.3	5.2	-5.0
3	6.6	-6.2	6.8	-6.4	6.6	-6.2	6.7	-6.3
4	6.9	-6.4	6.8	-6.3	7.0	-6.5	6.8	-6.3
5	6.6	-6.2	6.9	-6.5	7.0	-6.5	6.8	-6.3
6	7.9	-7.2	7.8	-7.1	8.0	-7.3	8.1	-7.4
7	6.8	-6.3	6.2	-5.8	5.9	-5.6	5.6	-5.4
8	6.8	-6.4	6.5	-6.1	7.5	-6.9	6.9	-6.4
9	5.7	-5.4	5.4	-5.1	5.5	-5.2	5.7	-5.4
10	5.7	-5.4	5.4	-5.2	5.6	-5.3	5.8	-5.5
11	4.8	-4.7	4.9	-4.8	5.0	-4.8	5.0	-4.8
12	4.8	-4.6	4.9	-4.7	4.9	-4.8	5.0	-4.8
13	6.3	-5.9	5.4	-5.2	5.9	-5.6	5.7	-5.4
14	6.1	-5.8	5.8	-5.5	5.7	-5.4	5.5	-5.2
15	6.6	-6.1	6.2	-5.8	6.0	-5.7	5.8	-5.5
16	7.0	-6.5	6.5	-6.1	6.2	-5.8	6.1	-5.7
17	6.7	-6.3	6.4	-6.0	6.3	-5.9	6.4	-6.0
18	5.9	-5.6	5.8	-5.5	5.5	-5.3	5.3	-5.1
19	6.2	-5.8	6.0	-5.7	5.7	-5.4	5.5	-5.2
20	5.2	-5.0	5.2	-5.0	5.5	-5.2	5.7	-5.5

F-3. Continued.

Material: Sand

Run No.	Repetition No. 1 % Error		Repetition No. 2 % Error		Repetition No. 3 % Error		Repetition No. 4 % Error	
	<u>Max</u>	<u>Min</u>	<u>Max</u>	<u>Min</u>	<u>Max</u>	<u>Min</u>	<u>Max</u>	<u>Min</u>
21	5.6	-5.3	6.0	-5.7	5.7	-5.4	5.5	-5.2
22	5.1	-4.9	5.3	-5.0	5.5	-5.3	5.7	-5.4
23	6.4	-6.0	5.9	-5.6	5.2	-5.0	4.9	-4.8
24	7.0	-6.5	6.1	-5.8	5.5	-5.3	5.3	-5.1
25	5.4	-5.2	5.0	-4.8	6.0	-5.7	5.4	-5.2
26	6.5	-6.1	6.4	-6.0	6.0	-5.6	6.3	-5.9

Table F-3. Continued

Material: Aluminum

Run No.	Repetition No. 1 % Error		Repetition No. 2 % Error		Repetition No. 3 % Error		Repetition No. 4 % Error		Repetition No. 5 % Error	
	<u>Max</u>	<u>Min</u>	<u>Max</u>	<u>Min</u>	<u>Max</u>	<u>Min</u>	<u>Max</u>	<u>Min</u>	<u>Max</u>	<u>Min</u>
1	6.7	-6.3	6.0	-5.7	6.5	-6.1	5.9	-5.6	6.7	-6.2
2	7.1	-6.6	6.6	-6.2	6.1	-5.8	6.1	-5.7	5.9	-5.6
3	5.5	-5.3	5.7	-5.4	5.6	-5.4	5.5	-5.3	5.7	-5.4
4	5.4	-5.1	5.6	-5.4	6.0	-5.7	6.4	-6.0	5.7	-5.4
5	5.6	-5.3	6.0	-5.6	6.2	-5.9	5.7	-5.4		
6	6.5	-6.1	5.9	-5.6	5.5	-5.3	5.6	-5.3	5.9	-5.6
7	6.3	-6.0	6.0	-5.6	5.7	-5.4	5.8	-5.5	6.1	-5.8

Using the above values of relative error and Eq. III-11, the relative error in the prediction of Nusselt number is given below:

Relative Error in $Nu_w =$

$$\left(\frac{1 \pm \delta_d}{1 \pm \delta_E}\right)^{.09} (1 \pm \delta_d)^{0.50} \left(\frac{(1 - \epsilon_{mf}(1 \pm \delta_E))}{(1 - \epsilon_{mf})(1 \pm \delta_E)}\right)^{0.36} \quad (F-4)$$

Using Eq. F-4 and the values of δ_E and δ_d given above, the maximum errors in the predicted Nusselt number were calculated and are presented in Table F-4.

The maximum range of predicted Nusselt numbers is ± 7 percent and this range is shown in the figures in Chapter III.

Table F-4. Relative Error in the Predicted Nusselt Number

Material	Particle Size d_p (μm)	ϵ_{mf}	Relative Error in Nu_w	
Glass	106	.47	+5.0	-4.8
	230	.44	+4.8	-4.6
	465	.42	+4.7	-4.5
	613	.43	+4.8	-4.6
Polyethylene	246	.59	+5.8	-5.6
	494	.62	+6.1	-5.8
	754	.64	+6.3	-6.1
Sand	105	.52	+5.3	-5.1
	223	.45	+4.9	-4.7
	670	.50	+5.2	-4.9
Aluminum	314	.62	+6.1	-5.8
	423	.67	+6.6	-6.4

APPENDIX G

THE EVALUATION OF THE PHYSICAL PROPERTIES OF FERRITE TC-71

A literature search was made to find the physical properties of ferrite TC-71 which was used in the second series of experiments discussed in Section IV of this thesis. This search was unsuccessful as was a request to the manufacturers (TDK of Japan) to supply any relevant data. It was therefore decided to carry out a series of experiments to determine the physical properties needed for this study. These experiments are described below and it should be noted that all evaluations were carried out on 6 torroids of TC-71 supplied by TDK. The experiments described in Section IV all used powdered ferrite, also supplied by TDK, and it is assumed that the physical properties of the solid torroids and powder were the same.

G-1. Evaluation of Density

The density of the ferrite torroids was easily calculated since the dimensions of the torroids could be measured accurately as could their mass. The computed density of the ferrite was $\rho_s = 4780 \text{ kg/m}^3$.

G-2. Evaluation of Specific Heat Capacity

For the evaluation of the specific heat capacity of ferrite a small calorimeter was constructed from aluminum and is illustrated in Figure G-1. From Figure G-1 it can be seen that the aluminum calorimeter was placed in a water bath whose temperature was

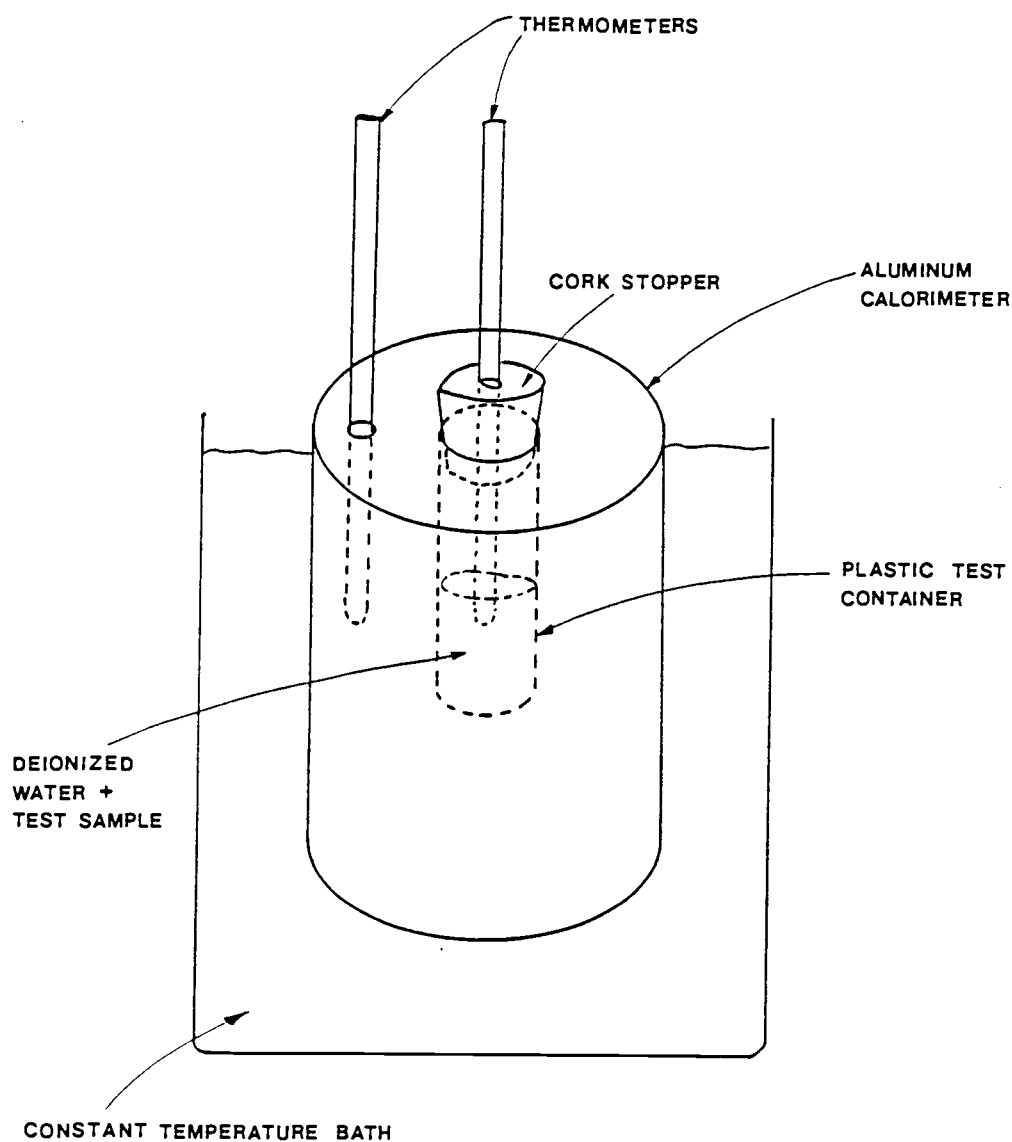


Figure G-1. Experimental Equipment Used in the Evaluation of the Specific Heat Capacity of Ferrite TC-71.

maintained by a VWR-DYLA-DUAL hot plate. In the center of the aluminum cylinder (calorimeter) was placed a thin walled Plexiglass tube which was plugged at one end with a cork. Two thermometers (120-134⁰F range) were used to measure the temperature of the aluminum block and contents of the Plexiglass tube.

The experimental procedure used for the evaluation of the heat capacities of various materials was as follows. First a 25 ml sample of deionized water was placed in the Plexiglass tube. The heater was adjusted to give a bath temperature of approximately 132⁰F and when the temperature of the deionized water reached close to the bath temperature its temperature was recorded at one minute intervals. At some point (5-7 minutes after recording the deionized water temperature) a sample of known weight of the material of interest was added to the deionized water. The temperature of the water sample mixture was then recorded at one minute intervals for a further 8-12 minutes.

By plotting the temperature history of the contents of the Plexiglass tube, it is possible to extrapolate back to the point at which the sample was added to the water. An energy balance at this point will then yield the specific heat capacity of the sample.

Samples of aluminum, brass, stainless steel and ferrite TC-71 were used and the results for these four materials are presented in Table G-1 along with the reported literature values for the three metals.

Table G-1. Results of Specific Heat Capacity Measurements

Material	Specific Heat Capacity From Experiment	Specific Heat Capacity From Literature	% Error
	$C_{p,s}$, kJ/kg·K	$C_{p,s}$, kJ/kg·K	
Brass	393	381	+3.1
Stainless Steel	392	460	-14.8
Aluminum	1024	938	+9.3
Ferrite TC-71	648	-	-

It can be seen that the results for the three known metals compare favorably with the literature values. Thus the specific heat of ferrite TC-71 is taken as 648 kJ/kg·K.

An example calculation for the aluminum sample is given below.

G-2-1. Example Calculation

A 14.60g sample of aluminum initially at 69.8°F (21.0°C) was dropped into a 25ml sample of deionized water 5 minutes after the start of the experiment. The temperature history of the deionized water sample is given in Table G-2 and plotted in Figure G-2.

From Figure G-2, the extrapolated temperature of the deionized water sample just after addition is given as 121.5°F (49.72°C). This is the temperature that the deionized water sample would have been just after the aluminum sample was added if the two samples had reached instantaneous thermal equilibrium. For this situation an energy balance gives:

$$M_{wt} C_{p,wt} (T_{wt,1} - T_{wt,2}) = M_{AL} C_{p,AL} (T_{AL,2} - T_{AL,1})$$

and putting in numerical values we get:

$$\begin{aligned} & (25.0)(10^{-3})(4180)(53.83 - 49.72) \\ & = (14.60)(10^{-3})(C_{p,AL})(49.72 - 21.00) \end{aligned}$$

therefore,

$$C_{p,AL} = \frac{(25)(4180)(4.11)}{(14.60)(28.72)} = 1024 \text{ kJ/kgK}$$

Table G-2. The Temperature History of the Deionized Water Sample During the Experimental Determination of the Specific Heat of Aluminum.

Time (minutes)	Temperature ($^{\circ}\text{F}$)	Temperature ($^{\circ}\text{C}$)
0	127.6	53.11
1	127.8	53.22
2	128.1	53.39
3	128.4	53.56
4	128.6	53.67
5	128.9	53.83
6	122.6	50.33
7	123.8	51.00
8	124.8	51.56
9	125.7	52.06
10	126.5	52.50
11	127.2	52.89
12	127.8	53.22
13	128.3	53.50

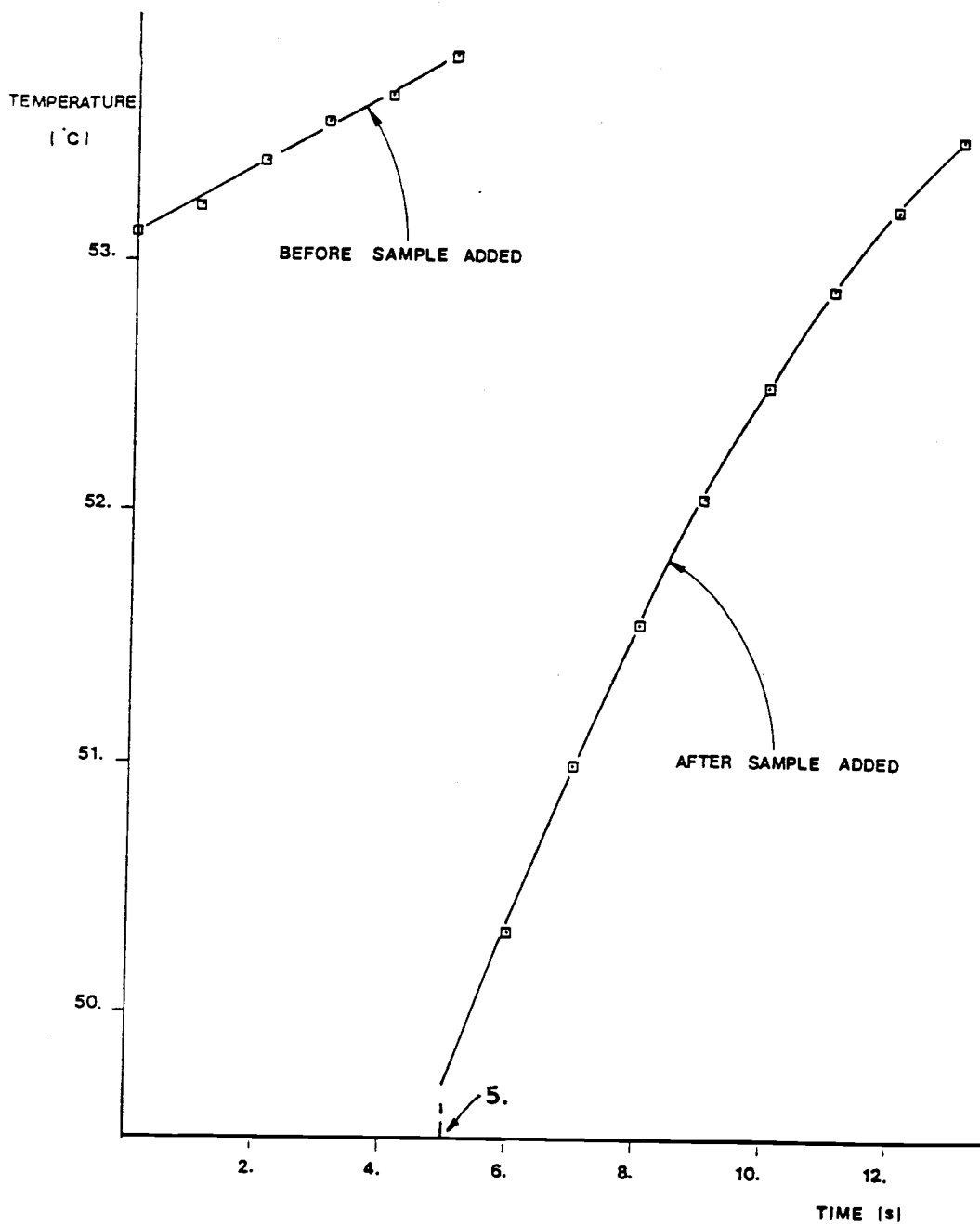


Figure G-2. Heating Curve for the Experimental Determination of the Specific Heat Capacity of Aluminum.

G-3. Evaluation of Thermal Conductivity

The equipment used to evaluate the thermal conductivity of ferrite TC-71 is illustrated in Figure G-3. The apparatus consists of a thin walled cylindrical copper heating element with a thermocouple imbedded in the wall half way along its length. A thin walled brass annulus with two thermocouples imbedded in its wall serves as the outer part of the container and the sample which consists of a hollow cylinder fits tightly between the outer brass wall and the inner heating element. Both ends of the device are insulated with expanded polystyrene discs. The experimental procedure simply consists of passing a known current through the heating element and observing the voltage drop across the heater and the temperature of the inner and outer walls once steady state has been reached.

Ignoring heat losses from the ends of the equipment the steady state heat conduction through the sample is given by:

$$\dot{q} = -2\pi r L k_s \frac{dT}{dr} \quad (G-1)$$

Eq. G-1 integrates to give the following expression:

$$\dot{q}_r = -2\pi \bar{k}_s L \frac{(T_2 - T_1)}{\log_e(r_2/r_1)} \quad (G-2)$$

where \bar{k}_s is the thermal conductivity of the sample evaluated at the arithmetic mean temperature, i.e., $(T_2 + T_1)/2$. From Eq. G-2, it is

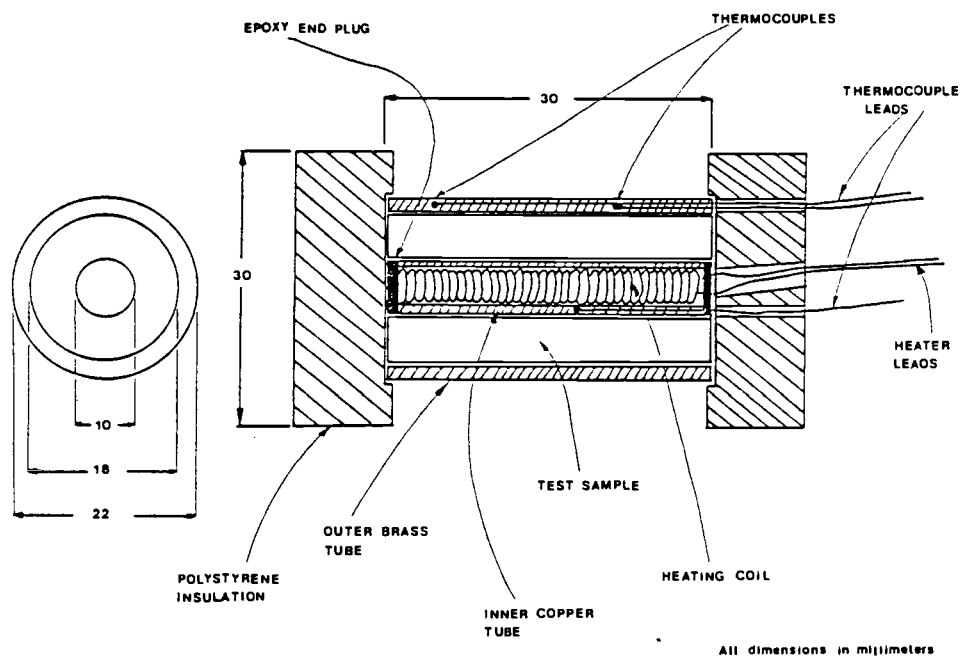


Figure G-3. Experimental Equipment used to Determine the Thermal Conductivity of Ferrite TC-71.

obvious that for a given experiment the only unknown is \bar{k}_s . Actually this is not true since there will be some heat losses. However, by calibrating the equipment using a material of known thermal conductivity it will be possible to estimate the heat losses from the equipment for a given average sample temperature and hence correct for heat losses for samples of unknown thermal conductivity.

The equipment was calibrated using a sample of tetrafluoroethylene (Teflon) which was estimated to have a thermal conductivity of the same order of magnitude as the ferrite TC-71. Figure G-4 shows the results for the Teflon sample as the measured conductivity from Eq. G-2 versus the average sample temperature, i.e., $(T_1 + T_2)/2$. The line shown in Figure G-4 represents the thermal conductivity of Teflon according to the correlation of Settlege and Siegle (63). An F-test for this data yields that at an alpha level of 0.01 we must accept the hypothesis that the data did indeed come from the correlation line. Hence the data represents the best estimate of the thermal conductivity of Teflon and should not be adjusted for any heat losses.

The thermal conductivity of the ferrite torroids turned out to be several times greater than that of Teflon. Thus in order to get a reasonable temperature drop across the sample the experiment was conducted at quite a high temperature, i.e., $\bar{T} = 121^\circ\text{C}$. The thermal conductivity of the ferrite at this temperature was found to be 1.78 W/m·K and this is the value reported in Section IV of this thesis.

THERMAL CONDUCTIVITY
OF TEFLON

[W/m·K]

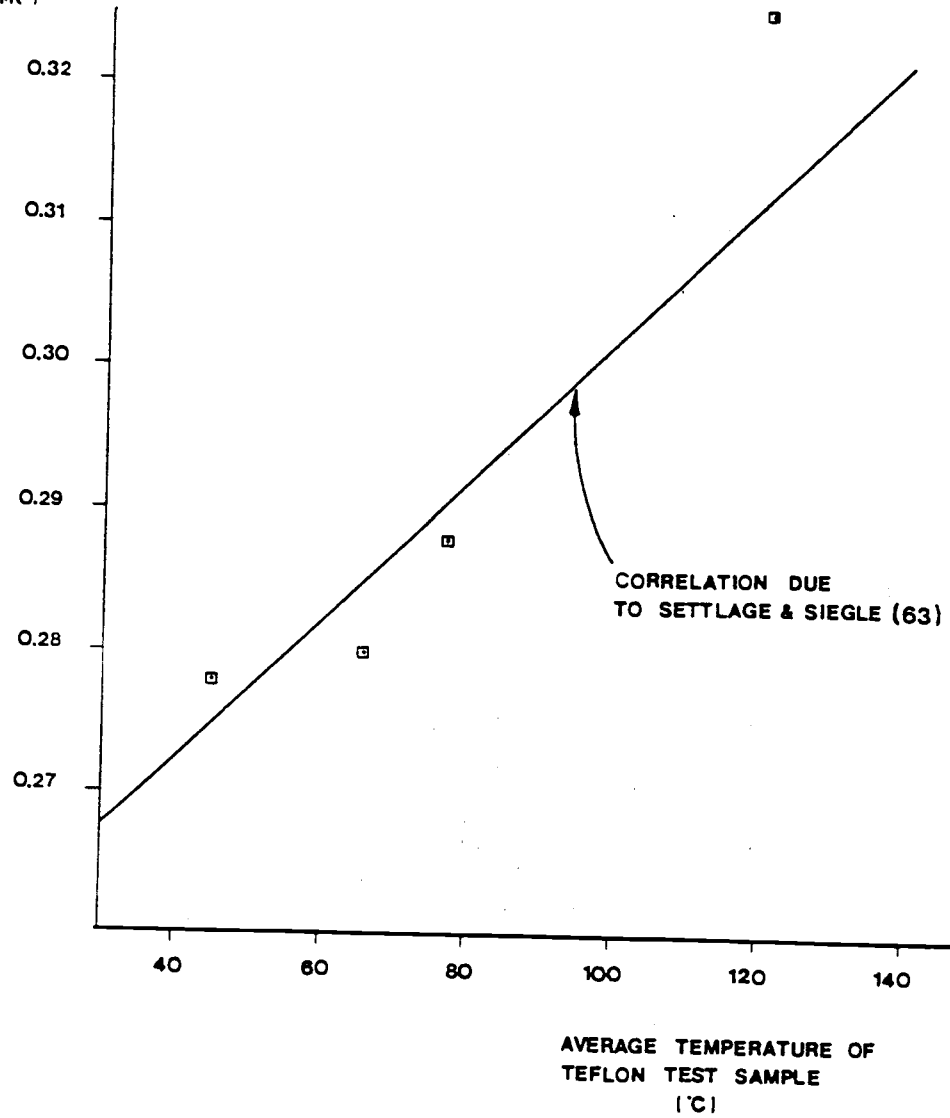


Figure G-4. Temperature vs. Thermal Conductivity Curve for Teflon.

G-4. Evaluation of Magnetic Permeability as a Function of Temperature

In order to correctly interpret the results of the unsteady state experiments described in Section IV, it is necessary to know how the magnetic properties of the ferrite TC-71 change with temperature.

For this purpose two 1.25 gram ferrite samples homogeneously dispersed in 10 grams of silica sand were used. The ferrite/sand samples were placed in a short 5mm O.D. plexiglass tube with both ends plugged. This container was then wrapped in expanded polystyrene foam and placed inside a 22mm O.D. PVC tube plugged at both ends. The sample container is illustrated in Figure G-5. The whole container was then immersed in a water bath at known temperature and allowed to come to thermal equilibrium (about 45 minutes). Once the sample had reached the temperature of the bath it was quickly removed, wiped dry and inserted into the left hand fluidized bed. The change in voltage induced by the sample and amplified by the ferrite sensor was recorded. The change in voltage of a reference ferrite sample was also recorded to act as a control on the amplifier gain.

In all, eight measurements were made at different temperatures for two ferrite/sand samples. These results are given in Table G-3.

The corrected output voltages are plotted as a function of temperature in Figure G-6. From Figure G-6, it is apparent that up to a temperature of about 67-70°C there is a gradual increase in output voltage indicating an increase in magnetic permeability of

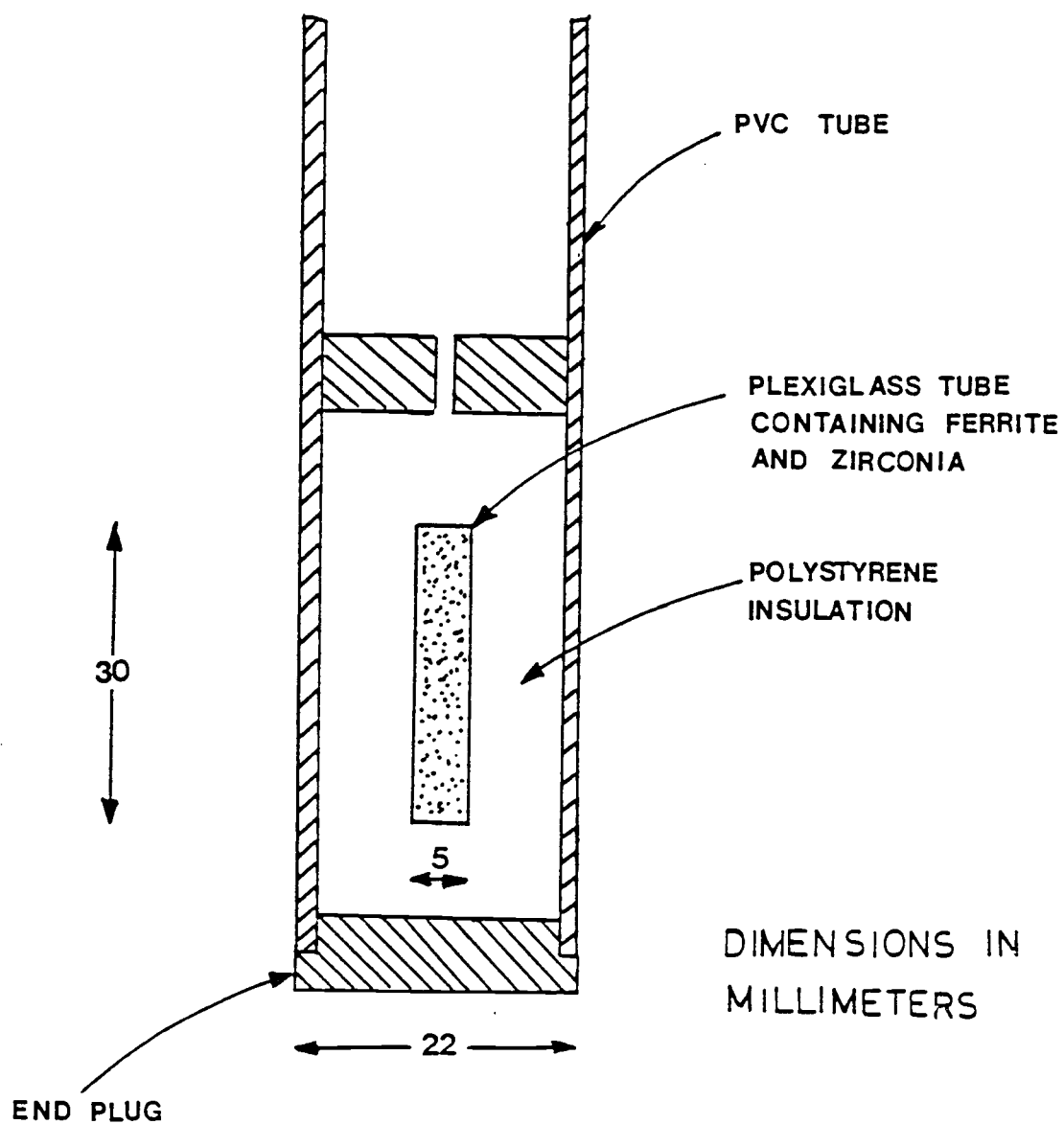


Figure G-5. Sample Container Used in the Magnetic Permeability vs. Temperature Experiments.

Table G-3. The Change in Magnetic Properties of Ferrite TC-71 with Temperature.

Temperature $T(^{\circ}\text{C})$	Change for Reference Sample	Voltage Change for Sample 1		Voltage Change for Sample 2	
	ΔV_{ref} (Volt)	ΔV_1	$\Delta V_{1,\text{corr}}^*$	ΔV_2	$\Delta V_{2,\text{corr}}^*$
18	0.245	0.374	0.374	0.378	0.378
32	0.249	0.417	0.410	0.397	0.391
60	0.245	0.434	0.434	0.401	0.401
63	0.246	0.436	0.434	0.401	0.399
68.5	0.244	0.429	0.431	0.397	0.399
77	0.236	0.166	0.172	0.188	0.195
84	0.241	0.069	0.070	0.094	0.096
100	0.245	0.028	0.028	0.039	0.039

* these values corrected to $\Delta V_{\text{ref}} = 0.245\text{v}$

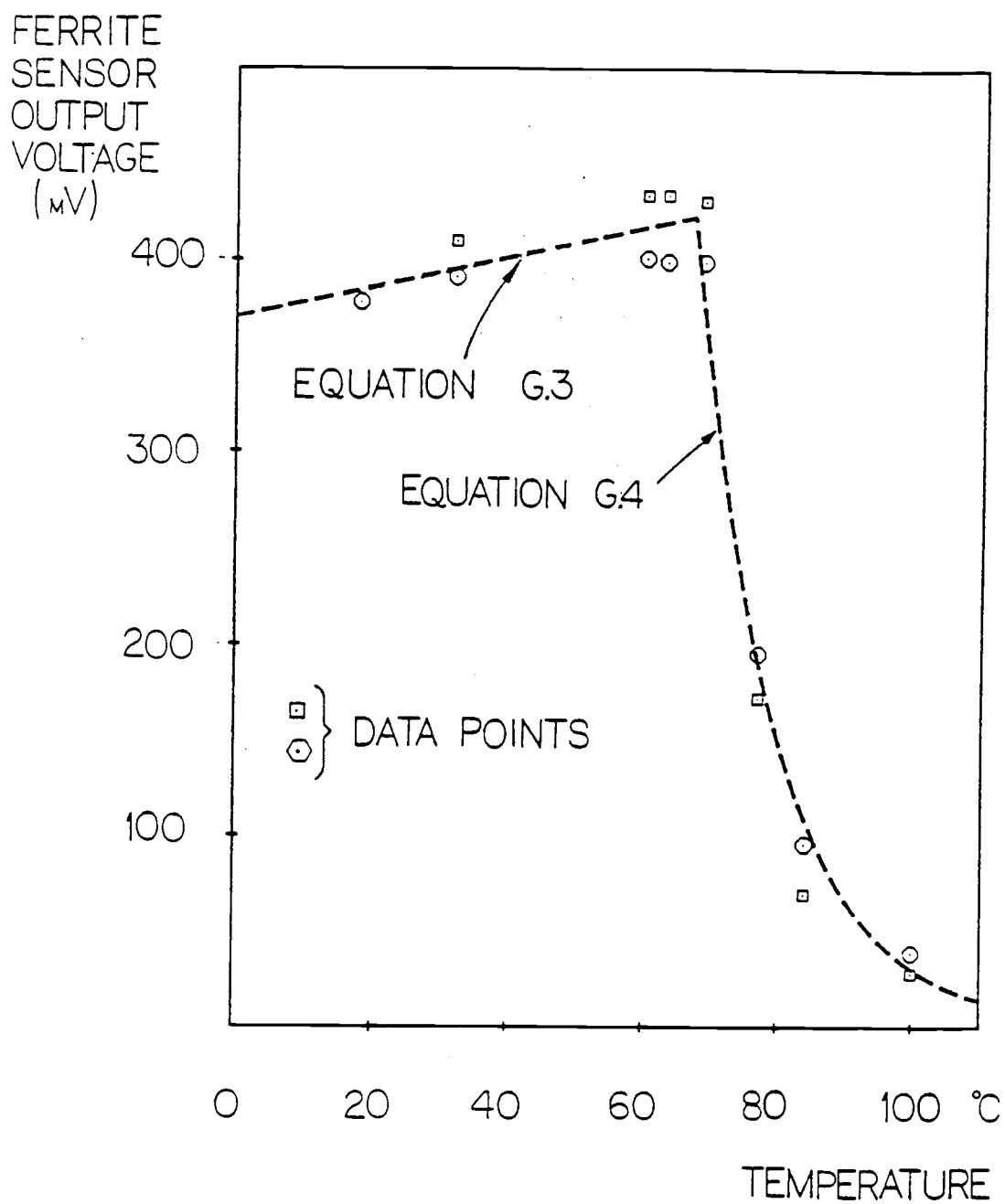


Figure G-6. Ferrite Sensor Output Voltage vs. Temperature of a 1.25 g Ferrite TC-71 Sample.

the ferrite. At temperatures above 70°C there is a sharp reduction in the output voltage corresponding to a decrease in magnetic permeability.

In the analysis of data given in Part IV of this thesis it is necessary to have an explicit relationship between the output voltage of the ferrite sensor and the temperature of the ferrite sample. For this purpose the data shown in Figure G-6 was correlated using the following equations and these equations are shown in Figure G-6 as dotted lines.

$$V_o = 0.37 + 0.053 \theta \quad \text{for } \theta \leq 1 \quad (\text{G-3})$$

$$V_o = 88.0 \exp(-5.34\theta) \quad \text{for } \theta > 1 \quad (\text{G-4})$$

where:

$$\theta = T/67$$

Eqs. G-3 and G-4 above represent the output voltage of a 1.25 gram ferrite sample homogeneously dispersed in a non-magnetic substance. The output voltage must be adjusted for different ferrite sample sizes and also for any changes in amplifier gain since Eqs. G-3 and G-4 are based on the reference sample having an output voltage of 0.245 volts.

APPENDIX H

FERRITE SENSOR - ELECTRONIC CIRCUITRY

H-1. Introduction

This magnetic ferrite sensor is based on a synchronous detection system developed by T.J. Fitzgerald of TRW, Inc., Redondo Beach, California and modified by R.T. Chan of Virginia Polytechnic Institute, Blacksburg, Virginia.

The circuit diagrams, blockflow diagrams, circuit board layouts and location of test points and expected wave forms are given in Figures H-1 through H-8. A list of the integrated circuits and auxillary board connections are given in Tables H-1 and H-2. The description of the operation of the ferrite sensor, etc. which follows is copied from the operations manual prepared by R.T. Chan and is repeated here for completeness.

H-2. Description of Electronic Circuits

A high stability, low distortion sine wave tuned to about 950Hz and 20V peak-to-peak (pep) is generated by E7 and associated components. This is buffered and inverted by E8 and E14, respectively, and passed onto buffer-drivers, A and B. The circuit is capable of delivering a peak-to-peak drive voltage of 40V to the bridge components, thus giving an effective doubling of gain over single-ended grounded drive. This feature is selectable by an internal, circuit board mounted switch, c, S5. The bridge difference signal is amplified by an instrumentation amplifier

AD 521, C, with programmable gain determined by the switch setting of d, S1-4. Gain may be 2, 4, 8, 16, 32, or a binary combination thereof. A gain of 12 or less should be chosen, with 8 as the optimum for the present bridge components.

The AC component of the instrumentation amplifier output is passed to the X1 input of the AD 534 multiplier, D, and is multiplied by the input sine wave at the Y1 input. The multiplier output has a characteristic frequency of two times that of the inputs.

The multiplier output is passed to a positive peak amplifier, E1 and E7, to establish a stable reference level for the differentially connected low pass amplifier, E8, thus giving a low ripple output voltage proportional to the multiplier output, and an indication of the amount of magnetic material in the cavity of the sensor coil causing the disturbance. The low ripple output is once more amplified by a second stage of amplifier, H7. The gain and filter time constant of this stage can be changed between times 1 or times 2 by switch, p, S2, and between 20mS or 70mS by switch, p, S3, respectively. Also, a digital baseline correction circuit is incorporated into this stage allowing the baseline to be reset back to zero volts with a press of button, p, S5. This feature may be defeated by switch, p, S4. Finally, the output is taken out by a BNC connector.

The digital baseline correction acts on the last stage of the amplifying chain so that its own error will not be amplified in the process of correcting the baseline. The circuit is based on a

sampling staircase generator composed of integrated circuits L and M, control circuits G, H, I, J, and K, and their associated passive components. When the staircase voltage is equal to that of the input voltage, sampled by a simple sample-and-hold circuit composed of H1 and H14, the staircase generator is turned off, and the 8-bits corresponding to the offset in the output stage are stored in the counter, M. The stabilized voltage is then summed (by reconnecting the baseline correction circuit to the output stage) in the inverting input of the output stage, H7, to give the stage a zero volts output. The baseline correction circuit operates with an 8-bit resolution, or a total of 256 steps, in a voltage range of -12.5V to +12.5V. Therefore, each step size is about 0.1V and the correction can only be to zero volt plus or minus 1 bit, i.e., plus or minus 0.1V.

Since the correction circuit can only correct an error range within plus and minus 12.5V, any error outside this range cannot be corrected. If the error is outside this range, the digital baseline correction circuit will lock up until the internal hold capacitor has discharged back to within the operation range. This process could take several seconds. The source of the large offset voltage should be removed before continued use.

A special feature built into the auxiliary circuit card is a phase tracking network based on a Phase Locked Loop device, N, and a Voltage Controlled Oscillator, P. The network tracks the instrumentation amplifier output (down to 50mV amplitude minimum) and generates a sine wave with identical phase but an amplitude

trimmed to that of the one generated by the sine wave oscillator, F7. The phase tracking sine wave is used to replace the one from F7 at the input, Y1, of the multiplier. This is done to remove the uncertainty of the phase lag introduced by the coils in the bridge circuit which could lead to an unstable output voltage. The negative peak output of the multiplier, thus stabilized, can undergo a peaking amplifier with a much shorter filter time constant and yet achieve a stable output voltage.

H-3. Calibration of Sensor

Ideally, the Bridge network should be perfectly balanced electrically and in components, however, neither can be done easily. It is found that when the bridge null trimmer is used to get the minimum output at the instrumentation amplifier with no ferrite material in the cavity, the ferrite sensor responded sluggishly and possibly not linearly with small quantities of ferrite.

Therefore, the bridge is operated in a controlled imbalanced state achieved by adjusting the bridge null trimmer to obtain about 1V (less than 4V) peak-to-peak output at the instrumentation amplifier. This gives an optimal sensitivity in one of the coils in the positive direction and with linear response, since the coil is imbalanced and is driven in the same direction. The other coil gives a nearly identical response, but in the negative direction, with a small quantity of ferrite. With a larger quantity of ferrite, the response once again becomes non-linear as the null point is approached. The reason for this is that, since the bridge

network is originally imbalanced, the addition of ferrite into the coil cavity drives it towards the balanced direction, reducing the output of the instrumentation amplifier and eventually imbalancing it again in the other direction. The output, therefore, goes towards negative at first and then positive.

Either test coil may be chosen to give a positive response by adjusting the bridge null trimmer to unbalance the bridge in the direction of the chosen coil.

In order to optimize the instrument the bridge null trimmer should be adjusted to give as close to 1V pep at the output of the instrumentation amplifier as possible and observing that the response of the ferrite sensor to a small ferrite sample inserted into the two coil cavities are the same in amplitude but opposite in direction. Achieving this should give the best result. Ascertain that the sample coil will give a positive response with a sample inserted, and keep the other coil as the reference coil.

The phase tracking circuit also has to be calibrated to be used. This involves adjusting the PLL sine amplitude to give the same output as the one from the main circuit sine oscillator in order that the response to a given quantity of ferrite is the same when the phase tracking circuit is switched in and out.

A source of noise at the output comes from the main circuit card oscillator operating in a class B mode. The crossover notches that occur as the sine wave crosses the ground level are passed onto the instrumentation amplifier and amplified as distortion. The end result is a noisy, and unstable baseline at the output. To reduce

this effect, the oscillator, buffer, and inverter are pulled to operate in a high dissipative class A mode by output biasing resistors tied in to the positive supply rail. Consequently, the integrated circuit, (F), must be heat sunk, and warm-up time is also increased to allow time to reach thermal equilibrium, reducing thermal drift while in operation. The unit should be kept from draft to reduce temperature drift when operating. An alternative method, and probably a better idea, is to operate the unit without the back cover and kept vertical, giving the best cooling possible to the electronics.

To reduce 60Hz noise pickup by the coils, the coils should be placed as closed to each other as possible so that noise may be picked up by both coils at the same time, and be rejected by the high common mode rejection of the instrumentation amplifier.

H-4. Gain Adjusting Methods

Gain may be effected by one of following three methods.

1. Change of instrumentation amplifier gain setting...dipswitch, "d,Sl-4," combination. These are arranged in a simple binary weighted scale of gains of (2), 4, 8, 16, and 32, and can give a combination of these values (except 2) by switching in the appropriate switches. Up to a total gain of 60 is possible with the switches all engaged, however, about 16 is the maximum gain that can be operated with the present coils, with a gain of 8 as the optimal. Keep in mind that the output of the

instrumentation amplifier should be less than 4V pep and visibly free from distortion for optimal operation. Also, keep in mind that if the output is too large, the baseline correction circuit can no longer correct for a null baseline. Reduce the gain to obtain correct operation.

2. Change to a balanced bridged-drive configuration...circuit board mounted switch, "C,S5." An effectively doubled gain may be had by increasing the drive voltage two times over the normal single-ended grounded drive. As with the previous method, the instrumentation amplifier output must be smaller than 4V pep to keep the main output within bounds for the baseline correction circuit to function correctly.
3. Panel mounted gain switch..."p, S2." The gain may simply be doubled or halved by this switch. This method is the most preferred of the three methods.

Table H-1. Integrated Circuits Used in Ferrite Sensor.

Label Appearing on Circuit Diagrams	Integrated Circuits
A, B	LH 0002CN
C	AD 521JD
D	AD 534JD
E, F, H, L	LM 324CN, TL 074N, or MC344004N
G	AD 7510JD
I, K	74C74
J	4011
M	XR 2240N
N	4046
O, Q	LM 349N
P	XR 2206N
All Diodes	1N4148
Q1, Q3	2N3904
Q2	MFP 102

Table H-2. Connections to 8 pin Auxillary Card

Pin Number	Connection
1	+ 15V
2	no connection
3	no connection
4	tracking phase select
5	-15V
6	tracking phase input
7	ground
8	tracking phase output

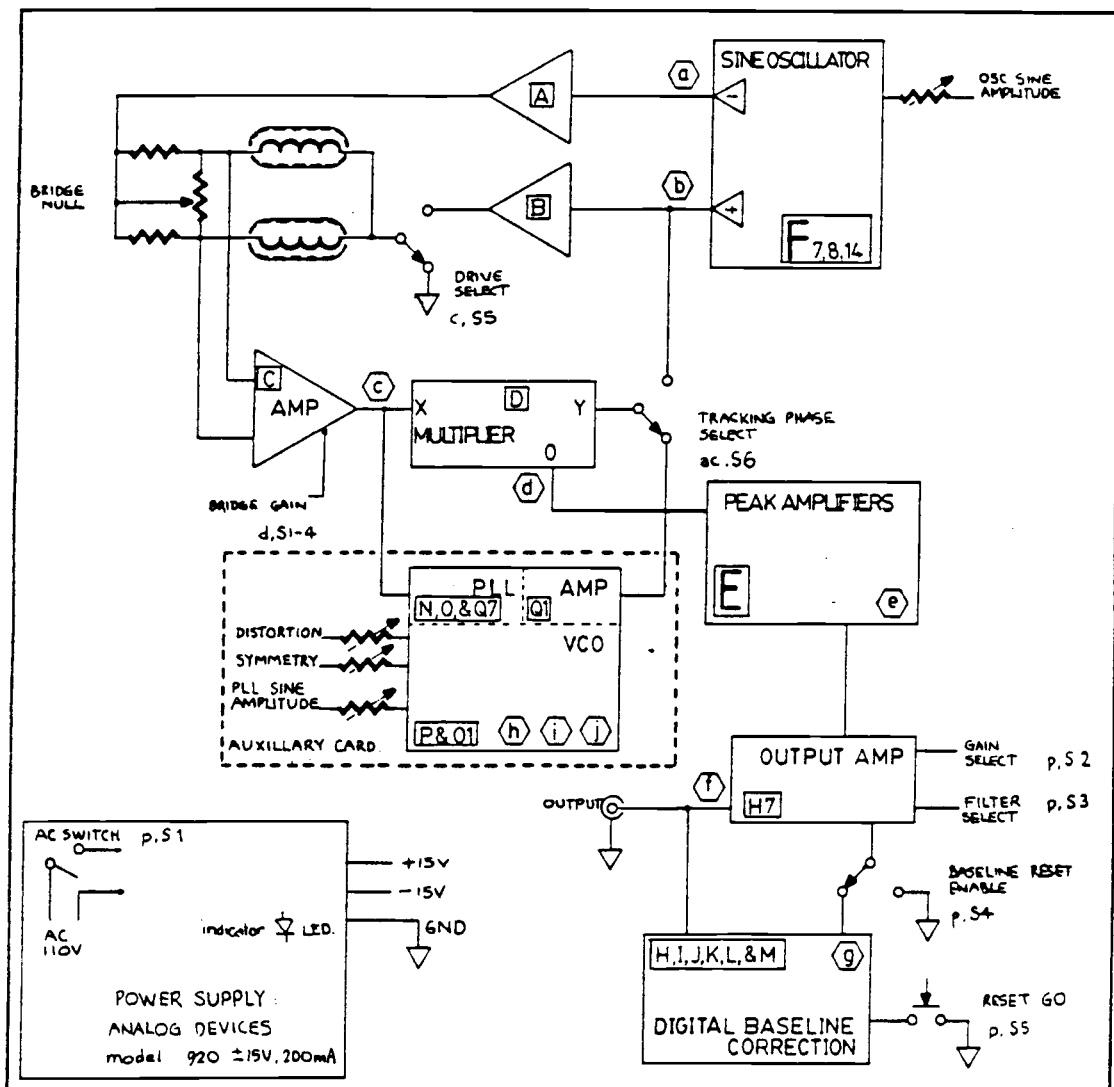


Figure H-1. Block Diagram of Circuit.

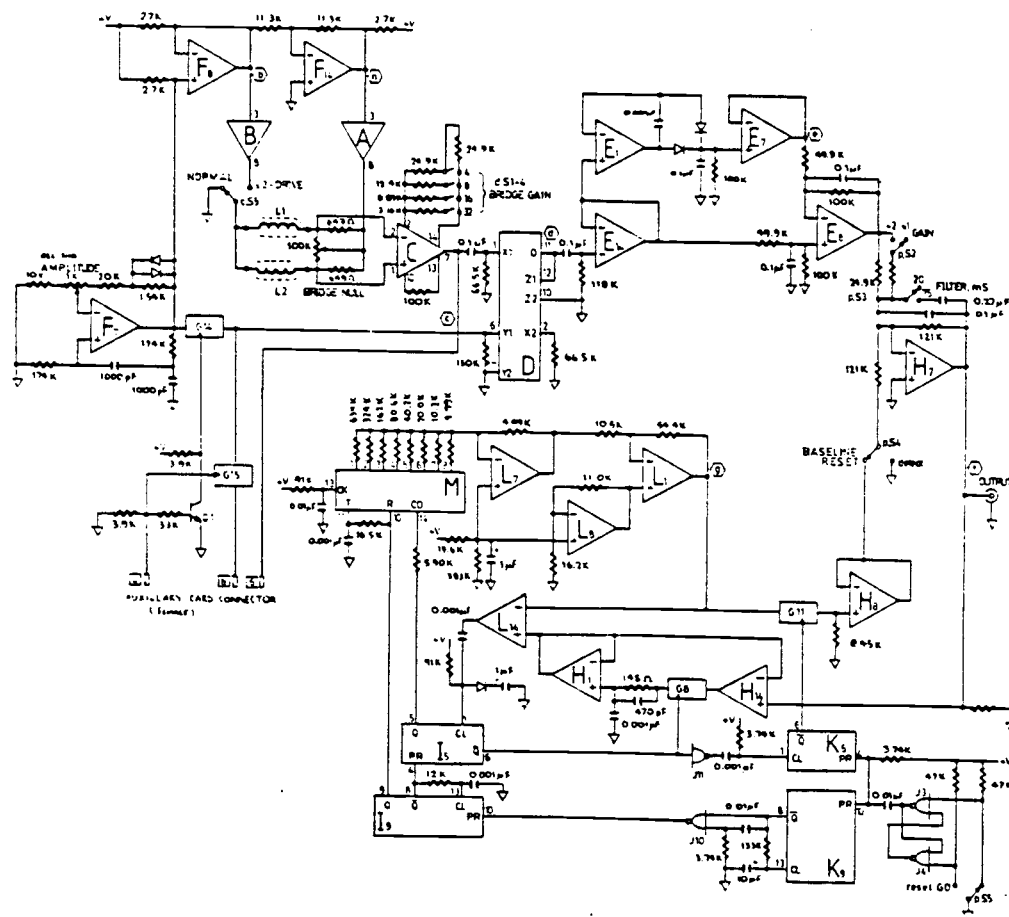


Figure H-2. Schematic Diagram of Main Circuit.

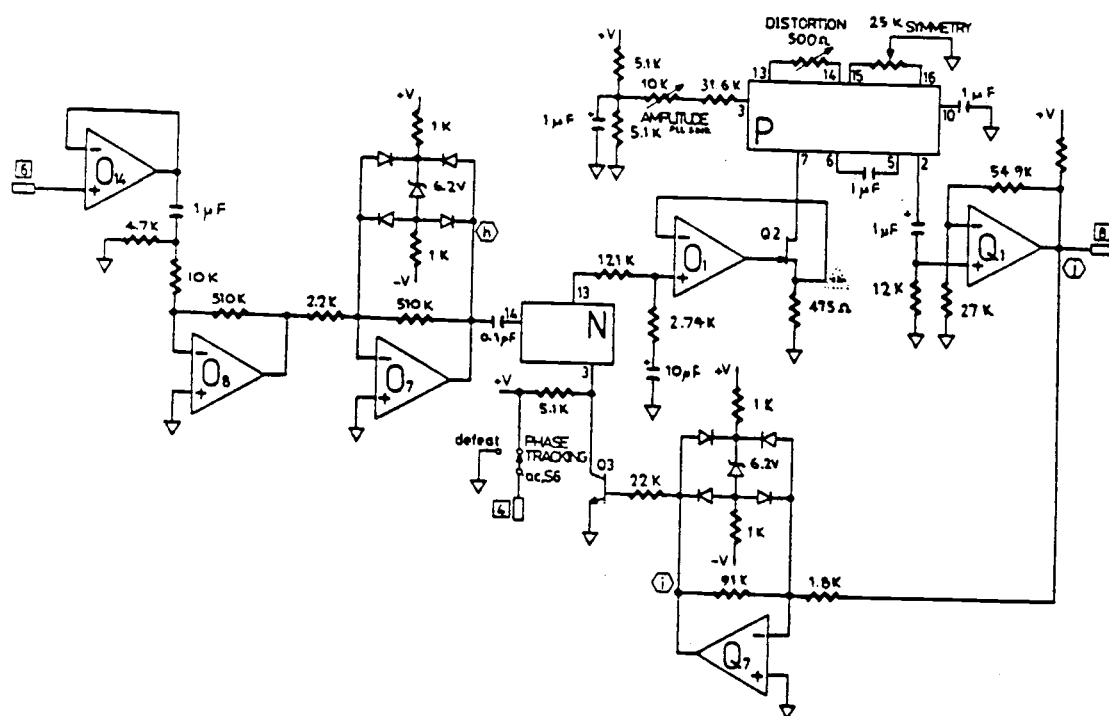


Figure H-3. Schematic Diagram of Auxillary, Phase Tracking, Card.

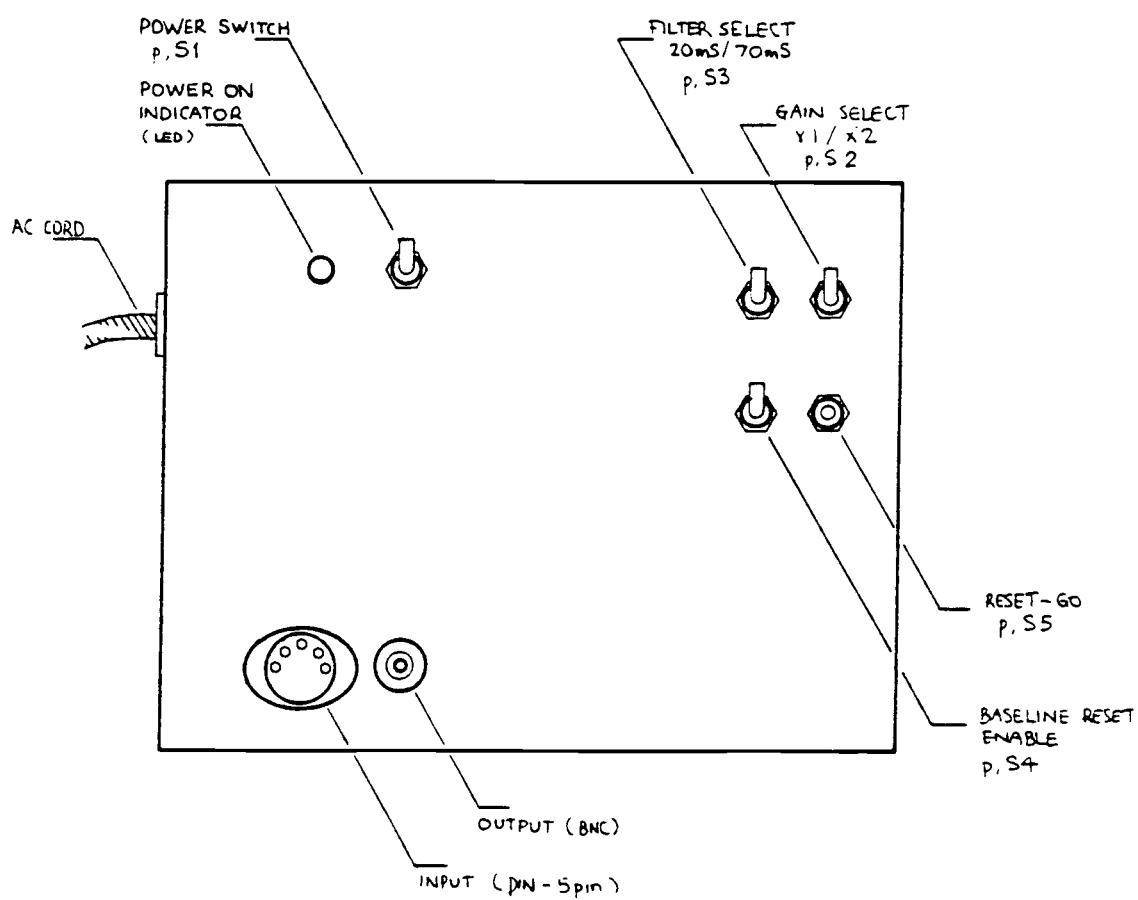


Figure H-4. Front Panel Layout.

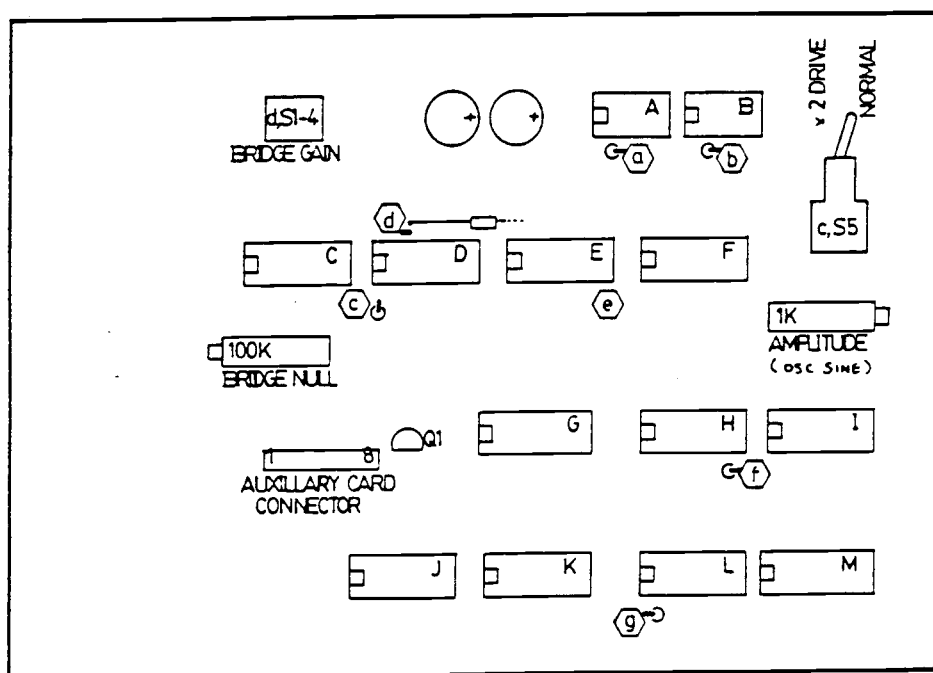


Figure H-5. Layout of Main Circuit Amplifier Card.

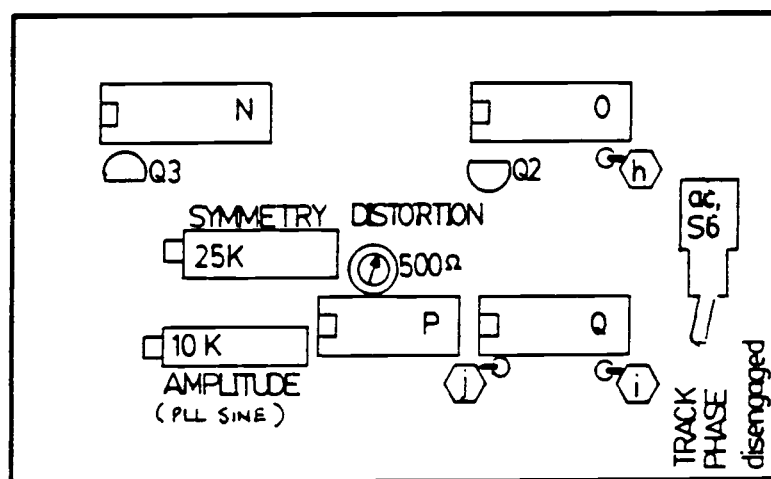


Figure H-6. Layout of Auxillary Card.

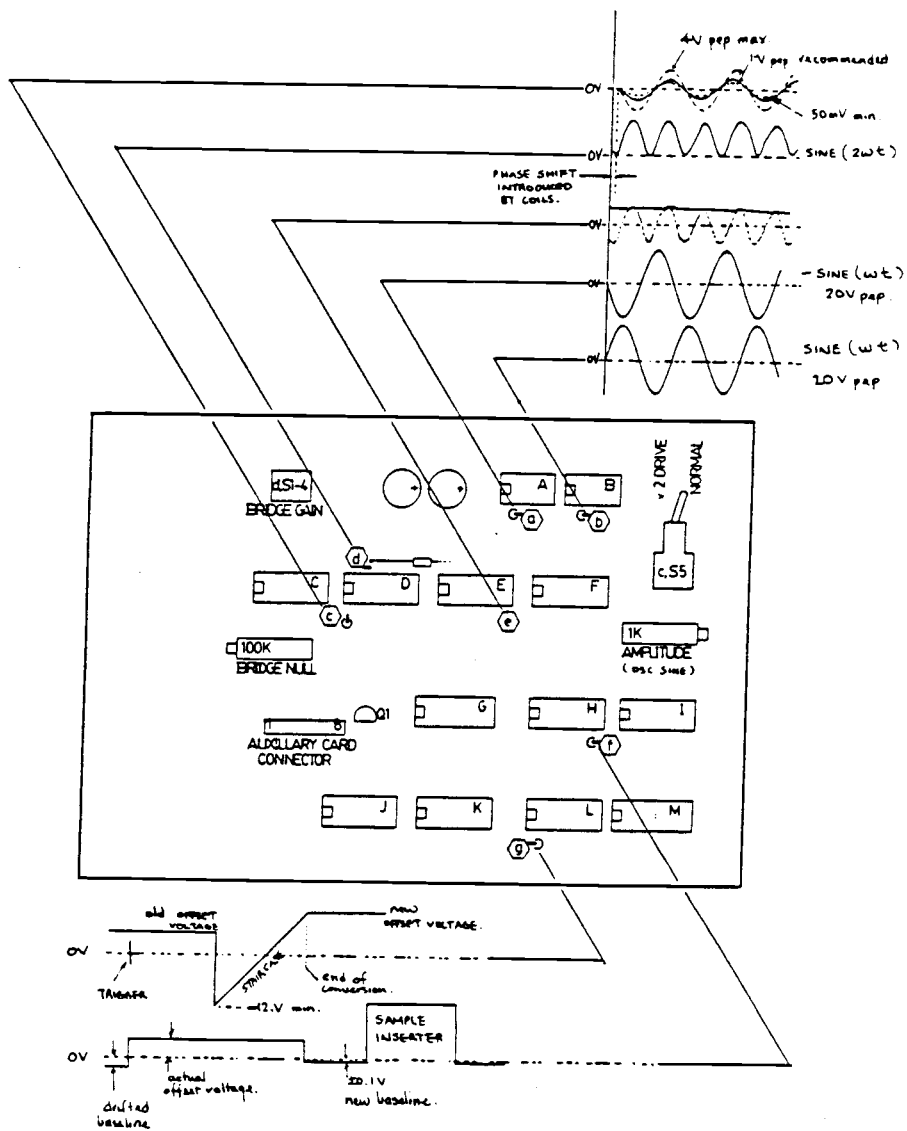


Figure H-7. Key Waveforms on Main Circuit Card.

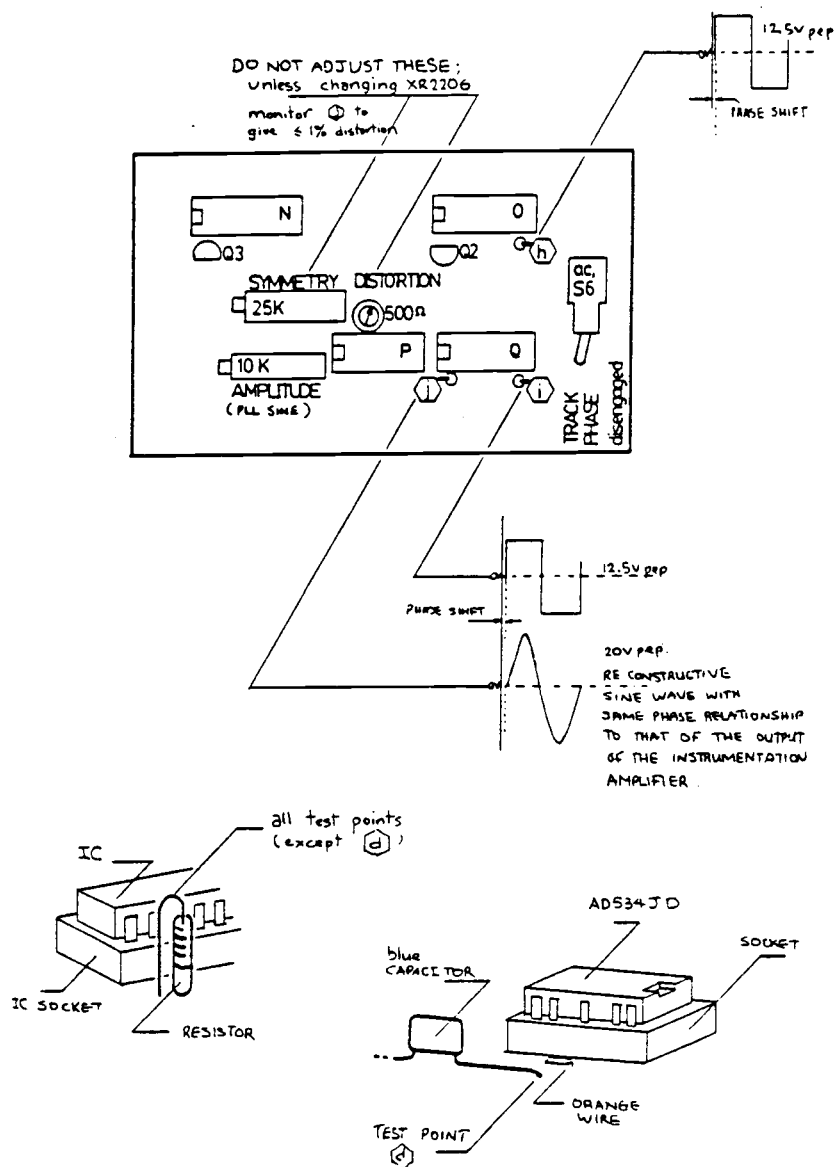


Figure H-8. Key Waveforms on Auxillary Card, and Test Points.

APPENDIX I

DETERMINATION OF SIZE DISTRIBUTION AND

 u_{mf} OF FERRITE TC-71 AND ZIRCONIAI-1. Size Distribution of Ferrite TC-71

The particle size distribution of the 1kg sample of ferrite TC-71 supplied by TDK Corporation (Japan) was determined by Tyler screen analysis. The results are presented in Table I-1.

I-2. u_{mf} for Ferrite TC-71 and Zirconia

The ferrite and zirconia were sieved into various size cuts and for each of these cuts the minimum fluidization velocity u_{mf} was determined. The method of determining the u_{mf} was the standard one of measuring the pressure drop across the bed for different superficial air velocities. The velocity at which the bed pressure drop becomes constant is taken to be u_{mf} . Figure I-1 shows the results for the 50⁻-60⁺ zirconia cut and the value of u_{mf} is indicated. The results for all the size cuts of ferrite and zirconia are given in Table I-2.

The data in Table I-2 was checked for consistency using the correlation due to Wen and Yu (64) and repeated below:

$$u_{mf} = \frac{d_p^2 (\rho_s - \rho_g)g}{1650 \mu g} \quad (I-1)$$

Table I-1. Particle Size Distribution of Ferrite TC-71

Size Cut	Average Particle Size	Mass Collected	Mass Fraction
Tyler Screen No.	\bar{d}_p ($\times 10^6 \text{m}$)	(g)	x_i
40 ⁺	425.0	0.15	0.0010
40 ⁻ -45 ⁺	390.0	0.44	0.0032
45 ⁻ -50 ⁺	327.5	11.64	0.0836
50 ⁻ -60 ⁺	275.0	28.88	0.2074
60 ⁻ -70 ⁺	231.0	24.29	0.1744
70 ⁻ -80 ⁺	196.0	23.14	0.1661
80 ⁻ -100 ⁺	165.0	21.14	0.1518
100 ⁻ -120 ⁺	137.5	13.97	0.1003
120 ⁻ -140 ⁺	115.5	8.87	0.0637
140 ⁻ -170 ⁺	98.0	4.12	0.0296
170 ⁻ -200 ⁺	82.5	1.14	0.0082
200 ⁻ -230 ⁺	69.0	0.35	0.0025
230 ⁻	63.0	<u>1.14</u>	<u>0.0082</u>
		<u>139.27</u>	<u>1.0000</u>

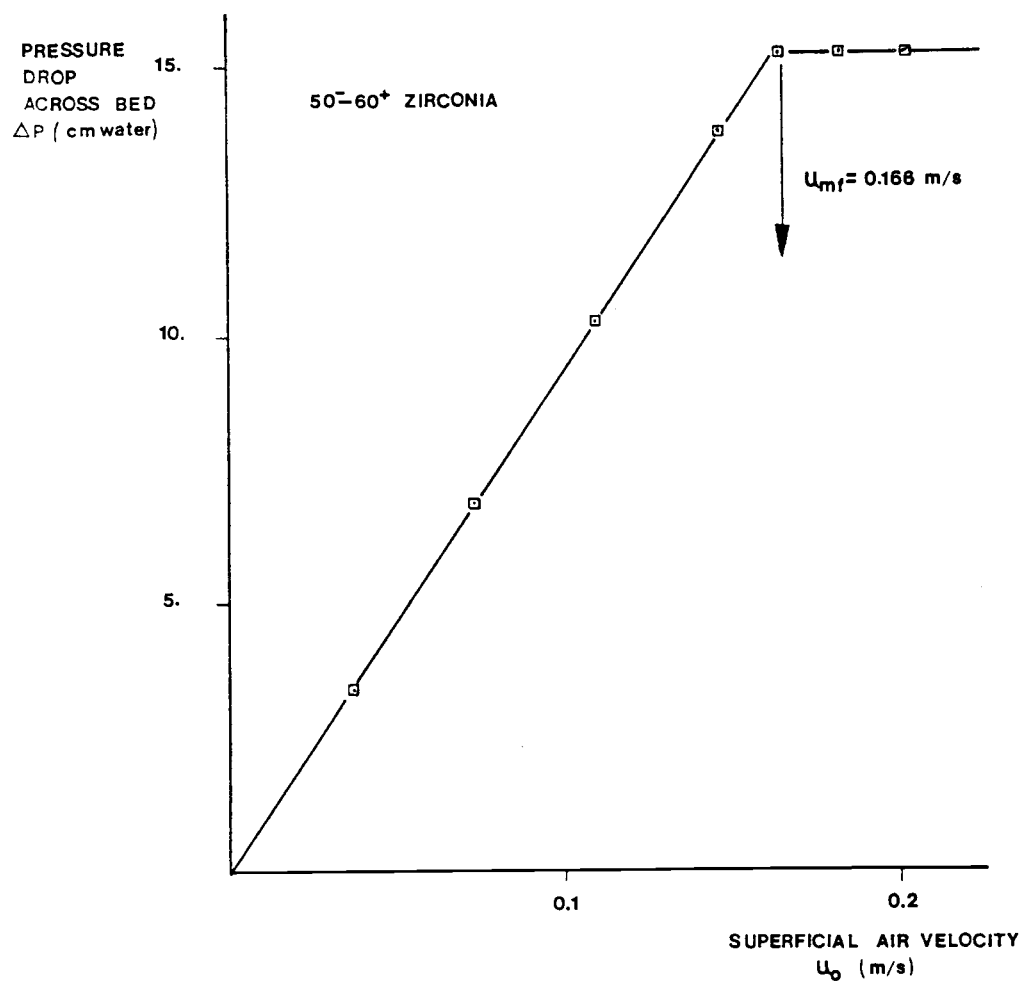


Figure I-1. Pressure drop vs. Superficial Velocity for 50-60⁺ Zirconia.

Table I-2. u_{mf} for Ferrite TC-71 and Zirconia

Size Cut	Average Particle Size	u_{mf} Ferrite	u_{mf} Zirconia
Tyler Screen No.	\bar{d}_p (μm)	(m/s)	(m/s)
45 ⁻ -50 ⁺	327.5	0.141	
50 ⁻ -60 ⁺	275.0	0.110	0.166
60 ⁻ -70 ⁺	231.0	0.103	0.103
70 ⁻ -80 ⁺	196.0	0.068	0.082
80 ⁻ -100 ⁺	165.0	0.047	0.065
100 ⁻ -120 ⁺	137.5	0.030	0.050
120 ⁻ -140 ⁺	115.5	0.022	0.030

Eq. I-1 suggests that a plot of u_{mf} vs. d_p^2 should be a straight line for a given gas-solid system. Figure I-2 compares the data for zirconia and ferrite with Eq. I-1. The agreement of data and correlation is good for both systems indicating that the data is consistent.

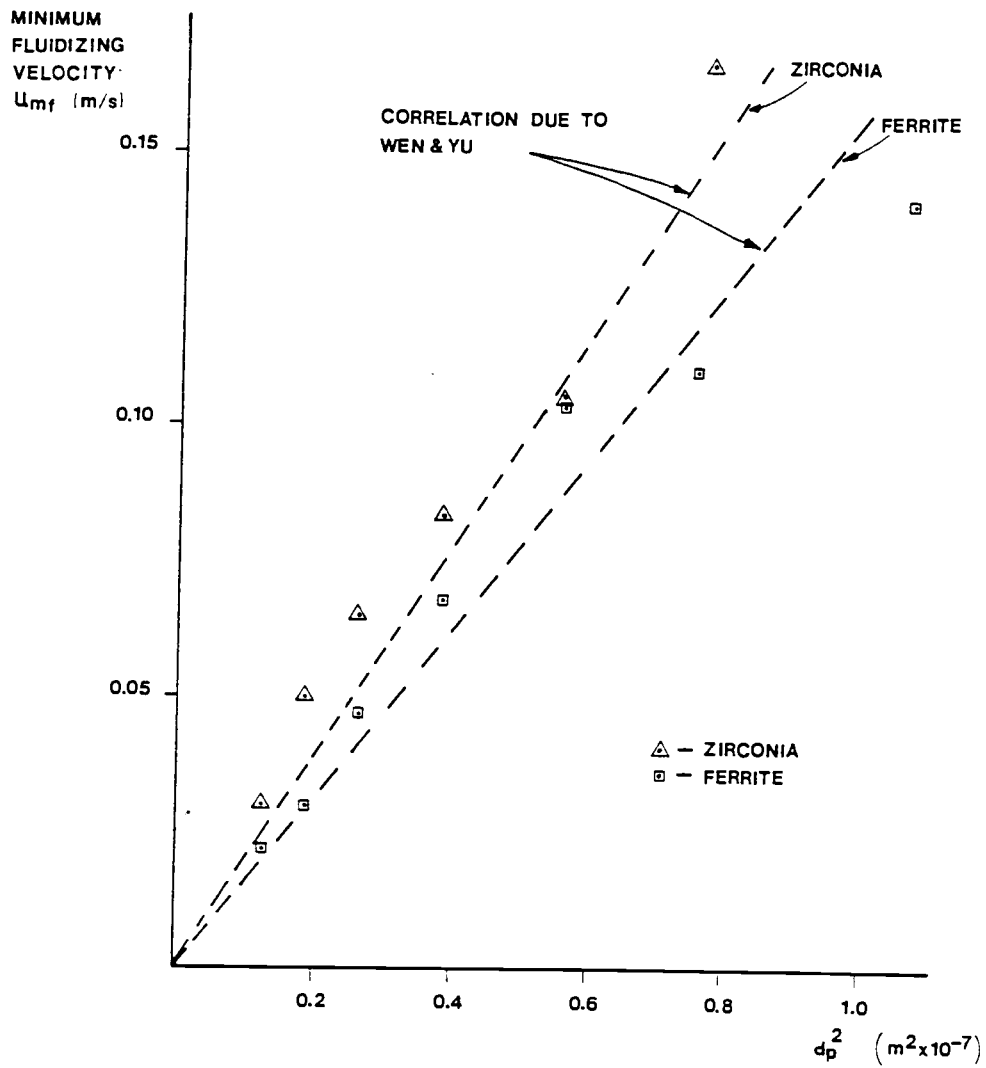


Figure I-2. Comparison of Data for Zirconia and Ferrite TC-71 with the Correlation Due to Wen and Yu (64).

APPENDIX J
COMPUTER PROGRAMS

The following two programs are listed in this section:

MIXING -- data acquisition program for hot and cold mixing
experiments.

TPROFL -- program to generate the voltage-temperature profiles
according to the model developed in Chapter IV.

```

PROGRAM MIXING
INTEGER*2 IDATA(5000),BASE,CHAN,GAIN,TRIG,VALUE
INTEGER*2 FUNI,NS,BIT,BVAL,JDATA(20)
INTEGER*2 TR,IC,IN,INS,VAL,GN,DATB1(20),DATB2(20)
EXTERNAL ADALAB,INIT,TRIGER,FASTAD,DIGIN
OPEN(6,FILE='MIXDAT',STATUS='NEW')
BASE=768
CALL INIT(BASE)
WRITE(*,*)'FREQ='
READ(*,*) IFREQ
WRITE(*,*)'INTERVAL FOR INTEGRATION'
READ(*,*) SAMPL
WRITE(*,*) 'GAIN='
READ(*,*) GAIN
IOFFST=3
50 BIT=1
GN=8
VAL=(1193210/10000-4)/2
TR=1
IC=2
IN=0
INS=10
CALL TRIGER(TR,VAL)
CALL FASTAD(IC,GN,IN,INS,JDATA(1))
GN=256
VAL=(1193210/10000-4)/2
TR=1
IC=4
IN=0
INS=10
CALL TRIGER(TR,VAL)
CALL FASTAD(IC,GN,IN,INS,DATB1(1))
GN=256
VAL=(1193210/10000-4)/2
TR=1
IC=7
IN=0
INS=10
CALL TRIGER(TR,VAL)
CALL FASTAD(IC,GN,IN,INS,DATB2(1))
CALL DIGIN(BIT,BVAL)
IF(BVAL.EQ.1) GOTO 50
CHAN=2
FUNI=0
NS=10*IFREQ
TRIG=1
VALUE=(1193210/IFREQ-4)/2
CALL TRIGER(TRIG,VALUE)
CALL FASTAD(CHAN,GAIN,FUNI,NS,IDATA(1))

```

```

INTEGR=INT(FLOAT(IFREQ)*(SAMPL+.00000001))
IC=4
GN=256
IN=0
INS=10
TR=1
VAL=(1193210/10000-4)/2
CALL TRIGER(TR,VAL)
CALL FASTAD(IC,GN,IN,INS,DATB1(11))
TR=1
VAL=(1193210/10000-4)/2
IC=7
IN=0
INS=10
GN=256
CALL TRIGER(TR,VAL)
CALL FASTAD(IC,GN,IN,INS,DATB2(11))
IDEND=NS+1-INTEGR
DO 60 I=1,10
IX=DATB1(I)
IX1=DATB2(I)
CALL TEMP(IX,T1,256,IOFFST)
CALL TEMP(IX1,T2,256,IOFFST)
WRITE(6,62) JDATA(I),T1,T2
62  FORMAT(2X,I6,2F10.2)
60  CONTINUE
DO 30 J=1,IDEND,INTEGR
ISM=0
JK=J+INTEGR-1
DO 40 I=J,JK
ISM=ISM+IDATA(I)
40  CONTINUE
JDAT=ISM/INTEGR
WRITE(6,12) J,JDAT
12  FORMAT(2X,2I6)
30  CONTINUE
DO 100 I=11,20
IX=DATB1(I)
CALL TEMP(IX,T1,256,IOFFST)
IX=DATB2(I)
CALL TEMP(IX,T2,256,IOFFST)
WRITE(6,101)T1,T2
101  FORMAT(2X,2F10.2)
100  CONTINUE
CLOSE(6)
END

```



```
SUBROUTINE TEMP(IX,T,IG,IOFF)
C0=.2265846
C1=24152.11
C2=67233.42
C3=2210340.
C4=-860963915.
C5=4.83506E+10
C6=-1.18452E+12
C7=1.38690E+13
C8=-6.33708E+13
X=5.*FLOAT(IX-IOFF)/2047./FLOAT(IG)
T=C0+C1*X+C2*X**2+C3*X**3+C4*X**4+C5*X**5+C6*X**6
1  +C7*X**7+C8*X**8
RETURN
END
```

```

PROGRAM TPROFL
DIMENSION TX(2600), V(2600), T(2600), VC(2600), VEXP(2600)
COMMON/DAT1/SF, THETA F, THETA I, A1, D2, D1
EXTERNAL FINT1, FINT2
OPEN(4, FILE='ERDAT', STATUS='NEW')
OPEN(3, FILE='VCONV', STATUS='OLD')

C
C
C *****
C
C THIS PROGRAM GENERATES THE OUTPUT VOLTAGE VS TIME PROFILE FOR
C THE HEATING OF A SAMPLE OF DIFFERENT SIZED LOW CURIE POINT
C FERRITE MATERIAL. EACH PARTICLE IS ASSUMED TO HEAT UP INDEPEND
C ENTLY AND ISOTHERMALLY. THE INPUT VARIABLES ARE:
C D1.....SMALLEST PARTICLE DIAMETER IN SAMPLE (MICRO-M)
C D2.....LARGEST PARTICLE DIAMETER IN SAMPLE (MICRO-M)
C THETA I.....INITIAL TEMPERATURE OF SAMPLE (TSAMPLE/67.0)
C THETA F.....FINAL TEMPERATURE OF SAMPLE (TBED/67.0)
C H.....HEAT TRANSFER COEFFICIENT (W/M2.K)
C VHF.....FINAL OUTPUT VOLTAGE FOR HOT RUN (AT THETA F)
C
C *****
C
C WRITE(*,*) 'ENTER READ OPTION...1,2,3'
C READ(*,*) IFLAG
C DO 55 I=102, 2600, 2
C IF(IFLAG.EQ.1) THEN
C   READ(3,*) TX(I), VEXP(I), DM2, DM3
C ELSE
C   IF(IFLAG.EQ.2) THEN
C     READ(3,*) TX(I), DM2, VEXP(I), DM3
C   ELSE
C     READ(3,*) TX(I), DM2, DM3, VEXP(I)
C   ENDIF
C ENDIF
55 CONTINUE
C
C WRITE(*,*) 'D1='
C READ(*,*) D1
C WRITE(*,*) 'D2='
C READ(*,*) D2
C WRITE(*,*) 'THETA I='
C READ(*,*) THETA I
C WRITE(*,*) 'THETA F='
C READ(*,*) THETA F
C WRITE(*,*) 'H='
C READ(*,*) H
C WRITE(*,*) 'VHF='
C READ(*,*) VHF
C

```

```

RHOS=4780.
CPS=648.
TH=(THETAF-THETA1)/(THETAF-1.)
A1=6.*H/(RHOS*CPS)
T1=D1*ALOG(TH)/A1
T2=D2*ALOG(TH)/A1

SF=.285*0.5/(.245*1.25)
VHFP=SF*88.0*EXP(-5.34*THETAF)
SFACT=VHF/VHFP
DELTIM=0.002
NS=10
T(1)=0.00
V(1)=1000.*( .37+.053*THETA1)*SF*SFACT
DO 10 I=1,2500
  T(I+1)=DELTIM*FLOAT(I)
  IF(T(I+1).LE.T1) THEN
    CALL SIMPSON(D1,D2,FINT1,NS,T(I+1),XINT)
    V(I+1)=SFACT*1000.*XINT
  ELSE
    ENDF
  IF(T(I+1).GT.T1.AND.T(I+1).LE.T2) THEN
    DINTM=A1*T(I+1)/ALOG(TH)
    CALL SIMPSON(DINTM,D2,FINT1,NS,T(I+1),XINT1)
    CALL SIMPSON(D1,DINTM,FINT2,NS,T(I+1),XINT2)
    V(I+1)=SFACT*1000.*(XINT1+XINT2)
  ELSE
    ENDF
  IF(T(I+1).GT.T2) THEN
    CALL SIMPSON(D1,D2,FINT2,NS,T(I+1),XINT3)
    V(I+1)=SFACT*1000.*XINT3
  ELSE
    ENDF
10  CONTINUE
    DO 15 J=2600,1,-1
      IF(J.LT.100) THEN
        V(J)=V(100)
      ELSE
        V(J)=V(J-99)
      ENDF
15  CONTINUE

```

 THE NEXT PART OF THE PROGRAM CONVOLUTES THE GENERATED PROFILE
 CONTAINED IN V(I) AND GENERATES THE TIME SHIFTED PROFILE VC(I)

```

K=6
DO 25 I=100,2600
N=I
SUM=0.
N1=N-98
IC=-1
DO 35 J=N1,N
IC=IC+1
IT=(-1)**IC
FX=2.
IF(IT.LT.0) FX=4.
IF(IC.EQ.0) FX=1.
IF(IC.EQ.98) FX=1.
35 SUM=SUM+V(J)*FX*EXP(-(FLOAT(98-IC))/FLOAT(K))
CONTINUE
VC(I)=SUM/3./FLOAT(K)
25 CONTINUE

DO 45 I=102,2600,2
WRITE(4,*)TX(I),VEXP(I),VC(I)
45 CONTINUE
CLOSE(4)
CLOSE(3)
STOP
END

```

SUBROUTINE SIMPSON(X1,X2,FUNX,NS,TX,XINT)
 COMMON/DAT1/SF,THETAF,THETA1,A1,D2,D1

THIS SUBROUTINE INTEGRATES THE FUNCTION SPECIFIED IN FUNX
 FROM X1 TO X2 USING 2*NS EQUALLY SPACED INTERVALS AND SIMPSONS
 ALGORITHM.

```

NC=2*NS
DELH=(X2-X1)/FLOAT(NC)
SUM1=FUNX(TX,X1)
DO 100 I=1,NC
X=X1+DELH*FLOAT(I)
LAB=2*((I+2)/2-1)
XFACT=4.
IF(LAB.EQ.1) XFACT=2.
IF(I.EQ.NC) XFACT=1.
100 SUM1=SUM1+XFACT*FUNX(TX,X)
CONTINUE
XINT=SUM1*DELH/3.
RETURN
END

```

```
FUNCTION FINT1(TX,D)
COMMON/DAT1/SF,THETAF,THETAI,A1,D2,D1

FINT1=SF*(0.37+0.053*(THETAF-(THETAF-THETAI)*EXP(-A1*TX/D)))
1 / (D2-D1)
RETURN
END

FUNCTION FINT2(TX,D)
COMMON/DAT1/SF,THETAF,THETAI,A1,D2,D1

FINT2=SF*(88.0*EXP(-5.34*(THETAF-(THETAF-THETAI)*EXP(-A1*TX/D
1 )))) / (D2-D1)
RETURN
END
```

APPENDIX K

PRELIMINARY STUDIES ON THE FERRITE SENSOR

K-1. Sensitivity Variation Within Detector Coil

The object of this study was to determine whether the sensitivity of the detector coil was uniform throughout its volume. The fluidized bed was first placed within the coil and secured in position. A test sample weighing 1.5 grams and containing a homogeneous mixture of 50 percent ferrite and 50 percent zirconia (by weight) was made up. The zirconia and ferrite mixture was placed in a cylindrical container 8mm O.D. and 17mm long. This test sample was then inserted into different parts of the fluidized bed and the response voltage of the ferrite sensor was recorded. The results of this study are given in Figure K-1 which shows the position and corresponding output voltage for the different sample locations within the fluidized bed. The sensitivity of the coil is seen to vary slightly over the fluidized bed. However, this variation has a maximum of only 14 percent and is ignored in the analysis of data given in Section IV of this thesis.

K-2. Linearity of the Ferrite Sensor Amplifier

It is important in the mixing experiments described in Section IV of this work that the ferrite sensor amplifier is linear. The term linear, as used here, refers to the ability of the amplifier to produce an output voltage signal which is directly proportional to the amount of magnetic material present within the fluidized bed.

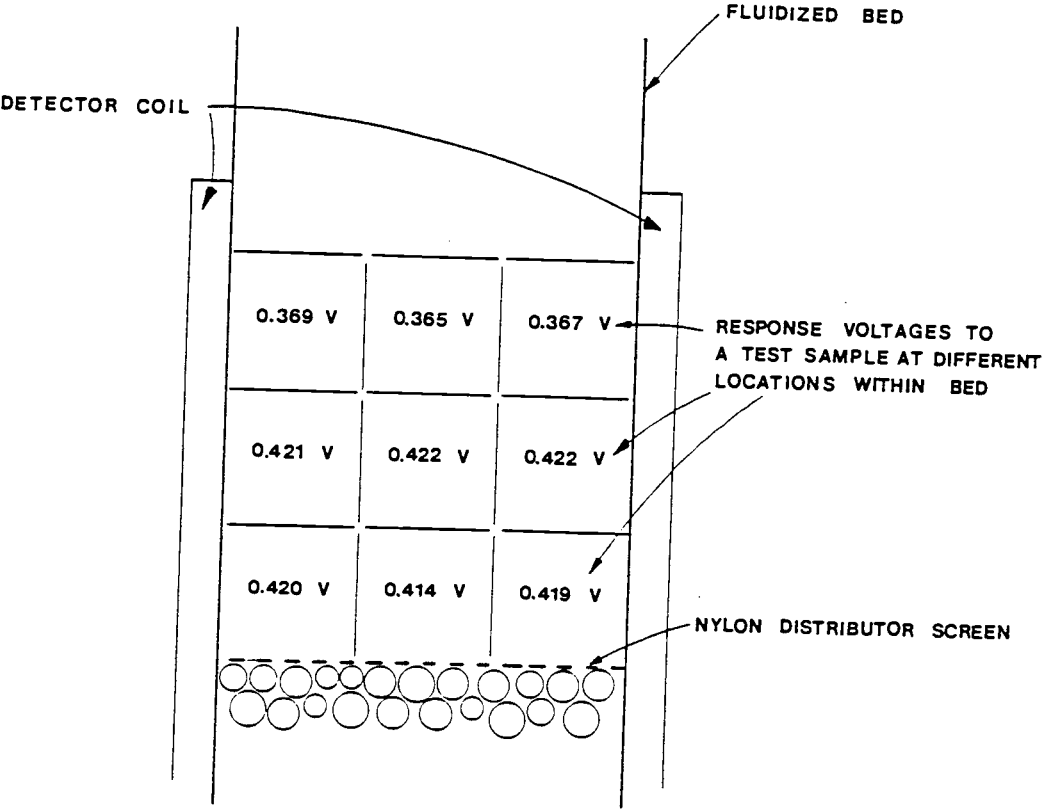


Figure K-1. Sensitivity Map of the Detector Coil.

The experimental technique used to check the linearity of the ferrite sensor is described below.

First 60 grams of zirconia were placed in the fluidized bed. The offset voltage was noted and the output signal for a known control test sample was recorded. A preweighed sample of ferrite TC-71 was then added to the zirconia and the bed was then fluidized for 1 minute to ensure the complete mixing of ferrite with zirconia. The output voltage from the sensor was then recorded. The bed was then emptied and the procedure repeated with a different mass of ferrite TC-71. The results of this study are given in Table K-1 and plotted in Figure K-2.

From Figure K-2 it is evident that the ferrite sensor amplifier is indeed linear over the range of ferrite samples used here.

K-3. Ferrite Sensor Amplifier Gain

Over the period of time that a single set of experiments are carried out the amplifier gain is essentially constant. This is verified by the output voltages of the control test sample given in Table K-1. However, over the period of time that the hot and cold mixing experiments were carried out, approximately two weeks, the amplifier gain was found to drift. This change in gain simply affects the magnitude of the output voltage, the linearity of the amplifier is unaffected.

One cause of the change in amplifier gain is whether the detector coil is heated or not. The effect of heating the coil to 100°C, which is approximately its temperature during a hot mixing

Table K-1. Linearity Experiments on Ferrite Sensor

Mass of Ferrite (grams)	Control Test Sample Output (V)	Ferrite Sample Sample Output (V)	Adjusted* Output for Ferrite Sample (V)
0.5	0.281	0.187	0.190
1.0	0.280	0.365	0.372
1.5	0.282	0.564	0.570
2.0	0.282	0.764	0.772

* These voltages are adjusted to give the equivalent output for a control test sample output of 0.285 volts.

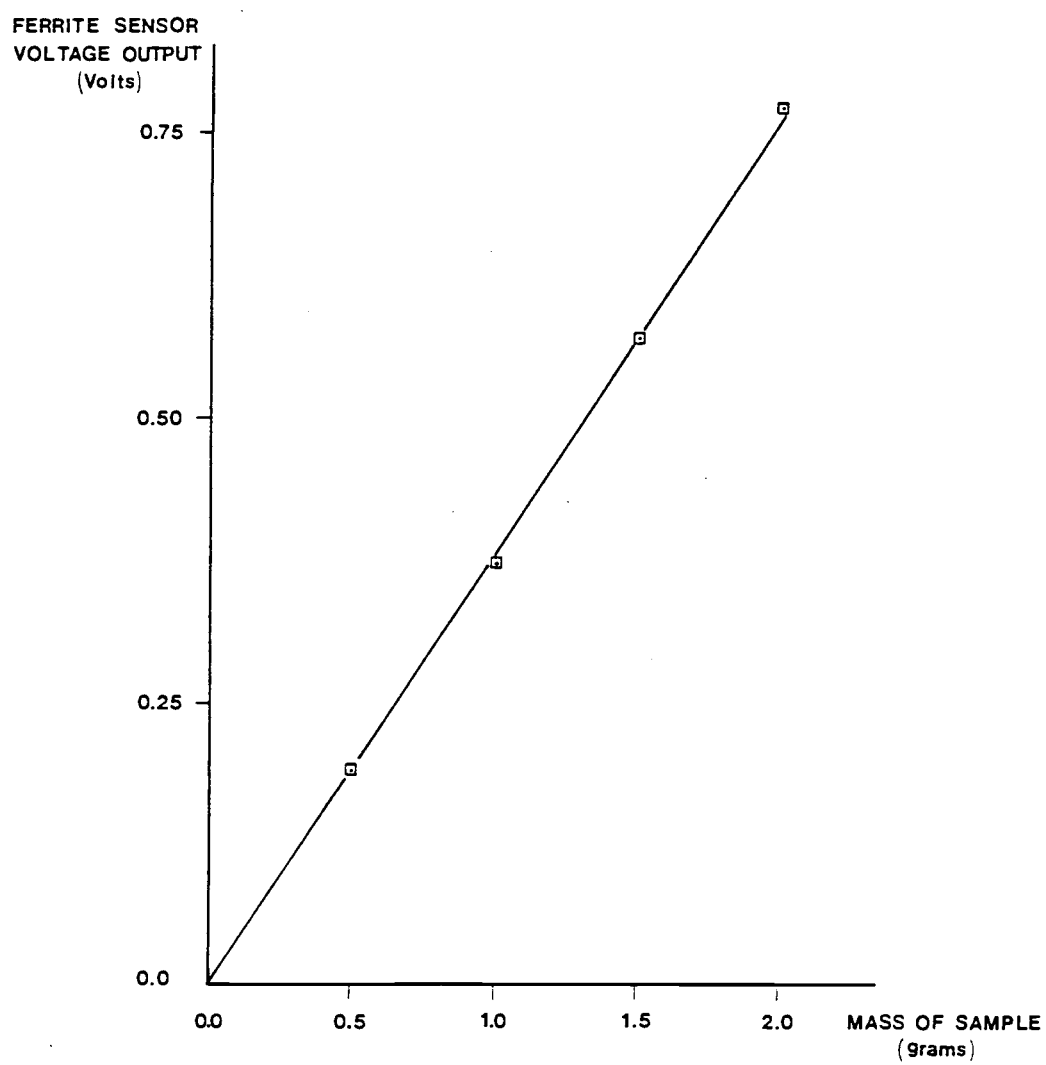


Figure K-2. Results of Linearity Test on Ferrite Sensor.

run, was investigated. The results indicated that the gain decreased by approximately 20 percent compared with that obtained with the coils at ambient conditions. This result is confirmed by the difference in the initial data for the hot and cold mixing runs given in Appendix L. The initial signal level for the hot mixing runs is approximately 200mV which is 20 percent lower than the 250mV initial signal level for the cold mixing studies. Other small differences exist between the hot mixing data for systems A, B, and C compared with data for systems D, E, and F. These changes in signal magnitude do not greatly affect the heat transfer coefficients obtained by comparing the model developed in Section IV with the experimental data.

For this reason, small changes in amplifier gain were used in the simulations of Section IV to improve the fit of the data with the model. These changes in gain only change the magnitude of the signal not its position in time.

K-4. The Effect of Sample Shape on Output Voltage

The effect of the shape of the sample injected into the fluidized bed on the initial output voltage was investigated. As pointed out previously in Section IV, the voltage output obtained when the ferrite sample is homogeneously mixed in the fluidized zirconia depends only on how much ferrite is present in the bed. However, the initial output voltage is higher than the final steady state value. This initial signal level depends upon several factors, one of these being the shape of the sample.

Several differently shaped containers were made from different diameter plastic tubes. One gram of ferrite was added to each container and the whole unit sealed with epoxy resin. Each container was placed in the fluidized bed and the output voltage measured. A control sample was used to check the gain of the amplifier for each experiment. The results of these experiments are given in Table K-2 and Figure K-3. In Figure K-3 the output voltage is plotted against the length to diameter ratio of the sample. The results indicate that the output voltage from the ferrite sensor increases linearly with an increase in the length to diameter ratio.

This result is not surprising since a high length/diameter ratio means that the sample is like a vertical rod. This shape has a long magnetic path in the vertical direction. The lines of magnetic flux will concentrate in the sample thus causing a large change in impedance of the coil. This shape of sample, therefore, offers a long low resistance path for the magnetic lines of flux. As the L/D ratio decreases, the sample gets shorter and fatter until it becomes disc or coin shaped. For this case, the sample offers a low resistance path over a very short distance, i.e., the height of the disc. The impedance of the coil is, therefore, changed only a relatively small amount. Hence the output voltage is much lower.

The output voltage of a homogeneously dispersed 1 gram ferrite sample is also indicated in Figure K-3. The L/D ratio of the homogeneously dispersed sample in 60g of zirconia is approximately 1.25. The corresponding output voltage from Figure K-3 should be 0.460V while the actual voltage is about 0.370V. This difference is

Table K-2. Results of Experiments on the Effect of the Sample Shape on the Output Voltage of the Ferrite Sensor

Length/ Diameter	Control Sample Output Voltage (V)	Sample Output Voltage (V)	Adjusted* Output Voltage for Sample (V)
0.63	0.299	0.365	0.348
0.63	0.296	0.360	0.347
2.42	0.293	0.730	0.710
2.42	0.298	0.733	0.701
0.22	0.291	0.253	0.248
0.22	0.295	0.240	0.232
0.08	0.299	0.252	0.240
0.08	0.301	0.251	0.238
1.00	0.302	0.429	0.405
1.00	0.299	0.444	0.423

* These voltages are adjusted to give the equivalent output for a control test sample output of 0.285 volts.

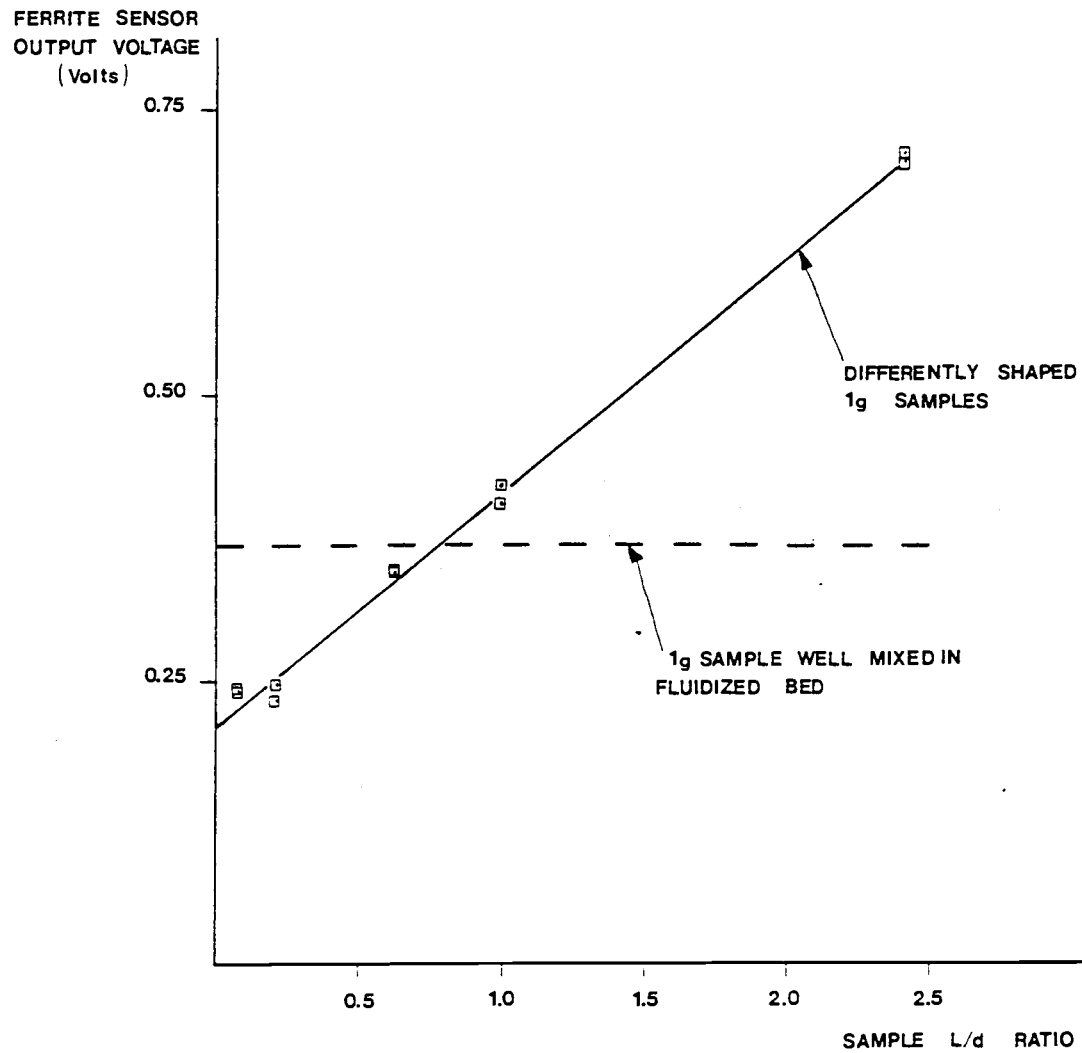


Figure K-3. Output Voltage vs. Length/Diameter Ratio of Ferrite Sample.

due to the fact that the data in Figure K-3 is for pure ferrite while the homogeneous sample is ferrite diluted with zirconia. This dilution effectively separates the ferrite particles and causes the lines of magnetic flux to be less concentrated thus reducing the impedance of the coil. This reduction in impedance in turn reduces the output voltage from the ferrite sensor.

K-5. Some Qualitative Observations on the Response
of the Ferrite Sensor to Changes in the Composition
of the Injected Sample and Other Related Parameters

In the course of carrying out the preliminary studies discussed above several observations about the ferrite sensor response were made. These observations are listed below:

1. Large fluctuations in output signal occur when a pure ferrite sample is injected into the fluidized bed. If a homogeneous diluted sample, 50 percent weight of ferrite and 50 percent zirconia, is injected the fluctuations in signal are substantially reduced. For this reason a 50/50 zirconia/ferrite sample was used in the mixing studies.
2. When the ferrite sample has become well mixed in the fluidized bed the output signal is steady with a noise level of approximately $\pm 10\text{mV}$ for system F. This noise level increases with particle size and increasing levels of fluidization (u_o/u_{mf}).

3. The initial value of the output signal (at $t=0$) when a mixed ferrite/zirconia sample is injected into the bed corresponds to the signal obtained when that sample is placed in the bed but not allowed to mix.

APPENDIX L
EXPERIMENTAL RESULTS FOR HOT AND COLD
MIXING STUDIES DISCUSSED IN CHAPTER IV

L-1. Cold Mixing Studies

Figures L-1 through L-5 illustrate the results for the cold mixing studies on systems B-F.

L-2. Hot Mixing Studies

Figures L-6 through L-20 illustrate the results for the hot mixing studies on systems B-F.

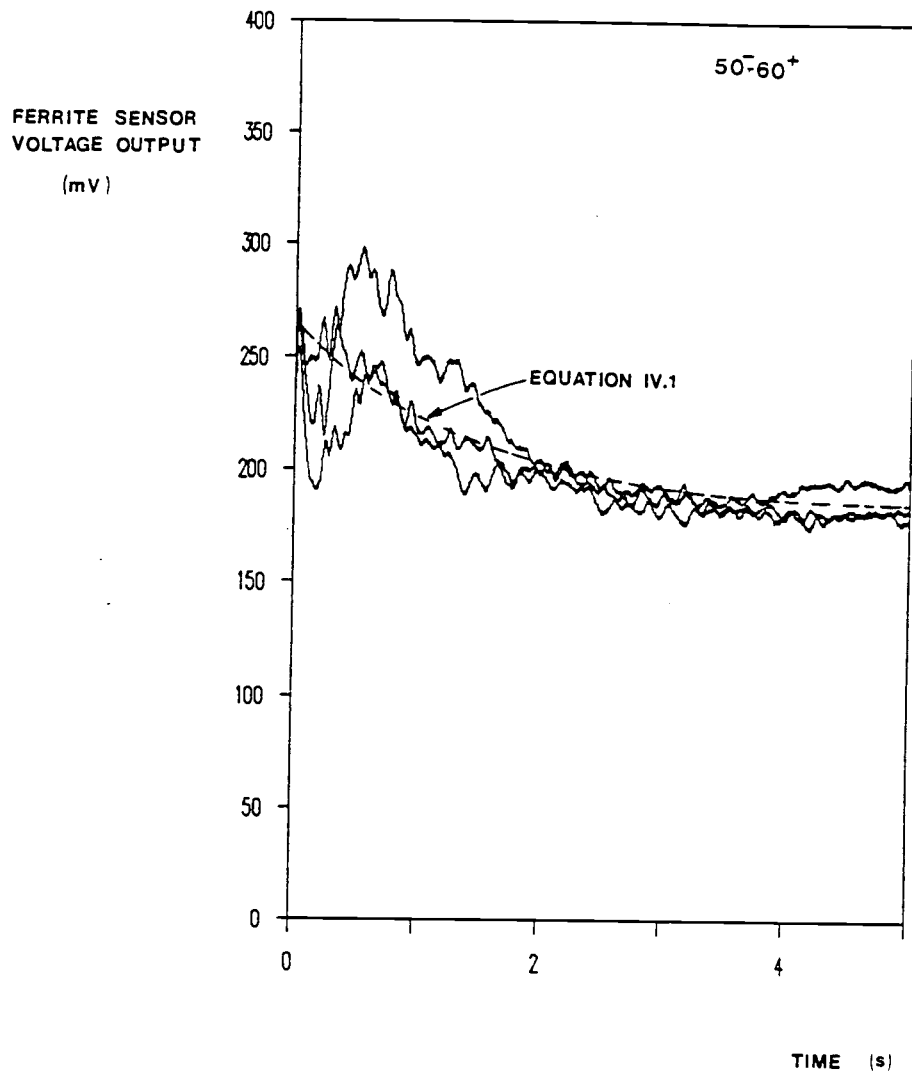


Figure L-1. Results for the Cold Mixing Studies on System B.

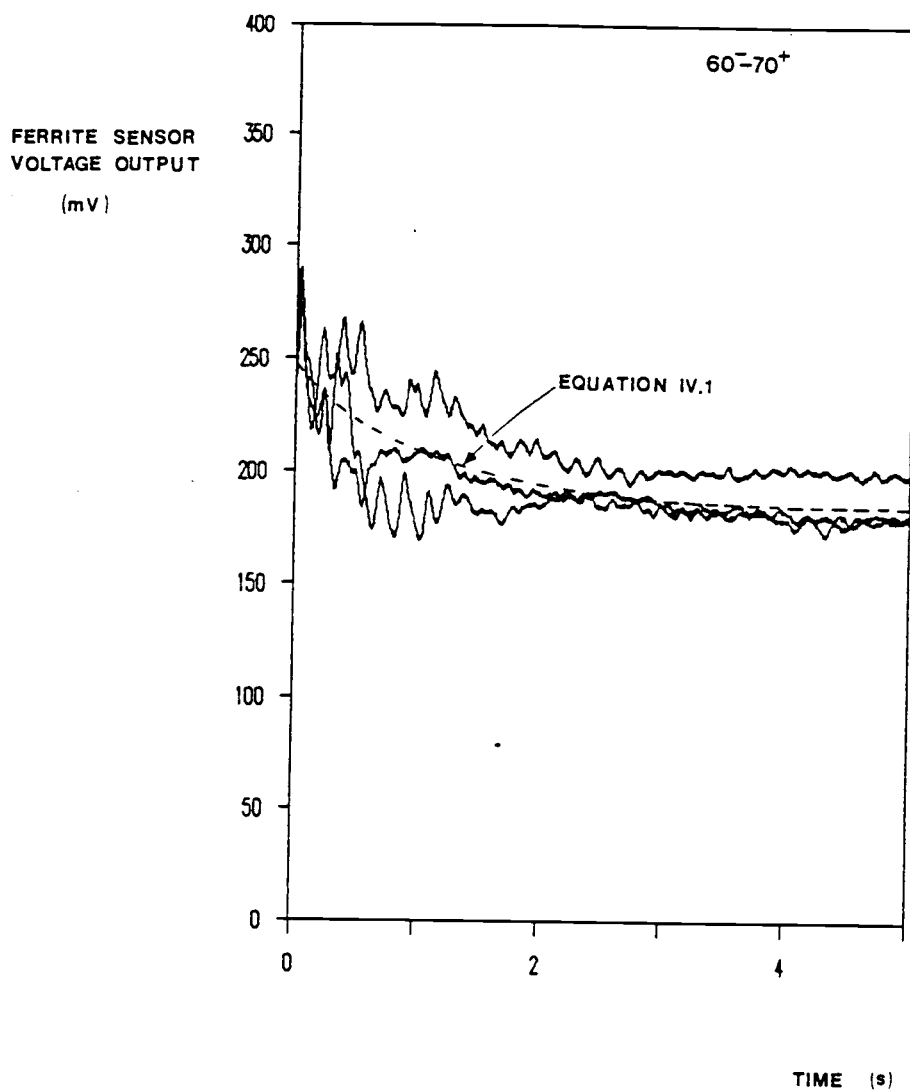


Figure L-2. Results for the Cold Mixing Studies on System C.

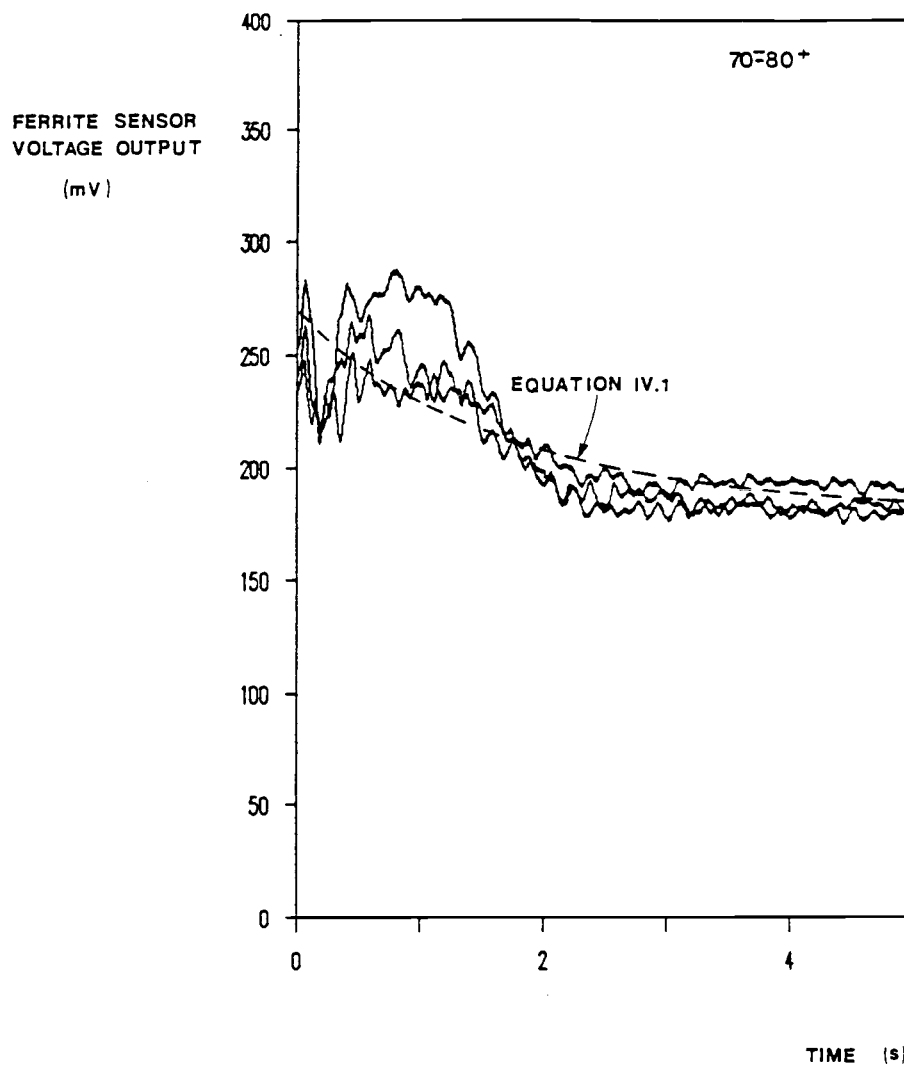


Figure L-3. Results for the Cold Mixing Studies on System D.

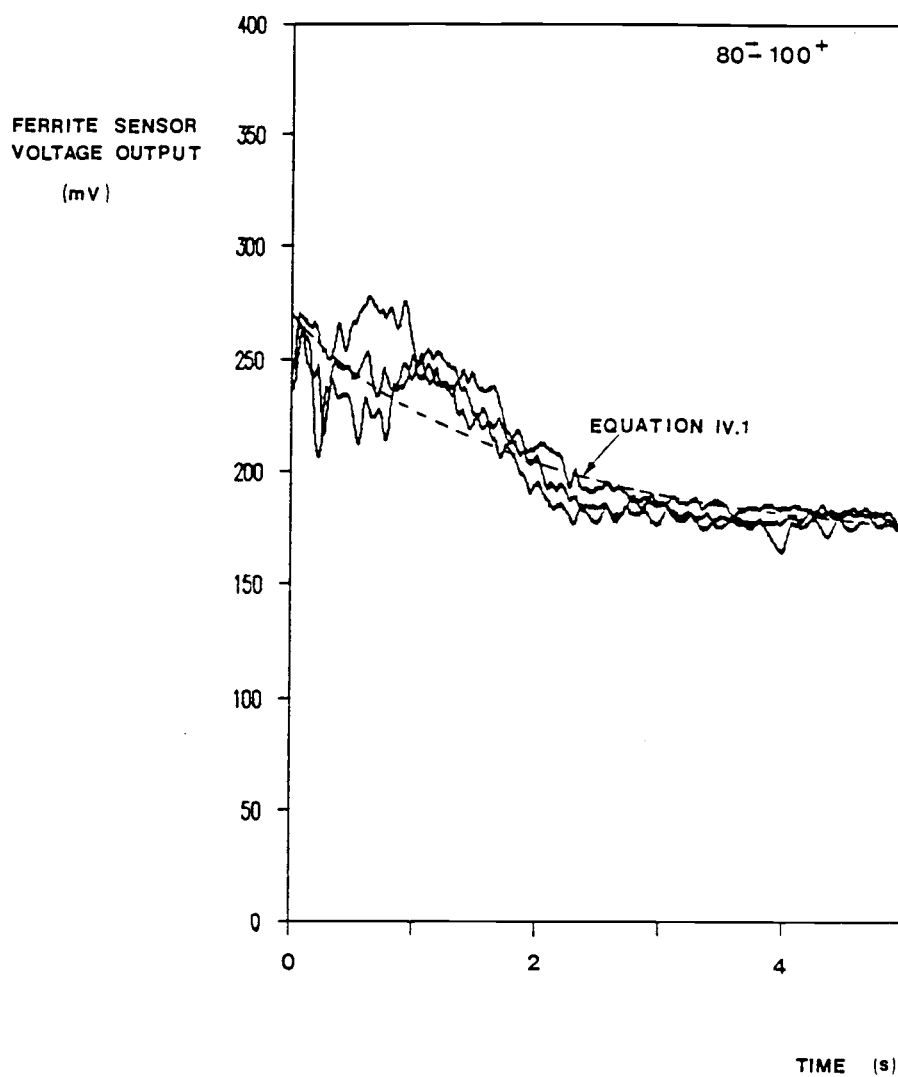


Figure L-4. Results for the Cold Mixing Studies on System E.

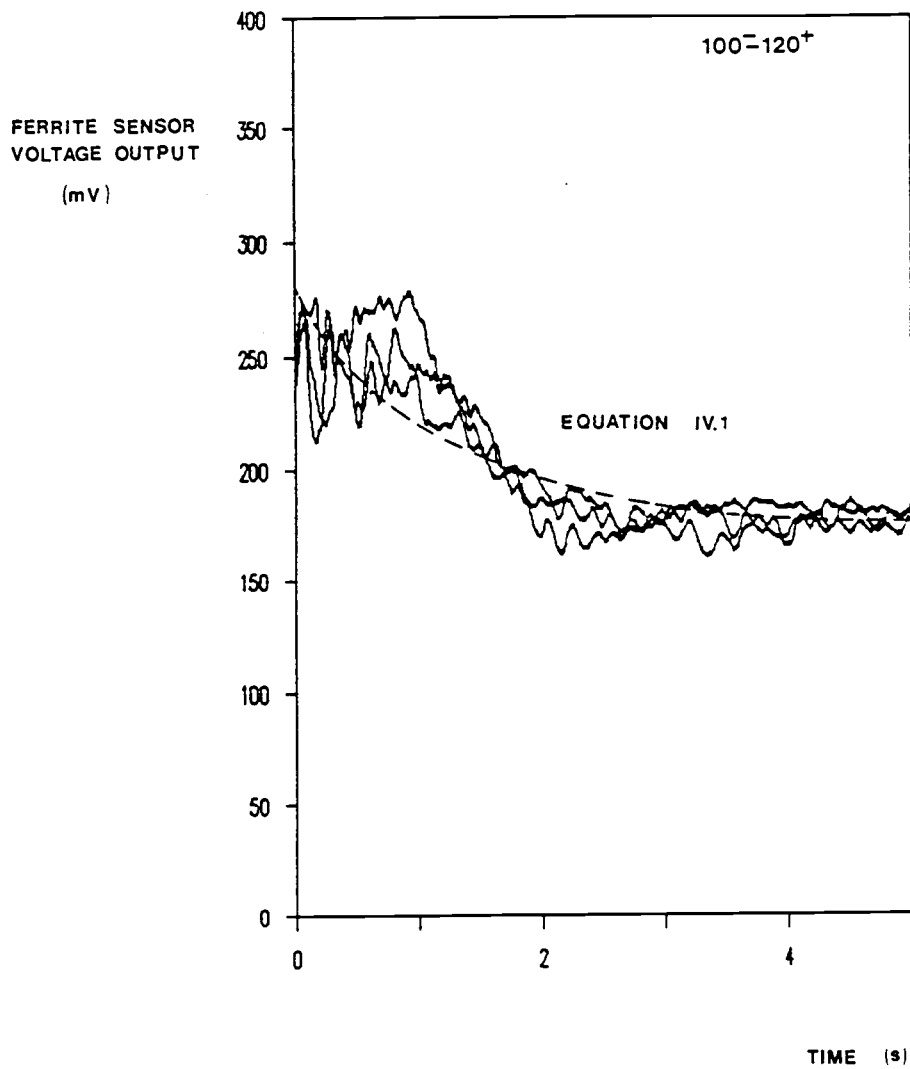


Figure L-5. Results for the Cold Mixing Studies on System F.

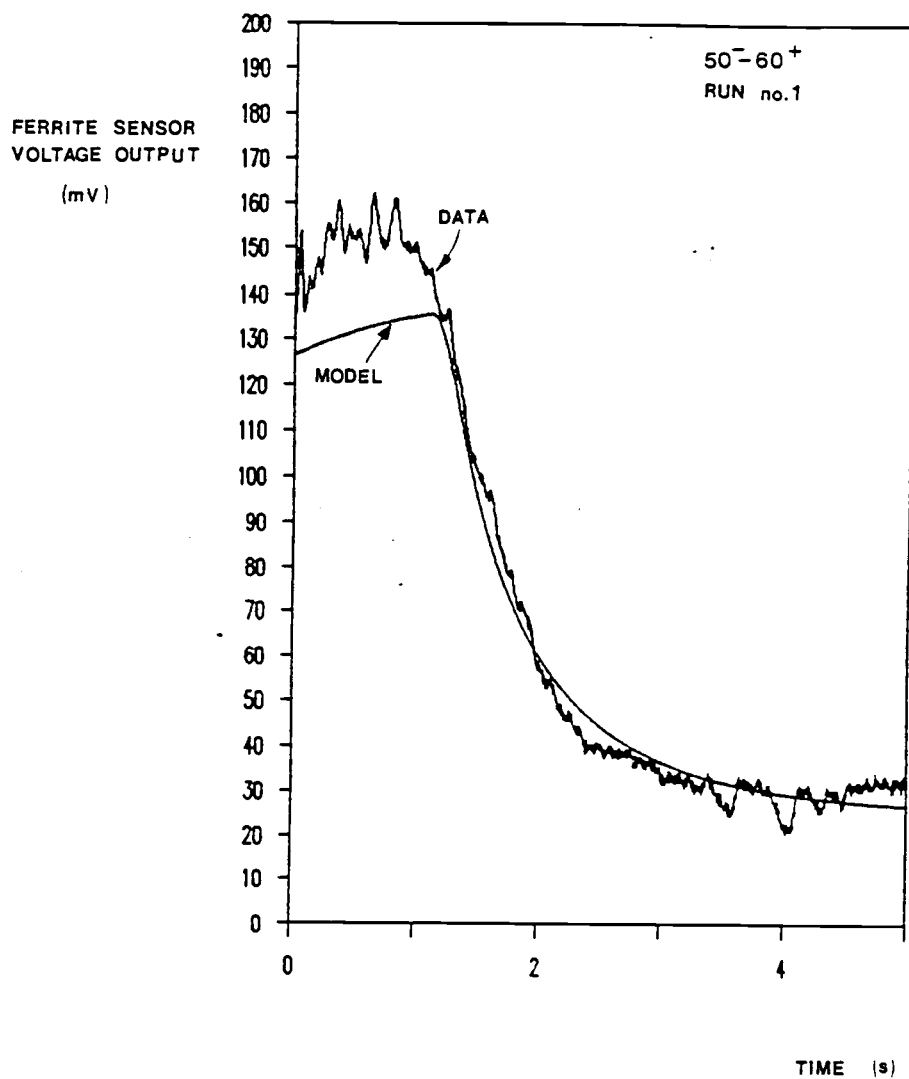


Figure L-6. Results for the Hot Mixing Studies on System B, Run No. 1.

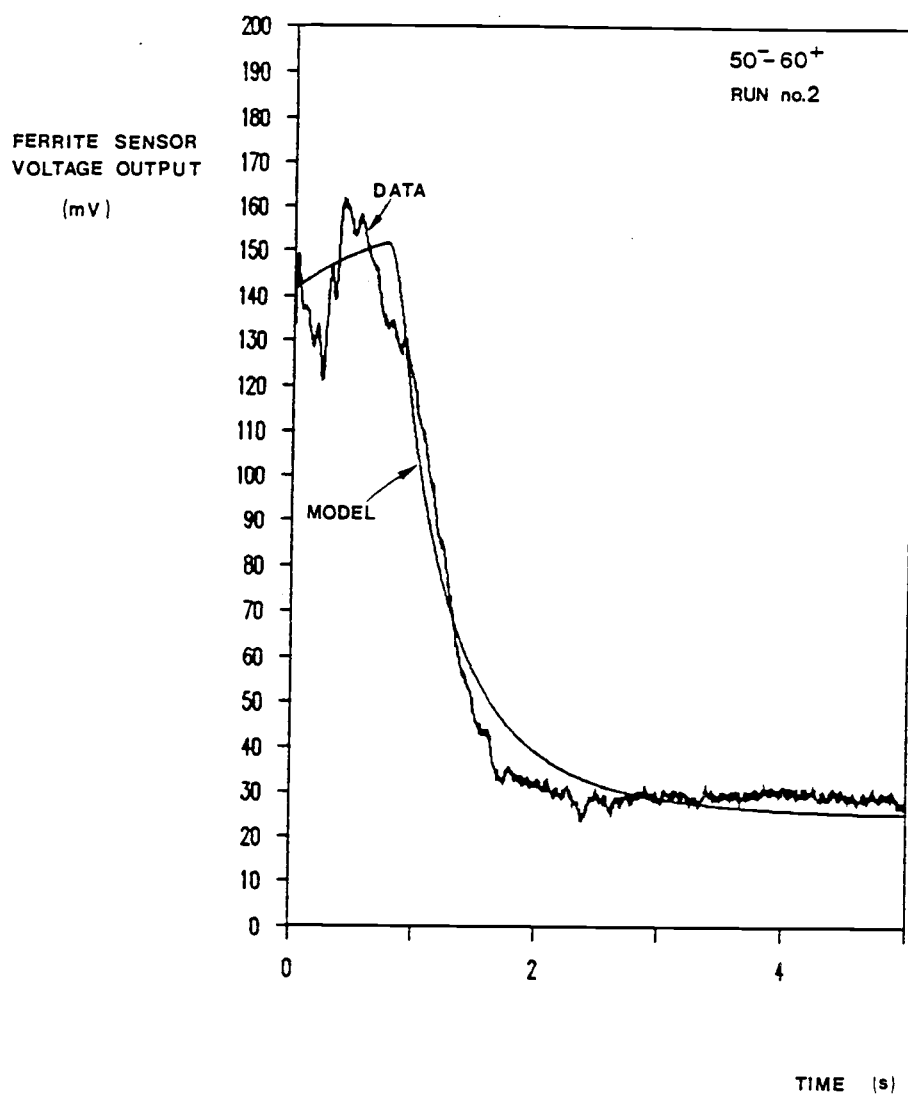


Figure L-7. Results for the Hot Mixing Studies on System B, Run No. 2.

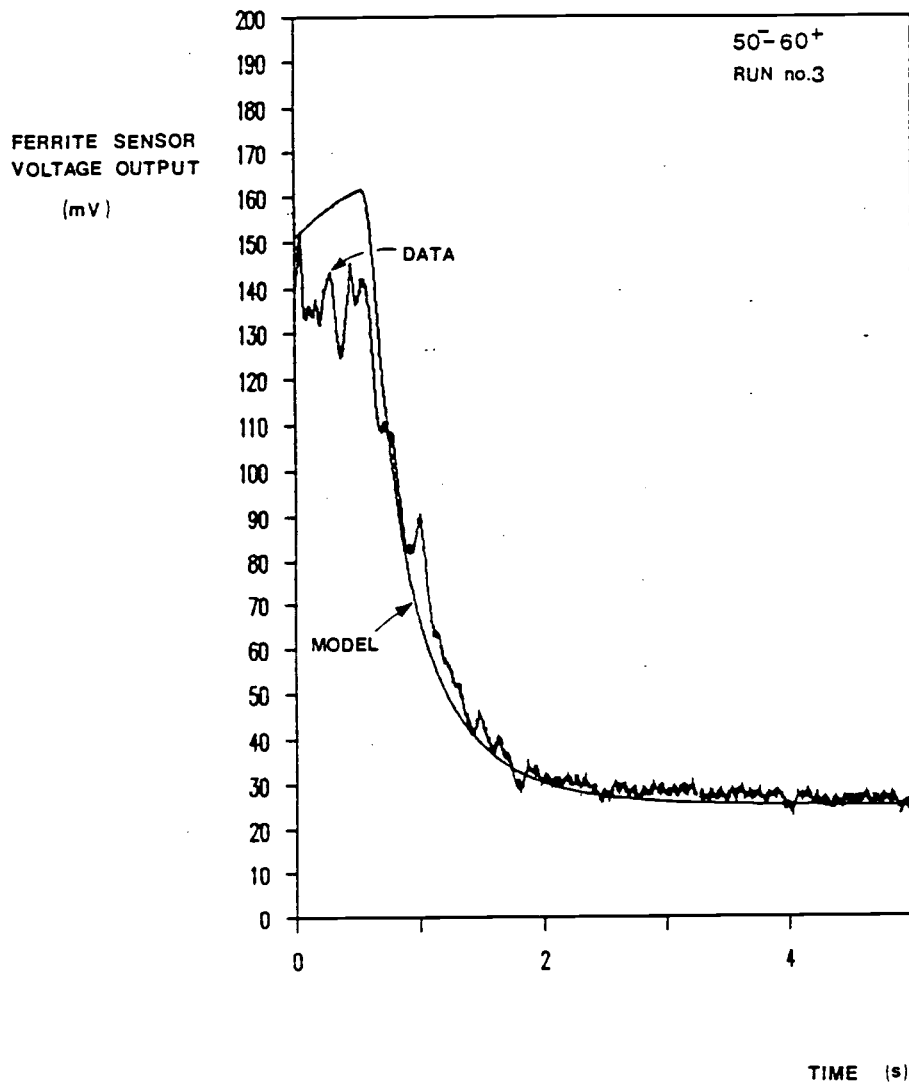


Figure L-8. Results for the Hot Mixing Studies on System B, Run No. 3.

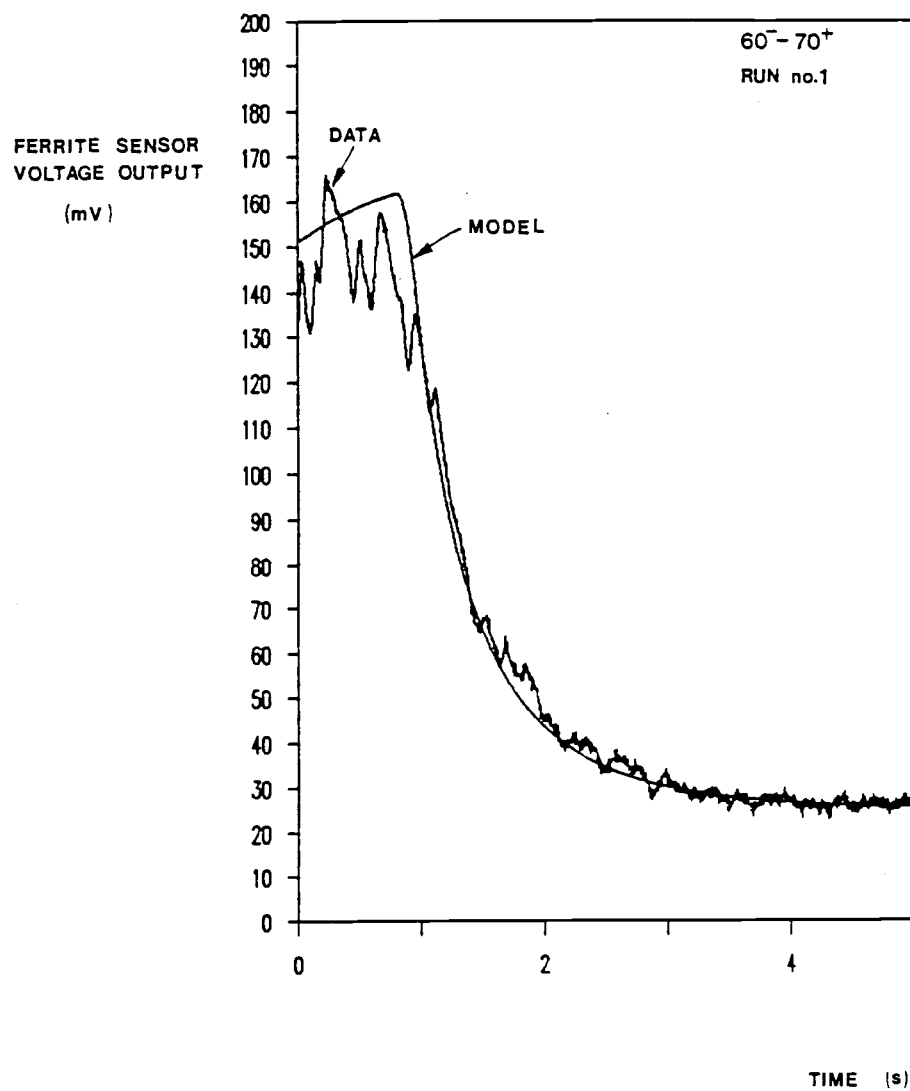


Figure L-9. Results for the Hot Mixing Studies on System C, Run No. 1.

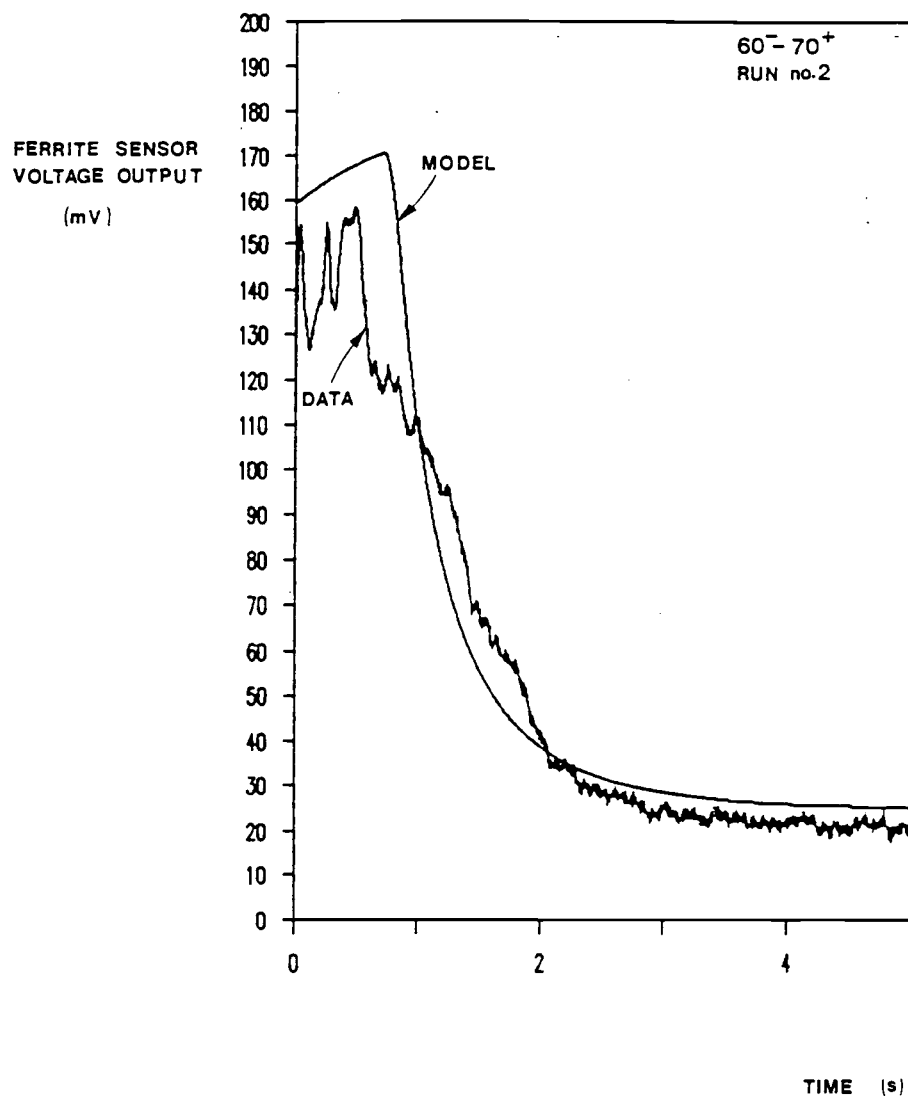


Figure L-10. Results for the Hot Mixing Studies on System C, Run No. 2.

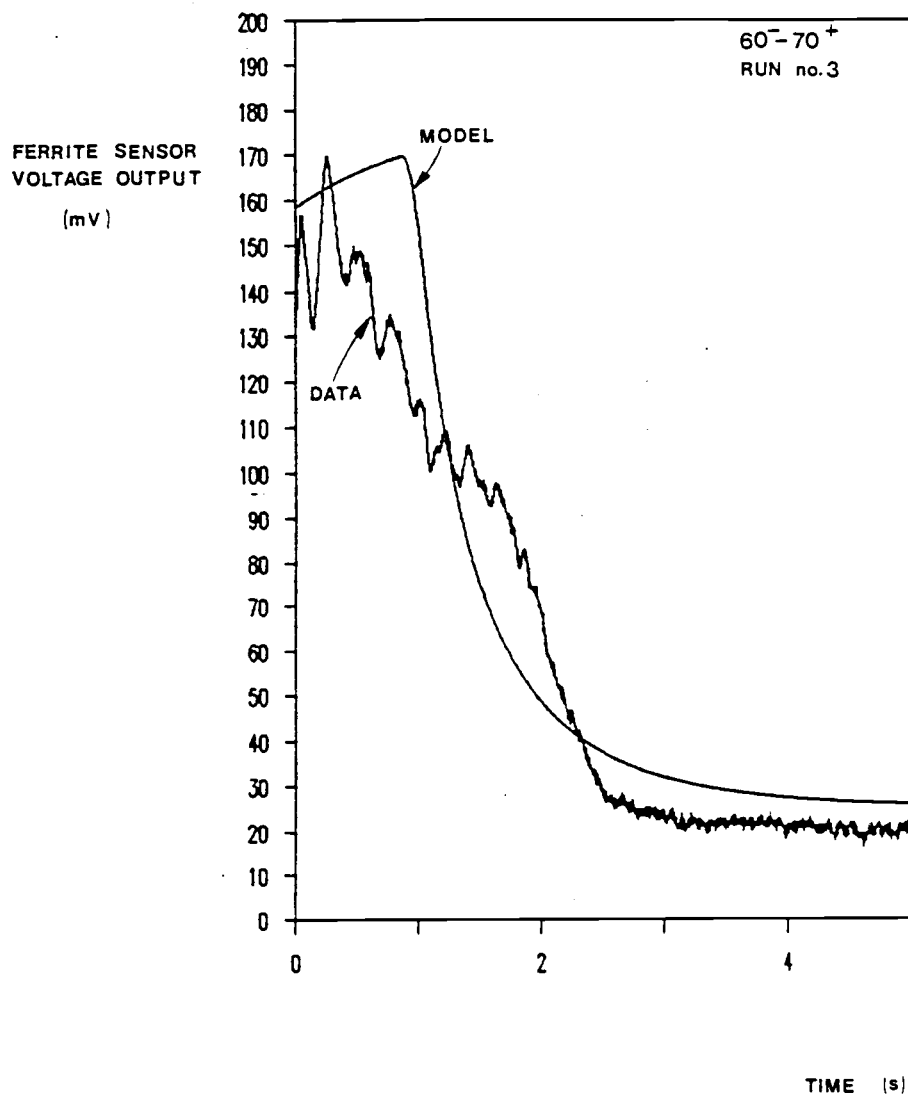


Figure L-11. Results for the Hot Mixing Studies on System C, Run No. 3.

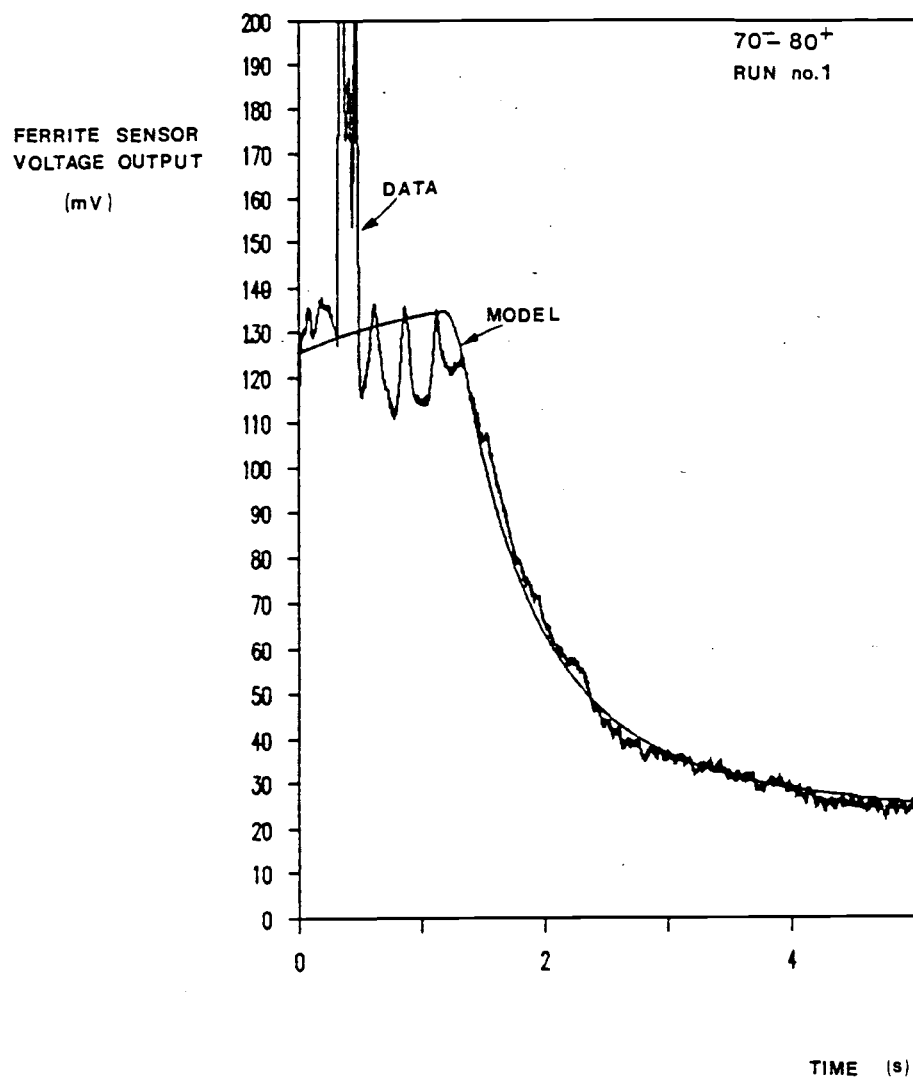


Figure L-12. Results for the Hot Mixing Studies on System D, Run No. 1.

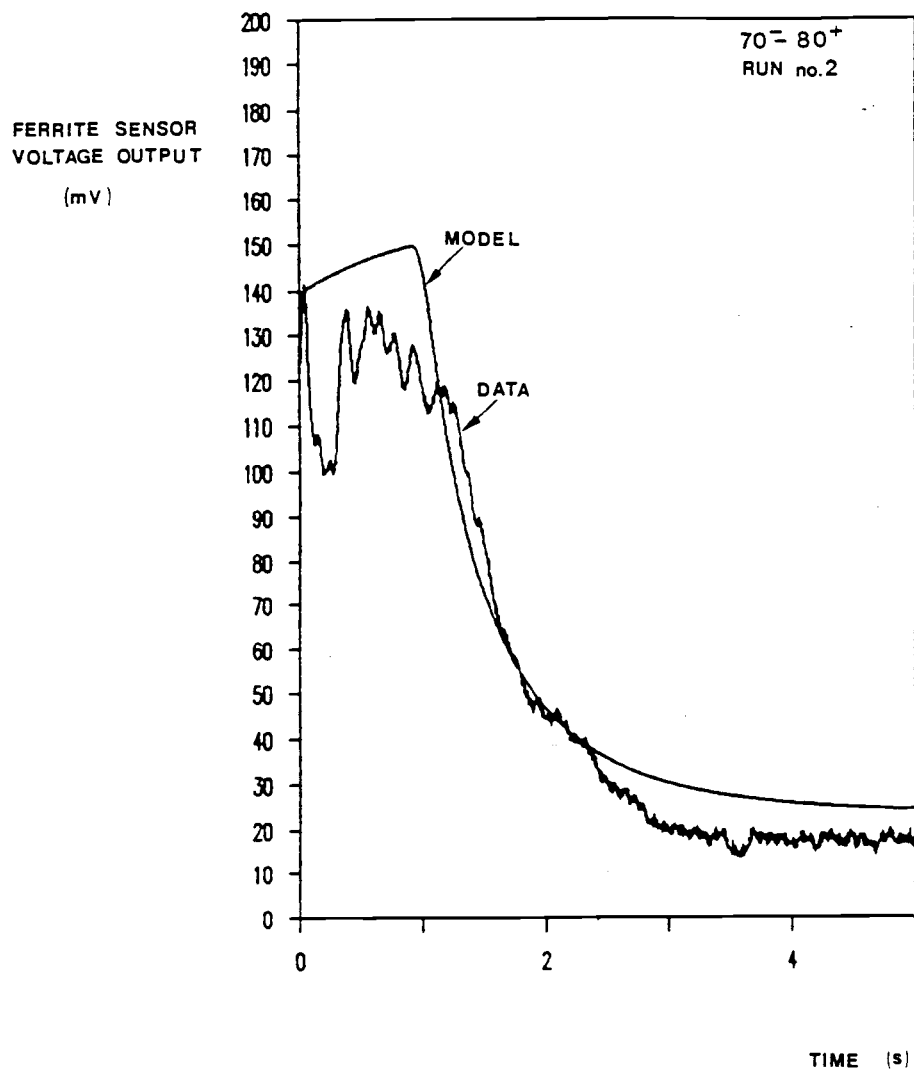


Figure L-13. Results for the Hot Mixing Studies on System D, Run No. 2.

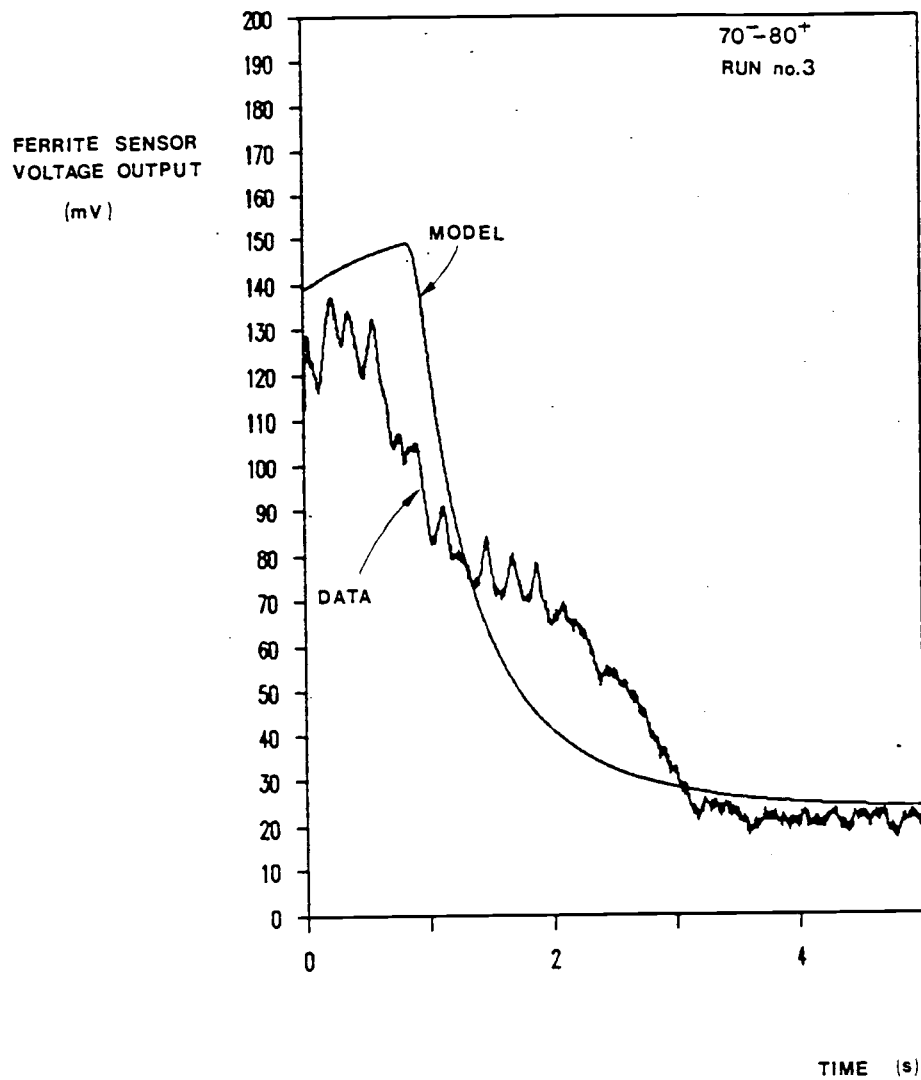


Figure L-14. Results for the Hot Mixing Studies on System D, Run No. 3.

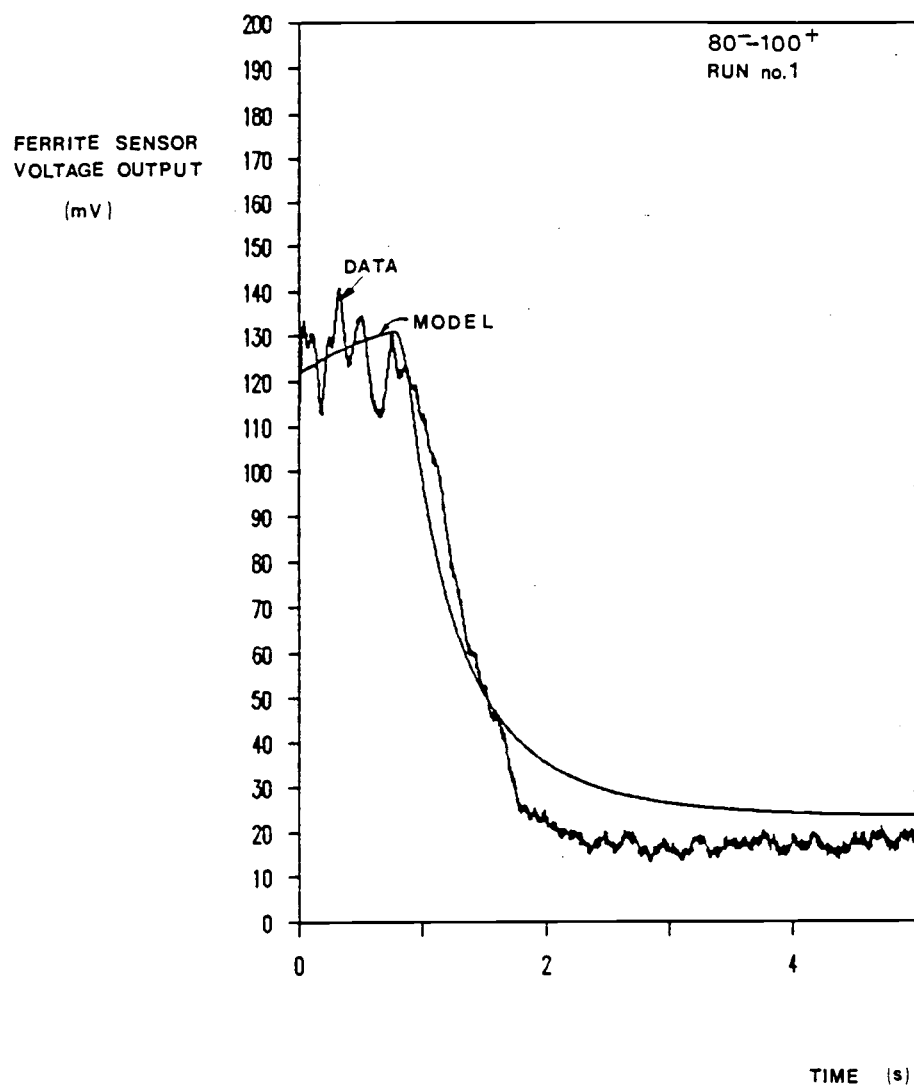


Figure L-15. Results for the Hot Mixing Studies on System E,
Run No. 1.

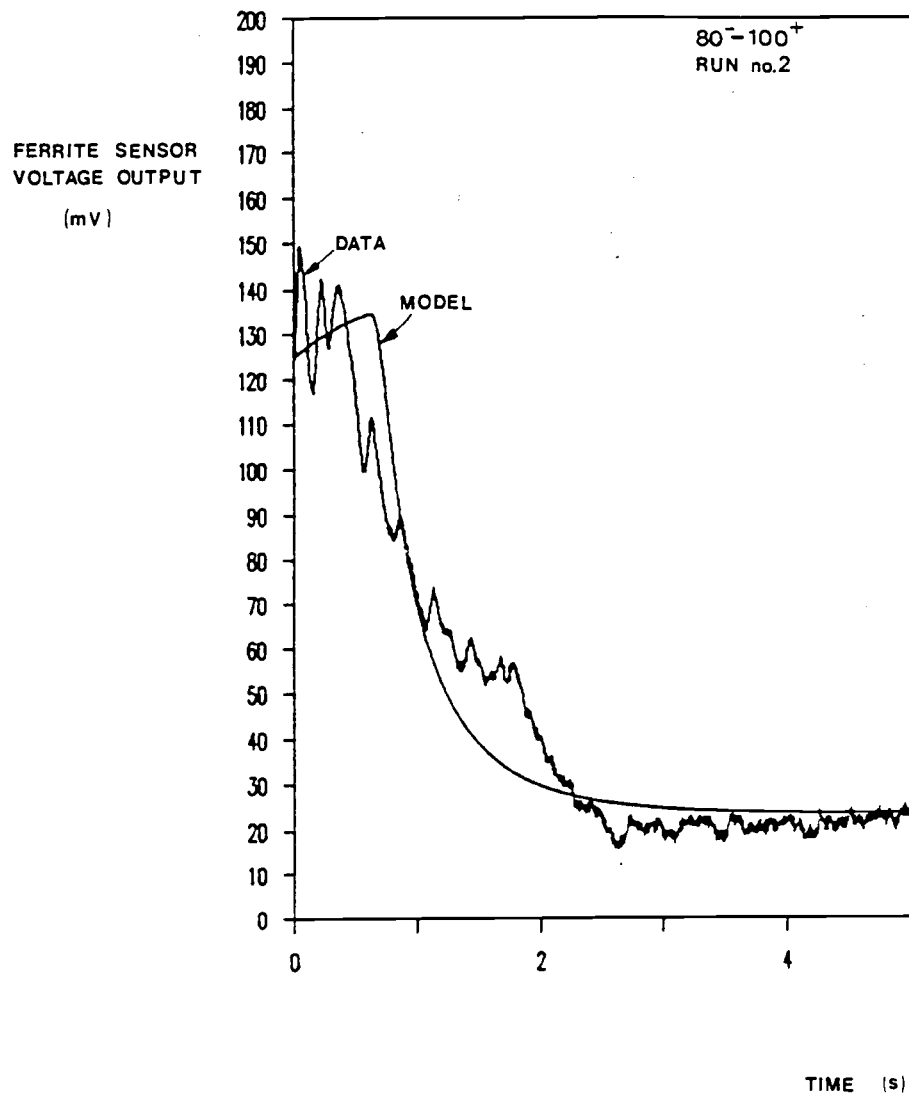


Figure L-16. Results for the Hot Mixing Studies on System E,
Run No. 2.

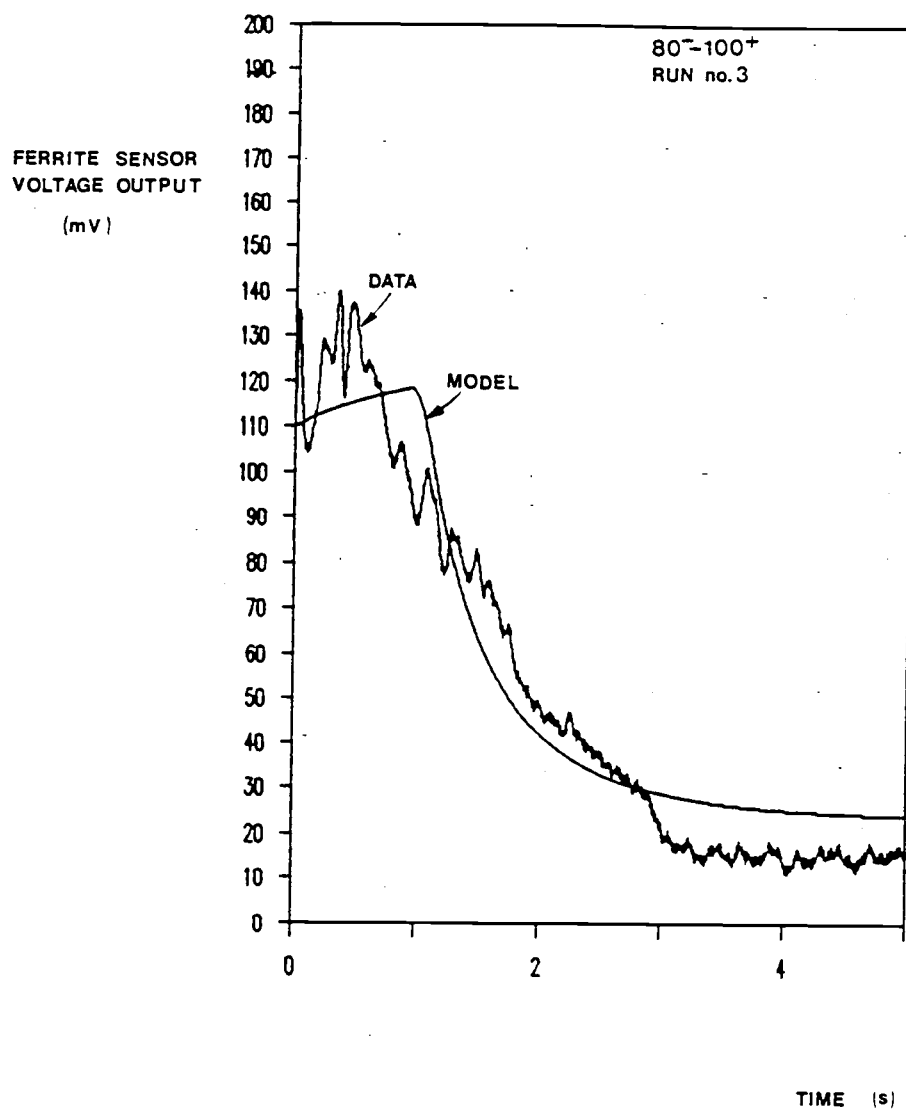


Figure L-17. Results for the Hot Mixing Studies on System E, Run No. 3.

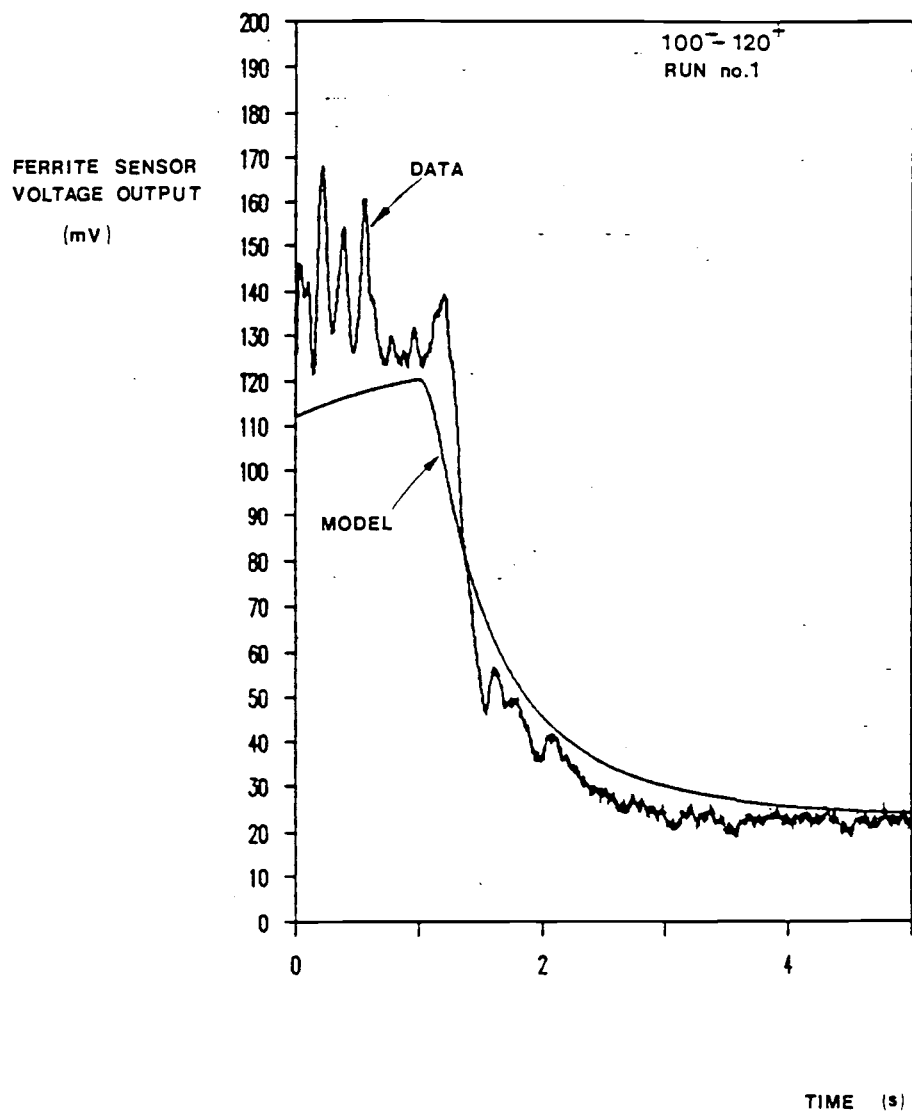


Figure L-18. Results for the Hot Mixing Studies on System F, Run No. 1.

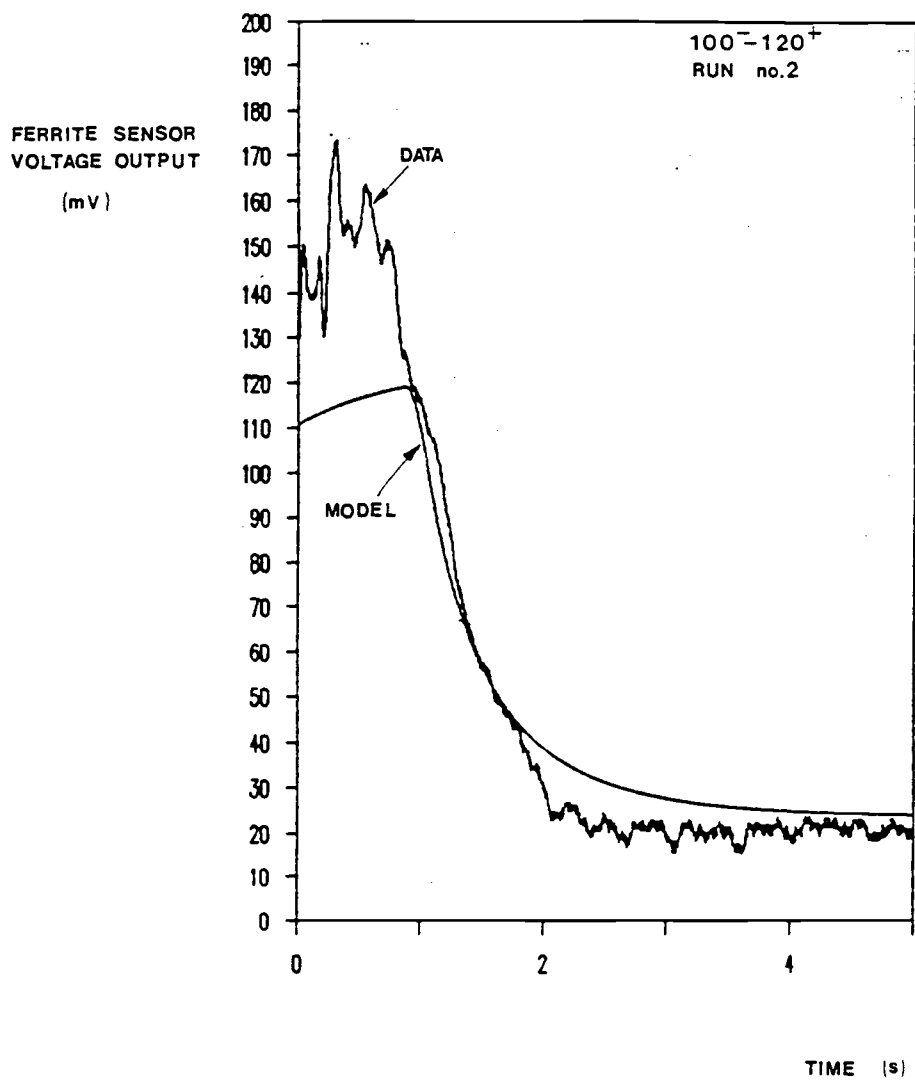


Figure L-19. Results for the Hot Mixing Studies on System F, Run No. 2.

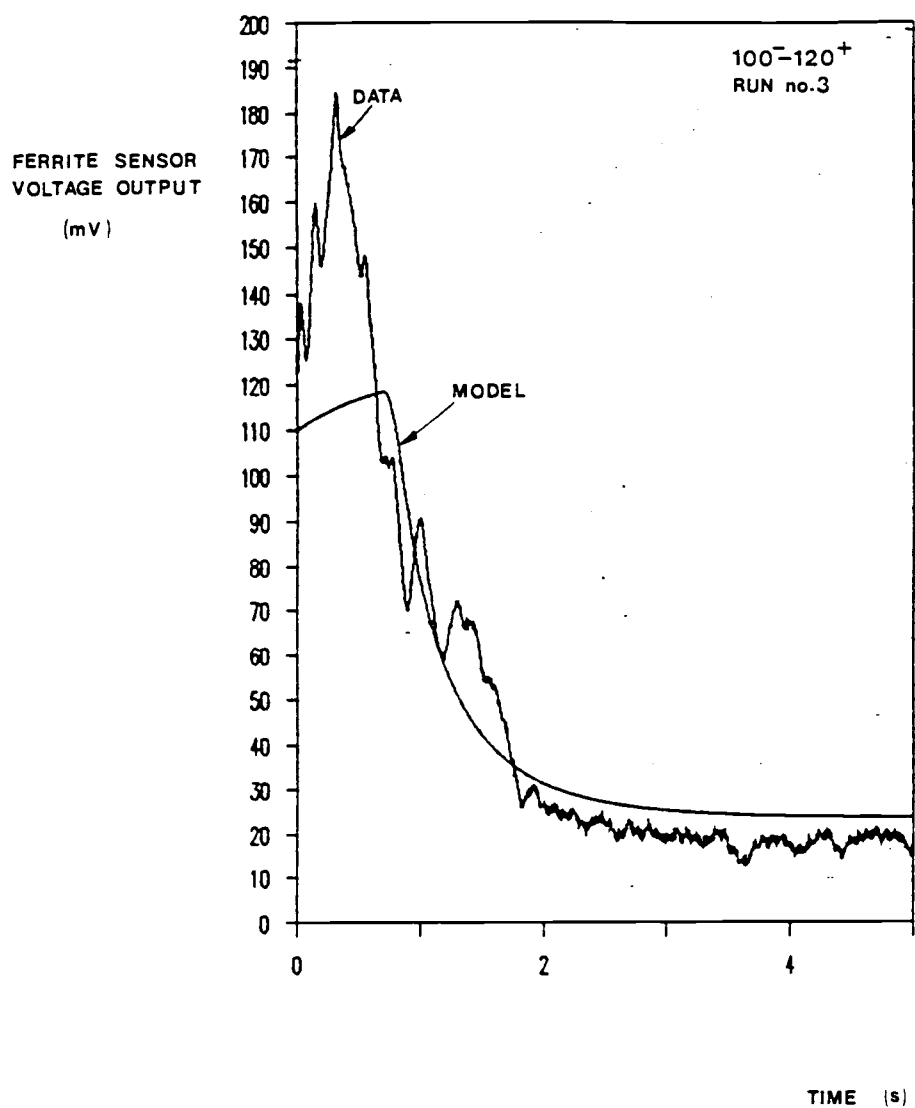


Figure L-20. Results for the Hot Mixing Studies on System F, Run No. 3.